Modelling and optimal climate control of the crop production process in Chinese solar greenhouses

Weituo Sun

A thesis submitted in partial fulfilment of the requirements of Nottingham Trent University for the degree of Doctor of Philosophy

May 2024

Abstract

The Chinese solar greenhouse (CSG), known for its low cost of operation, is a prevalent greenhouse type in Northern China. Climate control of CSG is required for efficient crop production with high yield and quality at low energy and resource costs. However, current heuristic control schemes have limited success in maximising the net revenue of CSG cultivation. Optimal control presents a promising method for improving efficiency of greenhouse production, but few optimal CSG climate control systems have been developed. On the one hand, a well-designed and thoroughly validated integrated model of CSG climate and crop growth, which serves as a basis for optimal control, is unavailable. On the other hand, a user-friendly optimal control algorithm for climate management of a standard CSG without the local controller is currently unavailable. This project aims to model the crop production process and generate an applicable optimal climate control approach for standard CSGs. Firstly, this study developed a lettuce growth model that describes the effects of a broad range of greenhouse climates, including air temperature with extreme conditions, humidity, CO_2 concentration, and shortwave radiation on dynamics of the single state variable, structural crop dry weight. Secondly, we developed and evaluated a CSG climate model to predict indoor radiation, temperature, humidity, and CO_2 based on external weather, greenhouse structure, crops, and controls. Thirdly, the two developed models were synthesized into an integrated CSG climate-crop growth model, which was validated and then smoothed for control purposes. Fourthly, an optimal control system for CSG climate management using event-driven receding horizon design incorporated with real-time feedback was designed and evaluated. Performance comparisons were conducted among ideal optimal control, open loop optimal control, closed loop optimal control, and control supervised by growers. This study provides system models and an optimisation framework for implementing optimal control theory in practical CSG cultivation.

Acknowledgements

My PhD journey lasted for many years, filled with challenges and setbacks. Now it has come to an end. Looking back, there are so many people to thank.

Firstly, I must express my deep gratitude to my director of studies, **Prof. Chungui Lu**. You provided me the opportunity to pursue my PhD study at NTU in the UK, allowing my research career to continue. Thank you for supporting me in every aspect, from thesis writing, experiment design, and procedure settlement to my personal life. Your dedication to research and attitude towards life will influence me forever.

I sincerely thank my co-supervisor, **Dr Anne Coules**, for her guidance throughout my project and meticulous revisions to my writing. I am also grateful to my independent accessor, **Prof. Philippe Wilson**, for his valuable advice at Annual Monitoring.

I am extremely grateful for the sponsorship from NTU. Thank all staff at the ARES School and the Doctoral School. Many thanks to **Dr Richard W. Yarnell**, **Dr Ruth Bromiley-Miller**, **Dr Helen Hicks**, and **Dr Sherran Clarence** for helping me solve various problems and access to seminars and trainings. I feel fortunate to have met colleagues and fellows in Sustainable Agriculture Research Group, **Katherine Hardy**, **Soojin Oh**, **Sulochana Gunasena**, **Gadelhag Mohmed**, **Gultekin Hasanaliyeva**, **Xanthea Heynes**, and **Helen Baxter**, thank you for your companionship and assistance. Additional thanks to my external examiner, **Prof. Ruchi Choudhary**, from University of Cambridge.

I transferred my PhD study from Wageningen University in The Netherlands, and I also appreciate this experience. I am sincerely grateful to my promotor, **Prof. Eldert van Henten**, for opening the door to modelling and control for me. Many thanks to my daily supervisors, **Dr Simon van Mourik** and **Dr Daniel Reyes Lastiri**, for their detailed guidance on my proposal, research, and experiments. I am also thankful to **Prof. Peter Groot Koerkamp**,

Dr Rachel van Ooteghem, **Dr Bert van't Oosfer**, and **Dr Cecilia Stanghellini** for their support, knowledge sharing, and fruitful discussions. I would like to express my sincere gratitude to my lovely and talented fellow PhD students from Farm Technology Group and Horticulture and Product Physiology Group: **Yuexiang Chen**, **David Katzin**, **Henry James Payne**, **Bo Zhou**, **Mengting Zhou**, **Junfeng Gao**, **Yuqi Zhang**, **Yongran Ji**. Thanks to all my doctoral classmates and organisers in the WUR-CAAS program. I will not forget the days we spent together preparing for the IELTS and studying in Beijing and Wageningen.

Special thanks to **Prof. Qichang Yang** from Chinese Academy of Agricultural Sciences, my respected mentor, for his unwavering support in my PhD project.

I could not have completed my PhD research without the strong support of the leaders and my colleagues at Intelligent Equipment Research Center, Beijing Academy of Agriculture and Forestry Sciences: **Prof. Wenzhong Guo**, **Prof. Chunjiang Zhao**, **Prof. Liping Chen**, **Prof. Wengang Zheng**, **Dr Lichun Wang**, and **Prof. Xiaoming Wei**. Thanks to Hongke Farm for providing the experimental greenhouses and crop cultivation management.

Finally, my biggest thanks go to my wife, **Ning Lu**, who is beautiful, kind, and brave, and has supported me unconditionally. Thanks to my son, **Tianyu Sun**, for bringing happiness into my life and to my parents for their support of our family.

Looking forward, I will remain grateful and contribute to the advancement of global technology and sustainable agriculture. I would like to end up with two sentences that always encourage me through my PhD study journey:

It is never too late to start anything from now.
A little faith goes a long way.

List of publications

Published papers

Weituo Sun, Xiaoming Wei, Baochang Zhou, Chungui Lu, Wenzhong Guo. Greenhouse heating by energy transfer between greenhouses: System design and implementation, Applied Energy, 2022, 325: 119815. https://doi.org/10.1016/j.apenergy.2022.119815.

Chen Fan, **Sun Weituo**, Yu Wenya, Wei Xiaoming, Zhou Baochang, Li Youli, Guo Wenzhong. Analysing light and thermal environment and insulation performance of a multi-span greenhouse with external insulation. Transactions of the Chinese Society of Agricultural Engineering, 2023, 39(6): 194-203. https://doi.org/10.11975/j.issn.1002-6819.202212081.

Gadelhag Mohmed, Xanthea Heynes, Abdallah Naser, **Weituo Sun**, Katherine Hardy, Steven Grundy, Chungui Lu. Modelling daily plant growth response to environmental conditions in Chinese solar greenhouse using Bayesian neural network. Scientific Reports, 2023, 13(1): 4379. https://doi.org/10.1038/s41598-023-30846-y.

Zhou Bo, **Sun Weituo**, Guo Wenzhong, Zhou Baochang, Shi Lei, Li Guangju. Analysis and optimization of greenhouse gutter effect on radiation distribution inside multi-span greenhouses based on dynamic model. Transactions of the Chinese Society for Agricultural Machinery, 2021, 52(5): 286-292. https://doi.org/10.6041/i.issn.1000-1298.2021.05.031.

Sun Weituo, Zhou Bo, Xu Fan, Shang Chao, Chungui Lu, Guo Wenzhong. Performance of positive pressure fan-pad cooling system and cooling load model for Chinese solar greenhouse. Transactions of the Chinese Society of Agricultural Engineering, 2019, 35(16): 214-224. https://doi.org/10.11975/j.issn.1002-6819.2019.16.024.

Papers to be submitted

A lettuce growth model responding to a broad range of greenhouse climates

A full-scale climate model of the Chinese solar greenhouse

An integrated model of Chinese solar greenhouse climate and crop growth for control

Event-driven receding horizon optimal control of Chinese solar greenhouse climate

Contents

List of figures

List of tables

Nomenclature

Latin symbols

A_C	gross canopy assimilation rate, kg (CO_2) m^{-2} (gro) s^{-1}
$A_{C,gh}$	gross canopy assimilation rate at the whole greenhouse level, kg (CO_2) m^{-2} (gro) s^{-1}
A_{cov}	surface area of CSG cover or envelope, m^2
A_{cul}	effective cultivated area of greenhouse, m^2
A_L	gross assimilation rate of individual leaves, kg (CO_2) m^{-2} (leaf) s^{-1}
$A_{L,C}$	gross leaf assimilation rate at a whole canopy level, kg (CO_2) m^{-2} (leaf) s^{-1}
$A_{L,c,n}$	net leaf assimilation rate only limited by CO_2 concentration, kg (CO_2) m^{-2} (leaf) s^{-1}
$A_{L,li}$	gross leaf assimilation rate at canopy depth l_i, kg (CO_2) m^{-2} (leaf) s^{-1}
$A_{L,mm}$	maximum endogenous photosynthetic capacity, kg (CO_2) m^{-2} (leaf) s^{-1}
$A_{L,sat}$	potential gross leaf assimilation rate at light saturation, kg (CO_2) m^{-2} (leaf) s^{-1}
$A_{L,sat,n}$	net leaf assimilation rate at light saturation, kg (CO_2) m^{-2} (leaf) s^{-1}
$A_{vent,r}$	maximum opening area of CSG roof vent, m^2
$A_{vent,r,U}$	controlled opening area of CSG roof vent, m^2
$A_{vent,s}$	maximum opening area of CSG side vent, m^2
$A_{vent,s,U}$	controlled opening area of CSG side vent, m^2
C_{1_2}	convective heat flux from object 1 to object 2, W m^{-2} (gro)
cap	heat capacity of CSG object, J $°C^{-1}$ m^{-2} (gro)
cap_{MC}	capacity of indoor air to store CO_2, kg m^{-2} (gro)
cap_{MV}	capacity of indoor air to store water, kg m^{-2} (gro)
C_{buf}	amount of stored carbohydrates in the buffer, kg (CH_2O) m^{-2} (gro)
$C_{buf,max}$	maximum buffer capacity for diurnal assimilates storage, kg (CH_2O) m^{-2} (gro)
c_d	discharge coefficient of CSG vent openings, -
c_H	constant for calculating maximum electron transport rate, J mol^{-1}
c_{hfw}	ratio of head fresh weight to head dry weight of the lettuce crop, -
$CO2_{out}$	CO_2 concentration of the outdoor air, µmol mol^{-1}
$c_{p,a}$	specific heat capacity of air at constant pressure, J kg^{-1} $°C^{-1}$
$c_{p,L}$	specific heat capacity of crop leaves, J kg^{-1} $°C^{-1}$
$c_{p,obj}$	specific heat capacity of the CSG object, J kg^{-1} $°C^{-1}$
$c_{r,I}$	canopy reflection coefficient for shortwave radiation, -
$c_{r,PAR}$	canopy reflection coefficient for PAR, -
$c_{rc,1}$	coefficient of the quadratic term of the fitting for carboxylation resistance description, m s^{-1} $°C^{-2}$
$c_{rc,2}$	coefficient of the linear term of the fitting for carboxylation resistance description, m s^{-1} $°C^{-1}$
$c_{rc,3}$	constant term of the fitting for carboxylation resistance description, m s^{-1}
$c_{Rd,25,r}$	maintenance coefficient for the root at 25°C, kg (CH_2O) kg (dry matter) s^{-1}
$c_{Rd,25,sh}$	maintenance coefficient for the shoot (leaf) at 25°C, kg (CH_2O) kg

	(dry matter) s^{-1}
c_S	constant for calculating maximum electron transport rate, J mol^{-1} K^{-1}
c_T	temperature difference factor, m s^{-1} $K^{-1/2}$
$c_{w,cd}$	combined wind pressure coefficient for empirically describing wind effect ventilation rate, -
$c_{w,r}$	wind pressure coefficient of CSG roof vent, -
$c_{w,rs}$	global wind pressure coefficient of CSG vent openings, -
c_α	factor that converts assimilated CO_2 into sugar equivalents in the photosynthesis process, -
c_β	factor that converts carbohydrates to structural material due to the growth respiration and synthesis, -
c_ζ	scaling factor that accounts for the faster diffusion of H_2O compared to CO_2 in crossing stomata, -
$c_{\sigma r,1}$	coefficient 1 for root ratio description, plants kg^{-1}
$c_{\sigma r,2}$	coefficient 2 for root ratio description, -
D	vector of external weather
D_{1_2}	conductive heat flux from object 1 to object 2, W m^{-2} (gro)
e_{air}	vapour pressure of indoor air, Pa
E_{air_out}	Sensible heat exchange between indoor and outdoor air caused by air exchange, W m^{-2} (gro)
E_c	crop transpiration rate, kg m^{-2} (gro) s^{-1}
$e_{c,a}$	leaf to air vapour pressure difference, equal to VPD, Pa
$E_{c,gh}$	crop transpiration rate at the whole greenhouse level, kg m^{-2} (gro) s^{-1}
E_J	activation energy of the maximum electron transport rate, J mol^{-1}
e_{out}	vapour pressure of outdoor air, Pa
$e_{s,2}$	saturated vapour pressure of object 2 at its temperature, Pa
$e_{s,air}$	saturated vapour pressure of greenhouse air, Pa
$e_{s,can}$	saturated vapour pressure of the canopy at its temperature, Pa
$e_{s,sr,in}$	saturated vapour pressure of the south roof inner surface at its temperature, Pa
E_{so}	soil evaporation rate inside the greenhouse, kg m^{-2} (gro) s^{-1}
$F_{1,2}$	view factor of object 1 to object 2, -
$F_{1,sky}$	view factor of an internal surface of the CSG to sky, -
$f_{I,s}$	radiation dependency for stomatal resistance, -
$f_{I,SLA}$	factor accounting for the effect of radiation on *SLA*, -
$f_{Tc,s}$	temperature dependency for stomatal resistance, -
$f_{Xc,s}$	CO_2 dependency for stomatal resistance, -
$f_{Xh,s}$	humidity dependency for stomatal resistance, -
$f_{Xh,SLA}$	factor accounting for the effect of air humidity on *SLA*, -
g	acceleration of gravity, m s^{-2}
g_{ae}	total air exchange rate of the CSG, m^3 m^{-2} (gro) s^{-1}
g_{inf}	air exchange rate due to infiltration, m^3 m^{-2} (gro) s^{-1}
g_{nv}	CSG natural ventilation rate, m^3 m^{-2} (gro) s^{-1}
$g_{vent,r}$	natural ventilation rate when only roof vent is opened, m^3 m^{-2} (gro) s^{-1}
$g_{vent,rs}$	natural ventilation rate when both roof and side vents are opened, m^3 m^{-2} (gro) s^{-1}
h_{1_2}	convective heat transfer coefficient between object 1 and object 2, W m^{-2} °C^{-1}
h_{buf}	buffer dependent inhibition function for canopy assimilation, -
H_{gh}	average height of the CSG, m

$H_{vent,r}$	vertical dimension of CSG roof vent, m
$H_{vent,rs}$	vertical distance between mid-points of CSG roof and side vents, m
I	shortwave radiation at the top of the canopy, W m^{-2} (gro)
I_{can}	absorbed shortwave radiation by the canopy, W m^{-2} (gro)
$I_{L,ref}$	arbitrary reference absorbed shortwave radiation by leaves corresponding to SLA_{ref}, W m^{-2} (leaf)
I_n	normal incident solar radiation, W m^{-2}
I_{obj}	absorbed shortwave radiation (solar radiation) by CSG object, W m^{-2} (gro)
I_{out}	horizontal outdoor solar radiation, W m^{-2}
J	net economic return; cost function
J_{max}	maximum electron transport rate, µmol (e-) m^{-2} (leaf) s^{-1}
$J_{max,25}$	maximum electron transport rate at 25°C, µmol (e^-) m^{-2} (leaf) s^{-1}
k_I	extinction coefficient for shortwave radiation, -
k_{PAR}	extinction coefficient for PAR, -
k_R	extinction coefficient for longwave radiation, -
L	running costs of the controllable objects for climate conditioning
L_{1_2}	latent heat flux from object 1 to object 2, W m^{-2} (gro)
LAI	leaf area index, m^2 (leaf) m^{-2} (gro)
LAI_{gh}	leaf area index at the whole greenhouse level, m^2 (leaf) m^{-2} (gro)
L_{c1}	length of connecting line between roof ridge and bottom angle of north wall, m
L_{c2}	length of connecting line between bottom angle of south roof and apex of north wall, m
Le	Lewis number for CO_2 in air at 25 °C, -
Le_v	Lewis number for water vapour in air, -
l_f	leaf characteristic dimension, taken as the mean leaf width in wind direction, m
L_{gro}	span of the CSG, m
l_i	canopy depth, m^2 (leaf) m^{-2} (gro)
L_{nr}	length of the north roof, m
L_{nw}	height of the north wall, m
L_{obj}	characteristic length of CSG object, m
L_{sr}	arc length of the south roof, m
$L_{sr,c}$	length of the line connecting bottom to ridge of south roof, m
MC_{air_out}	CO_2 flux from the indoor air to the outdoor air generated by air exchange, kg m^{-2} (gro) s^{-1}
M_{CO2}	molar mass of CO_2, kg mol^{-1}
M_v	molar mass of water (and vapour), kg mol^{-1}
MV_{1_2}	water vapour flux from object 1 to object 2, kg m^{-2} (gro) s^{-1}
n	the nth day of the year, -
N_{inf}	air infiltration rate of the CSG, h^{-1}
P	vector of model parameters
PAR_a	absorbed photosynthetically active radiation (PAR), W m^{-2} (leaf)
$PAR_{a,li}$	absorbed PAR for a specific leaf layer at canopy depth l_i, W m^{-2} (leaf)
p_b	reduction fraction of the external thermal blanket to η_{inf}, -
$Q_{10,gr}$	Q_{10} factor for crop growth, -
$Q_{10,Rd}$	Q_{10} value for maintenance respiration, -
$Q_{10,Rso}$	Q_{10} value for soil respiration, -
$Q_{10,\Gamma}$	Q_{10} value for CO_2 compensation point, -

R_{1_2}	longwave radiation heat flux from object 1 to object 2, W m^{-2} (gro)
R_{1_sky}	longwave radiation heat flux from an internal surface of the CSG to sky, W m^{-2} (gro)
r_b	boundary layer resistance, s m^{-1}
r_{bh}	boundary layer resistance or aerodynamic resistance to convective heat transfer, s m^{-1}
r_{bv}	boundary layer resistance to diffusion of H_2O, s m^{-1}
r_c	carboxylation resistance, s m^{-1}
r_{CO2}	total leaf resistance to CO_2 diffusion, s m^{-1}
R_d	crop maintenance or dark respiration rate, kg (CH_2O) m^{-2} (gro) s^{-1}
$R_{d,25}$	leaf maintenance (dark) respiration rate at a reference temperature of 25 °C, kg (CH_2O) m^{-2} (gro) s^{-1}
$R_{d,gh}$	crop maintenance respiration rate at the whole greenhouse level, kg (CO_2) m^{-2} (gro) s^{-1}
R_g	gas constant, J mol^{-1} K^{-1}
RGR_{max}	maximum relative growth rate that depends on temperature, s^{-1}
$RGR_{max,20}$	maximum relative growth rate of dry matter at 20°C, s^{-1}
$r_{H2O,min}$	minimum possible internal crop resistance to H_2O, s m^{-1}.
RH_{out}	relative humidity of the outdoor air, -
R_n	net radiation of the crop, W m^{-2}
r_s	stomatal resistance, s m^{-1}
R_{sm}	soil microbial respiration rate in greenhouse, kg (CO_2) m^{-2} (gro) s^{-1}
$R_{so,0}$	soil respiration rate at a reference temperature of 0 °C, kg (CO_2) m^{-2} (gro) s^{-1}
r_{sv}	stomatal resistance to diffusion of H_2O, s m^{-1}
r_t	turbulence resistance, s m^{-1}
s	slope of smoothing functions
SLA	specific leaf area of new leaves, expressing the amount of leaf area per unit shoot dry matter, m^2 (leaf) kg^{-1} (leaf)
SLA_{ref}	reference SLA at the reference absorbed shortwave radiation by leaves $I_{L,ref}$ and relative humidity $X_{h,ref}$, m^2 (leaf) kg^{-1} (leaf)
t	time, s
t_0	initial time for optimisation
$T_{0,K}$	0 °C in Kelvin, = 273.15 K
$T_{1,K}$, $T_{2,K}$	temperatures in Kelvin of object 1 and object 2, K
$T_{25,K}$	25 °C in Kelvin, = (25 + $T_{0,K}$) K
t_{AST}	local time measured in hours, -
T_c, T_{can}	canopy temperature, °C
$T_{c,K}$	canopy temperature in Kelvin, = (T_c + $T_{0,K}$) K
$T_{c,RGR}$	temperature to achieve the saturation relative growth rate, °C
t_{cover}	covering time of the thermal blanket, s
T_{dp}	dew point temperature of the outdoor air, °C
t_f	final time for optimisation
T_{obj}	temperature of CSG object, °C
T_{out}	outdoor air temperature, °C
$T_{out,K}$	outdoor air temperature in Kelvin, K
$T_{sky,K}$	effective sky temperature in Kelvin, K
$T_{so,cs}$	constant soil temperature, °C
$t_{uncover}$	time for rolling up the thermal blanket, s
$t_{vent,r,off}$	closing time of roof vent, s

$t_{vent,r,on}$	opening time of roof vent, s
$t_{vent,s,off}$	closing time of side vent, s
$t_{vent,s,on}$	opening time of side vent, s
U	vector of greenhouse controls
U_b	control of position of the CSG thermal blanket, [-]
u_{ice}	presence of the ice layer, [-]
$U_{vent,r}$	control of aperture of the roof vent, ranging from 0 to 1, -
$U_{vent,s}$	control of aperture of the side vent, ranging from 0 to 1, -
v_a	wind speed inside the greenhouse, m s^{-1}
v_e	outdoor wind speed, m s^{-1}
V_{gh}	CSG volume, m^3
X	vector of model state variables determined by numerically solving differential equations
X_c	CO_2 concentration of greenhouse air, µmol (CO_2) mol^{-1} (air)
X_d	crop dry weight, kg m^{-2} (gro)
X_d	crop dry weight, kg m^{-2} (gro)
X_h	relative humidity of greenhouse air, -
$X_{h,ref}$	arbitrary relative humidity corresponding to SLA_{ref}, -
X_{hfw}	head fresh weight of the crop, kg m^{-2} (gro)
X_t	greenhouse air temperature, °C
$X_{t,K}$	indoor air temperature in Kelvin, K
Y	vector of model state variables obtained through analytical solutions
z	Auxiliary parameter to ensure differentiability
Greek symbols	
α	absorptivity to shortwave radiation, -
α_{sr}	absorptivity of composite south roof to shortwave radiation, -
β_I	relative change in *SLA* per unit change in absorbed shortwave radiation by leaves, m^2 (leaf) W^{-1}
β_{sml}	coefficient to characterise level of soil surface moisture in CSGs, -
β_{Xh}	relative change in *SLA* per unit change in relative humidity, -
γ	psychrometric constant, Pa $°C^{-1}$
Δ	slope of the saturation curve of the psychrometric chart, Pa $°C^{-1}$
δ_L	average thickness of the crop leaves, m
δ_{obj}	thickness of the CSG object, m
δ_s	solar declination, °
ε	light use efficiency by photorespiration, kg (CO_2) J^{-1} (absorbed)
ε_{obj}	emissivity of object, -
ε_0	light use efficiency at very high CO_2 concentration in the absence of photorespiration, kg (CO_2) J^{-1} (absorbed)
ε_{inss}	porosity of the insect screen that mainly depends on the mesh count, -
η_{inf}	characterization of tightness of the cover to air infiltration, -
η_{inss}	ratio between the ventilation rate with and without an insect screen, -
θ_{ghz}	azimuth angle of the CSG, °
θ_h	solar altitude angle, °
θ_h'	solar altitude angle without constraints in range, °
θ_i	solar incidence angle for the south roof, °
$\theta_{i,nr}$	solar incidence angle for the north roof, °
$\theta_{i,nw}$	solar incidence angle for the north wall, °
θ_{nr}	north roof angle, °
θ_{nw}	north wall angle, °

θ_r	angle of refraction formed when solar rays pass from air into transparent covering, °
θ_{sr}	south roof angle, °
θ_z	solar azimuth angle, °
κ	reflectivity to shortwave radiation, -
κ_{sr}	equivalent reflectivity of south roof to shortwave radiation, -
$\kappa_{sr,0}$	base reflectivity of south roof to shortwave radiation, -
λ	heat conductivity coefficient, W m^{-1} °C^{-1}
λ_b	average thermal conductivity coefficient of thermal blanket, W m^{-1} °C^{-1}
λ_{sm}	correction factor for soil microbial respiration, -
λ_v	latent heat of water vaporization, J kg^{-1}
$\lambda_{v,d}$	latent heat for water vapour deposition, J kg^{-1}
π_a	refractive index of air, -
π_{tc}	refractive index of transparent covering, -
ρ_a	air density, kg m^{-3}
ρ_c	plant density, plants m^{-2} (gro)
ρ_{CO2}	CO_2 density, kg m^{-3}
$\rho_{CO2,0}$	CO_2 density at temperature of $T_{0,K}$, kg m^{-3}
ρ_L	density of crop leaves, kg m^{-3}
ρ_{obj}	density of the CSG object, kg m^{-3}
σ	Stefan-Boltzmann constant, W m^{-2} K^{-4}
σ_{area}	scale factor of solid surface area to indoor ground area, -
σ_{buf}	ratio of the maximum buffer capacity to crop dry weight, -
σ_{CO2}	factor that converts unit of CO_2 concentration, kg m^{-3} (μmol mol^{-1})$^{-1}$
σ_{PAR}	ratio of PAR to shortwave radiation, -
σ_r	ratio of the root dry weight to the crop dry weight, -
σ_{sha}	shading ratio of north wall, -
τ	transmissivity to shortwave radiation, -
τ_{sr}	equivalent transmissivity of south roof to shortwave radiation, -
$\tau_{sr,0}$	base transmissivity of south roof to shortwave radiation, -
Φ	income by selling the harvested product of the greenhouse production
φ	local latitude, °
χ	absolute humidity of air, kg m^{-3}
ψ	transmittance to longwave radiation, -
ω	hour angle, °
Γ	CO_2 compensation concentration, μmol (CO_2) mol^{-1} (air)
Γ_{T20}	reference value of the CO_2 compensation point at 20 °C, μmol (CO_2) mol^{-1} (air)

Subscripts

1	object 1
2	object 2
air	air inside the CSG
b	thermal blanket
b,o	outermost layer of thermal blanket
can	crop canopy
cs	soil layer with constant temperature
e	external surface
gro	indoor ground
ice	ice layer

in	internal surface
K	temperature in Kelvin
nr	north roof
nw	north wall
nw(j)	layer '*j*' of north wall, with '*j*' ranging from 1 to 'j_{max}'
obj	CSG object
out	outdoor air
sky	sky
so	soil
so(i)	layer '*i*' of soil, with '*i*' ranging from 1 to 'i_{max}'
so,cs	soil layer with constant temperature
sr	south roof
tc	transparent covering of the south roof
Special characters	
,	further limitations for the content before it
_	from the former to the latter
Abbreviation	
CSG	Chinese solar greenhouse
DSS	decision support system
Exp_1	Experiment 1
Exp_2	Experiment 2
Exp_3	Experiment 3
GA	genetic algorithm
LAI	leaf area index
LSE	LogSumExp function
MIMO	multi-input multi-output
MPC	model predictive control
PAR	photosynthetically active radiation
PID	proportional-integral-derivative
RMSE	root mean square error
RRMSE	relative root mean square error
SISO	single-input single-output
SLA	specific leaf area
VPD	vapour pressure deficit

Chapter 1

Introduction

This Chapter introduces the general background and motivation, research objective and research questions, and outline of the thesis.

1.1 General background and motivation

The rapid population growth and climate change have intensified global food security challenges. In 2023, around 733 million people experienced hunger, equivalent to one in every eleven people globally (FAO, IFAD, UNICEF, WFP, & WHO, 2024). According to the United Nations (2024), the global population is projected to reach nearly 9.7 billion by 2050, substantially increasing the demand for food production. However, expanding arable land offers limited potential to meet this demand due to constraints on land and water resources, along with the growing impact of extreme weather events (IPCC, 2019). A more promising solution lies in improving crop production efficiency on existing agricultural land. In this context, greenhouse horticulture, featuring the controlled environment that significantly boosts crop yields and resource use efficiency compared to traditional open field farming, is emerging as an effective strategy for mitigating current and future food insecurity issues.

Greenhouse horticulture is a capital-, technology-, labour-, and resource-intensive industry characterized by high input and output (Stanghellini, van't Oosfer, & Heuvelink, 2019). Improving greenhouse production efficiency has always been the central theme, which involves increasing crop yields while simultaneously reducing energy and resource consumption to achieve higher net returns. These efforts ultimately contribute to ensuring a stable supply of high-yield crop products, enhancing the sustainability of the industry, and reducing carbon footprint throughout the production process.

The Chinese solar greenhouse (CSG), which is featured with a low cost of operation, is a common greenhouse type in Northern China. It is suitable for operation by both farmers and enterprises and plays a pivotal role in overwinter production. In 2022, the total area of CSGs used for vegetable production was approximately 0.54 million hectares, representing 23.5% of the total greenhouse area dedicated to vegetables. Additionally, 288 hectares of CSGs were newly constructed in 2022 (T. Li, 2023). As a result, the annual production of protected vegetables in China reached 260 million tons, with over 30% contributed by CSGs. Lettuce

is a globally important horticultural crop, with an annual production of approximately 27 million tons, primarily produced in Asia, North America, and Europe (FAOSTAT, 2024). China is the largest producer of lettuce, accounting for more than 55% of global production. Moreover, lettuce is one of the main crops cultivated in CSGs. For example, In the Beijing region, lettuce accounted for 9.6% of the total vegetable planting area, making it the most cultivated leafy vegetable, and CSGs covered about 37.6% of the total lettuce planting area (Fan et al., 2021).

As shown in Figure 1.1 and Figure 1.2, The CSG has significant structural differences in comparison with greenhouses in the Netherlands, Israel and Spain (Pardossi, Tognoni, & Incrocci, 2004; Vanthoor, 2011) regarding envelope and controllable components. The cambered south roof, north wall, and thermal blanket enable the CSG to perform well on daylight access, heat storage, and insulation.

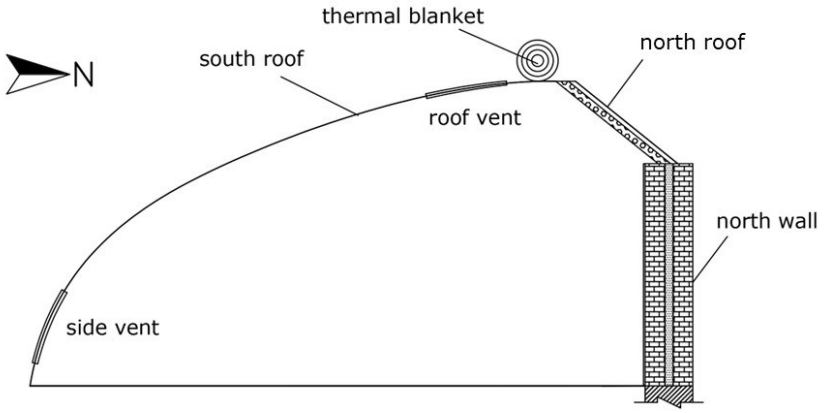

Figure 1.1 Cross-section of the Chinese solar greenhouse. For a standard CSG, the envelope consists of a north wall, a north roof, a south roof, and two side walls. The south roof is covered by transparent material. Vents and the thermal blanket are essential and controllable structural components for climate control.

Figure 1.2 Outside (left) and inside (middle and right) views of the Chinese solar greenhouse. Soil culture is common in practical CSG production.

Due to its excellent thermal insulation and heat storage properties, the CSG can produce vegetables and fruits in Northern China (32–43°N) mostly without additional heating (Tong, Christopher, & Li, 2009). The ability to produce does not necessarily imply efficiency. Efficient production of crop products with high yield and quality is the development trend of the CSG (W Sun, Zhang, Yang, Xue, & Guo, 2017). However, this is limited by unfavourable climate conditions inside the CSG, such as excessively high or low air temperature and humidity, deficient CO_2 concentration, and insufficient light. The problem comes down to a lack of equipment and strategies for CSG climate management in practice.

Recent developments in general-purpose climate conditioning equipment make it easy to adjust the CSG climate. Moreover, systems for active heat storage and release (Lu, Zhang, Fang, Ke, & Yang, 2017; W. Xu, Guo, & Ma, 2022), systems using greenhouse surplus air heat (X. He et al., 2022; Weituo Sun et al., 2015), and other specialised climate conditioning approaches for the CSG (K. Cao et al., 2019) have been investigated in view of energy saving and emission reduction of pollution gas. However, past research on CSG cultivation focused mainly on actuator development; it rarely focused on control strategies. The effects of operating time and positions of the thermal blanket on indoor temperature have been studied (Y. Liu, Ding, & Zhang, 2004; Tong, Christopher, Li, & Bai, 2010), but they do not orient to dynamic control. At present, most CSG climate control schemes are heuristic in practice, based on the experience of growers and suppliers as well as empirical horticultural research. They are implemented by manual operation or by simple on-off and PI-like controllers. In

order to obtain the expected CSG climate, growers can define and adjust the setpoints of the controller (Van Straten, Van Willigenburg, Van Henten, & Van Ooteghem, 2010). However, these settings do not account for future dynamics, resulting in poor performance of current CSG climate control schemes when it comes to maximising the net revenue of crop production (D. Xu, S. Du, & L. G. Van Willigenburg, 2018).

The optimisation of greenhouse climate control involves considering the advantages of the marketable product in relation to the operating costs of the climate conditioning equipment during its operation (Van Henten, 1994a). This situation represents a classic instance of an optimal control issue. Differing from conventional greenhouse climate control, the optimal control fully exploits scientific quantitative knowledge concerning the greenhouse, equipment, and crop. Such knowledge is captured in a mathematical dynamic model that anticipates greenhouse-crop dynamics affected by control adjustments with weather predictions. Furthermore, the goal of the greenhouse crop production process, which usually comes down to maximising net profit, is also specified in a mathematical cost function. The greenhouse optimal control theory emerged in the 1960s in Europe and has gradually formed many relatively mature control systems and algorithms (Chalabi, Biro, Bailey, Aikman, & Cockshull, 2002a, 2002b; I Ioslovich, 2009; I Ioslovich, Gutman, & Linker, 2009; Lin, Zhang, & Xia, 2021; Ouammi, 2021; Tap, 2000; Van Beveren, Bontsema, Van Straten, & Van Henten, 2015; Van Henten, 1994a, 2003; Van Henten & Bontsema, 2009; Van Ooteghem, 2010; Van Straten et al., 2010; D. Xu, S. Du, & G. Van Willigenburg, 2018; D. Xu, Du, & Van Willigenburg, 2019), which make significant gains in financial efficiency possible. These current optimal control systems mainly target modern muti-span greenhouses, i.e. the Venlo-type greenhouse. Although the CSG has a different configuration than a multi-span greenhouse, optimal control systems have a large potential to improve its economic performance and relieve growers from unnecessary tasks. However, few optimal CSG climate control systems have been developed, and their contribution to the possible efficiency improvement of CSG cultivation in terms of crop yield, energy and resources, or net revenue is not clear.

The majority of present CSGs, that is, the standard CSGs, lack additional climate conditioning equipment and automatic control systems (Qi, Wei, & Zhang, 2017). They only have roof and side vents for natural ventilation, as well as the thermal blanket for heat preservation, as the two kinds of essential and controllable structural components. The climate control in such a standard CSG is manipulated fully by hand and based on the grower's experience. On the contrary, to my best knowledge, the high-tech CSGs equipped with multiple climate conditioning facilities with continuous adjustment and an automated on-line controller, as targeted in the optimal control investigation of CSG cultivation by Dan Xu et al. (2018), do not exist.

Using a model-based control mechanism, the performance of an optimal climate control system for greenhouse crop production largely depends on the accuracy of its underlying process model, although control algorithms, such as receding horizon (Kuijpers, Antunes, van Mourik, van Henten, & van de Molengraft, 2022), can improve system robustness to some extent. As the primary control objective is to improve the economic performance of greenhouse cultivation (Van Henten, 1994a; Dan Xu et al., 2018), the system model must accurately predict greenhouse climate-crop growth dynamics affected by control adjustments and weather disturbances, based on which the optimal control problem solving can link energy consumption with crop revenue to seek optimised control trajectories. Meanwhile, given the unavoidable uncertainties in the system model and weather forecasts, achieving a global optimum across the entire crop growth cycle is impractical. Instead, optimal control algorithms and systems should be tailored for robust practical applications, fully considering the current industry landscape, specific greenhouse configurations, and user expectations. To apply optimal control theory in practical CSG production, an optimal climate control system for standard CSGs should be developed, based on an accurate system model and an applicable control algorithm.

Therefore, **on the one hand**, an integrated model of CSG climate and crop growth that explicitly describes the entire CSG crop production process is necessary to serve as a basis. This integrated model should be able to anticipate indoor climate and crop dynamics based

on external weather, greenhouse structure, and greenhouse controls, with acceptable accuracy, high computational efficiency, and robust generalisation. However, such a well-designed and thoroughly validated integrated CSG climate-crop growth model for control is not available. As modelling the greenhouse crop production process involves complex mechanism descriptions and this project takes lettuce, which is one of the most important horticultural crops, as the target crop, the generation of the integrated model will combine a lettuce growth model and a CSG climate model. **First**, since extreme temperatures frequently occur inside CSGs with limited climate conditioning capabilities, and optimal control of humidity attribute is crucial, the lettuce growth model should describe the effects of a broad range of greenhouse climates, including air temperature with extreme conditions, humidity, CO_2 concentration, and shortwave radiation, on crop state dynamics. **Second**, it is necessary to have a process-based CSG climate model that can integratively simulate all four climate attributes inside CSGs, incorporating the description of crop activities for a particular cultivar, i.e. the lettuce. This climate model should also undergo a thorough evaluation in CSG lettuce production scenarios, using measured crop states and greenhouse controls. Such two individual models are not available in the literature. **On the other hand**, an optimal control algorithm designed for standard CSGs without local controllers is required. The optimal control problem definition and the overall control process planning should be centred around the grower, fully considering the grower's greenhouse production objective, acceptable labour input, and the accuracy of manual operations. This algorithm is yet to be designed and evaluated.

This optimal climate control system for CSG cultivation will act as a decision support system. By using the control strategies recommended by the system, the CSG climate management is anticipated to achieve more efficiency than a conventional control supervised by the grower, and higher net revenue can be obtained from crop production.

1.2 Research objective

The objective of this project is to generate and evaluate an optimal climate control system

for standard CSGs, including the development of required models that simulate the CSG crop production process and an applicable optimal control algorithm that supports decision-making for growers. To apply optimal control theory in CSG climate management, we mainly address the following research questions:

1. To what levels can the accuracy of the lettuce growth model and the CSG climate model based on explicit process descriptions be achieved across the entire crop growth cycle, and how do these accuracies change upon model integration?
2. How much influence do current differentiating practical climate control scenarios have on net economic return in standard CSG cultivation?
3. What is the potential efficiency improvement of crop production inside a standard CSG by using optimal control over a conventional control supervised by the grower, and to what degree can it be achieved in practical production?

1.3 Outline

The organisational structure of this thesis is shown in Figure 1.3.

Chapter 2: Methodology

This chapter will introduce the methodologies, data, and codes that were used throughout this project, focusing on experiment design and model evaluation. Three CSG lettuce cultivation experiments were conducted to gather data for model calibration, validation, and control system evaluation. The setup for these experiments, from experiment design, CSGs preparation, and lettuce planting to data collection, will be detailed, followed by the data processing for simulations and an overview of the outdoor weather conditions. Then, the modelling methodology, coupling strategy, model calibration and validation methods, as well as the method for optimal control, will be illustrated. In addition, the software and programming used for simulations will be presented.

Chapter 3: A lettuce growth model responding to a broad range of greenhouse climates

No dynamic and mechanism model for lettuce growth includes the effects of air temperature with extreme conditions and humidity. In this chapter, a lettuce growth model that describes the effects of a broad range of greenhouse climates on crop dry weight dynamics will be developed, calibrated, and validated. Firstly, we will provide a model overview and detail the model equations describing lettuce growth as functions of air temperature with extreme conditions, relative humidity, CO_2 concentration, and shortwave radiation. Then, parameter calibration will be performed at both sub-model and model levels, together with generating all the parameters. Finally, the model will be validated by comparing measured and simulated crop dry weights. We will further evaluate model performance in leaf area index (*LAI*) simulations, analyse the role of the model framework and hypothesis, and summarise the effects of humidity. In addition, model universality and limitations will be discussed.

Chapter 4: A full-scale climate model of the Chinese solar greenhouse

A thoroughly tested process-based CSG climate model that integratively simulates the four attributes of shortwave radiation, air temperature, humidity, and CO_2 concentration, and describes crop activities targeting lettuce, is currently unavailable. This chapter will design and evaluate a full-scale CSG climate model that describes the effects of outdoor weather, greenhouse structure, cultivated crops, and greenhouse controls on the indoor climate of a standard CSG. Initially, the framework and assumptions of the model will be overviewed. Then, the model will be explicitly described from eleven subsections. Model parameterisation will be conducted by classifying parameters into general parameters and those dependent on the simulated CSG. Finally, the model performance in predicting all four climate factors will be evaluated, along with the exploration of contributions of energy and mass fluxes to indoor climates. Heat fluxes inside the north wall and indoor soil, as well as the ice layer formation, will also be analysed, followed by discussions on the universality, limitations, and perspective of the model.

Chapter 5: An integrated model of Chinese solar greenhouse climate and crop growth for control

A well-designed and thoroughly validated integrated model of Chinese solar greenhouse climate and crop growth for control is not available. This chapter will establish and evaluate such an integrated greenhouse climate-crop growth model for CSG lettuce production by combining the two previous models developed in Chapters 3 and 4. Firstly, the model synthesis will be performed, followed by model smoothing, which will include constructing smoothed equations and determining introduced parameters. Then, the integrated model will be validated in terms of both indoor climate and crop state predictions. Further, the validated model will be used for exploratory modelling to investigate the influence of practical control scenarios on crop production output in standard CSGs. Finally, the performance of the smoothed model will be re-evaluated, followed by discussions on the applicability, limitations, and improvement directions of the model.

Chapter 6: Event-driven receding horizon optimal control of Chinese solar greenhouse climate

A user-friendly optimal climate control system for crop production of a standard CSG without the local controller is currently unavailable. This chapter will generate and evaluate such an optimal control system, which takes the integrated model presented in Chapter 5 as a basis and employs an event-driven receding horizon design with real-time feedback to enhance system robustness while ensuring user-friendliness. Firstly, the optimal control system formulation, focusing on the development of the climate control algorithm that includes the definition of optimal control problem and controller design, will be explicitly described. Next, simulation trials will be conducted among ideal optimal control, open loop optimal control, and control supervised by the grower, exploring the efficiency improvement of crop production inside standard CSGs by using optimal climate control. Then, the feasibility of implementing the closed loop optimal control will be investigated, along with answering the extent to which ‘optimal’ can be realised in practice. Finally, the costs of deploying the proposed control system, model simplification, and methods for solving the optimal control problem will be discussed.

Chapter 7: Conclusion

This chapter will present the conclusion of the PhD research project, summarising the overall achievement of the research objective, application prospects of the research outputs, and insights from each chapter. Subsequently, it synthesises insights from the main research chapters to explore the contributions, potential uptake, and avenues for improvement of this project from both knowledge and engineering perspectives. The outlook will be discussed from the following three aspects: model simplification based on sensitivity analysis, setpoint tracking optimal control of high-tech CSGs, and optimal control of CSG climate assisted by data-driven method.

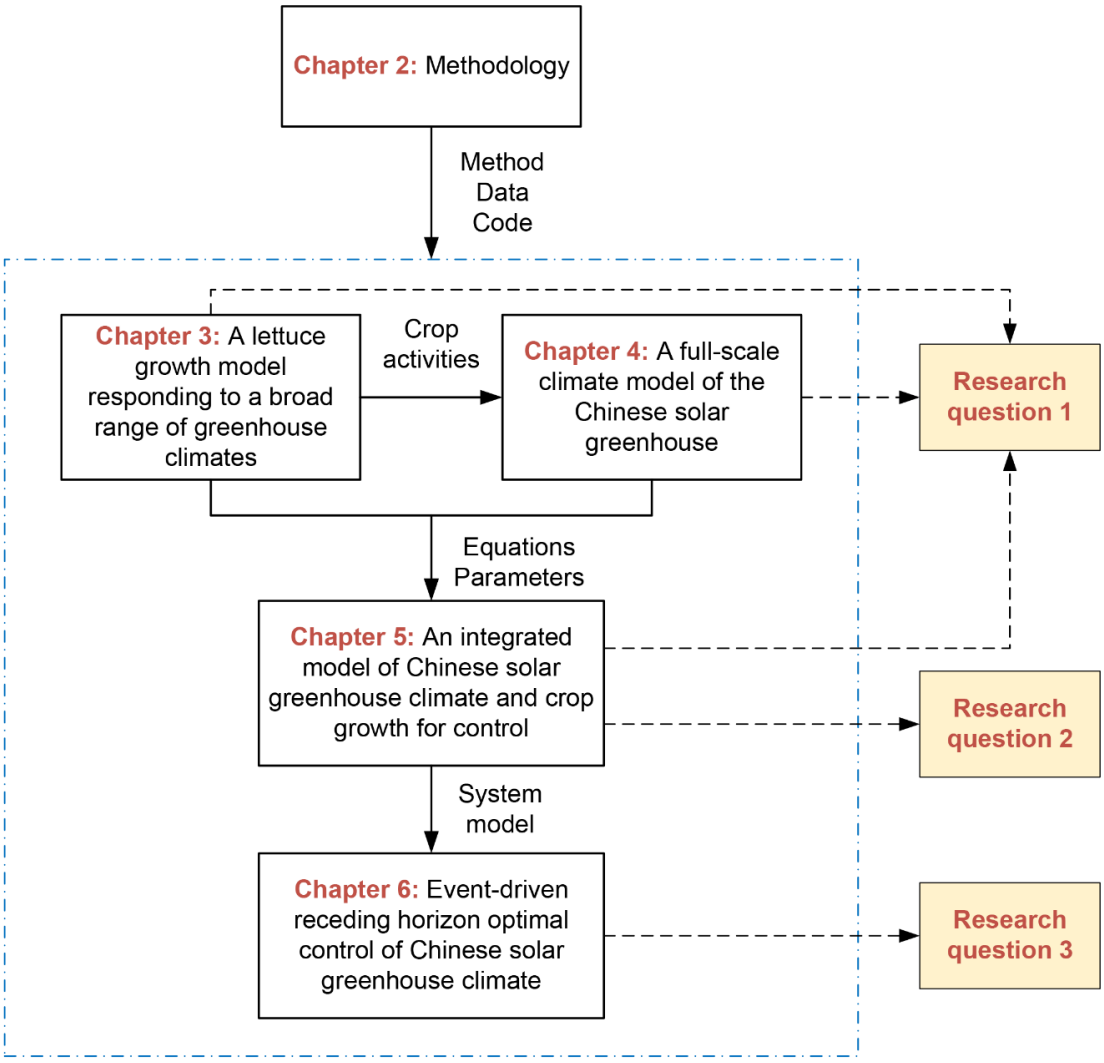

Figure 1.3 Organisational structure of the thesis and relationships between the main chapters.

Chapter 2

Methodology

This chapter illustrates the process of data collection and processing, basic methods for modelling and optimal control, and coding for simulations that support the entire research.

2.1 Experiment design

In order to obtain data for model calibration and validation, as well as for performance evaluation of the optimal control system, three experiments were conducted across different CSG systems, focusing on lettuce cultivation over different periods. These experiments were carried out from 9 April to 14 May 2020, from 24 November 2020 to 18 January 2021, and from 25 January to 16 March 2022 and were named sequentially as Experiment 1 (Exp_1), Experiment 2 (Exp_2), and Experiment 3 (Exp_3). They spanned warm, cold, and cold-warm weather conditions, enabling the collected greenhouse climate cover from extremely low to extremely high temperatures, and involved two different CSGs.

As indicated in Table 2.1, these three experiments served different purposes in various chapters. In Chapter 3, the lettuce growth model was studied using Exp_1, Exp_2, and Exp_3. The experiment performed in the cold season was used for global calibration, and the other two in warm and cold-warm seasons were used for model validation. Thus, Exp_2 served as the calibration experiment for crop model development, while Exp_1 and Exp_3 served as the first and second validation experiments, respectively. In Chapter 4, which focused on the CSG climate model, Exp_1 and Exp_3 were used for validation, considering that Exp_2 was dedicated to crop model calibration, while crop activity descriptions in the climate model were directly sourced from the crop model. Moreover, Exp_1 and Exp_3, involving both cold and warm weather conditions, provided sufficient representation for evaluating model performance and facilitated comparative analysis for potential optimisation directions. Chapter 5 utilised all three experiments for the evaluation of the integrated model of CSG climate and lettuce growth. To exclude the potential impact of crop senescence, data from the last five days of each experiment were uniformly discarded. Additionally, Exp_3 was selected to study the impact of various climate control practices on CSG production output through modelling exploratory. In Chapter 6, all three experiments participated in providing data support for case studies on the performance evaluation of the optimal control algorithms.

Table 2.1 Usage and naming conventions of the experiments in different chapters.

Experiment	Date	Chapter 3: Crop model	Chapter 4: Climate model	Chapter 5: Integrated model	Chapter 6: Control
Exp_1	9 Apr 2020-14 May 2020	Validation	Validation	Validation	Simulation trial
Exp_2	29 Nov 2020-18 Jan 2021	Calibration	/	Validation	Simulation trial
Exp_3	30 Jan 2022-16 Mar 2022	Validation	Validation	Validation Modelling exploratory	Simulation trial

2.1.1 Experimental greenhouses

The experimental CSGs were located in Fangshan District, Beijing, China (39.62° N, 115.96° E). They were oriented from east to west, consisting of the north wall, side walls, the back roof, and the south roof made of single-layer plastic film. The south roof had two vents that opened from east to west: one at the bottom and one at the top. It was covered with a thermal blanket at night in cold seasons. No extra energy-consuming climate conditioning equipment was used during the experiments.

The CSG in Exp_1 (Figure 2.1A) had a ground area of approximately 585 m^2, with a width of 7.50 m and a length of 78.0 m. The CSG used for Exp_2 and Exp_3 (Figure 2.1B) had a floor area of approximately 652 m^2, with a width of 7.55 m and a length of 86.3 m. The indoor ground of CSGs for Exp_1, Exp_2, and Exp_3 was bare soil. The specific CSG structure, dimensions, and materials are listed in Table 2.2, based on which the greenhouse dependent parameters required by the CSG climate model can be obtained directly or derived. To aid understanding, Figure 2.2 is provided to show the main CSG dimensions in Table 2.2, taking the CSG used for Exp_2 and Exp_3 as an example.

During the experiments, the CSG climate was regulated in accordance with the rules observed in typical CSG horticultural practices. The growers operated the thermal blanket and side and roof vents to regulate the indoor climate and optimise crop production for both

high yield and quality.

Figure 2.1 Experimental Chinese solar greenhouses. A: used for Exp_1; B: used for Exp_2 and Exp_3.

Table 2.2 Structure, dimensions, and materials of CSGs used for model validation.

NO.	Item	CSG for Exp_1	CSG for Exp_2 and Exp_3
1	Azimuth angle	5 ° west of south	5 ° west of south
2	Ridge height	3000 mm	4100 mm
3	Horizontal projection distance between ridge and north wall	690 mm	1320 mm
4	CSG height at 1/6 segment point of south roof projection	1630 mm	2000 mm
5	CSG height at 1/2 segment point of south roof projection	2581 mm	3300 mm
6	CSG height at 5/6 segment point of south roof projection	2975 mm	4010 mm
7	Average height	2350 mm	3110 mm
8	Span	7500 mm	7550 mm
9	Length in east-west direction	78.0 m	86.3 m

10	Height of north wall	2200 mm	3050 mm
11	North wall angle	90 °	90 °
12	North wall inner surface	10 mm cement mortar	10 mm cement mortar
13	North wall outer surface	10 mm cement mortar	50 mm extruded polystyrene board + 2 mm cement mortar
14	North wall interlayer	410 mm hollow brick wall	454 mm hollow brick wall
15	Length of north roof	1055 mm	1690 mm
16	North roof angle	49 °	39 °
17	North roof inner surface	50 mm extruded polystyrene board + 2 mm cement mortar	50 mm extruded polystyrene board + 2 mm cement mortar
18	North roof outer surface	50 mm extruded polystyrene board + 2 mm cement mortar	50 mm extruded polystyrene board + 2 mm cement mortar
19	North roof interlayer	80 mm reinforced concrete prefabricated board	80 mm reinforced concrete prefabricated board
20	Indoor ground	Bare soil	Bare soil
21	Aisle	/	600 mm wide concrete aisle
22	South roof arc length	7955 mm	8005 mm
23	South roof angle	24 °	33 °
24	Transparent covering	0.08 mm PO film	0.08 mm PO film
25	Side wall inner surface	10 mm cement mortar	10 mm cement mortar
26	Side wall outer surface	10 mm cement mortar	50 mm extruded polystyrene board + 2 mm cement mortar
27	Side wall interlayer	370 mm hollow brick wall	423 mm hollow brick wall
28	Thermal blanket inner surface	/	0.5 mm PE woven fabric (white outside, black inside)
29	Thermal blanket outer surface	/	0.5 mm PE woven fabric (white outside, black inside)
30	Thermal blanket interlayer	/	20 mm black rubber-plastic insulation material
31	Roof vent type	Pull film	controlled by thermal blanket
32	Roof vent width	400 mm	400 mm
33	Insect screen at roof vent	40 mesh with a wire diameter of 0.17 mm	40 mesh with a wire diameter of 0.17 mm
34	Side vent type	Pull film	Roll film
35	Side vent width	1000 mm	1000 mm
36	Insect screen at side vent	40 mesh with a wire diameter of 0.17 mm	40 mesh with a wire diameter of 0.17 mm
37	Equipment configuration	2 fans (1370×1370 mm) coupled with wet pad	/

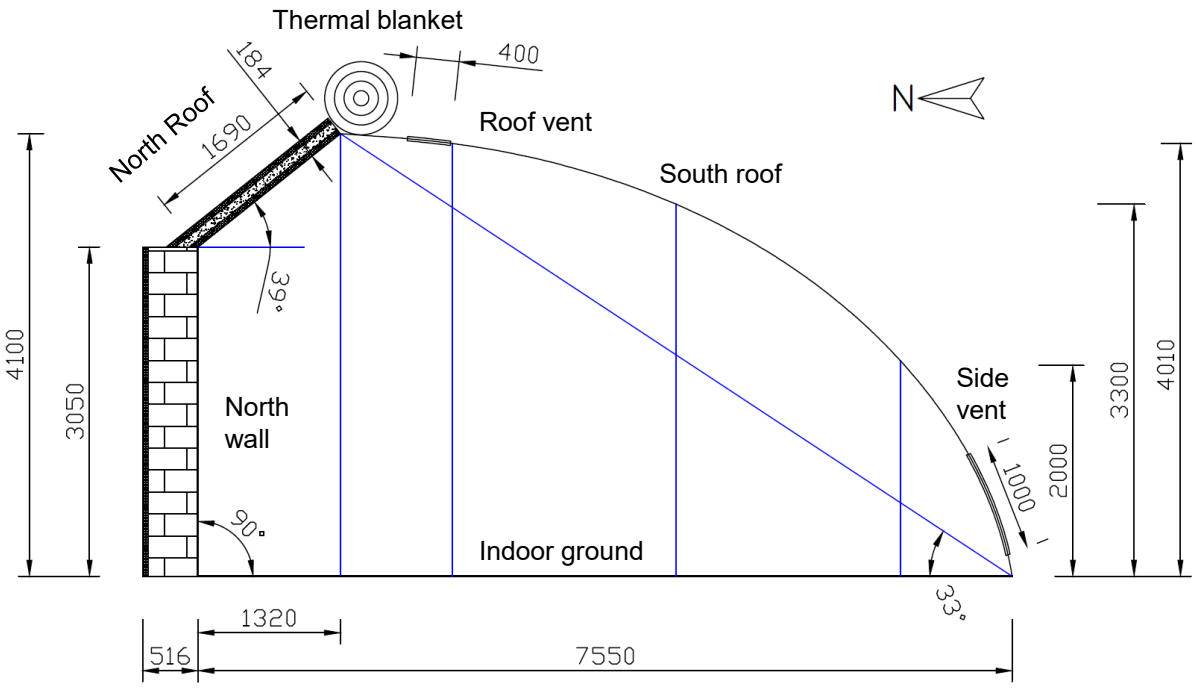

Figure 2.2 Greenhouse parameters of the CSG used for Exp_2 and Exp_3 on the cross-section (unit: mm). The blue lines are the auxiliary lines.

2.1.2 Lettuce planting

The cultivar of the lettuce (*Lactuca sativa*) selected for the experiments was Tiberius RZ (41-27) (produced by Rijk Zwaan, The Netherlands), which is increasingly used for greenhouse lettuce production in China. Lettuce plants were sown and raised in the nursery substrate inside a seedling greenhouse. Then, they were transplanted to soil inside CSGs.

In Exp_1, the lettuce seedlings were transplanted when they had 10 main leaves. The plants were cultivated in east-west rows (Fig. 2.3a), which occupied parts of the greenhouse floor area with a length of 72.6 m and total width of 3.60 m. There were 255 plants per row, so the row density was 3.51 plants m^{-1}. There were 12 rows and 3060 plants in the greenhouse, that is, 11.71 plants m^{-2} (gro). In this study, the developed model is oriented to lettuce cultivation with an effective cultivated area-based, instead of an arbitrary ground area-based, plant density. This makes the model practical and universal. The unit ground area on which

the simulated crop dry weight and other states are based is the effective cultivated area. This effective area depends on the upper limit of ground area occupied by a single plant. Considering the lettuce's genetic characteristics and harvesting size for commercial purposes, the model limits the maximum ground area occupied by a single lettuce to 0.32×0.32 m square centred on the planting site. This limitation works in dividing the boundary of an effective cultivated area and preventing the density from being too low. If not, the model will easily overestimate crop growth and lose its universality. This is because, like most other models, this model assumes that the canopy infinitely spreads in the selected ground area. However, many blank areas exist outside the cultivation area and even between plants inside the greenhouse. The global calibration of the lettuce growth model below contributes to the implicit plant density of the model, as the density input is used solely to calculate single-plant dry weight for determining the root-to-shoot ratio, while crop states measured for global calibration are based on the effective cultivation area.

In Exp_2, the lettuce seedlings were transplanted when they had 4 main leaves. The plants were cultivated in east-west rows (Fig. 2.3b), and the cultivated area had a length of 78.1 m and total width of 4.50 m. There were 265 plants per row, so the row density was 3.39 plants m^{-1}. There were 15 rows and 3975 plants in the greenhouse, and the plant density was 11.31 plants m^{-2} (gro). In Exp_3, the lettuce seedlings were transplanted when they had 5 main leaves. The plants were cultivated in north-south ridges, with 4 rows of crops on each ridge (Fig. 2.3c). The cultivated area had a total length of 59.0 m and a width of 6.25 m. There were 18 plants per row; thus, the row density was 2.88 plants m^{-1}. There were 236 rows and 4248 plants in the greenhouse, that is 11.52 plants m^{-2} (gro).

The greenhouse climate control during the growing period was manipulated manually according to the rules used in regular CSG horticulture practice. Supply of water and fertiliser was also in line with the growers' experience with the control objective of being most beneficial to crop growth. Note that the model uses only environmental factors as external inputs, and it is assumed that water and fertiliser levels were adequate in the experiments.

Figure 2.3 Experimental greenhouses and lettuce cultivation. a: Exp_1; b: Exp_2; c: Exp_3.

2.1.3 Data collection

During the three experiments, crop growth indicators and greenhouse climate measurements were recorded. To ensure uniform data, buffer zones were set factitiously to mitigate the effects of CSG side walls and the entrance door on indoor climate and lettuce growth. The remaining was the sampling zone, where the lettuce samplings and climate measurements were performed (Figure 2.4). The sampling zone was divided into 3 blocks for destructive crop measurements, and an equal number of plants were randomly selected for harvest from each block to consider the impact of greenhouse climate gradients. Throughout the growing season, samples were collected every 5 days in the three experiments: 18 plants in Exp_1 and Exp_2, and 6 plants in Exp_3. One exception was the first sampling; the samples were the seedlings for transplanting, and 6 plants were sampled given the uniform nursery climate. Dry and fresh weights of both root and shoot, leaf area, canopy diameter, and other growth indicators were determined for each plant. Dry weight was obtained after oven drying at 105℃ for 30 min and then 70 ℃ until the samples had constant weight, and it was measured by an

analytical balance (accuracy: 0.001 g). Leaf area was measured by a portable leaf area meter (LI-3000C, USA, accuracy: within ± 2% for samples >50 cm^2).

Greenhouse climate includes solar radiation (shortwave radiation), air temperature, relative humidity, and CO_2 concentration at a height of 1.5 m above the CSG ground. Of which, air temperature, relative humidity and CO_2 were measured and recorded by a portable data logger (ESPEC THCO2, Japan, accuracy: CO_2 ± 50 ppm) with sensors (RSH-3020, Japan, accuracy: temperature ±0.3 ℃, relative humidity ± 2.5%). Solar radiation was measured by pyranometers (Kipp&Zonen CMP6, The Netherlands, sensitivity: 5-20μV/W/m²) and recorded by Campbell CR1000 (USA) data logger. Climatic data was recorded with a time step of 5 minutes. The specific layout of climate measurement points is shown in Figure 2.4.

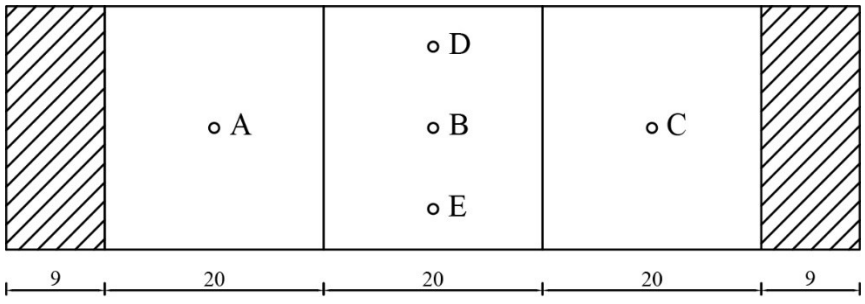

Figure 2.4 Lettuce sampling area and layout of climate measurement points (unit: m, taking Exp_1 for example). Measurement points of temperature, humidity and CO_2 are located at A-E points. Measurement points of shortwave radiation are located at A-C points. Shadow areas denote buffer zones where lettuce is cultivated but not sampled. The model study uses the average values of these measuring points and samples.

The outdoor weather data include horizontal solar radiation, air temperature, relative humidity, CO_2 concentration, and wind speed. They were measured by a self-assembled weather station installed on top of a CSG inside the agricultural park where our experiments were conducted. Solar radiation was measured by a CMP6 pyranometer (Kipp&Zonen, The Netherlands, sensitivity: 5-20μV/W/m²). Air temperature and humidity were measured by

an HMP155A air temperature and relative humidity sensor (Vaisala, Finland, accuracy for air temperature is ± (0.226 - 0.0028 × temperature) ℃ in the range of -80 to 20 ℃ and ± (0.055 + 0.0057 × temperature) ℃ in the range of 20 to 60 ℃, accuracy for relative humidity is ± (1.0 + 0.008 × reading) % at the temperature levels of -20 to 40 ℃). Outdoor wind speed was measured using a 034B wind sensor (MetOne, USA, accuracy: 0.1 m s^{-1} when < 10.1 m s^{-1}, ±1.1% of true when > 10.1 m s^{-1}). The above data were recorded by Campbell CR1000 (USA) data logger. The CO_2 concentration of outdoor air was measured and recorded by a portable data logger (ESPEC THCO2, Japan, accuracy: CO_2 ± 50 ppm). All outdoor weather data were collected in 5-minute intervals.

The growers manipulated and recorded controls of the thermal blanket and side and roof vents. The control of vents was divided into five levels: fully closed, 1/4 open, 1/2 open, 3/4 open, and fully open. The thermal blanket was required to be either fully open or fully closed. The moments of greenhouse control actions were recorded using the initial time of controls.

The collected weather, climate, crop, and control data were derived from three experiments, differing in the CSGs used, cultivation patterns, and experimental periods. These datasets, in digital form, were used as inputs or outputs for calibrating and validating the lettuce growth model, the CSG climate model, and the integrated model under development. The experiments were designed with diverse greenhouse crop production scenarios to provide a broad range of data; if the developed models can accommodate this data variety, it would confirm their robust generalisation capability. The models were structured to identify and respond to different CSG cultivation scenarios primarily through model inputs and definitions. For example, structural parameters specific to each CSG and seasonal weather conditions were inputs for the climate and integrated models. Time-varying indoor climates provided inputs for the crop model. In various cultivation patterns, plant densities differed but served as an input for the crop model. Meanwhile, using a defined plant density based on effective cultivation area, the models could disregard row orientation impacts. Additionally, different transplanting dates were reflected by the initial crop and climate states, configured as input settings during simulation runs.

2.1.4 Crop data processing

In Exp_1, performed in the warm season, the roof and side vents were almost always open, resulting in good ventilation and a relatively uniform climate inside the greenhouse. At the same time, lettuce cultivation had a great demand for irrigation in high temperatures. Due to the east-west cultivation pattern, in which the drip irrigation belt extended a long distance of half the CSG length, insufficient irrigation for some plants might occur. Therefore, the top 12 of the 18 lettuce samples in crop dry weight were selected for model study to avoid potential water and fertiliser stress. In Exp_2 and Exp_3, seedlings were transplanted in the cold season, and the recovering period lasted for several days. In order to ensure that the data used for model calibration and validation were representative, the measurements of the second sampling performed on the fifth day from the transplanting date (Day 0) were selected as the initial states of model simulations. As to the analysis above, the initial crop states used for crop model simulations are listed in Table 2.3.

The crop data processing for these three experiments and the initial states used for simulation are applicable to all chapters. Additionally, in the simulations of the CSG climate model and the integrated CSG climate-crop growth model, the initial climate states adopted the measured data, while other CSG object states were estimated.

Table 2.3 Initial crop states used for the lettuce growth model simulations.

Experiment number	Plant density [plants m^{-2}]	Initial crop dry weight of individual plant [g $plant^{-1}$]	Initial crop dry weight [kg m^{-2} (gro)]	Initial leaf area of individual plant [cm^2 $plant^{-1}$]	Initial leaf area index [-]	Initial buffer storage [kg (CH_2O) m^{-2} (gro)]
Exp_1	11.71	0.3889	4.5538×10^{-3}	146.47	0.1715	0
Exp_2	11.31	0.1112	1.2578×10^{-3}	37.63	0.0426	0
Exp_3	11.52	0.1716	1.9766×10^{-3}	86.50	0.0996	0

2.1.5 Outdoor climate overview

The primary function of CSGs is to produce vegetables overwinter. The validation experiments for the climate and integrated models focused on these periods and spanned warm, cold, and cold-warm weather conditions, making the evaluation results more representative. Table 2.4 summarises the outdoor weather data, including their average values and standard deviations. Outdoor climate conditions differ in the three experiments, providing a more diverse environment and more comprehensive data for model validation. As previously mentioned, the experimental data used to validate the CSG climate model was consistent with that for the crop model, which could make it easier to compare the performance of the crop model, climate model, and integrated model. If no actual measurements were available, the assumed outdoor CO_2 concentration was 400 μmol mol^{-1} (ppm) (Katzin, van Mourik, Kempkes, & van Henten, 2020).

Table 2.4 Averages of the outdoor weather conditions in the validation experiments for the CSG climate and integrated models. Numbers in the brackets are the standard deviations.

Experiment	Date	n [-]	I_{out} [MJ m^{-2} d^{-1}]	T_{out} [°C]	RH_{out} [-]	$CO2_{out}$ [ppm]	v_e [m s^{-1}]
Exp_1	9 Apr 2020-14 May 2020	100-135	21.1 (6.6)	18.0 (6.7)	0.50 (0.30)	410 (90)	1.60 (1.16)
Exp_2	29 Nov 2020-18 Jan 2021	334-18	8.7 (1.5)	-5.5 (6.4)	0.58 (0.25)	458 (32)	0.81 (0.92)
Exp_3	30 Jan 2022-16 Mar 2022	30-75	13.1 (3.5)	1.2 (7.5)	0.48 (0.22)	400 (0)	0.85 (1.01)

2.2 Basic methods for modelling and optimal control

2.2.1 Modelling methodology and coupling strategy

A variety of models have been developed for simulating greenhouse climate and crop growth

dynamics. These models include simple statistical models such as the logistic growth forms (Tei, Aikman, & Scaife, 1996), mechanistic models like the greenhouse and tomato models developed by Vanthoor (2011), machine learning models represented by neural networks (Mohmed et al., 2023), computational fluid dynamics (CFD) models specialised in simulating airflow processes and climate distributions (Norton, Sun, Grant, Fallon, & Dodd, 2007), and functional-structural models combining mechanistic elements with plant morphology and used as digital twins for simulation (Rohde & Forni, 2023). In this study, we focus on constructing mechanistic models based on detailed process descriptions. Mechanistic models, also known as process-based or explanatory models, are mathematical representations that simulate the fundamental biological, physical, and chemical processes governing a system. They explain the system behaviour at an upper integration level by integrating processes from lower integration levels (Reidsma & Descheemaeker, 2019). The choice of mechanistic models can be beneficial in four aspects. First, they are highly interpretable and have low dependence on extensive datasets. Second, they are expected to generalise better across varying conditions than data-driven models. Third, they offer higher computational efficiency compared to multi-dimensional models. Fourth, the modular structure of mechanistic models allows for seamless integration of the individual greenhouse climate and crop growth models to describe the entire greenhouse crop production process.

The development of the lettuce growth model and the CSG climate model follows the phases outlined in Figure 2.5. Both models are developed for greenhouse climate control purposes and will eventually be coupled to describe the CSG lettuce production process. To define the system boundaries, the targeted system configuration, model inputs, outputs, and underlying assumptions should be clarified. Specifically, the crop model addresses potential production scenarios, where crop growth is influenced exclusively by the greenhouse shoot environment. The model inputs include the air temperature (including extremes), humidity, CO_2 concentration, and shortwave radiation. Crop growth dynamics are represented through outputs such as crop dry weight and leaf area index. Correspondingly, the CSG climate model targets the standard CSG configuration, relying on structural components for greenhouse climate regulation. It captures dynamics of the four climate attributes and other

CSG object states, responding to outdoor weather, greenhouse structure, crop states, and greenhouse controls. Further details are provided in the model assumptions, which primarily serve to simplify the system under study. Both mechanistic models are built upon a complete model framework, illustrated by a schematic diagram and further detailed in the model overview section. This section covers the core processes and innovative aspects that shape the conceptual model. While the framework introduces novel elements, the fundamental theories remain consistent with those of most other mechanistic models. In particular, the crop model relies on dry matter accumulation, calculated as the net difference between photosynthesis and respiration, while the greenhouse climate model is based on energy and mass balance principles.

Transforming the conceptual model into a quantitative form involves establishing equations and performing parameterisation. The model equations encompass input variables, state variables that generally correspond to model outputs, intermediate variables such as rate variables, and model parameters, governed by specific rules. The simulated system is characterised by state variables at different time points, and their rates of change in time are formalised by differential equations, with time units in seconds, allowing for instantaneous simulation of CSG climate and crop growth. Solving these differential equations is essential to depict the dynamic system behaviour. Model outputs that do not require iterative calculations, such as indoor shortwave radiation, are determined by analytical equations. For model reduction, some state variables can be described by algebraic equations. Data gathering and processing have been detailed in Section 2.1. Methods for model programming, calibration, and validation will be illustrated in subsequent sections. Note that several steps shown in Figure 2.5 might be repeated multiple times during the model development process.

The generation of the integrated model combines all state variables from the lettuce growth model and the CSG climate model into a unified framework, directly merging their equations while preserving constant parameters. During programming, careful attention must be paid to the conversion of model inputs and state variables between the integrated model and individual component models. The integrated model will subsequently be employed for

modelling exploratory and optimal control analysis.

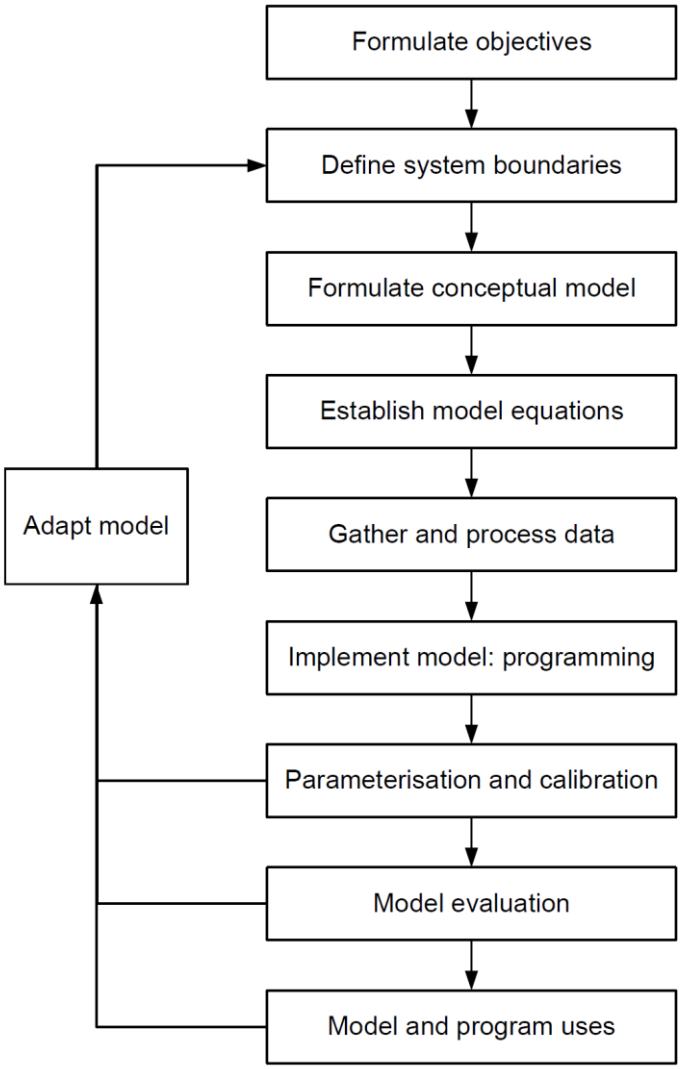

Figure 2.5 Phases of model development. It is adapted from the diagram by Reidsma and Descheemaeker (2019).

2.2.2 Model calibration and validation methods

The goal of model evaluation or validation is to assess the effectiveness of the model in achieving the objectives of the modelling project. In this study, we aim to determine whether the developed models have sufficient prediction accuracy to meet control requirements. To achieve this, all three developed models are evaluated by comparing simulation results with

measured data of the system behaviour at the upper integration level, utilising both graphical interpretation and statistical analysis. Graphical analysis compares the dynamic trends between simulated and observed values, qualitatively identifying periods of overestimation or underestimation and overall trends, while quantitative analysis employs statistical metrics. The selection of model output variables for comparison with measured data is based on the modelling objectives and data availability.

In the study of the lettuce growth model, greenhouse climate data with 5-minute intervals were used as model inputs. Model performances were evaluated by comparing the measured and simulated crop dry weights, using the root mean square error (*RMSE*) and the relative root mean square error (*RRMSE*). The two common metrics are defined as follows,

$$RMSE = \sqrt{\frac{1}{n}\sum_{i=1}^{n}(y_i^m - y_i^s)^2} \tag{2.1}$$

$$RRMSE = \frac{100}{\overline{y^m}}\sqrt{\frac{1}{n}\sum_{i=1}^{n}(y_i^m - y_i^s)^2} \tag{2.2}$$

where y_i^m and y_i^s are measured and simulated values at the same timepoint, n is the number of measurements, $\overline{y^m}$ is the average of measured values. While the *RMSE* measures the absolute magnitude of prediction errors, the *RRMSE* expresses the error as a percentage relative to the sample mean. The latter allows us to deal with datasets with different units or scales and compare the performance across crop models. Taking reference from the evaluation of a field crop model (Jamieson, Porter, & Wilson, 1991), the performance of modelling lettuce growth is considered to be excellent if *RRMSE* < 10%, good if the *RRMSE* is between 10% and 20%, acceptable if the *RRMSE* is between 20% and 30%, and poor if *RRMSE* > 30%.

Following the criteria for publishing crop model papers (Sinclair & Seligman, 2000), the

prediction of the critical crop growth indicator, LAI, throughout the simulated growth cycle was also considered in the model evaluation. Additionally, the simulation and presentation of another state variable, the amount of stored carbohydrates in the buffer, were conducted to assess the role of the model framework and underlying hypothesis.

Similar to the evaluation of the crop model, the performance of the CSG climate model was also evaluated in quantitative terms using *RMSE* and *RRMSE*. Simulated shortwave radiation (I), air temperature (X_t), air humidity (X_h), and CO_2 concentration (X_c) inside the CSG were compared with the measured values. The smaller the values of *RMSE* and *RRMSE*, the better the model performance on climate predictions. However, there are no established standards for defining how accurate the greenhouse climate models should be (Katzin, van Henten, & van Mourik, 2022), especially for models used for climate control. In the model investigation by Vanthoor (2011) for optimal greenhouse design, it was assumed that when $RRMSE \leq 10\%$, the model was considered to have good performance. Based on our current understanding, assessing the performance of CSG climate models using this criterion is challenging due to the complexity of the CSG system, the absence of standardised CSG construction methods, the highly integrated descriptions, and the required simulation over the entire growth cycle for control purposes. In this study, the performance evaluation for the CSG climate model adopts the same criteria as those used for the crop model.

Predictions of the crop and climate states are integrated and jointly evaluated in the integrated model. Consequently, the rules for evaluating the integrated model of CSG climate and lettuce growth can refer to those for the individual crop and CSG climate models. That is, all developed models employ the same model evaluation methods.

Model parameterisation is crucial for formulating a quantitative model. In this study, most parameters were derived from the literature, while others were determined through direct measurements and model calibration. Specially, the parameters of the CSG climate model or components are categorised into two types: general parameters and CSG-dependent parameters.

Model calibration involves adjusting parameters to ensure that simulated results agree with measurements as closely as possible. Typically, calibration follows a sensitivity analysis, which helps identify parameters that have strong influence on the model output (Wallach, Makowski, Jones, & Brun, 2019). However, this approach is uncommon in simulating greenhouse crop production processes (Katzin et al., 2022). In our study, calibration was also conducted without a preliminary sensitivity analysis; instead, we directly targeted newly introduced or other unsupported parameters. As noted by Reidsma and Descheemaeker (2019), ideal model calibration uses data from the lower integration level to parameterise the model, which corresponds to our local calibration approach. It focuses on sub-models where parameters are fitted using experimental data according to the prescribed equations. Furthermore, global calibration was conducted at a higher integration level to minimise the *RRMSE* and maximise the agreement between model outputs and observed data. This global calibration was applied only to the parameter estimation of the crop model. Given that only two parameters required global calibration, we used the grid search method for optimisation, which involves a systematic and exhaustive exploration of the parameter space by evaluating all possible combinations within specified ranges and intervals. This optimisation method is simple to implement and increases the likelihood of identifying the global minimum.

Note that separate datasets are needed for model calibration and validation to ensure an unbiased assessment of model performance. While Exp_2 was used for the global calibration of the crop model, it could also be employed for the evaluation of the CSG climate model and the integrated model. This is acceptable because the latter two models incorporate additional components and dynamics not directly calibrated with Exp_2.

2.2.3 Method for optimal control

Several classic books and studies have detailed the theory of optimal control in greenhouse cultivation (Van Straten et al., 2010; Dan Xu et al., 2018). Here we summarise the main line of thought for developing the optimal control system and solving the associated optimal

control problem. Designing a practical, closed-loop optimal control system of greenhouse climate can be separated into three parts. The first task is to create a quantitative mathematical system model in state-space form, in our case the integrated model of CSG climate and crop growth. The second task is to define the optimal control problem, which includes specifying the system model, initial state, external inputs, control constraints, state constraints, and the cost function, considering a fixed final time without terminal constraints. The third task is to schedule the overall control process, that is to conduct the so-called controller design, focusing on addressing the determination of how exactly the feedback should take place. Together, the second and third tasks contribute to the optimal control algorithm to be developed in this project.

Net profit is the primary concern of growers and is also the most used performance criterion in optimal control investigations. The objective of the optimal control is to maximise the net economic return of CSG lettuce cultivation, which can be described as (Van Henten & Bontsema, 2009):

$$J(U) = \Phi\left(X(t_f)\right) - \int_{t_0}^{t_f} L(X, Y, U, D, P, t)dt \tag{2.3}$$

where, X represents state variables that appear with a time derivative in the system model, such as indoor air temperature, relative humidity, CO_2 concentration, and crop dry weight; Y represents state variables that can be obtained analytically, such as indoor solar radiation; U represents greenhouse controls; D represents external disturbances; P represents parameters that clarifies the specific greenhouse structure and cultivation scenario; t is time; $J(U)$ is the net economic return, also namely as cost function, objective function, or performance criterion, $\Phi\left(X(t_f)\right)$ represents the income by selling the harvested product of the greenhouse production, $L(X, Y, U, D, P, t)$ represents running costs of the controllable objects for climate conditioning, t_0 is the initial time for optimisation, and t_f is the final time for optimisation. The period from t_0 to t_f is the crop growth cycle considered

by the open loop optimal control, where t_0 can be the time of lettuce transplanting or the end of the recovering period, while t_f corresponds to the harvest time. In the case of receding horizon optimal control, the initial and final times of the relatively short horizon, where prediction and problem solution are located, are time-varying.

The solution to an optimal control problem comprises the optimal control strategy, the associated optimal state trajectory or system behaviour, and the minimum value of the cost function. Optimal control problems can be solved using various approaches. Analytical methods, such as the calculus of variations and Pontryagin's Maximum Principle, provide theoretical frameworks for deriving necessary optimality conditions (Van Henten, 1994a). Numerical methods, such as gradient-based algorithms, rely on the first derivative of the objective function with respect to the control variables to iteratively approximate the solution. However, traditional analytical and gradient descent methods face significant challenges when applied to systems with high-dimensional state variables and nonlinear dynamics (Srinivasan, Palanki, & Bonvin, 2003), such as greenhouse production systems. These challenges include high computational complexity and a tendency to converge to local optima. In contrast, global optimisation algorithms, such as the genetic algorithm (GA), offer substantial advantages (Jin et al., 2020). GA encodes control strategies and employs selection, crossover, and mutation to efficiently search for optimal solutions (Lambora, Gupta, & Chopra, 2019). GA was selected for solving the optimal control problem in this study, considering that it does not require gradient information and is particularly effective for solving complex nonlinear systems with constraints.

2.3 Source code

Model implementation requires programming. The code used for the design, simulation, and visualisation of the lettuce growth model is available in MATLAB format (MATLAB R2021b, The MathWorks) at Mendeley Data (http://dx.doi.org/10.17632/r7z9ttvkyh.1). The inputs of this code template, including greenhouse climate, initial crop states, and plant density, are from Exp_3. The built-in ODE45 solver is used to solve the differential equations,

which employs the Runge-Kutta method with a variable time step for efficient computation. This open-source code allows readers to understand, use, and improve our model conveniently.

The CSG climate model and the integrated model are also programmed with MATLAB software (MATLAB R2023a, The MathWorks). The differential equations are solved using the ODE45 solver, in which the ‘fsolve’ function is employed to address specific energy balance equations.

In investigating the optimal control system, the optimal control problem is solved using the genetic algorithm function ‘ga’ provided by the Global Optimization Toolbox in MATLAB (MATLAB R2023a, The MathWorks), which is known for its robustness and efficiency in finding global optima.

Chapter 3

A lettuce growth model responding to a broad range of greenhouse climates

In this chapter, a lettuce growth model that describes the effects of a broad range of greenhouse climates, including air temperature with extreme conditions, humidity, CO_2 concentration, and shortwave radiation, on crop dry weight dynamics is developed, calibrated, and validated.

3.1 Introduction

To generate an efficient optimal control system for climate management of greenhouses cultivating lettuce, an accurate lettuce growth model with robust generalisation is essential. Theoretically, the lettuce growth model should describe the complete effects of greenhouse climate variables. In particular, shortwave radiation, CO_2 concentration, air temperature and humidity (Stanghellini et al., 2019).

As reviewed by van Holsteijn (1980), the quantitative analysis of growth for lettuce dates back to the 1960s, providing valuable insights for subsequent modelling work. Current lettuce growth models can be generally distinguished according to two levels of production situation: potential production and nitrogen-limited production. Ido Seginer, Buwalda, and van Straten (1999) developed a lettuce model with two compartments (structure and vacuole) to simulate lettuce growth and nitrate content under limited nitrogen supply. This model was derived from their previous model for potential production (Ido Seginer, van Straten, & Buwalda, 1998) by introducing a nitrogen balance of the vacuoles and was subsequently modified to cover severe nitrogen-stress scenarios by extending a storage compartment for excess carbon (Ido Seginer, 2003). Its parameterisation was later optimised based on sensitivity and correlation analysis by Ilya Ioslovich, Moran, and Gutman (2005). The above 'Nicolet' model, which describes the effects of indoor air temperature, CO_2 concentration, and light, as well as nitrogen in the nutrient solution, can serve as the basis for greenhouse climate and nutrient controls to prevent excessive nitrate content in crops (I Seginer, Linker, Buwalda, Van Straten, & Bleyaert, 2003), as well as for rapid fault detection in hydroponic systems (Mathieu et al., 2006). However, optimal climate control requires the crop model to describe the potential production where water and nutrients are adequately provided, and only meteorological conditions determine the growth rate (Goudriaan & Van Laar, 1994). This study focuses on the simulation of lettuce growth in response to the shoot environment.

Several models are available in the literature for dynamic numerical simulation of potential lettuce growth. Early lettuce models were primarily empirical, using logistic, Gompertz, and

other sigmoidal forms (Shimizu, Kushida, & Fujinuma, 2008; Stützel & Chen, 2020; Tei et al., 1996), and have continued to attract research attention over the last decade (Carini et al., 2019; Q. Li, Gao, Zhang, Ni, & Mao, 2022). These simple statistical models struggle to explicitly account for the effects of greenhouse climate dynamics. With advances in artificial intelligence, more sophisticated data-driven models represented by neural networks have been developed for lettuce growth simulation. Their effectiveness and feasibility in simulating crop growth, yield, and physiological factors have been demonstrated (Chang, Chung, Fu, & Huang, 2021; Mohmed et al., 2023; Mokhtar et al., 2022). However, achieving high prediction accuracy and robust generalisation for practical applications requires vast amounts of data for model training, which presents a significant challenge as it often relies on obtaining crop growth indicators through destructive sampling.

Currently, mainstream lettuce growth models are mechanistic, the most commonly used in formulating control systems (Rohde & Forni, 2023; Ido Seginer, Shina, Albright, & Marsh, 1991; Van Henten, 1994a; D. Xu et al., 2018; D. Xu et al., 2019). Mechanistic crop models are expected to generalise better than data-driven models since their development specifically describes processes that influence the state dynamics based on physical, chemical, and biological principles. To generate and solve analytical relationships for CO_2 concentration optimisation in commercial greenhouse lettuce production, Critten (1991) modified an early mechanistic lettuce growth model by (Sweeney, Hand, Slack, & Thornley, 1981), which originally included structural and storage dry weights as state variables, to a simplified model with one state by assuming the two weights to be equal. They mainly explain the effects of horizontal radiation and CO_2 concentration. The original model was later optimised to more sensitively incorporate instantaneous and long-term effects of temperature dynamics on photosynthesis and was extensively validated by Pearson, Wheeler, Hadley, and Wheldon (1997). Van Henten (1994a) developed both one-state and two-state lettuce growth models for optimal greenhouse climate management. The one-state model uses structural dry weight as the single state variable, assuming that carbohydrates produced by photosynthesis are partly consumed by maintenance respiration, with the remainder used for growth. In contrast, the two-state model (Van Henten, 1994b) considers total dry weight

as comprising structural and non-structural dry weights. The growth of structural dry matter derives from the transformation of non-structural materials into structural components, with its rate dependent on temperature and the non-structural material proportion. Both models predict the crop dry weight and leaf area index responding to greenhouse climate attributes, including shortwave radiation, CO_2 concentration, and air temperature within a limited range of 5-40 ℃. The Eldert lettuce models have been applied in optimal control studies (Van Henten, 1994a; Van Straten et al., 2010; Dan Xu et al., 2018) and adapted as a TRNSYS component for energy analysis (Talbot & Monfet, 2024). In addition, models based on the framework for potential growth can extend to describe nitrogen accumulation in crops using the turgor maintenance hypothesis (Ido Seginer et al., 1998; K. Zhang, Burns, Broadley, & Turner, 2003), which also fall within the scope of those supporting optimal climate control. Despite their strong generalisation ability and reported good performance, existing process-based lettuce growth models, which hold potential as a basis for optimal greenhouse climate control, are incomplete and lack sufficient motivation for complex control scenarios, thus constraining their practical applicability.

The first limitation of current lettuce models is the lack of describing the impact of air humidity on growth. Humidity is an important physical aspect of the greenhouse air that the crop releases water vapour via transpiration. It affects biochemical and morphogenetic processes, such as stomatal conductance, leaf cell elongation, and nutrient absorption (Bakker, 1991; Collier & Tibbitts, 1984; Monteith, 1995; Xinying Zhang et al., 2020). The sensitivity of crop growth to humidity levels is crop species dependent (Mortensen, 1986; Rawson, Begg, & Woodward, 1977). But in general, crop growth is inhibited by extreme humidity situations (very high or low humidity). Hence, including the effects of humidity in the crop growth model has considerable potential to improve model accuracy. With such a model, the optimal control strategies and humidity trajectories will be computed by trade-off additionally concerning the effects of control actions on crop growth induced by humidity changes, leading to a control approach that is much closer to the actual optimum. In contrast, with a model excluding humidity effects, the humidity trajectories will be determined by setpoints and subject to control of other climate variables. For instance, Van Henten (1994a)

and Tap (2000) accomplished humidity control by requiring the greenhouse relative humidity to stay between a lower and an upper limit, assuming that humidity does not affect crop production between these limits. A sensitivity analysis of the optimal control problem revealed that humidity control strongly influences greenhouse climate control performance, highlighting the need for a detailed description of humidity effects on crop growth (Van Henten, 2003).

Secondly, current lettuce growth models are primarily developed for typical greenhouse climate conditions. They cannot comprehensively account for the adverse effects of extreme temperatures, especially lacking a robust mechanism to fully describe growth inhibition beyond impacts on leaf photosynthesis, have not been tested under these extreme conditions, or even do not allow for such inputs. For instance, an extremely low night temperature benefits dry matter accumulation in their simulations due to the low consumption of maintenance respiration but inhibits the actual crop growth. Consequently, the optimal control system, in the absence of state constraints, might excessively reduce nighttime temperatures inside the greenhouse, potentially undermining efforts to enhance production efficiency. There is no doubt that crop growth will be inhibited by non-optimal temperature levels (Thompson, Langhans, Both, & Albright, 1998; Van Ploeg & Heuvelink, 2005; Volente, 2022). However, temperature fluctuations are allowed in greenhouse climate control to save energy and obtain higher net revenue (Körner & Van Straten, 2008; Stanghellini et al., 2019). Furthermore, extreme temperatures frequently occur inside greenhouses with low-tech climate conditioning devices, such as the Chinse solar greenhouse (CSG) (Weituo Sun et al., 2015). Therefore, the crop model must also adequately describe the relevant crop processes to a wide range of greenhouse air temperatures.

In addition, mechanistic crop models that describe dry matter accumulation based on the differences between photosynthesis and respiration often face challenges in effectively simulating the early stages of crop growth that are sink-limited. As stated by Tei et al. (1996), no successful attempt was made to explain how sink demand can limit growth. This issue still exists in modelling lettuce growth. The model framework and underlying hypothesis

designed in this study to fully describe temperature effects can implement the inhibition for sink-limited growth. Lastly, present lettuce models are established at the canopy level, with growth measured by biomass accumulation per unit ground area. However, the specific area for determining the default plant density has not been disclosed. The impact of plant density on model development will be reflected at least in model calibration. Since crop cultivation cannot occupy the entire greenhouse ground due to space needed for walkways, operations, and equipment, it is critical for the practical optimal control to measure the effective cultivation area, focusing on upper limits, and to ensure that the crop model component implies the effective cultivated area-based plant density.

In greenhouse horticulture, tomatoes are another representative crop. TOMSIM and TOMGRO, two widely recognized mechanistic models, have been developed to simulate the potential growth, development, and yield dynamics of tomatoes in response to greenhouse temperature, CO_2, and light conditions (E Heuvelink, 1999; E Heuvelink & Bertin, 1994; Jones, Dayan, Allen, Van Keulen, & Challa, 1991). Vanthoor, De Visser, Stanghellini, and Van Henten (2011) later extended the current tomato yield models with two lumped temperature-dependent growth inhibition functions. These tomato models, which account for complex processes involving developmental stages, provide valuable insights for developing other crop models. For instance, sink strengths of plant organs can be quantified by potential growth rates. However, they fall short of addressing the above gaps in lettuce growth modelling, including describing humidity effects, developing a robust temperature response mechanism, simulating early growth stages, and implementing the effective cultivation area-based plant density. Moreover, it is evident that the integration and validation of such elements in a lettuce growth model are lacking.

In summary, to efficiently deploy optimal control in greenhouse climate management, a mechanistic lettuce growth model that completely describes the effects of greenhouse climate dynamics, particularly with respect to humidity and extreme temperatures, is currently unavailable. Therefore, this chapter aims to describe, calibrate, and validate such a lettuce growth model that responds to a broad range of greenhouse climates, including

shortwave radiation, CO_2 concentration, air temperature with extreme conditions, and air humidity. The developed model is expected to have sufficient accuracy and robust generalisation. We assume that water and nutrients are readily available. Pests, diseases, and weeds are not considered. The model consists of a set of first-order differential equations and simulates instantaneous dynamics of crop growth to facilitate the link with existing greenhouse climate models and its integration into optimal control methods. The main contributions and innovations are as follows:

- Proposing a novel model framework that performs dry matter accumulation and buffer evolution in parallel, along with the underlying hypothesis of virtual buffer flows and canopy photosynthesis inhibition, by which effects of air temperature, including extreme conditions, on crop growth are adequately described, and early growth stages can be effectively simulated.
- Extending the description of humidity effects regarding stomatal resistance and the specific leaf area (SLA) of new leaves.
- Simplifying expressions of leaf carboxylation resistance and root ratio by fitting, and imposing constraints on the maximum ground area occupied by a single plant for the implicit plant density.
- Performing three field experiments, which cover a broad range of greenhouse climates, to calibrate and evaluate the model, as well as analyse the performing mechanism.

3.2 Model description

3.2.1 Model overview

The lettuce growth model is essentially based on earlier crop growth models (Goudriaan & Van Laar, 1994; Spitters, Van Keulen, & Van Kraalingen, 1989; Van Henten, 1994a; Van Ooteghem, 2010). It is extended with a temperature-dependent growth inhibition function on the basis of buffer evolution, achieved by the new crop model framework (Figure 3.1), and a set of humidity-related equations.

The state of the lettuce crop is described by a single state variable, structural dry weight, that is, the crop dry weight. The model describes the effects of a broad range of greenhouse climates, including air temperature with extreme conditions, humidity, CO_2 concentration, and shortwave radiation on lettuce growth. The model simulates instantaneous crop growth on a time scale of one second, requiring model inputs to be in time series marked in seconds but allowing for input data of different time intervals.

The proposed model framework performs two parallel sets of mass flows: dry matter accumulation and buffer evolution. The model assumes that the lettuce has a virtual carbohydrate (CH_2O) buffer, also namely assimilate pool, temporarily storing assimilate. The buffer affects crop photosynthesis through the diurnal courses of its carbohydrate storage. Unlike most other crop models, this buffer does not participate in dry matter formation as a dry matter component. Instead, it is only used for regulating photosynthesis.

The processes for dry matter accumulation are as follows. The carbohydrates produced by canopy photosynthesis are partially used for maintenance respiration. The remaining carbohydrates are converted into structural material and partitioned among various plant organs. In conversion, part of the weight is lost by growth respiration.

The rate of canopy photosynthesis serves as a basis for dry matter accumulation. It is calculated by integrating assimilation rates over the canopy leaf layers obtained through the photosynthesis-light response of individual leaves. That rate depends mainly on the radiant energy absorbed by the canopy, canopy temperature, CO_2 concentration and air humidity inside the greenhouse. Since the lettuce model is supposed to work in extreme climate conditions where the constant leaf resistances to CO_2 diffusion do not apply, a model including the humidity effect is used to compute the stomatal resistance. For leaf morphogenesis, the SLA of new leaves is defined in relation to climate factors that include humidity and radiation.

The processes for buffer evolution are as follows. The buffer receives carbohydrates

produced by canopy photosynthesis. Simultaneously, the carbohydrates stored in the buffer flow to maintenance respiration and the process of growth conversion or partitioning. The partitioning of the produced dry matter is determined by the maximum growth rate (sink strength) of organs or the whole crop. That is the maximum growth rate of the whole crop described by a function of instantaneous temperature calls for an equal buffer flow rate towards the conversion process. As adverse air temperatures, both during the day and night, inhibit the partitioning, the carbohydrate flows distributed from the buffer to the conversion process are accordingly reduced. Then, the carbohydrate amount in the buffer is more likely to reach high levels during daytime photosynthesis. The photosynthesis rate is inhibited when the carbohydrate amount reaches the maximum storage capacity of the buffer. The effects of extreme temperatures, beyond their instantaneous impact on photosynthesis, are incorporated into the model by describing the above hypothesis of buffer flows and photosynthesis inhibition.

For simplicity, the root ratio is described as a descriptive logarithmic function of the individual plant dry weight. Also, a descriptive function fitted from complex equations describes the leaf carboxylation resistance, enabling the model to allow temperature inputs in large ranges.

The two parallel sets of mass flows share paths but differ in logic. In dry matter accumulation, there is no restriction on the mass flow to growth conversion after photosynthesis. However, in buffer evolution with virtual mass flows, the mass flow to growth conversion performs the potential growth rate of the crop.

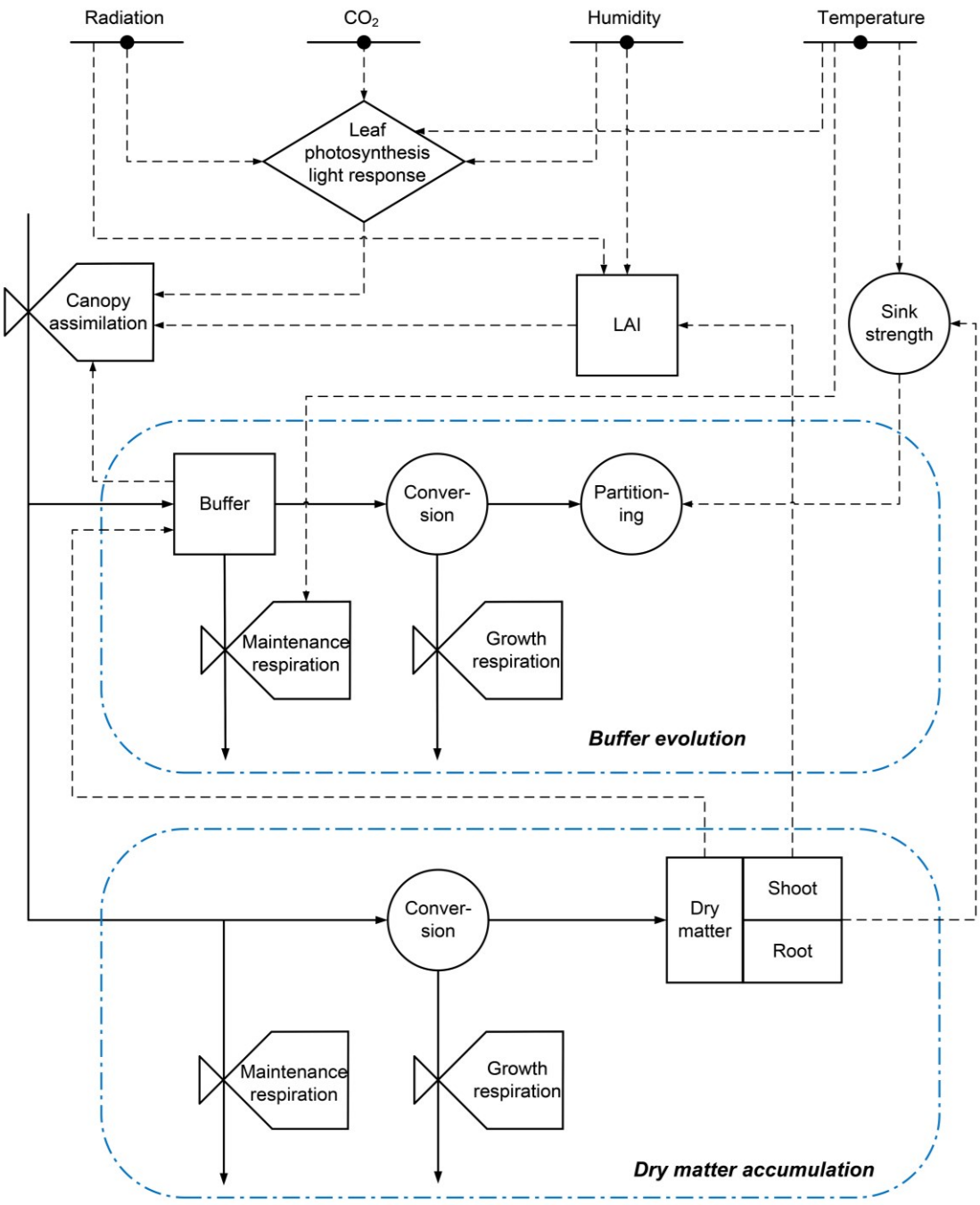

Figure 3.1 Schematic diagram of the lettuce growth model using a modelling formalism of Forrester. The boxes are state variables of the model, valves are rate variables, circles are auxiliary variables, and the straight lines crossing solid circles represent input variables. The dashed lines represent information flows, and the solid lines represent mass flows.

3.2.2 Model equations

3.2.2.1 Dry matter production

In line with the crop growth formulation by SUCROS1 (Goudriaan & Van Laar, 1994; van Laar, Goudriaan, & van Keulen, 1997) and the one-state variable lettuce growth model (Van Henten, 1994a), the basis for calculating dry matter production is the net CO_2 assimilation rate of the canopy. A buffer-related inhibition function is introduced to deal with particular growth cases caused by extreme climate conditions. This gives rise to the following description of the dry matter production,

$$\frac{dX_d}{dt} = c_\beta \cdot \left(c_\alpha \cdot A_C \cdot h_{buf} - R_d\right) \tag{3.1}$$

where X_d [kg m^{-2} (gro)] is the crop dry weight, A_C [kg (CO_2) m^{-2} (gro) s^{-1}] is the gross canopy assimilation rate, R_d [kg (CH_2O) m^{-2} (gro) s^{-1}] is the crop maintenance respiration rate, c_β [-] is the factor converts carbohydrates to structural material due to the growth respiration and synthesis, c_α [-] is the factor converts assimilated CO_2 into sugar equivalents in the photosynthesis process, h_{buf} [-] is the buffer dependent inhibition function for canopy assimilation, t [s] is the time. Eq. (3.1) asserts that the assimilates give priority to maintenance respiration. Then, all the remaining assimilates are used for structural dry matter production. In this model and most other crop growth models, A_C has already subtracted photorespiration consumption, which is the so-called apparent gross assimilation rate. Accordingly, the net assimilation rate means the gross assimilation rate minus the maintenance respiration rate.

3.2.2.2 Assimilation inhibition

The buffer storage status affects canopy photosynthesis. This model assumes that when the carbohydrate storage approaches the maximum buffer capacity, further carbohydrates cannot

be stored, and photosynthesis will be inhibited. In this case, the canopy assimilation does not stop but offsets the instantaneous carbohydrate consumption for biomass maintenance and potential crop growth. The buffer dependent inhibition function h_{buf} is described by

$$h_{buf} = \begin{cases} 1, & C_{buf} < C_{buf,max} \\ \min\left(\dfrac{R_d + \dfrac{RGR_{max} \cdot X_d}{c_\beta}}{c_\alpha \cdot A_C}, 1\right), & C_{buf} = C_{buf,max}\ (A_C \neq 0) \end{cases} \tag{3.2}$$

Where RGR_{max} [s^{-1}] is the maximum relative growth rate that depends on temperature, C_{buf} [kg (CH_2O) m^{-2} (gro)] is the amount of stored carbohydrates in the buffer, $C_{buf,max}$ [kg (CH_2O) m^{-2} (gro)] is the maximum buffer capacity for diurnal assimilates storage.

A two-state variable crop growth model supposes that plant dry matter can be divided into structure and storage. The rate of structural growth depends on the amount of storage substrate present (Thornley & Hurd, 1974). Our model assumes the lettuce crop only has structural dry matter. In the line of dry matter accumulation, there is no restriction on the mass flow to growth conversion after photosynthesis. While in the other parallel line of buffer evolution, whenever the carbohydrates in the buffer are available, they flow to growth conversion based on the maximum growth rate (sink strength). In other words, the structural growth rate for buffer design is sink determined. The maximum relative growth rate RGR_{max} is adapted from (Van Henten, 1994b)

$$RGR_{max} = \begin{cases} RGR_{max,20} \cdot Q_{10,gr}^{\frac{T_c - 20}{10}}, & T_c \leq T_{c,RGR} \\ RGR_{max,20} \cdot Q_{10,gr}^{-\frac{T_c - 20}{10}}, & T_c > T_{c,RGR} \end{cases} \tag{3.3}$$

where $RGR_{max,20}$ [s^{-1}] is the maximum relative growth rate of dry matter at 20 °C, $Q_{10,gr}$ [-] is the Q_{10} factor for crop growth, T_c [°C] is the canopy temperature, which is assumed to be equal to the air temperature X_t [°C] in this model, $T_{c,RGR}$ [°C] is the temperature to achieve the saturation relative growth rate.

Vanthoor (2011) set the maximum buffer capacity to a fixed value of 20×10^{-3} kg (CH_2O) m^{-2} (gro), assuming that it is equal to the sum of carbohydrates produced at potential photosynthesis on a daily basis. However, a biomass-varying storage capacity is needed to realise the inhibition function of the buffer. According to Goudriaan, Van Laar, Van Keulen, and Louwerse (1985), if the plant does not have sufficient sinks, a buffer storage level rising above 20% on a dry weight basis will gradually diminish the carboxylation conductance and assimilation rate. So, in this model, the maximum buffer capacity $C_{buf,max}$ is assumed as

$$C_{buf,max} = \sigma_{buf} \cdot X_d \tag{3.4}$$

where σ_{buf} [-] is the ratio of the maximum buffer capacity to crop dry weight.

The evolution of stored carbohydrates in the buffer is determined by carbohydrate flow from actual photosynthesis as well as flows to maintenance respiration and growth conversion processes. These flows do not contribute to an empty buffer unless they can increase the buffer storage. The variation of the amount of stored carbohydrates in the buffer C_{buf} is described by

$$\frac{dC_{buf}}{dt} = c_\alpha \cdot A_C \cdot h_{buf} - R_d - \frac{RGR_{max} \cdot X_d}{c_\beta}, \qquad 0 \le C_{buf} \le C_{buf,max} \tag{3.5}$$

3.2.2.3 Canopy Assimilation

The gross canopy assimilation rate A_C is described by

$$A_C = A_{L,C} \cdot LAI \tag{3.6}$$

where $A_{L,C}$ [kg (CO_2) m^{-2} (leaf) s^{-1}] is the gross leaf assimilation rate at a whole canopy level, LAI [m^2 (leaf) m^{-2} (gro)] is the leaf area index.

$A_{L,C}$ is obtained from the weighted average assimilate rate over the horizontal leaf layers of the canopy. This is achieved using a three-point Gaussian integration (Goudriaan, 1986). The cumulative LAI at each leaf layer is used to express the canopy depth l_i [m^2 (leaf) m^{-2} (gro)] that locates leaf layers. From top to bottom, the canopy depth ranges between zero and *LAI*. The three selected canopy depths are

$$l_i = \left\{0.5 - \sqrt{0.15},\ \ 0.5,\ \ 0.5 + \sqrt{0.15}\right\} \cdot LAI, \qquad i = \{1,\ \ 2,\ \ 3\} \tag{3.7}$$

The gross leaf assimilation rate at a whole canopy level $A_{L,C}$ is described by

$$A_{L,C} = \frac{A_{L,l_1} + 1.6 \cdot A_{L,l_2} + A_{L,l_3}}{3.6} \tag{3.8}$$

where $A_{L,l1}$, $A_{L,l2}$ and $A_{L,l3}$ [kg (CO_2) m^{-2} (leaf) s^{-1}] are the gross leaf assimilation rates of the selected three leaf layers from up to down, respectively. The integrated value is obtained by applying a weighting factor of 1.6 to the value at the canopy depth of $0.5 \cdot LAI$ and 1.0 to both other values.

3.2.2.4 Leaf area expansion

During the early stages of crop growth, leaf area expansion is mainly controlled by temperature, which affects cell division and elongation, rather than by the availability of assimilates. As a result, leaf area increases approximately exponentially over time. In the later stages of development, the expansion of the leaf area becomes progressively limited by the supply of assimilates (Spitters et al., 1989). As reviewed by (Marcelis, Heuvelink, & Goudriaan, 1998), simulating leaf area on the basis of simulated leaf biomass increment and the SLA of new leaves has been used in several models. The crop growth in the early stages is essentially sink-limited, equivalent to growing in quite low temperatures and high radiation levels. This situation can also be described by the simulated leaf dry mass variation and the SLA of new leaves that imply the sink inhibition implemented by the buffer. Hence

LAI is uniformly described by

$$\frac{dLAI}{dt} = \frac{dX_d}{dt} \cdot (1 - \sigma_r) \cdot SLA \tag{3.9}$$

where *SLA* [m^2 (leaf) kg^{-1} (leaf)] is the SLA of new leaves, expressing the amount of leaf area per unit shoot dry matter for new leaves, σ_r [-] is the ratio of the root dry weight to crop dry weight.

SLA was defined as a function of irradiance, ambient temperature and CO_2 concentration in TOMGRO models (Dayan et al., 1993a; Jones et al., 1991). Further, *SLA* depends mainly on temperature and is much less affected than by irradiance and CO_2 concentration (Dayan et al., 1993b). So Gary, Barczi, Bertin, and Tchamitchian (1994) and Gijzen et al. (1997) proposed to use temperature and physiological age to describe the leaf expansion rate. However, according to the model calibration at the sub-model level in Chapter 3.3, radiation shows a much stronger correlation with *SLA* than temperature. In addition, when air is dry, cell elongation is reduced, leading to smaller leaves. Larger and thinner lettuce leaves are produced at high relative humidity (Bradbury & Ahmad, 1996; Tibbitts & Bottenberg, 1976). Hence, in this model, *SLA* depends on radiation, humidity and a reference *SLA*.

$$SLA = SLA_{ref} \cdot f_{I,SLA} \cdot f_{Xh,SLA} \tag{3.10}$$

Where SLA_{ref} [m^2 (leaf) kg^{-1} (leaf)] is the reference *SLA* at the reference absorbed shortwave radiation by leaves $I_{L,ref}$ [W m^{-2} (leaf)] and the reference relative humidity $X_{h,ref}$ [-], $f_{I,SLA}$ [-] is the factor accounting for the effect of radiation on *SLA*, $f_{Xh,SLA}$ [-] is the factor accounting for the effect of air humidity on *SLA*.

Referring to the expression form of climate determinant factor for *SLA* by Jones et al. (1991), $f_{I,SLA}$ is described by

$$f_{I,SLA} = \frac{1}{1 + \beta_I \cdot \left(I_{L,ref} - I_{can}/LAI\right)} \tag{3.11}$$

where β_I [m^2 (leaf) W^{-1}] is the relative change in *SLA* per unit change in absorbed shortwave radiation by leaves, $I_{L,ref}$ [W m^{-2} (leaf)] is an arbitrary reference absorbed shortwave radiation by leaves corresponding to SLA_{ref}, I_{can} [W m^{-2} (gro)] is the absorbed shortwave radiation by canopy.

Similarly, $f_{Xh,SLA}$ is described by

$$f_{Xh,SLA} = \frac{1}{1 + \beta_{Xh} \cdot \left(X_{h,ref} - X_h\right)} \tag{3.12}$$

where X_h [-] is the air relative humidity, β_{Xh} [-] is the relative change in *SLA* per unit change in relative humidity, $X_{h,ref}$ [-] is an arbitrary relative humidity corresponding to SLA_{ref}.

3.2.2.5 Photosynthesis-light response

The gross assimilation rate of individual leaves A_L [kg (CO_2) m^{-2} (leaf) s^{-1}] can be described by a negative exponential photosynthesis-light response curve. See details in Appendix A.

3.2.2.6 Leaf resistance

The total leaf resistance for CO_2 transport from ambient air to the chloroplast is determined by adding stomatal, boundary layer and carboxylation resistances. When the CO_2 concentration is measured above the canopy, the so-called turbulence resistance must be added because the CO_2 concentration in free air is less variable than that within the canopy (Goudriaan, 1982; Yin & Van Laar, 2005). Cuticular resistance, parallel to the stomatal resistance (Bot, 1983), also exists. However, it is much larger than stomatal resistance (Monteith & Unsworth, 2013). The contribution of the cuticle to CO_2 transfer is ignored in

this research. Then, the total leaf resistance to CO_2 diffusion r_{CO2} is described by

$$r_{CO2} = r_s + r_b + r_c + r_t \tag{3.13}$$

where r_s, r_b, and r_c [s m^{-1}] are the stomatal resistance, boundary layer resistance, and carboxylation resistance, respectively, r_t [s m^{-1}] is the turbulence resistance with an appropriate constant value.

In the literature, the stomatal and boundary layer resistances are often assumed constant for photosynthesis rate simulation. However, Van Ooteghem (2010) found that the photosynthesis models with dynamic resistances give a better description than those with constant resistances. During photosynthesis, CO_2 molecules follow the same path as water vapour (H_2O) but in the opposite direction. The dynamic resistances to CO_2 diffusion are mainly determined with an evaporation model that holds equations for the stomatal and boundary layer resistances to H_2O by Stangheilini (1987). Then, the stomatal resistance to diffusion of CO_2 is described by

$$r_s = c_\zeta \cdot r_{H2O,min} \cdot f_{I,s} \cdot f_{Tc,s} \cdot f_{Xc,s} \cdot f_{Xh,s} \tag{3.14}$$

in which c_ζ [-] is the scaling factor that accounts for the faster diffusion of H_2O compared to CO_2 in crossing stomata, $r_{H2O,min}$ [s m^{-1}] is the minimum possible internal crop resistance to H_2O.

And the radiation dependency $f_{I,s}$ is described by

$$f_{I,s} = \frac{\frac{I_{can}}{2 \cdot LAI} + 4.30}{\frac{I_{can}}{2 \cdot LAI} + 0.54} \tag{3.15}$$

The temperature dependency $f_{Tc,s}$ is described by

$$f_{Tc,s} = \begin{cases} 1 + 0.5 \cdot 10^{-2} \cdot (T_c - 33.6)^2, & I \leq 3 \\ 1 + 2.3 \cdot 10^{-2} \cdot (T_c - 24.5)^2, & I > 3 \end{cases} \quad (3.16)$$

The CO_2 dependency $f_{Xc,s}$ is described by

$$f_{Xc,s} = \begin{cases} 1\ , & I \leq 3 \\ 1 + 6.1 \cdot 10^{-7} \cdot (X_c - 200)^2, & I > 3 \wedge X_c < 1100 \\ 1.5\ , & I > 3 \wedge X_c \geq 1100 \end{cases} \quad (3.17)$$

The humidity dependency $f_{Xh,s}$ is described by

$$f_{Xh,s} = \frac{4}{\left(1 + 255 \cdot \mathrm{e}^{-0.54 \cdot 10^{-2} \cdot e_{c,a}}\right)^{0.25}} \quad (3.18)$$

where $e_{c,a}$ [Pa] represents leaf-to-air vapour pressure difference.

Differing from absorbed PAR per leaf area for a specific leaf layer in the canopy, I_{can} [W m^{-2} (gro)], which represents absorbed shortwave radiation by canopy, is calculated by

$$I_{can} = \left(1 - c_{r,I}\right) \cdot I \cdot (1 - e^{-k_I \cdot LAI}) \quad (3.19)$$

where $c_{r,I}$ [-] is the canopy reflection coefficient for shortwave radiation, k_I [-] is the extinction coefficient for shortwave radiation.

Since canopy temperature is assumed to be equal to air temperature and vapour pressure in leaves is always saturated, $e_{c,a}$ is equal to vapour pressure deficit (VPD) of greenhouse air. Then $e_{c,a}$ could be described by

$$e_{c,a} = e_{s,air} \cdot (1 - X_h) \quad (3.20)$$

And the saturated vapour pressure $e_{s,air}$ is described by (Stanghellini et al., 2019)

$$e_{s,air} = \begin{cases} 10^{2.7857+\frac{9.5 \cdot X_t}{265.5+X_t}}, & X_t < 0 \\ 10^{2.7857+\frac{7.5 \cdot X_t}{237.3+X_t}}, & X_t \geq 0 \end{cases} \tag{3.21}$$

The resistance offered by the boundary layer depends on leaf dimensions and windspeed. The boundary layer resistance to CO_2 diffusion, which is derived from that to convective heat transfer, is described by

$$r_b = Le^{0.67} \cdot \frac{1174 \cdot {l_f}^{0.5}}{\left(l_f \cdot |T_c - X_t| + 207 \cdot {v_a}^2\right)^{0.25}} \tag{3.22}$$

where Le [-] is the Lewis number for CO_2 in air at 25 ℃. $Le^{0.67}$ represents the ratio of boundary layer resistance for CO_2 diffusion to that for forced heat convection. l_f [m] is the leaf characteristic dimension, taken as the mean leaf width in the wind direction (Schuepp, 1993). v_a [m s^{-1}] is the wind speed inside the greenhouse.

Van Henten (1994a) used a second-order polynomial fitting to describe the carboxylation resistance. This polynomial only works within an air temperature range from 5 to 40 ℃. It does not apply to the optimal control that allows more extreme temperatures. The description of carboxylation resistance by Goudriaan and Van Laar (1994) and Van Ooteghem (2010) covers a wider temperature range. It is also more explanatory, since it defines the carboxylation resistance as the ratio of the effective Michaelis Menten constant for carboxylation to the maximum carboxylation rate, both of which are derived from Farquhar, von Caemmerer, and Berry (1980). In this model, we use a descriptive function of temperature like that by Van Henten (1994a) but derived from the simulation result by Van Ooteghem (2010) to describe the leaf carboxylation resistance r_c,

$$r_c = c_{rc,1} \cdot {T_c}^2 + c_{rc,2} \cdot T_c + c_{rc,3} \tag{3.23}$$

where $c_{rc,1}$ [m s^{-1} °C^{-2}], $c_{rc,2}$ [m s^{-1} °C^{-1}], and $c_{rc,3}$ [m s^{-1}] are coefficients of the second order polynomial fitting for the description of carboxylation resistance.

3.2.2.7 Respiration

Some carbohydrates generated are used in respiration to supply energy to sustain the current biostructures. A detailed description of the crop maintenance respiration rate R_d is provided in Appendix A.

3.2.2.8 Shoot/ root ratio

The ratio of shoot dry weight to root dry weight at some point depends on the accumulation of dry matter partitioning during the past growing period. The dry matter partitioning among plant organs is primarily regulated by the sink strengths of the organs. The sink strength is quantified by the maximum growth rate of the organ (Marcelis, 1996), which mainly depends on the development stage or heat sum (Penning De Vries & Van Laar, 1982). The development stages are usually distinguished based on the major phenological events, such as emergence (defined with a value of 0), anthesis (defined with a value of 1) and ripening (defined with a value of 2) (Goudriaan & Van Laar, 1994). For greenhouse climate control of lettuce cultivation, crop growth simulation will be located in a single development stage range between 0 and 1, especially from the transplanting date. Hence, Lazof, Bernstein, and Läuchli (1991) and Lazof and Bernstein (1999) used the leaf plastochron index (LPI) to define the development stage. As reviewed by Bakker, Bot, Challa, and van de Braak (1995), dry matter distribution towards roots generally decreases with plant size. Instead of calculating leaf and root dry weights by integration based on the partitioning factors that depend on the development stage, the root ratio σ_r [-] described as a function of the individual plant dry weight, is adopted. It is largely simplified and assumed to be accurate enough to

determine the shoot/ root ratio for the leafy vegetable.

$$\sigma_r = c_{\sigma r,1} \cdot \ln\left(\frac{X_d}{\rho_c}\right) + c_{\sigma r,2} \tag{3.24}$$

where $c_{\sigma r,1}$ [plants kg^{-1}] and $c_{\sigma r,2}$ [-] are coefficients for describing root ratio, ρ_c is plant density, plants m^{-2} (gro).

3.2.3 Parameter estimation and calibration

All the parameters of the lettuce growth model, including their values and sources, are listed in Table 3.1. These parameters remained constant throughout the simulations and are expected to apply to future model applications in greenhouse management for lettuce cultivation. Most of them were derived directly or estimated from the literature. Some model parameters were determined by means of model calibration at both the sub-model and model levels. The others were determined from physical properties. The selection of some of the model parameters is justified as follows.

Table 3.1 Parameterisation of the lettuce crop growth model

Parameter	value	unit	source
c_H	2.2×10^5	J mol^{-1}	Farquhar et al. (1980)
$c_{r,I}$	0.22	-	Goudriaan and Van Laar (1994)
$c_{r,PAR}$	0.07	-	Marcelis et al. (1998)
$c_{rc,1}$	0.315	m s^{-1} °C^{-2}	estimated from Van Ooteghem (2010)
$c_{rc,2}$	-27.35	m s^{-1} °C^{-1}	estimated from Van Ooteghem (2010)
$c_{rc,3}$	790.7	m s^{-1}	estimated from Van Ooteghem (2010)
$c_{Rd,25,r}$	1.16×10^{-7}	kg (CH_2O) kg (dry matter) s^{-1}	van Keulen, Penning de Vries, and Drees (1982)
$c_{Rd,25,sh}$	3.47×10^{-7}	kg (CH_2O) kg (dry matter) s^{-1}	van Keulen et al. (1982)
c_S	710	J mol^{-1} K^{-1}	Farquhar et al. (1980)

c_α	0.68	-	physical constant
c_β	0.8	-	Van Henten (1994a)
c_ζ	1.6	-	Goudriaan (1982)
$c_{\sigma r,1}$	-0.026	plants kg^{-1}	sub-model calibration
$c_{\sigma r,2}$	-0.076	-	sub-model calibration
E_J	3.7×10^{4}	J mol^{-1}	Van Ooteghem (2010)
$I_{L,ref}$	50.3	W m^{-2} (leaf)	sub-model calibration
$J_{max,25}$	210.15	µmol (e^-) m^{-2} (leaf) s^{-1}	Van Ooteghem (2010)
k_I	0.48	-	Van Ooteghem (2010)
k_{PAR}	0.9	-	Van Henten (1994a)
Le	1.47	-	Monteith and Unsworth (2013)
l_f	0.1	m	measurement
M_{CO2}	44×10^{-3}	kg mol^{-1}	physical constant
$Q_{10,gr}$	1.6	-	Sweeney et al. (1981)
$Q_{10,Rd}$	2	-	Goudriaan and Van Laar (1994)
$Q_{10,\Gamma}$	2	-	Goudriaan and Van Laar (1994)
R_g	8.314	J mol^{-1} K^{-1}	physical constant
$RGR_{max,20}$	1.54×10^{-6}	s^{-1}	global calibration
$r_{H2O,min}$	82	s m^{-1}	Stangheilini (1987)
r_t	50	s m^{-1}	Goudriaan (1982)
SLA_{rf}	47.93	m^2 (leaf) kg^{-1} (leaf)	sub-model calibration
$T_{c,RGR}$	25	°C	global calibration
v_a	0.09	m s^{-1}	Van Ooteghem (2010)
$X_{h,ref}$	0.75	-	sub-model calibration
β_I	-4.74×10^{-3}	m^2 (leaf) W^{-1}	sub-model calibration
β_{Xh}	0.912	-	sub-model calibration
ε_0	17×10^{-9}	kg (CO_2) J^{-1}	Goudriaan et al. (1985)
$\rho_{CO2,T0}$	1.98	kg m^{-3}	physical constant
σ_{buf}	0.2	-	estimated from Goudriaan et al. (1985)
σ_{PAR}	0.5	-	Stanghellini et al. (2019)
Γ_{T20}	40	µmol (CO_2) mol^{-1} (air)	Goudriaan and Van Laar (1994)

According to Goudriaan et al. (1985), if the plant lacks adequate sinks, an increase in buffer storage exceeding 20% on a dry matter basis will reduce the assimilation rate. Thus, the ratio of the maximum buffer capacity to crop dry weight σ_{buf} was set to 0.2. In addition, the primary assimilates, beyond what is needed for maintenance, are transformed into structural plant material. Considering the little difference in assimilate requirements to form a unit weight of leaves and roots (Spitters et al., 1989), the conversion factor of a lettuce crop c_{β} = 0.8 was set at the whole plant level (Van Henten, 1994a). Hence, the crop growth simulation can take the dry matter as substrates of the partition process rather than the primary carbohydrates by photosynthesis, which is the actual situation.

The response of leaf carboxylation resistance r_c to canopy temperature T_c was described by quadratic polynomial fitting in the range of 0 to 50 ℃ (Figure 3.2). The temperature interval for fitting was 0.1 ℃, and the corresponding carboxylation resistance data were derived from the simulation result of the model by Van Ooteghem (2010). Coefficients of the quadratic term $c_{rc,1}$, linear term $c_{rc,2}$, and constant term $c_{rc,3}$ were estimated to be 0.315 m s^{-1} $℃^{-2}$, -27.35 m s^{-1} $℃^{-1}$, and 790.7 m s^{-1}.

X_d /ρ_c [kg $plant^{-1}$] represents the individual plant dry weight. With its increase, the root ratio decreases logarithmically (Figure 3.3). To make the model parameters more universal, data from three experiments were used to estimate the coefficients of the logarithmic function. The coefficients of $c_{\sigma r,1}$ and $c_{\sigma r,2}$ were calculated to be -0.026 m^2 kg^{-1} and -0.076, respectively.

It is not easy to measure biomass and leaf area as frequently as measuring greenhouse climate (e.g., sampling every 5 minutes). The available crop data for calibrating the sub-model that describes the SLA of new leaves were sampled every five days. Thus, the *SLA* and *LAI* data were taken from the difference and average of two adjacent samples, respectively. Accordingly, the climate data used for calibration were averaged over five days, and only daytime data were counted since new leaves are mainly generated under the light. Calibration using average climate data is accepted since, as defined by Eq. (3.11) and (3.12), the effects of absorbed shortwave radiation per leaf area and air humidity on *SLA* are

respectively assumed to be linear. First, linear fitting slopes were calculated as -0.227 m^4 kg^{-1} W^{-1} for radiation and 43.69 m^2 kg^{-1} for humidity. Compared with temperature (R^2 = 0.122, *RMSE* = 11.569), radiation (R^2 = 0.351, *RMSE* = 9.947) and humidity (R^2 = 0.247, *RMSE* = 10.712) showed stronger correlations with *SLA*. Second, β_I and β_{Xh} were expressed by -0.227/SLA_{ref} [m^2 W^{-1}] and 43.69/SLA_{ref} [-] for calibration since they make sense only for a specific reference *SLA*. Third, SLA_{ref}, $I_{L,ref}$, $X_{h,ref}$ were estimated to be 47.93 m^2 (leaf) kg^{-1} (leaf), 50.3 W m^{-2} (leaf), and 0.75 by fitting (Figure 3.4) in the functional form of Eq. (3.10)-(3.12). Also, β_I and β_{Xh} were determined as -4.74×10^{-3} m^2 W^{-1} and 0.912.

As noted by Van Henten (1994b), interpreting the maximum relative growth rate of dry matter at 20 °C ($RGR_{max,20}$) is not entirely straightforward. While his study estimated this rate to be 5×10^{-6} s^{-1}, it would not be achieved in practice. Another parameter associated with the maximum relative growth rate was the temperature to achieve the saturation relative growth rate ($T_{c,RGR}$), which was newly introduced and lacked reference values within the model framework. In the absence of available data for local calibration of these two parameters, they were instead determined by global calibration. The global calibration, using data from Exp_2, aimed to minimise the *RRMSE* between the measured and simulated crop dry weights. A grid search method was used for reference to limit the range of parameters and traverse the parameter combinations. $RGR_{max,20}$ and $T_{c,RGR}$ were calibrated to be 1.54×10^{-6} s^{-1} and 25 °C, achieving the minimum *RRMSE* of 16.8%.

Figure 3.5 presents greenhouse climate inputs and the simulation result based on Exp_2 conducted during the cold season. Although growers made great efforts to regulate the greenhouse climate for lettuce cultivation, extreme thermal environments frequently occur, which is common in current CSGs. The simulation spanned 50 consecutive days, with the average air temperature of 18.2 °C during the day and 7.9 °C at night. The extremely low temperatures below 5 °C constituted 16% of the period and even briefly dropped to below zero in two nights with a minimum of -1.0 °C. Low temperatures were the main temperature stress in this calibration experiment. Over the simulation, the average humidity was 58% and 93% in the daytime and nighttime. Extremely high humidity levels, indicated by VPD lower

than 0.2 kPa (Stanghellini et al., 2019), accounted for 65% of the period, whereas extremely low humidity, with VPD higher than 1.0 kPa, accounted for 16%. Humidity stress, especially high humidity stress, occupied most of this period. Daily cumulative radiation was measured to be 1.9-6.9 MJ d^{-1}, with an average of 5.6 MJ d^{-1}. CO_2 was supplemented by natural ventilation, maintaining an average concentration of 533 ppm during the day and 614 ppm at night. In the early stages of lettuce growth, the daytime CO_2 concentration exceeding 400 ppm might be due to the decomposition of organic bottom fertiliser. The simulated dry matter weights closely mirrored the measured values, and underestimation existed except for the harvest timepoint. Through model calibrations at both sub-model and model levels, the model performance was evaluated to be good in simulating lettuce dry weight, with *RRMSE* = 16.8% and *RMSE* = 0.0081 kg m^{-2} (gro).

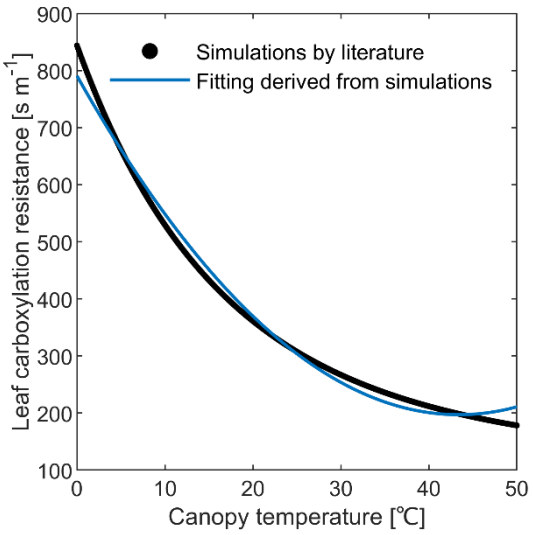

Figure 3.2 Fitting of the leaf carboxylation resistance. R^2 = 0.992, *RMSE* = 15.996.

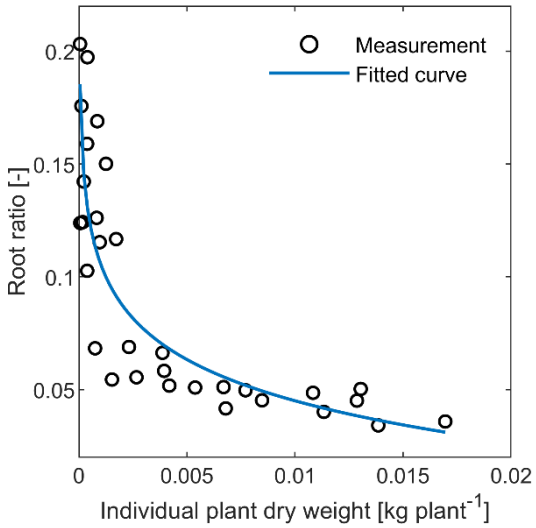

Figure 3.3 Root ratio variation along with the individual plant dry weight. $R^2 = 0.726$, $RMSE = 0.028$.

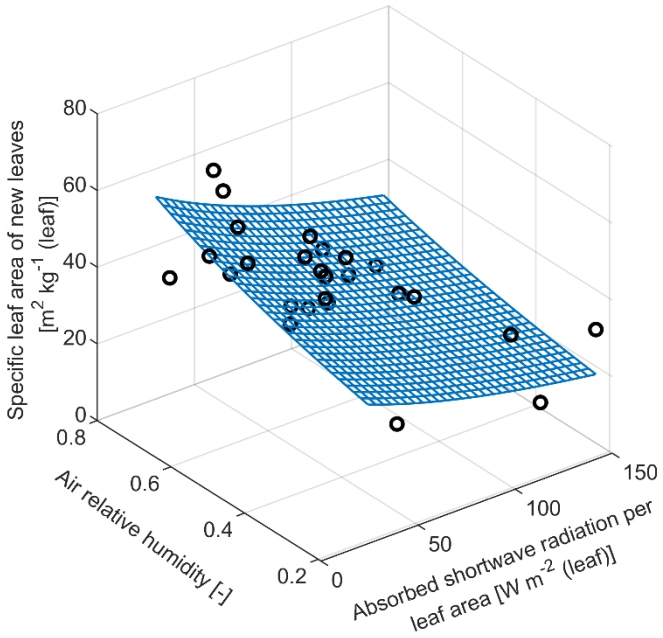

Figure 3.4 Effects of absorbed shortwave radiation by leaves and air humidity on the specific leaf area of new leaves. $R^2 = 0.380$, $RMSE = 9.928$.

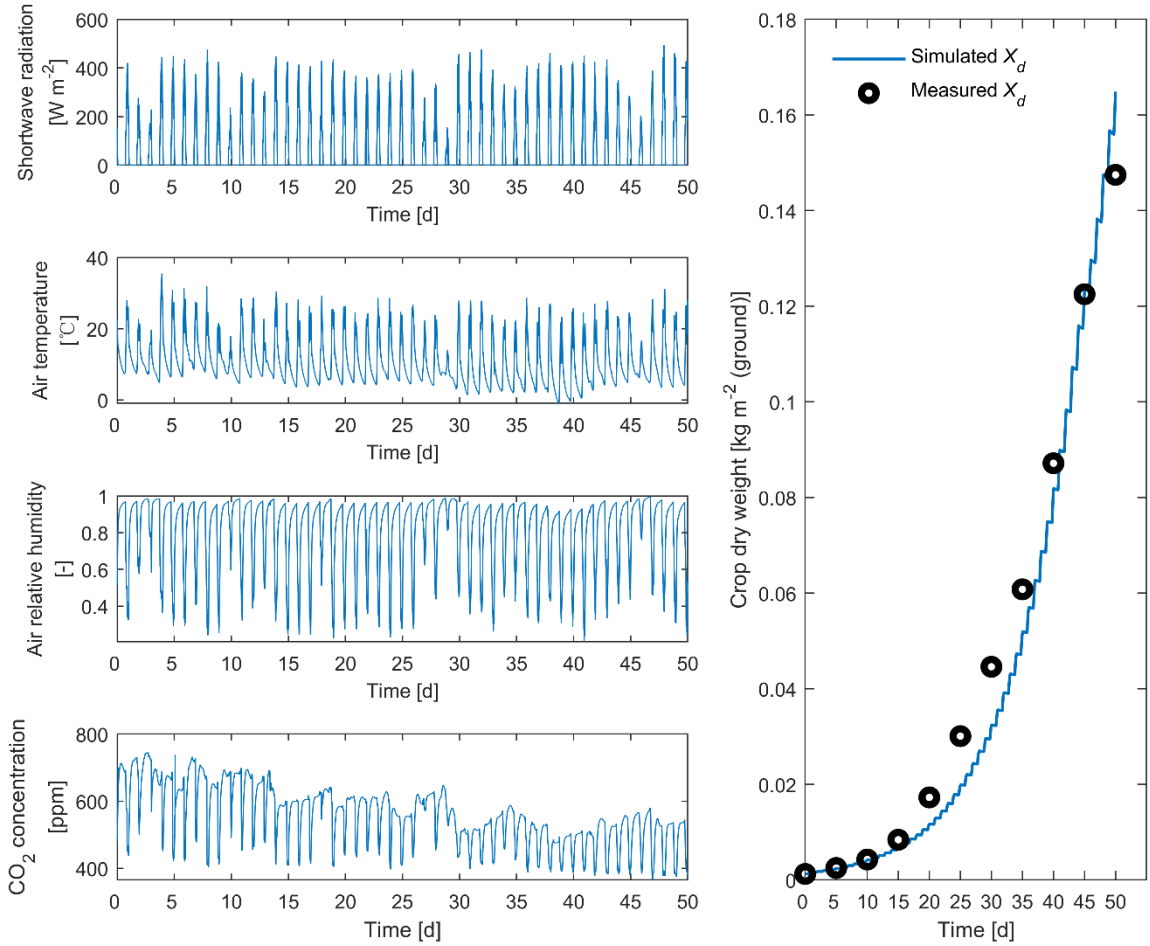

Figure 3.5 Five minutes averages of the greenhouse climate measurements, as well as the measured and simulated crop dry weights during the calibration experiment serving the global calibration. The simulation is from 15:00, 29 November 2020, to 15:00, 18 January 2021.

3.3 Results and discussion

3.3.1 Model validation

The model was validated using the observed data from Exp_1 and Exp_3. The model parameters in the validation simulations were kept constant with those (Table 3.1) contributed by the global calibration using data from Exp_2. The model inputs included the greenhouse climate (I, X_c, X_t, and X_h), initial crop states (X_d, LAI, and C_{buf}), and plant density

ρ_c. The initial X_d and LAI were measured values, while the initial C_{buf} was set to be 0 kg m^{-2} (Table 2.3). The model validation mainly compared the measured and simulated values of the crop dry weight, representing the state of lettuce growth in this study.

Figure 3.6 presents greenhouse climate inputs and the model validation result based on Exp_1 conducted during the warm season. The simulation spanned 35 consecutive days, from lettuce transplanting to harvesting, with the average air temperature of 24.3 ℃ during the day and 14.1 ℃ at night. The temperatures exceeding 30 ℃ constituted 17% of the period, reaching a maximum of 42.6 ℃, while the extremely low temperatures below 5 ℃ constituted only 3%, with a minimum of -0.8 ℃. High temperatures were the primary temperature stress during Exp_1. Over this validation process, the average humidity was 41% and 65% in the daytime and nighttime. Extremely high humidity levels, indicated by VPD lower than 0.2 kPa, accounted for 19% of the period, whereas extremely low humidity, with VPD higher than 1.0 kPa, accounted for 51%. Humidity stress, especially the low humidity stress, dominated this period. Daily cumulative radiation was measured to be 1.7-21.3 MJ d^{-1}, with an average of 15.5 MJ d^{-1}. CO_2 was supplemented by natural ventilation, maintaining an average concentration of 396 ppm during the day and 417 ppm at night. The simulated dry matter weights closely agreed with the measured values, with an overall overestimation. The model performance was acceptable in simulating the crop dry weight of the lettuce, with $RRMSE$ = 24.9% and $RMSE$ = 0.0131 kg m^{-2} (gro).

Figure 3.7 presents greenhouse climate inputs and the model validation result based on Exp_3 conducted during the cold-warm season. The simulation spanned 45 consecutive days, with the average air temperature of 20.9 ℃ during the day and 11.7 ℃ at night. The temperatures exceeding 30 ℃ constituted 4% of the period, reaching a maximum of 36.0 ℃, while the extremely low temperatures below 5 ℃ constituted only 1%, with a minimum of 3.9 ℃. The greenhouse climate was generally mild in Exp_3. Over this validation process, the average humidity was 60% and 95% in the daytime and nighttime. Extremely high humidity levels accounted for 61% of the period, whereas extremely low humidity accounted for 21%. Humidity stress, especially the high humidity stress, occupied most of this period.

Daily cumulative radiation was measured to be 0.8-13.3 MJ d^{-1}, with an average of 8.8 MJ d^{-1}. CO_2 maintained an average concentration of 395 ppm during the day and 490 ppm at night. The simulated dry matter weights closely mirrored the measured values with an overall underestimation. The model performance was good in simulating the crop dry weight of the lettuce, with *RRMSE* =10.5% and *RMSE* = 0.0070 kg m^{-2} (gro).

Through the three lettuce cultivation experiments in different seasons and greenhouses, specifically including an experiment for global calibration and two for validation, the model performance was evaluated. These experiments covered a wide range of greenhouse air temperature conditions, from extremely low to extremely high. They also had extreme humidity levels for a large proportion of time, which would affect crop growth activities (Stanghellini et al., 2019). Climate inputs also included seasonally fluctuating shortwave radiation and CO_2 concentration inside the greenhouse. Therefore, the greenhouse climate upon which the model evaluations were based was in a broad range, embodied in the complete coverage of temperature and humidity levels and climate varieties. The evaluation results showed that the model performance was good and acceptable. In essence, the developed model can precisely depict the response of lettuce growth to the broad range of greenhouse climates, providing a foundational crop model for optimally managing greenhouse climate in lettuce production. Further, it enables optimal control to be used for low-tech greenhouses with poor performance on climate conditioning and to bring humidity effects into problem-solving.

However, we cannot compare the developed model to others since none of the existing lettuce growth models have reported the *RRMSE* for states. For instance, Van Henten (1994a) adopted assessment criteria stating that the simulated dry weight should fall within a 95% confidence interval of the measured values for most of the time. Instead, almost all crop models compared the dynamic trends between simulated and observed values, lacking a quantitative index basis. This situation exists in other mainstream greenhouse crop models, such as tomato yield modelling (Dayan et al., 1993b; Vanthoor, De Visser, et al., 2011). Compared with greenhouse climate dynamics (Katzin et al., 2022), crop growth processes

are more complex and have more challenges in accurate predictions. Meanwhile, it is difficult for crop models to obtain data for calibration and validation in seconds or minutes. The quality of destructive samplings in a limited number, especially those performed near the harvest time where larger deviations can occur, strongly impacts the *RRMSE* calculation and model evaluation results. For example, in Exp_1, the *RRMSE* for crop dry weight could reach 17.5% if the last two samples were excluded. These may explain the rare presentation of *RRMSE* values in current greenhouse crop models. This study provides *RRMSE* values for simulating lettuce dry weight, which will benefit future comparative studies, while a qualitative description of its dynamic trends throughout the growth period remains essential.

Furthermore, in the global calibration aimed at minimising the *RRMSE* for crop dry weight, adjustments to model parameters tended to restrain crop growth in the early stages to prevent excessive growth during harvest. Consequently, the model consistently underestimated dry weights until lettuce harvest in Exp_2. Overestimations of crop dry weight at harvest time varied in all experiments. Exp_1 showed the most significant overestimation, with an *RMSE* of 0.0248 kg m^{-2} (gro) in the last two samples. This was primarily induced by high temperatures, which shortened the vegetative stage, triggering early bolting and stem elongation (Hao et al., 2018; Rosental, Still, You, Hayes, & Simko, 2021). Although the *SLA* related parameters were locally calibrated using the three sets of experimental data, including those collected as stem elongated that we observed in the experiments, the adverse impact of stem elongation can only be partially described. According to Eq. (3.9), the model assumes that shoot biomass is allocated only to leaves. Once lettuce stems grow excessively, the model overestimates the change rate in *LAI* and, thereby, crop dry weight. While this lettuce model is oriented towards the vegetative stage with sufficient accuracy to meet control requirements, it may not fully explain the effects of plant senescence. However, this limitation should not hinder its use in commercial greenhouses, as growers will ensure timely harvesting based on daily observations to maintain the quality and market value of the lettuce crop.

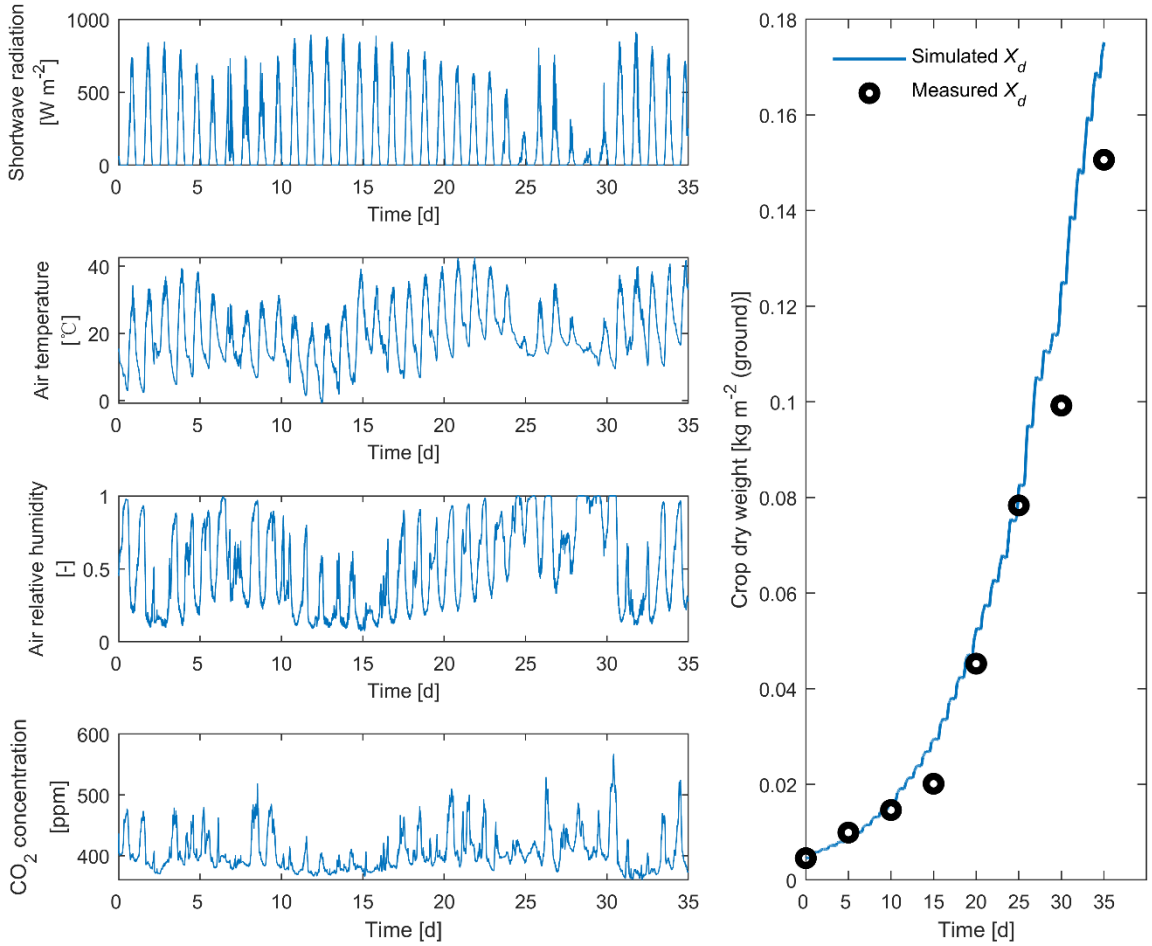

Figure 3.6 Five minutes averages of the greenhouse climate measurements, as well as the measured and simulated crop dry weights during the first validation experiment. The simulation for model validation is from 17:00, 9 April 2020, to 17:00, 14 May 2020.

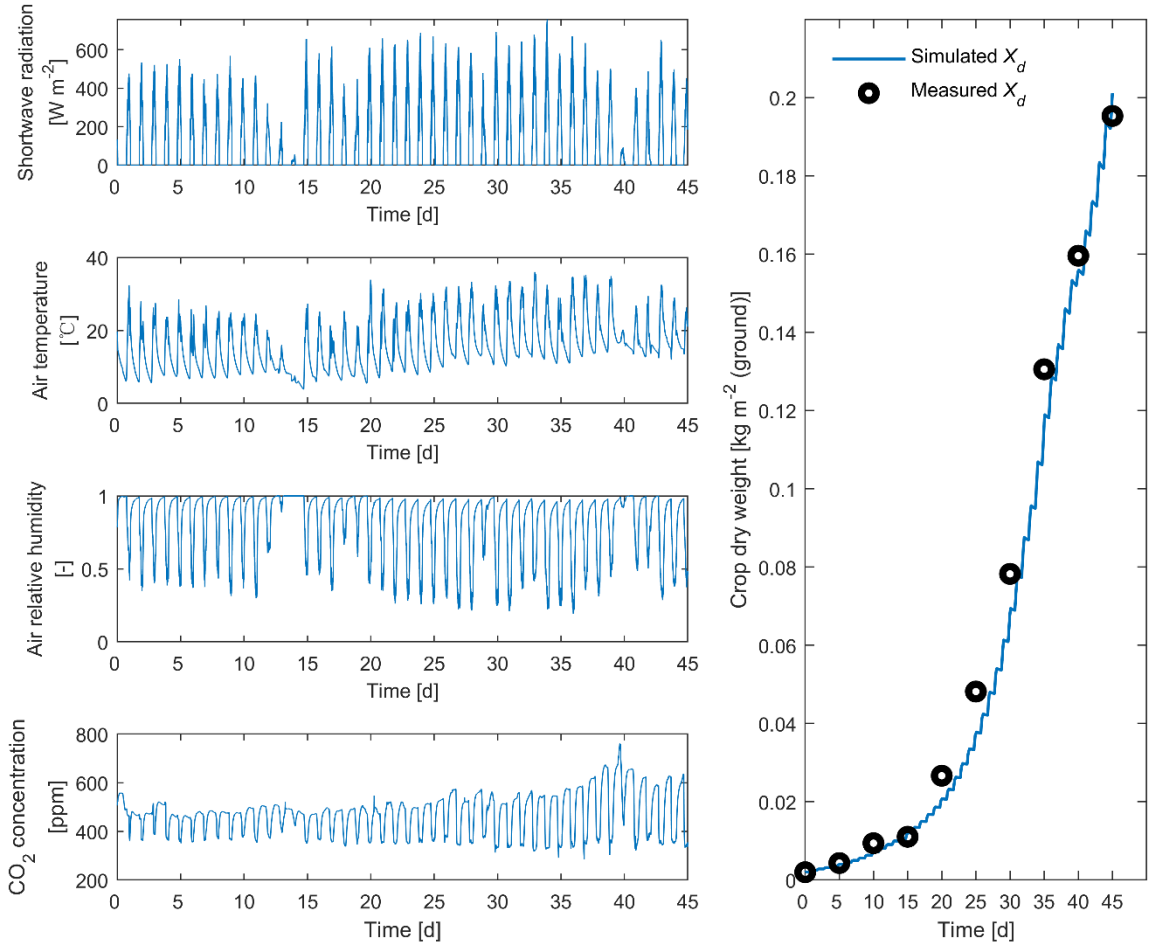

Figure 3.7 Five minutes averages of the greenhouse climate measurements, as well as the measured and simulated crop dry weights during the second validation experiment. The simulation for model validation is from 15:00, 30 January 2022, to 15:00, 16 March 2022.

3.3.2 Model performance of simulating *LAI*

In this model, *LAI* is one of the state variables, and it affects dry matter accumulation by influencing the canopy photosynthesis rate. Additionally, *LAI* itself holds significant importance in greenhouse climate control as a preferred indicator for providing crop information feedback, since it spans the entire lettuce growth cycle and is easier to identify than biomass (Rahimikhoob, Delshad, & Habibi, 2023). In Exp_2 (Figure 3.8a), the simulated *LAI* values exhibited the same trend as the measurements, consistently underestimating until harvest time, where a slight overestimation occur. The model

performance was good in simulating *LAI*, with an *RRMSE* of 12.1% and an *RMSE* of 0.2196 m^2 (leaf) m^{-2} (gro). In Exp_1 (Figure 3.8b), the simulated *LAI* followed a similar trend to the measured values but showed great overestimations near harvest, resulting in an *RRMSE* of 54.7% and an *RMSE* of 0.8164. In Exp_3 (Figure 3.8c), the simulated *LAI* followed the same trend as the measured values, with an overall underestimation. The *RRMSE* was 19.5%, and the *RMSE* was 0.5019, indicating a good model performance in simulating *LAI*.

During the late stages of crop growth under high temperatures, the model overestimated *LAI*, consistent with the reasons for overestimating crop dry weight. Similarly, excluding the last two samples in Exp_1 reduced the *RRMSE* for *LAI* to 12.9%. Therefore, during the vegetative growth stage concerned by commercial production, the model performed well in simulating *LAI* dynamics, accurately predicting them with *RRMSE* ranging from 12.1% to 19.5%. While the *LAI* and biomass interact, as Van Henten (1994a) found, their simulations differed in estimations, including the timing and magnitude of deviations. These differences are attributed to the model descriptions and samplings.

This study describes *SLA* as a function of radiation and humidity. The calibrated relative changes in *SLA* per unit changes of greenhouse climate imply the same trend with literature (Bradbury & Ahmad, 1996; Carotti et al., 2021); increasing humidity and decreasing radiation increase *SLA* of the lettuce. The inclusion of *SLA* enables the model to describe the response of leaf morphogenesis to climate, which can improve modelling accuracy. However, there is still much room for improvement in the *SLA* description, considering that its goodness of fit (R^2 = 0.380, *RMSE* = 9.928) has not yet reached an ideal state. Calibration using more data and modifying equation structure are the directions for improvement.

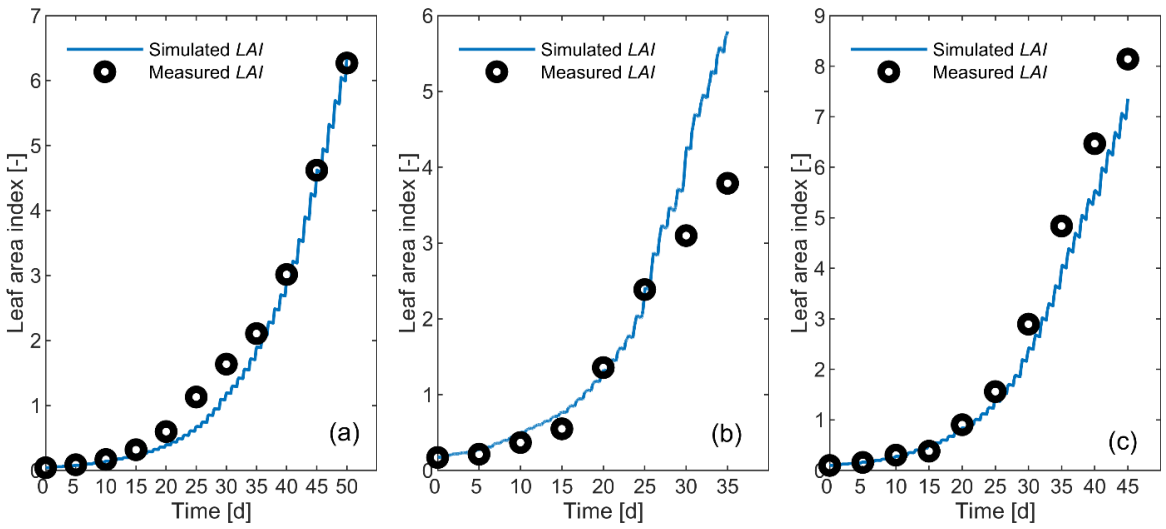

Figure 3.8 *LAI* simulations of the lettuce growth model using data from the calibration experiment (a), the first validation experiment (b), and the second validation experiment (c).

3.3.3 The role of model framework and hypothesis

To fully describe the effects of adverse temperature conditions, including extremely high and low temperatures, on crop growth, this study introduces a novel model framework that incorporates double parallel mass flows, along with the underlying hypothesis of buffer flows and canopy photosynthesis inhibition. Figure 3.9 illustrates changes in carbohydrate storage within the buffer. As buffer storage reaches or surpasses its maximum capacity, photosynthesis inhibition will happen until it falls below the capacity. During this state, the inhibition also becomes ineffective if the assimilation rate is lower than the combined respiration and potential growth rates. The model programming allows the buffer storage to exceed its maximum capacity at some point and then remain constant until the storage goes below the capacity as a result of dry matter increase, effectively practising the model description. In Exp_2, where the low temperature was the primary stress, photosynthesis inhibition lasted until the 42nd day in the simulation, constituting 41% of the total photosynthesis duration. In Exp_1, with high temperature as the primary stress, inhibition lasted until the 20th day, representing 27% of the total photosynthesis duration. In Exp_3, with temperatures transitioning from cold to warm, inhibition lasted until the 32nd day,

representing 33% of the total photosynthesis duration. Such inhibitions occur during vigorous photosynthesis in the daytime.

The proposed model framework and hypothesis worked in simulations, effectively characterising the effects of extreme temperatures on crop growth. Specifically, the model supplements the canopy-level assimilation inhibition, going beyond the direct effects of temperature on leaf photosynthesis and crop respiration. It particularly addresses the challenge of quantifying growth inhibition by extremely low temperatures at night, which might be reflected by the assimilation inhibition over the next few days. In essence, the instantaneous extreme temperatures, whether during the day or night, achieve this inhibition by additionally affecting potential growth rates and buffer flows, ultimately buffer revolution and canopy photosynthesis. Without this inhibition, the lettuce growth model would severely overestimate growth, which is a limitation of existing models for extreme environments.

In all three experiments, photosynthesis inhibition was lifted in the late stages of crop growth. This is due to the increased dry matter. On one side, the outlet buffer flows called by potential growth and maintenance respiration, along with buffer capacity, increase in proportion to crop dry weight. However, on the other side, the canopy photosynthesis, as the source flows, does not increase proportion to crop dry weight or *LAI* due to the limited light absorbed by the canopy within a unit ground area. The cessation of inhibition partially explains the tendency of the model to overestimate growth near harvest. In the calibration and two validation experiments, the crop dry weight leading to the complete disinhibition was 89.748×10^{-3}, 47.054×10^{-3}, and 77.737×10^{-3} kg m^{-2} (gro), respectively. Higher temperatures resulted in shorter inhibition durations and lower crop dry weight required for complete disinhibition, indicating that the model shows greater tolerance to high-temperature stress than to low-temperature stress. This difference is further supported by the value of $T_{c,RGR}$, which was calibrated to be 25 °C.

We have also observed photosynthesis inhibition during the initial stages of crop growth when the temperature is held constant at 25°C and does not contribute to the inhibition. The

inhibition can occur despite buffer flows to growth conversion at the maximum achievable growth rate. This finding aligns with reality (Spitters et al., 1989), suggesting that the sink strength, instead of the photosynthesis with excess supply, dominates the initial crop growth and leaf area expansion. Thus, the hypothesis enables the model to effectively simulate early growth, which is not addressed by current models primarily focusing on the balance between photosynthesis and respiration. It should be mentioned that the model is sensitive to the parameter of $RGR_{max,20}$, according to the calibration process. We expect interested researchers to calibrate this parameter using additional data or further optimise the expression of RGR_{max} and explore the specific physiological implications.

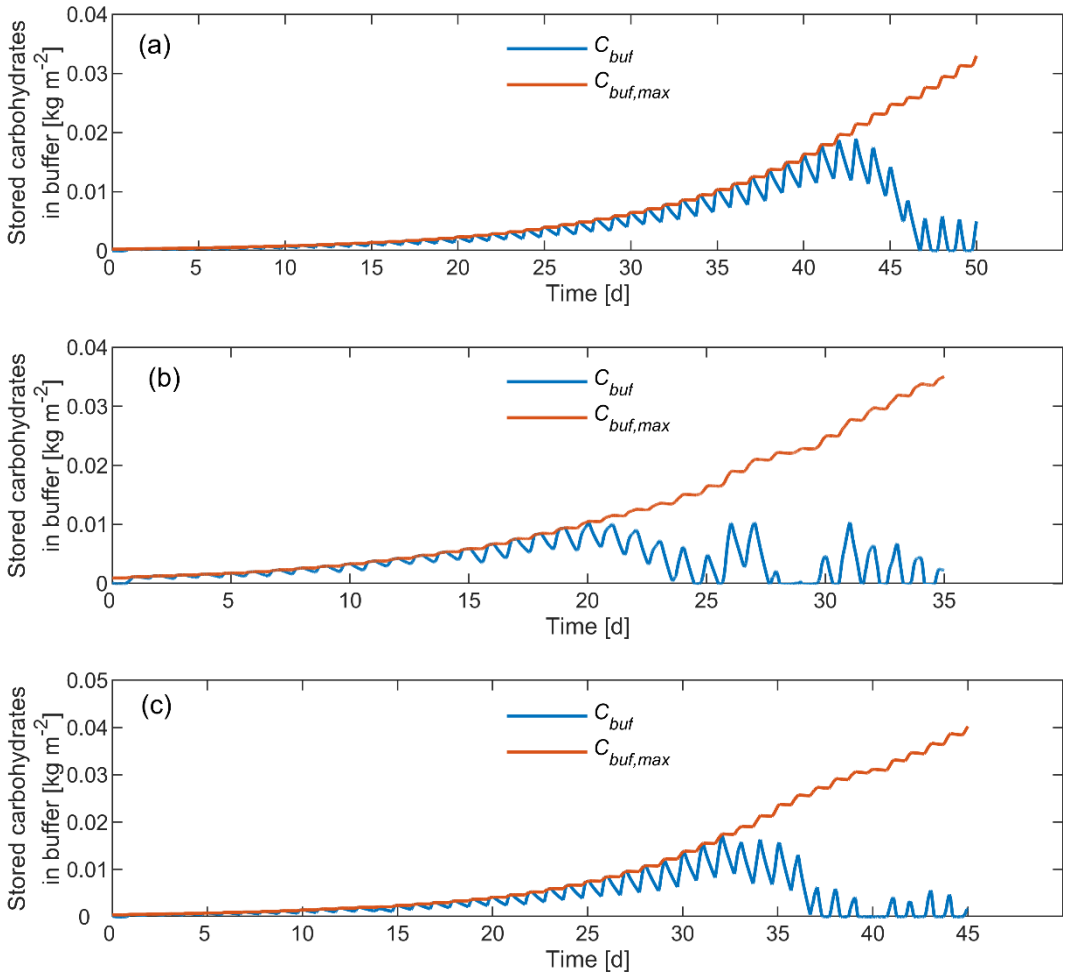

Figure 3.9 Buffer storage variations based on data from the calibration experiment (a), the first validation experiment (b), and the second validation experiment (c).

3.3.4 Effects of humidity on crop growth

In this model, air humidity affects lettuce growth from both biochemical and morphological perspectives, specifically by influencing stomatal resistance and *SLA*, and further canopy assimilation. As humidity increases, stomatal resistance and the total leaf resistance decrease (Figure 3.10), increasing the leaf photosynthesis rate. Concurrently, *SLA* increases along with the increase in humidity (Figure 3.4), promoting the leaf area expansion. Therefore, higher humidity levels benefit canopy photosynthesis and dry matter accumulation. However, increasing humidity may induce pest and disease issues and reduce transpiration (Stanghellini et al., 2019), affecting water and nutrient uptake, both of which are not considered by the potential model of this study.

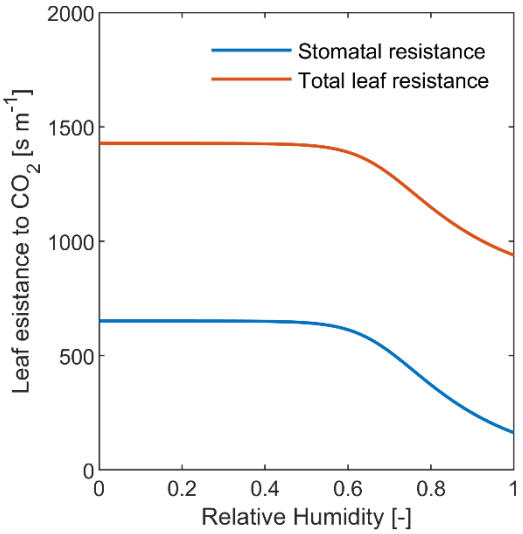

Figure 3.10 Leaf resistances to CO_2 diffusion as a function of T_c, X_h, X_c, and I, with T_c = 25 °C, X_c = 600 µmol (CO_2) mol^{-1} (air), I = 300 W m^{-2} (gro), and LAI = 3 m^2 (leaf) m^{-2} (gro).

3.3.5 Universality and limitations

The developed lettuce growth model belongs to the potential model category, only responding to the shoot environment inside the greenhouse. It has been demonstrated to respond to the broad range of greenhouse climates effectively and even works with sub-zero

temperature inputs. In all three experiments, the observed ranges of greenhouse climate variables were 0-915.6 W m^{-2} for shortwave radiation, -1.0-42.6°C for air temperature, 7%-100% for relative humidity, and 285-762 ppm for CO_2 concentration. However, these ranges of input data used for model calibration and validation will not constrain the universality of the lettuce growth model. In theory, the model is applicable to any potential greenhouse environment, provided that irreversible damage to crops, such as frost injury, does not occur. The model accurately predicts dry matter and leaf area dynamics during growth stages of interest in commercial lettuce production. Most knowledge of this process-based model can be extended to other crops. Also, the model simulates instantaneous crop dynamics and shares the same time scale as greenhouse climate models, allowing for the integrated description of the greenhouse crop production process from external weather to crop biomass. These enable the model to serve as a basis for optimal control of greenhouse climate, including those with limited climate conditioning capabilities.

Note that the right-hand sides of the differential equations are not entirely written in a continuously differentiable form, considering that the model usage is not restricted to control and not all optimisation control algorithms require continuous differentiability. For instance, genetic algorithms and particle swarm optimisation algorithms do not require it. Thus, we prefer to present the equations in their original form. However, for our subsequent integrated climate-crop model, we plan to use switching functions such as sigmoid and Gaussian functions to smooth and modify the original equations. This processing might accelerate the simulation and ensure that gradient-based optimisation algorithms can be employed.

The climate inputs for model evaluation, derived from low-tech greenhouses, include air temperature and humidity with extreme values, solar radiation passing through plastic film, and CO_2 concentration under natural ventilation. However, in modern multi-span greenhouses, CO_2 concentration is usually maintained at 700-1000 ppm during photosynthesis through CO_2 supplementation. This study lacks model validation under such high CO_2 concentrations. The description of stomatal conductance adopts the parameters given by Stangheilini (1987) for tomato, and subsequent research is needed to determine

these parameters for lettuce. Using the experimental data from this study, the one-state model by Van Henten (1994a) significantly overestimated growth predictions. Possible reasons include the imposed constraints on temperature inputs, as well as the influence of different cultivation practices where the Eldert model was developed for soilless cultivation while lettuce was grown in soil in our experiments. Inspired by these findings, we also expect interested researchers and technicians to conduct model evaluation or parameter calibration for soilless cultivation scenarios and other varieties. Furthermore, we leave the sub-model validation and further exploration of the proposed photosynthesis inhibition hypothesis to botanists. To explain the effects of lettuce plant senescence and enhance prediction accuracy, thermal time or chronological time could be introduced to characterize the decline in photosynthetic capacity with plant age, as suggested by Sweeney et al. (1981) and Pearson et al. (1997).

To use the developed model, the following preparations are necessary:

- Providing model inputs, including greenhouse climate data (shortwave radiation I, air temperature X_t, humidity X_h, and CO_2 concentration X_c) and initial value of crop states (crop dry weight X_d, LAI, and buffer storage C_{buf}).
- Identifying the recovering period, after which simulations can be performed.
- Counting the effective cultivated area and determining plant density ρ_c. The model defaults to an effective cultivation area-based plant density, where each lettuce plant occupies a limited ground area at maximum. The plant density is crucial for determining initial crop states and root ratio, and accurately predicting biomass and yield within the greenhouse or a specific area together with the counted effective area.

3.4 Summary

In this study, a lettuce growth model that describes the effects of a broad range of greenhouse climates on crop dry weight dynamics was developed, calibrated, and validated. The developed model is for optimal climate control purposes. It simulates instantaneous crop dynamics for the potential situation. The broad range of greenhouse climates include air

temperature with extremely low and high conditions, humidity, CO_2 concentration, and shortwave radiation. The model defaults to an effective cultivated area-based plant density, where a single plant occupies a limited ground area at maximum, making the model universal.

The model development focused on extending crop growth responses to extreme air temperatures and humidity. The model framework performs two parallel sets of mass flows: dry matter accumulation and buffer evolution. They share paths but differ in logic. The former processes contribute to crop growth, where the carbohydrates produced by canopy photosynthesis are partly consumed in maintenance respiration, and the remaining are converted into structural dry matter and partitioned among organs. The latter processes are only used for regulating canopy photosynthesis. The buffer carbohydrates flow to growth conversion based on the temperature-dependent maximum growth rate (sink strength) of the whole crop. As extreme temperatures inhibit the partitioning, the buffer storage might increase, and the canopy assimilation inhibition occurs when the storage reaches the buffer capacity. Humidity effects are quantified by describing stomatal resistance and the SLA of new leaves. In addition, for simplicity, leaf carboxylation resistance and root ratio are described as descriptive functions.

The model performance was demonstrated to be good and acceptable for a broad range of greenhouse climates. The simulated dry matter weights closely mirrored the measured values, with the *RRMSE* of 10.5-24.9% and the *RMSE* of 0.0070-0.0131 kg m^{-2}. High temperatures at harvest time might induce overestimations. The model predicted the LAI dynamics with an *RRMSE* of 12.1-54.7%. However, during the vegetative growth stage concerned by commercial production, it is considered to perform well, with *RRMSE* ranging from 12.1% to 19.5%. The proposed model framework and underlying hypothesis worked in simulations that the photosynthesis inhibition time accounted for 27-41% of the total photosynthesis time. They effectively characterise the effects of extreme temperatures on crop growth and enable the model to simulate early growth. Inhibition was lifted in the late stages of crop growth due to the increased dry matter. Moreover, the model showed greater tolerance to high-temperature than low-temperature stress. Higher humidity levels benefit canopy

photosynthesis by decreasing stomatal resistance and increasing *SLA*.

The model can serve as a basis for optimal management of greenhouse climate, including those with limited climate conditioning capabilities. This study offers the open source code of the model. The simulation requires model inputs of greenhouse climate, initial crop states, and plant density, and needs to identify the recovering period. Further study is expected to validate the model for more lettuce cultivation scenarios and introduce the effects of lettuce plant senescence.

Chapter 4

A full-scale climate model of the Chinese solar greenhouse

In this chapter, a CSG climate model that describes the effects of outdoor weather, greenhouse structure, crop states, and greenhouse controls on the indoor climate of a standard CSG is developed and evaluated.

4.1 Introduction

Greenhouse climate control can be made more efficient by using the theory of optimal control or model predictive control (W.-H. Chen & You, 2022; Tap, 2000), which fully exploits knowledge of the greenhouse and crop captured in dynamic models. For the CSG cultivation scenario, optimal climate control can improve income by 40% compared with conventional approaches (Dan Xu et al., 2018). To the best of our knowledge, very few optimal CSG climate control systems have been developed so far, and no such system has been applied to commercial CSG production. System model serves as a basis and determines the performance of the optimal control controller (Van Straten et al., 2010). In order to put optimal control of CSG climate into practice, it is necessary to have a suitable CSG climate model that can fully and accurately describe the effects of weather, greenhouse structure, crops, and controls on indoor climate. This model should also be able to incorporate the crop growth model for simulating the CSG production process.

A greenhouse climate model should simulate one or more of the following climate factors: temperature, humidity, CO_2 concentration, and radiation (Katzin et al., 2022). According to this principle, the number of the existing CSG climate models is approximately 50. Although the underlying mechanisms and some of the described processes are similar, these CSG climate models do not include those used for calculating heating and cooling requirements (M S Ahamed, H Guo, & K Tanino, 2018; Fu, Zhou, & Wang, 2020; Weituo Sun et al., 2019), determining surplus air heat energy (Weituo Sun, Wei, Zhou, Lu, & Guo, 2022), exploring thermal performance and heat transfer of CSG walls (M. Li et al., 2016; C Ma, Lu, Li, & Qu, 2010; Tong & Christopher, 2019), external thermal blanket (C. Liu et al., 2015) and indoor soil (Deng, 2021), optimising design of the wall (M. Li, Zhou, & Wei, 2015), north roof (Y. Cao, Jing, Zhao, Zou, & Bao, 2017) and south roof (Y. Zhang & Zou, 2017), as well as modelling only the ventilation rate and indoor air flows (Fang et al., 2016; Q. Zhang et al., 2012). The current CSG climate models can be generally classified into three categories, mechanistic (or process-based) model, data-driven model, and computational fluid dynamics (CFD) model. The earliest CSG climate model dates back to 1992 when D. Chen, Zheng,

Zhang, and Qiu (1992) developed an analytical model for calculating indoor direct solar radiation to assist in the transparent south roof design. Then, the CSG climate models have undergone rapid development for the potential purposes of model-based climate control, model-assisted structure design, exploratory modelling, and systems analysis.

In the past decade, thanks to the development of artificial intelligence technology, the most emerged CSG climate models are data-driven types. They mainly focus on predicting the temperature and humidity dynamics of greenhouse air using different modelling methods such as the improved extreme learning machine (ELM) (Zou, Zhang, Yao, & He, 2015), grey prediction (Qin, Ma, Chu, & Wu, 2016), the least squares support vector machine (LSSVM) with parameters optimised by improved particle swarm optimisation (PSO) (Yu, Chen, Hassan, & Li, 2016), continuous-discrete recursive error algorithm for online identification of model parameters (L. Chen, Du, Li, He, & Liang, 2017), twice cluster analysis and back propagation (BP) neural network (X. Chen et al., 2017), a combination of long short-term memory and gated recurrent unit neural networks (LSTM-GRU) (Qiao et al., 2022), long short-term memory (LSTM) networks optimised by the sparrow search algorithm (SSA) (Zu, Liu, Zhao, Li, & Li, 2023), and one-dimensional convolutional neural networks and gated recurrent unit (CNN-GRU) (Hu et al., 2023). These data-driven CSG climate models, mainly based on neural networks and machine learning, have been reported to perform well in thermal environment prediction. However, an effective data model with strong generalizability requires an extremely large amount of data for parameter identification (L. Chen et al., 2017), and the applicability of the current models is usually limited to certain CSG production scenarios, specifically those that are similar to the experiments from which the model training data was derived. In China, CSGs lack a unified construction standard and vary in form based on different local climate conditions, planting needs, cost control, etc. Furthermore, indoor cultivation and management practices also differ widely. The use of existing data-driven CSG climate models for control poses significant challenges.

CFD approach, aimed at quantifying fluid transport phenomena through a numerical solution of the conservation equations (Bournet & Rojano, 2022), has proven to be a

powerful tool for simulating air temperature and humidity changes and their distributions within the CSG (Fang, Yang, Zhang, Lu, & Zhou, 2015; Tong et al., 2009; G. Zhang et al., 2019; Zheng, Yang, & Liu, 2023). The CSG climate models using CFD simulation can be used in the north wall optimisation (X. Zhang, Wang, Zou, & Wang, 2016), south and north roof design (X. Wu et al., 2021), and span selection (Tong, Christopher, & Zhang, 2018). However, the complexity of the simulation and computationally intensive nature limit their application in model-based controls, especially in online control (Norton et al., 2007). Similar issues also exist with other 2D and 3D models (Y. Zhang et al., 2020).

Most of the optimal control or model predictive control systems for greenhouse climate management are based on mechanistic models (W.-H. Chen, Mattson, & You, 2022; I Ioslovich, 2009; Lin et al., 2021; Van Henten, 1994a), assuming the greenhouse air as a perfectively stirred tank. The mechanistic models are expected to generalise better than data-driven models. They incorporate the parameters of structure, controls, and crops of the greenhouse production system and take these parameters as model inputs. For different greenhouse scenarios, the underlying principles remain unchanged, and the mechanistic models can work properly with different model inputs. Meanwhile, the mechanistic models treating the greenhouse air as a uniform entity can have higher computational efficiency than CFD models (Katzin et al., 2022). Therefore, the CSG climate model suitable for control must be a mechanistic model, particularly at the current stage.

Early mechanistic CSG climate models paid more attention to simulating indoor solar radiation (D. Chen et al., 1992; Q. Chen, 1993; X. Li & Chen, 2004) since daylighting is crucial for the efficient production of CSGs that they rely on solar radiation as their primary energy source. Currently, radiation models still constitute the largest proportion (Han, Xue, Luo, Guo, & Li, 2014; Huang et al., 2020; Chengwei Ma et al., 2013; H. Xu et al., 2019). They employ an analytical approach, starting from defining extraterrestrial radiation to calculating the shortwave radiation absorbed by the envelope surfaces and ground inside the CSG. The focus was on determining the solar incidence angle on the south roof and further its transmissivity. The development of radiation models was mainly used to optimise the

design of greenhouse structures (Y. Cao et al., 2017; Xiaodan Zhang et al., 2020; Y. Zhang & Zou, 2017). Models simulating dynamics of air temperature (Meng, Yang, Bot, & Wang, 2009; Sanchez-Molina et al., 2017; Tong et al., 2009; C. Wu, Zhao, & Guo, 2007) and air humidity (Bi & Wu, 2012; Z. Guo & Yu, 2012; F. He, Ma, & Zhang, 2009) within the CSG have been developed consecutively. These models were based on energy and water vapour balances and employ numerical simulation methods. CO_2 concentration prediction models, which require careful consideration of ventilation, CO_2 supplementation, and crop and soil activities, were the least studied (Bi, Ma, Cong, & Zhu, 2010; Dong, 2005). Research on these single climate factor prediction models contributes a lot to the CSG modelling work but is insufficient for optimal control. Firstly, climate control is for the growth and development of crops, which respond to the comprehensive climates, including temperature, humidity, CO_2 concentration, and light, rather than to any single factor (Stanghellini et al., 2019). Secondly, the control of greenhouse equipment also affects the climate comprehensively, not just a single factor. For example, the roof vent opening will simultaneously influence temperature, humidity, and CO_2 levels inside the CSG, further influencing radiation by affecting condensation and frosting on the south roof inner surface. Furthermore, greenhouse climates interact with each other. Therefore, the CSG climate model for control purposes should be capable of effectively integrating and simulating the comprehensive climates inside the CSG, based on which optimal control algorithm can link equipment control with crop growth to seek optimized control schemes. To enhance the completeness, simulation accuracy, and universality of the CSG climate model, the simulated comprehensive climates should include shortwave radiation, air temperature, humidity, and CO_2 concentration inside the CSG, especially when coupling with a crop model that responds to these four attributes in optimal control systems.

CSG climate models that integratively describe two or more climate attributes are still relatively rare. R. Liu, Li, Guzmán, and Rodríguez (2021) developed a fast and practical one-dimensional transient model for CSG air temperature and humidity and stated that it could be used for decision-making support of greenhouse climate management. However, this model calculates the wall and ground temperatures using algebraic equations and implies

that the target objects have unidirectional internal heat transfer, with only their insulation properties being considered while their heat storage capabilities are ignored. This assumption applies to certain components in the Venlo type greenhouse (De Zwart, 1996) but might deviate from reality in CSG systems, especially for the north wall (nighttime heat release reaches 1.69 MJ m^{-2} d^{-1}) and indoor soil (nighttime heat release reaches 0.48 MJ m^{-2} d^{-1}) (Bai, Liu, Wang, Tong, & Meng, 2003). Moreover, this model does not comprehensively address CO_2 dynamics, validate the radiation calculations, and describe crop activities for a particular cultivar, though crop states significantly affect greenhouse climates. CSG climate models simulating three and four climate attributes have been reported by Jianfeng Zhang (2003) and X. Wang (2017). However, these models offer relatively simple descriptions of processes. They have not validated the sub-model of CO_2 concentration, nor have they evaluated model performance on simulating temperature, humidity, and shortwave radiation over a long period simultaneously. Furthermore, there is a lack of specific controls and crop states as model inputs.

In summary, a thoroughly tested mechanistic CSG climate model that integratively simulates four attributes of shortwave radiation, air temperature, humidity, and CO_2 concentration, with high computational efficiency and good generalization and universality, remains elusive. Such a model should describe crop activities and be validated with measured crop state inputs for a specific crop. The majority of present CSGs lack additional climate conditioning equipment (Qi et al., 2017). They, namely as standard CSGs, only have roof and side vents as well as the thermal blanket as the two essential and controllable structural components. Therefore, the objective of this study is to design and evaluate a full-scale CSG climate model that describes the effects of outdoor weather, greenhouse structure, cultivated crops, and greenhouse controls on the indoor climate of a standard CSG. The simulated CSG climate integrates all four attributes of shortwave radiation, air temperature, humidity, and CO_2 concentration. Full-scale is reflected in both inputs and outputs of the model. The target crop in this climate model is lettuce, and model validation was performed for the lettuce production scenario in the CSG. The developed model is expected to accurately predict CSG climate dynamics and serve as a basis for optimal control of the CSG climate, incorporating

a lettuce growth model responding to four or fewer climate factors.

Below are the key innovations of the study:

(1) A novel process based CSG climate model is designed, integratively describing dynamics of shortwave radiation, air temperature, air humidity, and CO_2 concentration inside the CSG that responds to weather, greenhouse structure, crops, and controls.
(2) It is the first time that the CSG climate model describes crop activities specifically targeting lettuce and is thoroughly evaluated in lettuce production scenarios using measured crop states and greenhouse controls.
(3) The model was extended to include the switch of condensation to deposition on the south roof, as well as the shading of the north wall by the north roof.
(4) The model also offers new insights into energy and mass balances, the definition of layers and surfaces, radiative fluxes, criteria for selecting convective heat transfer coefficients, latent heat fluxes, natural ventilation and air infiltration, soil microbial respiration and evaporation, as well as the association between cultivated area and indoor ground.

4.2 Model description

4.2.1 Model overview

4.2.1.1 Model framework

This model describes the effects of outdoor weather, greenhouse structure, cultivated crops, and greenhouse controls on the indoor climate of a standard CSG. It is classified as a mechanism model and is built on process descriptions, which can benefit the generalization of the model and provide insights into mechanisms influencing CSG climate variations. The model serves as a basis for model predictive control or optimal control of the CSG climate. It can also be used for analysis, exploratory modelling, and design optimization of CSG

systems. The development of this model integrates and optimizes previous research, as well as provides new insights and quantifications of CSG processes.

As shown in Figure 4.1, the target CSG climate attributes for simulation include shortwave radiation (I), air temperature (X_t), air humidity (X_h), and CO_2 concentration (X_c) inside the CSG. The shortwave radiation at the top of the canopy, which also serves as the climate input for the developed crop model, is selected to represent the CSG light environment. Auxiliary states like temperatures of CSG envelope surfaces, indoor ground, soil layers, north wall layers, and crop canopy are also involved. The radiation related states are expressed using analytical formulas. All other states have their rates of change described by differential equations, considering energy, water vapour, and CO_2 balances. The dynamics of these model states are modelled on a time scale of one second. For a given CSG, model inputs mainly include the external weather of horizontal solar radiation (I_{out}), air temperature (T_{out}), relative humidity (RH_{out}), CO_2 concentration ($CO2_{out}$), and wind speed (v_e), the controls of the thermal blanket (U_b), side vent ($U_{vent,s}$), and roof vent ($U_{vent,r}$), as well as the crop growth states of crop dry weight (X_d) and leaf area index (LAI).

To explain the processes from model inputs to outputs, the model development is detailed in the following subsections.

- **State variables**: Change rate of temperatures [°C], relative humidity [-], and CO_2 concentration [μmol (CO_2) mol^{-1} (air)] of CSG objects are expressed by balancing incoming and outgoing energy and mass flows.

- **Definition of layers and surfaces**: The CSG south roof is conceptualized as a dynamic composite layer consisting of a potential ice layer, a transparent covering, and an adjustable thermal blanket. Surfaces are defined for CSG objects. Further layering is performed to describe the temperature dynamics of the north wall and indoor soil with heat storage capabilities.

- **Capacities of CSG objects**: Heat capacities of the CSG air, canopy, indoor soil, and north wall, as well as capacities of indoor air to store water vapour and CO_2, are presented.

- **Radiative fluxes**: The shortwave radiation at the top of the canopy and absorbed by CSG envelope surfaces, indoor floor, and the canopy is ultimately described as a function of local latitude, date, and time, outdoor solar radiation, greenhouse structure and controls, LAI, and formation of the ice layer. These sub-models primarily focus on determinations of solar incidence angle, equivalent transmissivity and reflectivity of the composite south roof, as well as the shading ratio of the north wall. Longwave radiation heat fluxes are described among CSG surfaces, canopy, and sky, with a focus on determining the view factors.

- **Convective and conductive fluxes**: Criteria and assumptions for choosing convective heat transfer coefficients are systematically elaborated, extending the effects of controls and crop state. Also, this section describes heat conductions between adjacent layers and between non-adjacent surfaces within the CSG.

- **Latent heat fluxes**: Latent heat fluxes induced by crop transpiration, soil evaporation, and vapour condensation are described, with an expanded description addressing the transition from condensation to deposition on the south roof.

- **Vapour fluxes**: The water vapour away from the CSG through condensations and air exchange is quantified.

- **CO_2 fluxes**: CO_2 flux generated by air exchange is expressed.

- **Air exchange**: Natural ventilation, induced by the combined wind and buoyancy effects, is described for the two ventilation modes of only the roof vent being open and the roof and side vents being open, considering the resistance of insect screens. Air infiltration

is modelled to respond to wind speed and the temperature difference between indoor and outdoor air, with an introduction of the thermal blanket control to modify the cover tightness.

- **Crop activities**: This section summarises crop photosynthesis and respiration for lettuce, gives the specific calculation method of crop transpiration, and addresses the issues caused by the difference between an effective cultivated area and an indoor ground area.

- **Soil activities**: While the crop activity has covered root respiration, the soil respiration description only considers the soil microbial respiration rate. Soil evaporation is described by integrating the effects of greenhouse climate and specific moisture levels of greenhouse soil on evaporation.

Tracing back to the roots, all four CSG climate attributes are influenced by the model inputs of weather, greenhouse, crops, and controls. Simultaneously, the factors of shortwave radiation, air temperature, and air humidity interact with each other and collectively impact CO_2 concentration. CO_2 concentration does not affect other climate factors since the crop states serve as inputs in the CSG climate model. However, in an integrated CSG climate-crop growth model, all four climate factors will interact. In sub-models, the south roof is often treated as a particular case because of its dynamic composite layer characteristics. The target crop in this climate model is lettuce, and model validation was performed for the lettuce production scenario in the CSG. Hence, this study presents a climate model of the CSG that cultivates lettuce.

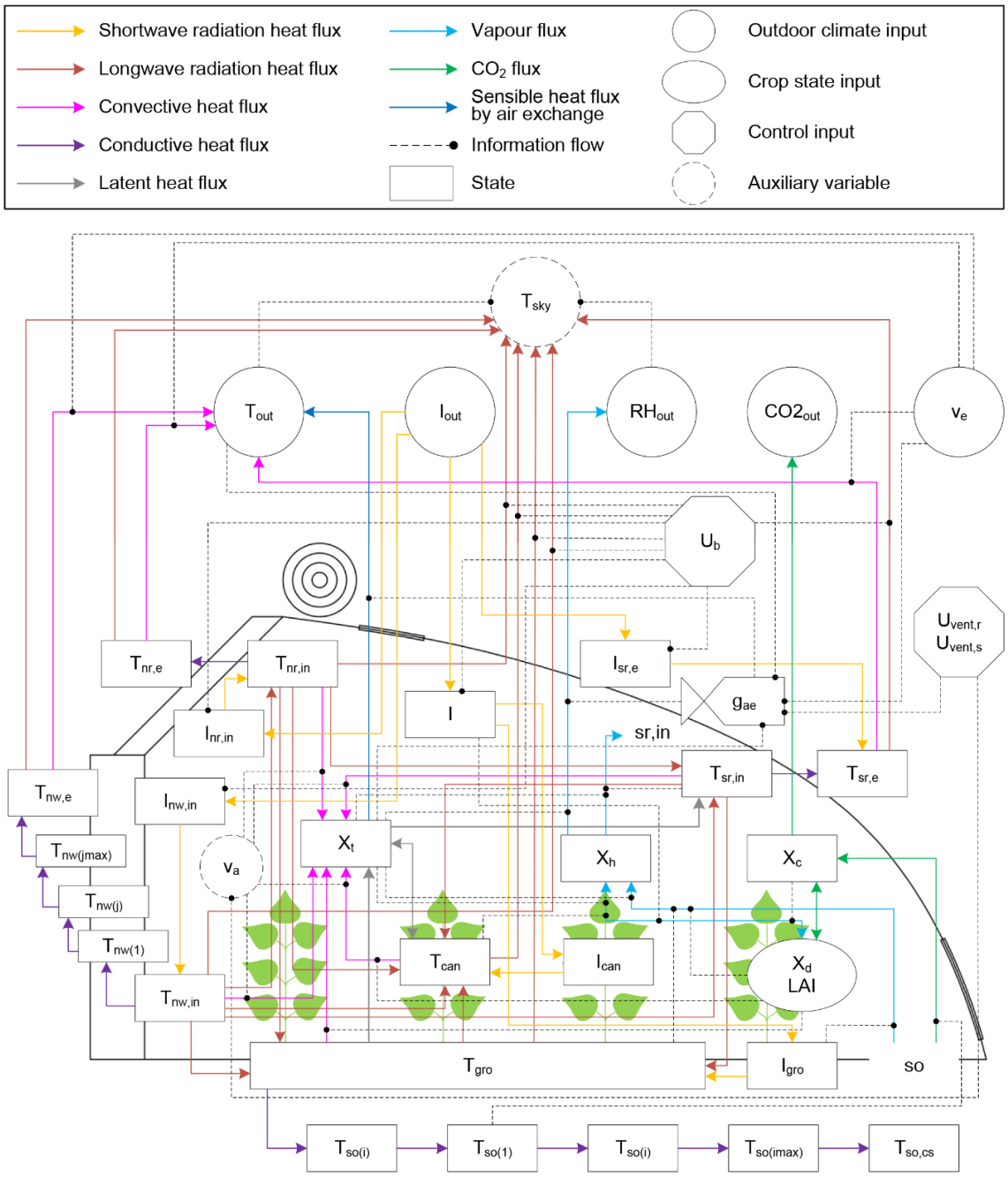

Figure 4.1 A schematic diagram of the CSG climate model. All energy and mass fluxes are involved. Information flows avoid intermediate variables as much as possible, tracing back to inputs and states. The two interacting objects, represented by variables, between which energy or mass flux occurs contribute to the information flow of this flux. The influence of the indoor climate on crop photosynthesis and respiration is not involved in this figure and can be found in schematic diagram of the lettuce growth model.

4.2.1.2 Model assumptions

The general assumptions of this model are as follows (see more detailed information in the section of model equations).

- The CSG air is considered a 'perfectly stirred tank', which means the spatial variability of air temperature, humidity, and CO_2 concentration is ignored.
- The CSG is considered to be infinitely extended in the east-west direction, ignoring the influence of side walls. Also, the property of the aisle is regarded as being consistent with the cultivation area. In addition, the model adopts an LAI at the whole greenhouse level instead of based on the effective cultivated area to address the impact of crops. Then, the CSG production system is assumed to be uniformly consistent in the longitudinal direction. Moreover, the distribution of radiation at the top of the canopy and on all CSG surfaces can be uniform.
- The model considers only one-dimensional heat transfer.
- The north and south roofs are considered not to have heat storage capacity.
- All the controls of CSG controllable structural components are assumed to be completed instantaneously.
- Corresponding to the crop model, this model assumes that water and nutrients are supplied adequately, based on which activities of the soil and crops are described.

4.2.2 Model equations

4.2.2.1 State variables

We focus on modelling CSG climate attributes, but it is important to note that the greenhouse is a holistic system where various objects interact. Therefore, other state variables, such as the indoor ground temperature, also need to be described. All states, except for radiation variables, have their rates of change described by differential equations. This is because radiation is only influenced by the current meteorological, greenhouse, and crop conditions,

while other states evolve from their values at the previous time step. The differential equations are based on three balances: energy balance, water vapour balance, and CO_2 balance. The right-hand side of these equations contains incoming and outgoing energy and mass flows, with the analysis focused on the state carriers (e.g., the inner surface of the north wall). Note that all fluxes are based on the indoor ground area, representing values per unit CSG ground area.

For energy and mass transfer processes, we used the following notational conventions: *C* denotes convective heat flux, *D* denotes conductive heat flux, *R* denotes longwave radiation heat transfer flux, *E* denotes sensible heat flux due to air exchange, *L* denotes latent heat flux, *MV* denotes water vapour flux, and *MC* denotes CO_2 flux. The inner surface is denoted by subscript 'in', while the outer surface is denoted by subscript 'e'. In the unit [W m^{-2} (gro)], '(gro)' is used to define the area as an indoor ground area. The symbols used in the crop growth model presented in Chapter 3 are continued in this model. Additionally, the notational conventions of this study are partially borrowed from the greenhouse climate model by Vanthoor (2011) and the surplus air heat model of CSG by Weituo Sun et al. (2022).

Temperatures of CSG objects

Greenhouse air temperature X_t is described by:

$$cap_{air}\frac{dX_t}{dt} = C_{can\_air} + C_{gro\_air} + C_{nw,in\_air} + C_{nr,in\_air} + C_{sr,in\_air} - E_{air\_out} \ [\mathrm{W\,m^{-2}\ (gro)}] \tag{4.1}$$

where cap_{air} [J $°C^{-1}$ m^{-2} (gro)] is the heat capacity of air inside the CSG, X_t [°C] is the greenhouse air temperature, t [s] is the time. Convective heat exchanges occur between indoor air and surrounding objects, including the canopy C_{can_air}, indoor ground C_{gro_air}, the internal surface of the north wall C_{nw,in_air}, the internal surface of the north roof C_{nr,in_air}, and the internal surface of the south roof C_{sr,in_air}. Sensible heat is also exchanged between the

indoor air and the outdoor air, which is caused by the air exchange brought about by natural ventilation and air infiltration E_{air_out}. The CSG commonly utilizes a steel frame structure, employing various frame types such as elliptical tubes, galvanized steel pipes, and galvanized steel pipes with additional lower chord trusses. In the east-west direction, the spacing between adjacent roof arch frames is approximately 1.0 m. The design of the steel frame structure prioritizes minimizing shading effects on the greenhouse while meeting load-bearing requirements. Hence, this model does not take into account the absorption of shortwave radiation by the steel frame and its involvement in other heat transfer processes. Also, the air does not directly absorb shortwave radiation nor participate in longwave radiation heat transfer processes.

The canopy temperature T_{can} is described by:

$$cap_{can}\frac{dT_{can}}{dt} = I_{can} - C_{can\_air} + R_{gro\_can} + R_{nw,in\_can} + R_{nr,in\_can} + R_{sr,in\_can} - R_{can\_sky} - L_{can\_air} + L_{air\_can} \quad [\mathrm{W\ m^{-2}\ (gro)}] \tag{4.2}$$

where cap_{can} [J °C^{-1} m^{-2} (gro)] is the heat capacity of the canopy inside the CSG. T_{can} [°C] is the canopy temperature, not equivalent to the greenhouse air temperature in this climate model. It is assumed to be uniformly consistent throughout the entire canopy. I_{can} [W m^{-2} (gro)] is the shortwave radiation (solar radiation) absorbed by the canopy. In addition to convective heat exchange with the indoor air C_{can_air}, crops in the greenhouse also experience longwave radiation heat transfer with the indoor ground R_{gro_can}, the internal surfaces of the CSG envelope R_{nw,in_can}, R_{nr,in_can}, R_{sr,in_can}, and the sky through the transparent covering of the south roof R_{can_sky}. There are also latent heat fluxes associated with the crops, induced by crop transpiration L_{can_air} and vapour condensation onto the canopy L_{air_can}. These two phase change processes lead to sensible heat loss and gain of the canopy, respectively.

The materials, composition, and design functions differ across various parts of the CSG

envelope, leading to differences in modelling their heat transfer processes. The north wall is primarily composed of insulation and thermal storage materials, serving as one of the main heat storage bodies in the CSG. To accurately simulate the greenhouse climate, a dynamic model is necessary to describe the temperature dynamics of the north wall in layers, identifying internal heat fluxes and depicting its thermal storage function. Further details on layering and surface definitions are provided in the subsequent sections. The temperatures of the internal surface $T_{nw,in}$, external surface $T_{nw,e}$, and layer 'j' $T_{nw(j)}$ of the north wall are described as follows. The layer 'j' is located between the two surfaces and is identified and numbered from the inside to the outside (Figure 4.1).

$$\begin{aligned} cap_{nw,in}\frac{dT_{nw,in}}{dt} &= I_{nw,in} - C_{nw,in\_air} - R_{nw,in\_gro} - R_{nw,in\_can} \\ &\quad - R_{nw,in\_nr,in} - R_{nw,in\_sr,in} - R_{nw,in\_sky} \\ &\quad - D_{nw,in\_nw(1)} \ [\mathrm{W\ m^{-2}\ (gro)}] \end{aligned} \tag{4.3}$$

$$cap_{nw(j)}\frac{dT_{nw(j)}}{dt} = D_{nw(j-1)\_nw(j)} - D_{nw(j)\_nw(j+1)} \ [\mathrm{W\ m^{-2}\ (gro)}] \tag{4.4}$$

$$cap_{nw,e}\frac{dT_{nw,e}}{dt} = D_{nw(jmax)\_nw,e} - C_{nw,e\_out} - R_{nw,e\_sky} \ [\mathrm{W\ m^{-2}\ (gro)}] \tag{4.5}$$

where $cap_{nw,in}$, $cap_{nw,e}$, $cap_{nw(j)}$ [J °C^{-1} m^{-2} (gro)] are the heat capacity of the internal surface, external surface, and the layer 'j' of the CSG north wall, respectively. $T_{nw,in}$, $T_{nw,e}$, $T_{nw(j)}$ [°C] are the temperature of the internal surface, external surface, and the layer 'j' of the CSG north wall, respectively. $I_{nw,in}$ [W m^{-2} (gro)] is the shortwave radiation absorbed by the internal surface of the north wall. The external surface of the north wall is assumed to receive negligible shortwave radiation. R_{nw,in_gro}, $R_{nw,in\_nr,in}$, $R_{nw,in\_sr,in}$, and R_{nw,in_sky} [W m^{-2} (gro)] are the longwave radiation heat fluxes between the north wall internal surface with the indoor ground, the north roof internal surface, the south roof internal surface, and the sky, respectively. $D_{nw,in\_nw(1)}$ [W m^{-2} (gro)] is the conductive heat flux from the internal surface to

layer 1 of the north wall. $D_{nw(j\text{-}1)\_nw(j)}$ [W m^{-2} (gro)] is the conductive heat flux from layer 'j-1' to layer 'j' of the north wall, and $D_{nw(j)\_nw(j+1)}$ [W m^{-2} (gro)] is the conductive heat flux from layer 'j' to layer 'j+1' of the north wall. The value of 'j' ranges from 1 to 'j_{max}' (Figure 4.1). The external surface of the north wall exchanges heat with the adjacent layer 'j_{max}' through conduction $D_{nw,jmax\_nw,e}$, with outdoor air through convection C_{nw,e_out}, and with the sky through radiative heat transfer R_{nw,e_sky}. $D_{nw(j\text{-}1)\_nw(j)}$ is equivalent to $D_{nw,in\_nw(1)}$ for the first layer, and $D_{nw(j)\_nw(j+1)}$ is equivalent to $D_{nw,jmax\_nw,e}$ for the layer 'j_{max}'.

The primary function of the CSG north roof is to provide insulation and capture as much radiation as possible, while its heat storage capacity and thermal lag effects can be neglected. Thus, this model regards the north roof as a whole for heat conduction analysis, with a consistent direction of heat flow internally. To facilitate model reduction, the temperatures of the internal surface $T_{nr,in}$ [°C] and external surface $T_{nr,e}$ [°C] of the north roof are determined using the following energy balance equations, rather than differential equations.

$$I_{nr,in} - C_{nr,in\_air} - R_{nr,in\_gro} - R_{nr,in\_can} + R_{nw,in\_nr,in} - R_{nr,in\_sr,in} - R_{nr,in\_sky} = D_{nr,in\_nr,e} \ [\text{W m}^{-2}\ (\text{gro})] \tag{4.6}$$

$$D_{nr,in\_nr,e} = C_{nr,e\_out} + R_{nr,e\_sky} \ [\text{W m}^{-2}\ (\text{gro})] \tag{4.7}$$

where $I_{nr,in}$ [W m^{-2} (gro)] is the shortwave radiation absorbed by the internal surface of the north roof. R_{nr,in_gro}, $R_{nr,in\_sr,in}$, and R_{nr,in_sky} [W m^{-2} (gro)] are the longwave radiation heat fluxes between the north roof internal surface with the indoor ground, the south roof internal surface, and the sky, respectively. $D_{nr,in\_nr,e}$ [W m^{-2} (gro)] is the conductive heat flux from the internal surface to the external surface of the north roof. C_{nr,e_out} [W m^{-2} (gro)] is the convective heat flux between the external surface of the north roof and the outdoor air. R_{nr,e_sky} [W m^{-2} (gro)] is radiative heat flux between the external surface of the north roof and the sky.

The CSG south roof serves for daylighting and is covered with an external thermal blanket for insulation at night. Additionally, frost formation might occur on the internal surface of the south roof after uncovering the thermal blanket. In this model, the CSG south roof is conceptualized as a dynamic composite layer consisting of a potential ice layer, a transparent covering, and an adjustable thermal blanket. Similar to the treatment of the north roof, the south roof is considered a unified entity for heat conduction analysis. The temperatures of the internal surface $T_{sr,in}$ [°C] and external surface $T_{sr,e}$ [°C] of the south roof can be determined by the following energy balance equations.

$$-C_{sr,in\_air} - R_{sr,in\_gro} - R_{sr,in\_can} + R_{nw,in\_sr,in} + R_{nr,in\_sr,in} + L_{air\_sr,in} = D_{sr,in\_sr,e} \ [\mathrm{W\ m^{-2}\ (gro)}] \quad (4.8)$$

$$D_{sr,in\_sr,e} = C_{sr,e\_out} + R_{sr,e\_sky} - I_{sr,e} \ [\mathrm{W\ m^{-2}\ (gro)}] \quad (4.9)$$

where $I_{nr,e}$ [W m^{-2} (gro)] is the shortwave radiation absorbed by the external surface of the north roof. Assuming that, in both transparent and opaque states, the solar radiation absorbed by the south roof is attributed solely to the absorption of its external surface. R_{sr,in_gro} [W m^{-2} (gro)] is the longwave radiation heat flux between the south roof internal surface and the indoor ground. $D_{sr,in\_sr,e}$ [W m^{-2} (gro)] is the conductive heat flux from the internal surface to the external surface of the south roof. $L_{air\_sr,in}$ [W m^{-2} (gro)] is latent heat flux from indoor air to the internal surface of the south roof, which is induced by vapour condensation onto the surface and leads to sensible heat gain of the internal surface. C_{sr,e_out} [W m^{-2} (gro)] is the convective heat flux between the external surface of the south roof and the outdoor air. R_{sr,e_sky} [W m^{-2} (gro)] is radiative heat flux between the external surface of the south roof and the sky.

Because of the high heat capacity of the indoor soil, layering is performed to describe its temperatures. The ground inside the CSG is typically bare soil, while there are rare cases where ground cloth is used. The detailed definitions of soil layers and surfaces can be found

in the following sections. The temperatures of the indoor ground and soil layers are described below:

$$cap_{gro}\frac{dT_{gro}}{dt} = I_{gro} - C_{gro\_air} - R_{gro\_can} + R_{nw,in\_gro} + R_{nr,in\_gro} + R_{sr,in\_gro} - R_{gro\_sky} - D_{gro\_so(1)} - L_{gro\_air} \ [\mathrm{W\ m^{-2}\ (gro)}] \quad (4.10)$$

$$cap_{so(i)}\frac{dT_{so(i)}}{dt} = D_{so(i-1)\_so(i)} - D_{so(i)\_so(i+1)} \ [\mathrm{W\ m^{-2}\ (gro)}] \quad (4.11)$$

where cap_{gro} and $cap_{so(i)}$ [J °C^{-1} m^{-2} (gro)] are the heat capacity of the indoor ground and soil layer 'i', respectively. T_{gro} and $T_{so(i)}$ [°C] are the temperature of the indoor ground and soil layer 'i', respectively. I_{gro} [W m^{-2} (gro)] is the shortwave radiation absorbed by the indoor ground. R_{gro_sky} [W m^{-2} (gro)] is the longwave radiation heat flux between the indoor ground and the sky. $D_{gro\_so(1)}$ [W m^{-2} (gro)] is the conductive heat flux from the indoor ground to soil layer 1. L_{gro_air} [W m^{-2} (gro)] is latent heat flux from indoor ground to CSG air due to soil evaporation, leading to sensible heat loss of the soil. $D_{so(i\text{-}1)\_so(i)}$ [W m^{-2} (gro)] is the conductive heat flux from layer 'i-1' to layer 'i' of the soil, and $D_{so(i)\_so(i+1)}$ [W m^{-2} (gro)] is the conductive heat flux from layer 'i' to layer 'i+1' of the soil. The value of 'i' ranges from 1 to 'i_{max}'. $D_{so(i\text{-}1)\_so(i)}$ is equivalent to $D_{gro\_so(1)}$ for the first layer. For the layer 'i_{max}', $D_{so(i)\_so(i+1)}$ is equal to the conductive heat flux from soil layer 'i_{max}' to the soil layer with constant temperature $D_{so,imax\_so,cs}$.

Humidity of greenhouse air

The relative humidity of the CSG air is described by:

$$cap_{MV}\frac{dX_h}{dt} = E_{c,gh} + E_{so} - MV_{air\_sr,in} - MV_{air\_can} - MV_{air\_out} \ (0 \le X_h \le 1) \ [\mathrm{kg\ m^{-2}\ (gro)\ s^{-1}}] \quad (4.12)$$

where X_h [-] is the relative humidity of greenhouse air, cap_{MV} [kg m^{-2} (gro)] is the capacity of indoor air to store water, $E_{c,gh}$ [kg m^{-2} (gro) s^{-1}] is the crop transpiration rate at the whole greenhouse level, E_{so} [kg m^{-2} (gro) s^{-1}] is the soil evaporation rate inside the greenhouse, $MV_{air\_sr,in}$ [kg m^{-2} (gro) s^{-1}] is the vapour flux from the indoor air to the internal surface of the south roof due to condensation or deposition, MV_{air_can} [kg m^{-2} (gro) s^{-1}] is the vapour flux from the indoor air to the canopy due to condensation, MV_{air_out} [kg m^{-2} (gro) s^{-1}] is the vapour flux from the indoor air to the outdoor air accompanying air exchange.

CO_2 concentration of greenhouse air

The CO_2 concentration of the greenhouse air is described by:

$$cap_{MC}\frac{dX_c}{dt} = R_{sm} + R_{d,gh} - A_{C,gh} - MC_{air\_out} \ \ [\text{kg m}^{-2}\ \text{(gro)}\ \text{s}^{-1}] \qquad (4.13)$$

where X_c [μmol (CO_2) mol^{-1} (air)] is the CO_2 concentration of the indoor air, cap_{MC} [kg m^{-2} (gro)] is the capacity of indoor air to store CO_2, R_{sm} [kg (CO_2) m^{-2} (gro) s^{-1}] is the soil microbial respiration rate inside the greenhouse, $A_{C,gh}$ [kg (CO_2) m^{-2} (gro) s^{-1}] is the gross canopy assimilation rate at the whole greenhouse level, $R_{d,gh}$ [kg (CO_2) m^{-2} (gro) s^{-1}] is the crop maintenance respiration rate at the whole greenhouse level, MC_{air_out} [kg m^{-2} (gro) s^{-1}] is the CO_2 flux from the indoor air to the outdoor air generated by air exchange.

4.2.2.2 Definition of layers and surfaces

The Composite Layer of the south roof

The CSG south roof is unique in the model descriptions because it has a dynamic layer. The CSG is equipped with an external thermal blanket that covers the transparent south roof during cold winter nights. When the thermal blanket covers the roof, it forms a composite

layer consisting of the roof and the blanket. During the day, the thermal blanket is rolled up to allow solar radiation to enter the greenhouse. As a result, the south roof of the CSG can vary depending on the controls of the thermal blanket.

Most CSG climate models, especially those predicting humidity, describe condensations. They only consider the conversion between latent and sensible heat, rather than describing influences of condensation on the thermal and optical properties of the south roof (F. He et al., 2009; R. Liu et al., 2021; Tong & Christopher, 2009). This is because the water formed by condensation will rapidly slide along the inner surface of the south roof or drip onto the indoor ground. It is assumed that condensation does not stay on the surface, especially since non-dripping films are widely used. Condensation on crop leaves follows a similar pattern. This model maintains this assumption. However, another process leading to the vapour flux from indoor air to the south roof cannot be neglected, which is deposition. This process has never been involved in existing CSG models. The water vapour deposition onto the inner surface of the south roof usually occurs after uncovering the thermal blanket on cold winter mornings. During this period, the surface temperature drops sharply and can easily fall below 0 ℃, as the thermal resistance of the south roof decreases significantly, while the indoor temperature has not yet risen. In addition to changing latent heat conversion accompanying vapour flows, the deposition will form an ice layer on the inner surface of the south roof and affect its conductive and optical properties. This model assumes that condensation shifts to deposition or frost formation when the inner surface decreases below 0 ℃. The formation of the ice layer will change the composition of the south roof.

This model regards the CSG south roof as a composite layer that consists of a conditional ice layer, a transparent covering, and a movable thermal blanket from inside to outside. The definitions and assumptions about the south roof are as follows:

(1) There are no gaps between the three layers.

(2) The presence of the ice layer is represented by u_{ice},

$$u_{ice} = \begin{cases} 1, & T_{sr,in} < 0 \cap e_{air} > e_{s,sr,in} \\ 0, & T_{sr,in} \geq 0 \cup e_{air} \leq e_{s,sr,in} \end{cases} [-] \quad (4.14)$$

where $T_{sr,in}$ [℃] is the temperature of the internal surface of the south roof, e_{air} [Pa] is the vapour pressure of indoor air, $e_{s,sr,in}$ [Pa] is the saturated vapour pressure of the south roof inner surface (can be the ice layer or transparent covering) at its temperature. Eq. (4.14) assumes that the ice layer forms when condensation occurs, and the temperature of the south roof inner surface is below 0 ℃. For model simplification, the appearance and disappearance of the ice layer are assumed to be instantaneous and do not consider the latent heat required for melting or sublimation. The thickness of the ice layer is defined to be 0.1 mm for relevant calculations.

(3) The controls of the thermal blanket are represented by U_b, with $U_b = 1$ when operated to cover the south roof and $U_b = 0$ when rolled up. Generally, the rolling up of the thermal blanket is mechanically driven from the south roof bottom to the top or vice versa, with a duration of 10-15 minutes, depending on the span of the greenhouse. The time required to cover the thermal blanket is slightly shorter than the uncovering time. For model simplification, the covering and uncovering of the thermal blanket are also assumed to be instantaneous.

(4) The presence or absence of the ice layer and the thermal blanket covering will not affect the convective heat transfer coefficients of the south roof but will affect its thermal conductivity.

(5) All three layers affect transmission, absorption, and reflection of the south roof for shortwave radiation, as well as emissivity for longwave radiation.

(6) Controls of the thermal blanket influence air infiltration of the CSG.

(7) The optical and thermophysical properties of the composite layer will be illustrated as a special case in the following sections.

Definition of layering and surfaces

In steady-state CSG models such as heating and cooling load models, the temperatures of

the CSG envelope surfaces and indoor floor are determined by solving simultaneous equations (Fu et al., 2020; Weituo Sun et al., 2019), and surface temperatures can stand on a virtual surface. The states of certain greenhouse objects are also calculated using algebraic equations in some dynamic models, such as temperatures of the screen and air above the screen in the Venlo type greenhouse (De Zwart, 1996) and the wall and ground temperatures in the CSG (R. Liu et al., 2021). However, employing algebraic equations implies that the target objects have unidirectional internal heat transfer, only considering their insulation properties while ignoring their heat storage capabilities. It allows the target object, inner surface, and indoor air to respond to weather changes instantaneously. This assumption applies to certain components in the muti-span greenhouse, but deviates completely from reality in CSG systems, especially for the north wall (nighttime heat release reaches 1.69 MJ m^{-2} d^{-1}) and indoor soil (nighttime heat release reaches 0.48 MJ m^{-2} d^{-1}) (Bai et al., 2003). It is common for the CSG north wall, composed of thermal insulation and storage materials, to exceed 0.5 m in thickness, and the direction of heat fluxes within it is not always from inside to outside. Heat fluxes with inconsistent directions exist within the north wall at different positions at the same time and at different times at the same position (M. Li et al., 2015; C Ma et al., 2010; Tong & Christopher, 2019).

Dynamic CSG climate models should respond to external disturbances and characterize the thermal inertia and time delay effects of the greenhouse system for accurate and more explanatory simulations. For CSG objects with thermal storage capacity, layering is necessary to describe their temperature dynamics, aiming to understand the direction of interior heat fluxes and the heat storage and release patterns of the CSG envelope and soil. Correspondingly, simulating the surface temperature of these CSG objects requires reliance on a substantial layer with thickness. The temperatures of both the south roof and north roof surfaces are determined by solving simultaneous equations; therefore, layering and surface definition are not necessary for them. If not, the south roof, without the thermal blanket being covered, will exhibit extreme sensitivity in its temperature states to heat flow changes due to the minimal heat capacity. Besides, the model should iteratively update the temperature of the newly formed surface layer of the south roof on the basis of the original surface

temperature, but accompanied by abrupt changes in heat flow. Current numerical simulation methods, such as the Euler method and the Runge-Kutta method, are challenging when dealing with such state simulations. Then, the definition of layering and surfaces of the CSG objects, including the north wall and indoor soil, are detailed as follows.

For the north wall, it is recommended to consider the thickness of its surface layer (internal or external) within the range of 1-100 mm. The surface layer is allowed to span multiple materials, adopting equivalent density, specific heat capacity, and thermal conductivity. Simultaneously, the radiative and convective processes of the defined surface should be based on the characteristics of the outermost or innermost layer material of the north wall. For indoor soil, it is similarly recommended that the indoor ground ranges from 1 to 100 mm in depth. If ground cloth is used, it should not affect the surface definition and conductive processes of the indoor ground. However, the radiative and convective processes should consider the influence of the ground cloth.

More detailed layering is required after surface definition for CSG objects with thermal storage capacity, mainly including the north wall and indoor soil. In common CSGs, the interlayer of the north wall consists of a single thermal storage material and can be uniformly divided into three layers. Allocating more layers can provide more details on temperature and heat flow dynamics, but this compromises computation efficiency and may lead to overly sensitive states. If the interlayer contains multiple-layer materials, layering for the north wall does not span materials, with the thickness of a single layer not exceeding 1/3 of the total wall thickness identified from the inner surface to the outer surface. The total number of layers for the north wall depends on its material composition and dimensions.

Within a depth of 0.5 m, excluding the indoor ground layer, the remaining soil is suggested to be divided into two layers since daily soil temperature fluctuations mainly occur within 0.5 m depth in CSGs (Deng, 2021; Huang, 2021; Weituo Sun et al., 2015). In addition, the temperature of the soil layer deeper than 1.0 m is insensitive to the diurnal cycle of air temperature and solar radiation (Kalogirou & Florides, 2004). Then, other soil layers are

defined to occupy depths of 0.5-1.0 m, 1.0-3.0 m. The external surface of the soil is defined as a 1 mm thick layer with constant temperature starting from a depth of 3 m. This constant soil temperature ($T_{so,cs}$) can be estimated by the annual average of local air temperature (X. Liu, Zhao, Shi, & Zhao, 2007). In temperate regions, it can be set to 15 ℃ (M S Ahamed et al., 2018; Weituo Sun et al., 2022). For a CSG with indoor ground being bare soil or covered by ground cloth, the soil will be divided into 5 layers.

4.2.2.3 Capacities of CSG objects

The heat capacity of the CSG air cap_{air} represents the heat energy required for every 1 ℃ change in greenhouse air per unit ground area. It is described as:

$$cap_{air} = H_{gh} \cdot \rho_a \cdot c_{p,a} \ \ [\text{J } ℃^{-1} \text{ m}^{-2} \text{ (gro)}] \tag{4.15}$$

where H_{gh} [m] is the average height of the CSG, representing the ratio of the volume of indoor air to the greenhouse ground area, ρ_a [kg m^{-3}] is the density of air, $c_{p,a}$ [J kg^{-1} ℃$^{-1}$] is the specific heat capacity of air at constant pressure. It should be noted that all expressions of energy and mass fluxes, as well as capacities of CSG objects in this model, refer to values per unit greenhouse ground area.

The heat capacity of the canopy cap_{can} can be described by

$$cap_{can} = LAI_{gh} \cdot \delta_L \cdot \rho_L \cdot c_{p,L} \ \ [\text{J } ℃^{-1} \text{ m}^{-2} \text{ (gro)}] \tag{4.16}$$

where LAI_{gh} [m^2 (leaf) m^{-2} (gro)] is the leaf area index at the whole greenhouse level, δ_L [m] is the average thickness of the crop leaves, ρ_L [kg m^{-3}] is the density of crop leaves, $c_{p,L}$ [J kg^{-1} ℃$^{-1}$] is the specific heat capacity of crop leaves. $\delta_L \cdot \rho_L$ [kg m^{-2} (leaf)] denotes the fresh leaf weight per unit leaf area.

The heat capacities of other CSG objects cap_{obj} can be described by the following general formula.

$$cap_{obj} = \frac{L_{obj} \cdot \delta_{obj}}{L_{gro}} \cdot \rho_{obj} \cdot c_{p,obj} \quad [\mathrm{J\ ^{\circ}C^{-1}\ m^{-2}\ (gro)}] \tag{4.17}$$

where L_{obj} [m] is the characteristic length of the CSG object, such as the height of the north wall, the arc length of the south roof, the width of the indoor ground, etc. L_{gro} [m] is the span of the CSG, δ_{obj} [m] is the thickness of the CSG object, ρ_{obj} [kg m^{-3}] is the density of the CSG object, $c_{p,obj}$ [J kg^{-1} °C^{-1}] is the specific heat capacity of the CSG object. This model assumes that the CSG production system is uniformly consistent in the longitudinal (east-west) direction. Therefore, all ratios with respect to the indoor ground area can be processed on the cross-section of the CSG.

To ensure that the mass transfer related outputs of the model are in the most common units and remain consistent with inputs of the crop model, the capacities of indoor air to store water vapour and carbon dioxide are represented by the following equations:

$$cap_{MV} = H_{gh} \cdot \frac{M_v}{R_g \cdot X_{t,K}} \cdot e_{s,air} \quad [\mathrm{kg\ m^{-2}\ (gro)}] \tag{4.18}$$

$$cap_{MC} = H_{gh} \cdot \sigma_{CO2} \quad [\mathrm{kg\ m^{-2}\ (gro)\ (\mu mol\ mol^{-1})^{-1}}] \tag{4.19}$$

where M_v [kg mol^{-1}] is the molar mass of water (and vapour), R_g [J mol^{-1} K^{-1}] is the general gas constant, $X_{t,K}$ [K] is the indoor air temperature in Kelvin, σ_{CO2} [kg m^{-3} (μmol mol^{-1})$^{-1}$] is the factor that converts the unit of CO_2 concentration from μmol (CO_2) mol^{-1} (air) to kg m^{-3}.

4.2.2.4 Radiative fluxes

shortwave radiation heat fluxes

Simulation of shortwave radiation heat fluxes in CSGs requires the utilisation of analytical models. Numerous researchers have focused on this work (Han et al., 2014; X. Li & Chen, 2004; Chengwei Ma et al., 2013; H. Xu et al., 2019) since daylighting is crucial for efficient production of CSGs that they heavily rely on solar radiation as their primary energy source. The modelling approach, taking the beam solar radiation simulation as an example, typically begins by defining extraterrestrial radiation based on the solar constant. Secondly, the normal incident solar radiation near the earth's surface is calculated considering atmospheric transparency, aerosphere mass (dependent on local solar altitude and elevation), and cloud cover. Direct and diffuse solar radiation components can be further separated based on the cloud cover coefficient or clearness index. Thirdly, the solar incidence angle on the roof surface is calculated based on the solar altitude angle, solar azimuth angle, and the slope and orientation of the surface. Fourthly, the transmissivity to beam solar radiation of a specific point on the south roof is determined according to the incidence angle. Meanwhile, the solar radiation intensity at that point can be established in combination with the determined normal incident radiation. Finally, employing a backward ray tracing method, the radiation intensity on the internal surfaces and indoor ground of the CSG is computed by associating them with the radiation incidence points on the south roof. Alternatively, the weighted average integration of transmissivities along the transparent curved surface is performed to obtain the equivalent transmissivity and the transmitted average solar radiation through the south roof (Huang et al., 2020).

Deducing the beam solar radiation normal to the sunrays, as described in the first two steps of modelling CSG related shortwave radiation dynamics, is outside the scope of this model. The model takes horizontal outdoor solar radiation as a given input variable. There are two points to consider in this regard. First, this model focuses on describing the influence of outdoor climate, greenhouse, controls, and crops on the CSG climate; using measured radiation data for model calibration and validation can benefit establishing a more precise correlation mechanism. Secondly, in future model applications for greenhouse management, outdoor solar radiation can be obtained based on historical data, commercial weather forecasts, or additional radiation prediction models. In order to simplify the model, instead

of using the backward ray tracing method, we calculate the equivalent transmittance of the south roof. Huang et al. (2020) discovered that using a curved surface to compute the equivalent beam transmissivity was more accurate than using the traditional simplified inclined planes. However, their model adopts an empirical transmissivity formula that is independent of the base transmittance, which might not apply to all CSG scenarios. As a result, the equivalent transmittance of the south roof calculated by our model is based on a simplified inclined plane. Correspondingly, the south roof points corresponding to the indoor surfaces share the same optical properties.

Measurements of solar energy are typically expressed as global solar radiation on a horizontal surface. To identify the amount of beam and scattered solar radiations, accurate detection of cloud cover or clearness index is crucial. However, current methods have their limitations (Huang, 2021). In correspondence with the developed crop model, the climate model of this study does not differentiate between beam and scattered solar radiations. Moreover, unlike Venlo-type greenhouses that use diffuse glass for uniform indoor lighting, CSGs rely mainly on direct solar radiation, especially on clear days, where direct radiation can constitute 80-90 % of the total indoor solar radiation (Q. Chen, 1993). In some simulations, diffuse radiation on the outdoor horizontal surface can be approximated to be 20% of total radiation on clear days (Tong et al., 2018). Therefore, the model defaults to consider properties of direct radiation when analysing shortwave radiation. Then, the subdivision of radiation involves shortwave radiation consisting of photosynthetically active radiation (PAR) and near-infrared radiation, PAR, and longwave radiation. The separation of PAR from shortwave radiation is attributed to the different extinction and reflection characteristics of crops to these two radiation types. As described in the crop model, this separation occurs after shortwave radiation enters the CSG. This is because common transparent cover materials used in CSGs, such as PE and EVA films, have nearly identical transmissivities to direct solar radiation and PAR, with base transmissivities exceeding 80% and the majority surpassing 85% (N. Wang, Ma, Zhao, Jiang, & Song, 2013).

The description of shortwave radiation acquisition by various CSG objects is primarily based

on the analysis above and adapted from previous studies (Kalogirou, 2022; Chengwei Ma et al., 2013; Martinez-Gracia, Arauzo, & Uche, 2019; H. Xu et al., 2019). The solar incidence angle for the south roof simplified as an inclined surface, can be described by:

$$cos\theta_i = cos\theta_{sr} \cdot sin\theta_h + sin\theta_{sr} \cdot cos\theta_h \cdot cos\left(\theta_z - \theta_{ghz}\right)\ [-] \tag{4.20}$$

where θ_i [°] is the solar incidence angle for the south roof, which represents the angle between the solar rays and the normal to the south roof surface, θ_{sr} [°] is the south roof angle, which denotes the angle between the line connecting the bottom to the ridge of the south roof and the horizontal indoor ground in the same cross-section, θ_h [°] is the solar altitude angle, denoting the angle between the solar rays and a horizontal plane, θ_z [°] is the solar azimuth angle, which denotes the angle of the solar rays measured in the horizontal plane from the due south for the northern hemisphere, with westward being positive, θ_{ghz} [°] is the azimuth angle of the CSG and westward from south is designated as positive.

The solar altitude angle θ_h can be calculated by,

$$sin\theta_h = sin\varphi \cdot sin\delta_s + cos\varphi \cdot cos\delta_s \cdot cos\omega\ \ (0 < \theta_h < 90)\ [-] \tag{4.21}$$

$$\delta_s = 23.45 \cdot sin\left(\frac{360}{365} \cdot (284 + n)\right)\ [\circ] \tag{4.22}$$

$$\omega = 15 \cdot (t_{AST} - 12)\ [\circ] \tag{4.23}$$

where φ [°] is the local latitude (north of the equator is taken as positive). δ_s [°] is the solar declination, which depends on the day n of the year; n = 1 for the date of January 1 and n = 365 for the date of December 31. ω [°] is the hour angle, being zero due south and positive for west. t_{AST} [-] is the local time measured in hours instead of the standard time, also known as apparent solar time. t_{AST} = 12 for the local solar noon and ω = 0 ° at noon.

The solar azimuth angle θ_z is described by,

$$sin\theta_z = \frac{cos\delta_s \cdot sin\omega}{cos\theta_h} \ [-] \tag{4.24}$$

The transmissivity of a film to solar radiation is relative to the solar incidence angle, film thickness, and refractive index of the film. Once a film is selected, its transmittance can be considered solely as a function of the solar incidence angle (D. Chen et al., 1992). The equivalent transmissivity of the south roof τ_{sr} can be estimated by an empirical formula (Chengwei Ma et al., 2013),

$$\tau_{sr} = \tau_{sr,0} \cdot \left(1 - 0.93^{90-\theta_i}\right) \cdot \left(1 - \frac{\theta_i}{1000}\right) \ [-] \tag{4.25}$$

where τ_{sr} [-] is the equivalent transmissivity of the south roof to shortwave radiation. $\tau_{sr,0}$ [-] is the base transmissivity of the south roof to shortwave radiation, which represents the transmissivity of the south roof to solar radiation when the incidence angle is 0 °.

Based on the Snell's Law and Fresnel equations, the equivalent reflectivity of the south roof to shortwave radiation κ_{sr} can be estimated by,

$$\kappa_{sr} = U_b \cdot \kappa_{sr,0} + (1 - U_b) \cdot \kappa_{sr,0} \cdot \frac{\frac{1}{2} \cdot \left(\frac{sin^2(\theta_r - \theta_i)}{sin^2(\theta_r + \theta_i)} + \frac{tan^2(\theta_r - \theta_i)}{tan^2(\theta_r + \theta_i)}\right)}{\left(\frac{\pi_a - \pi_{tc}}{\pi_a + \pi_{tc}}\right)^2} \ [-] \tag{4.26}$$

$$sin\theta_r = \frac{sin\theta_i \cdot \pi_a}{\pi_{tc}} \ [-] \tag{4.27}$$

where $\kappa_{sr,0}$ [-] is the base reflectivity of the south roof to shortwave radiation, π_a [-] is the refractive index of air, π_{tc} [-] is the refractive index of the south roof transparent covering, θ_r

[°] is the angle of refraction formed when solar rays pass from air into the transparent covering. Note that, the ratio of κ_{sr} to $\kappa_{sr,0,}$ applies to the single south roof transparent covering. It also applies to the double transparent layer combining the film covering and the ice layer since the Fresnel reflection at the air-film interface is significantly greater than that of the film-ice interface.

According to the horizontal outdoor solar radiation, the normal incident solar radiation can be calculated by,

$$I_n = \frac{I_{out}}{sin\theta_h} \ [-] \tag{4.28}$$

where I_n [W m^{-2}] is the normal incident solar radiation, that is, the solar radiation received by a surface perpendicular to the solar rays. I_{out} [W m^{-2}] is the horizontal outdoor solar radiation, which is the model input variable.

For the south roof in both transparent and opaque states, the total absorption of radiation is assumed to be the contribution of the external surface for describing energy balance purposes. The following formula can be used to calculate the amount of solar radiation absorbed by the external surface of the south roof.

$$I_{sr,e} = \frac{L_{sr,c}}{L_{gro}} \cdot \alpha_{sr} \cdot I_n \cdot cos\theta_i \ [\text{W m}^{-2}\ (\text{gro})] \tag{4.29}$$

where $I_{sr,e}$ [W m^{-2} (gro)] is the solar radiation absorbed by the external surface of the south roof, $L_{sr,c}$ [m] is the length of the line connecting the bottom to the ridge of the south roof, α_{sr} [-] is the absorptivity of the composite south roof to shortwave radiation.

When a beam of radiation is incident on the surface of a body, the reflectivity (κ), absorptivity (α), and transmissivity (τ) of the surface to this radiation are related by $\kappa + \alpha + \tau = 1$. For opaque CSG objects, such as the internal surface of the north wall, $\tau = 0$ and

$\kappa + \alpha = 1$. This principle derives from the first law of thermodynamics and applies to shortwave and longwave radiations in this model. Generally, absorptivity is deduced by reflectivity and transmissivity, which are easier to measure and determine. Assuming that, for the transparent composite layer, reflection occurs only at the interfaces of incidence between different media, while absorption permeates the entire layer. Besides, this model does not consider the influence of refraction on the direction of the incident solar rays.

For a two-layer object, its overall transmissivity (τ_{12}) and overall reflectivity (κ_{12}) can be estimated as follows:

$$\tau_{12} = \frac{\tau_1 \cdot \tau_2}{1 - \kappa_1 \cdot \kappa_2} \ [-] \tag{4.30}$$

$$\kappa_{12} = \kappa_1 + \frac{{\tau_1}^2 \cdot \kappa_2}{1 - \kappa_1 \cdot \kappa_2} \ [-] \tag{4.31}$$

where τ_1 and τ_2 [-] are, respectively, the transmissivity of the first and second layers. The first layer refers to the layer that the radiation initially reaches. κ_1 and κ_2 [-] are, respectively, the reflectivity of the first and second layers.

The CSG south roof is a dynamic composite layer with three layers. Normally, its overall transmittance can be determined by initially calculating the total transmittance of the thermal blanket and transparent cover based on Eq. (4.30). Subsequently, this double layer combining the thermal blanket and transparent cover is considered as the first layer, with the potential ice layer acting as the second layer, to obtain the roof transmissivity using Eq. (4.30). However, the determination can be simplified since the thermal blanket is opaque. Given the dynamics of the composite layer, the base transmissivity of the south roof to shortwave radiation can be described as,

$$\tau_{sr,0} = (1 - U_b) \cdot \frac{\tau_{tc} \cdot \left(1 - u_{ice} \cdot (1 - \tau_{ice})\right)}{1 - \kappa_{tc} \cdot \kappa_{ice} \cdot u_{ice}} \ [-] \tag{4.32}$$

where τ_{tc} [-] is the transmissivity of the south roof transparent covering to shortwave radiation, κ_{tc} [-] is the reflectivity of the south roof transparent covering to shortwave radiation. τ_{ice} [-] is the transmissivity of the ice layer to shortwave radiation from the transparent covering, κ_{ice} [-] is the reflectivity of the ice layer to shortwave radiation from the transparent covering. In this formula, all the given optical properties are for the perpendicular incidence shortwave radiation, corresponding to the parameters usually provided by manufacturers or measured in laboratories. Accordingly, in the optical superposition, there is no need to consider polarisation effects.

Similarly, the base reflectivity of the south roof to shortwave radiation $\kappa_{sr,0}$ can be estimated by,

$$\kappa_{sr,0} = U_b \cdot \kappa_b + (1 - U_b) \cdot \left(\kappa_{tc} + \frac{{\tau_{tc}}^2 \cdot \kappa_{ice} \cdot u_{ice}}{1 - \kappa_{tc} \cdot \kappa_{ice} \cdot u_{ice}} \right) \ [-] \tag{4.33}$$

where κ_b [-] is the reflectivity of the external surface of the thermal blanket to shortwave radiation.

The solar radiation at the top of the canopy inside the CSG is described by:

$$I = \tau_{sr} \cdot I_n \cdot sin\theta_h \ [-] \tag{4.34}$$

where I [W m^{-2} (gro)] is the solar radiation at the top of the canopy. Then, the solar radiation absorbed by the canopy and by the indoor ground can be described as,

$$I_{gro} = \alpha_{gro} \cdot I \cdot e^{-k_I \cdot LAI_{gh}} \ [\mathrm{W\ m^{-2}\ (gro)}] \tag{4.35}$$

$$I_{can} = \alpha_{can} \cdot I \cdot \left(1 - e^{-k_I \cdot LAI_{gh}}\right) \ [\mathrm{W\ m^{-2}\ (gro)}] \tag{4.36}$$

where I_{gro} [W m^{-2} (gro)] is the solar radiation absorbed by the indoor ground, I_{can} [W m^{-2} (gro)] is the solar radiation absorbed by the canopy, α_{gro} [-] is the absorptivity of the indoor ground to shortwave radiation, α_{can} [-] is the absorptivity of the canopy to shortwave radiation, k_I [-] is the extinction coefficient for shortwave radiation.

The north roof angle of the CSG is currently designed to be 42-50° that the north roof could receive as much solar radiation (T. Li, 2013). Therefore, besides the north wall and indoor floor, the solar radiation received by the north roof should be considered.

$$I_{nr,in} = \frac{L_{nr}}{L_{gro}} \cdot \alpha_{nr,in} \cdot \tau_{sr} \cdot I_n \cdot cos\theta_{i,nr} \ \text{[W m}^{-2}\text{ (gro)]} \tag{4.37}$$

$$cos\theta_{i,nr} = max\{-cos\theta_{nr} \cdot sin\theta_h + sin\theta_{nr} \cdot cos\theta_h \cdot cos(\theta_z - \theta_{ghz}), 0\} \ [-] \tag{4.38}$$

where $I_{nr,in}$ [W m^{-2} (gro)] is the solar radiation absorbed by the internal surface of the north roof, L_{nr} [m] is the length of the north roof, $\alpha_{nr,in}$ [-] is the absorptivity of the internal surface of the north roof to shortwave radiation, $\theta_{i,nr}$ [°] is the solar incidence angle for the north roof, θ_{nr} [°] is the north roof angle, which denotes the angle between the north roof and the indoor horizontal plane in the same cross-section. As the solar altitude angle and incidence angle increase, solar radiation is no longer incident on the internal surface of the north roof but on its external surface. Simultaneously, this shift in radiation incidence produces a shadow over the north wall. This model neglects the shortwave radiation absorption of the north roof external surface, especially considering the thermal blanket, rolled up and placed on the top of the roof, provides shading for the north roof.

The internal surface of the north wall wholly or partially receives solar radiation following solar altitude variation. Thus, the solar energy absorbed by the internal surface of the north wall can be calculated by,

$$I_{nw,in} = \frac{L_{nw}}{L_{gro}} \cdot \alpha_{nw,in} \cdot (1 - \sigma_{sha}) \cdot \tau_{sr} \cdot I_n \cdot cos\theta_{i,nw} \ \text{[W m}^{-2}\text{ (gro)]} \quad (4.39)$$

$$cos\theta_{i,nw} = -cos\theta_{nw} \cdot sin\theta_h + sin\theta_{nw} \cdot cos\theta_h \cdot cos\left(\theta_z - \theta_{ghz}\right) \ [-] \quad (4.40)$$

$$\sigma_{sha} = \frac{L_{nr}}{L_{nw}} \cdot \frac{cos(\theta_{nw} - \theta_h + \theta_{nr})}{sin(\theta_{nw} - \theta_h)} \ (0 \le \sigma_{sha} \le 1) \ [-] \quad (4.41)$$

where $I_{nw,in}$ [W m^{-2} (gro)] is the solar radiation absorbed by the internal surface of the north wall, L_{nw} [m] is the height of the north wall, $\alpha_{nw,in}$ [-] is the absorptivity of the internal surface of the north wall to shortwave radiation, $\theta_{i,nw}$ [°] is the solar incidence angle for the north wall, σ_{sha} [-] is the shading ratio of the north wall due to the shading by north roof, θ_{nw} [°] is the north wall angle, which denotes the angle between the north wall and the horizontal indoor ground in the same cross-section. The north wall angle is typically 90 °, but in certain instances, such as when the wall is made of thick, piled soil, this angle may exceed 90 °. The model accounts for one-dimensional heat transfer; thus, when only part of the north wall surface receives solar radiation, it is evenly distributed across the entire surface.

Longwave radiation heat fluxes

The longwave radiation heat transfer is ubiquitous, occurring among the various internal surfaces of the CSG, between the external surfaces and the sky, and from the internal surfaces through the south roof transparent covering to the sky. These longwave radiation heat fluxes can be described by the following two general formulas:

$$R_{1\_2} = \sigma_{area} \cdot \varepsilon_1 \cdot \varepsilon_2 \cdot F_{1,2} \cdot \sigma \cdot \left({T_{1,K}}^4 - {T_{2,K}}^4\right) \ \text{[W m}^{-2}\text{ (gro)]} \quad (4.42)$$

$$R_{1\_sky} = \sigma_{area} \cdot \varepsilon_1 \cdot \varepsilon_{sky} \cdot F_{1,sky} \cdot \sigma \cdot \psi_{sr} \cdot \left({T_{1,K}}^4 - {T_{sky,K}}^4\right) \ \text{[W m}^{-2}\text{ (gro)]} \quad (4.43)$$

Where R_{1_2} [W m^{-2} (gro)] is the longwave radiation heat flux from object 1 to object 2, and Eq. (4.42) is applicable to interactions among the various internal surfaces of the CSG, and between the external surfaces and the sky. R_{1_sky} [W m^{-2} (gro)] is the longwave radiation heat flux from an internal surface of the CSG to the sky, σ_{area} [-] is the scale factor of the solid surface area to the indoor ground area, $T_{1,K}$ and $T_{2,K}$ [K] are respectively the temperatures in Kelvin of object 1 and object 2, σ [W m^{-2} K^{-4}] is the Stefan-Boltzmann constant, ε_1 and ε_2 (-) are the emissivity of object 1 and object 2, respectively. For common transparent covering materials, the emissivity is 0.85 for glass (Vanthoor, 2011), 0.15 for polyethylene (PE) film (Yi Zhang, Ma, Liu, & Han, 2010), 0.62 for polyvinyl chloride (PVC) film, and 0.59 for ethyl vinyl acetate (EVA) film (Nijskens, Deltour, Coutisse, & Nisen, 1984). ε_{sky} [-] is sky emissivity, $F_{1,2}$ (-) is the view factor of object 1 to object 2, $F_{1,sky}$ [-] is the view factor of an internal surface of the CSG to the sky, $T_{sky,K}$ (K) is the effective sky temperature in Kelvin, ψ_{sr} (-) is the transmittance of south roof to longwave radiation, which is 0 for glass (Vanthoor, 2011; Yi Zhang et al., 2010), 0.75 for PE film (Yi Zhang et al., 2010), 0.33 for PVC film, and 0.38 for EVA film (Nijskens et al., 1984). For a multi-layer greenhouse cover, ψ_{sr} can be calculated following the same optical superposition rules for shortwave radiation using reflectivity and transmissivity data of each layer. To avoid introducing reflectivity, the total transmittance of the south roof to longwave radiation can be simplified as,

$$\psi_{sr} = (1 - U_b) \cdot \psi_{tc} \cdot \left(1 - u_{ice} \cdot (1 - \psi_{ice})\right) \ [-] \tag{4.44}$$

where ψ_{tc} [-] is the transmissivity of the south roof transparent covering to longwave radiation, ψ_{ice} [-] is the transmissivity of the ice layer to long radiation from the transparent covering.

The emissivity of the internal surface and external surface of the south roof are described as follows.

$$\varepsilon_{sr,in} = u_{ice} \cdot \varepsilon_{ice} + (1 - u_{ice}) \cdot \varepsilon_{tc} \quad [-] \tag{4.45}$$

$$\varepsilon_{sr,e} = U_b \cdot \varepsilon_{b,o} + (1 - U_b) \cdot \varepsilon_{tc} \quad [-] \tag{4.46}$$

where ε_{ice}, ε_{tc}, and $\varepsilon_{b,o}$ (-) are the emissivity of the ice layer, transparent covering, and the outermost layer of the thermal blanket, respectively.

Since the CSG extends in the east-west direction and side walls have been ignored in the model description, the radiant energy emitted to the east and west ends can be omitted. Then, the CSG cross-section is considered as a closed system. Moreover, this model ignores radiation heat exchange with outdoor ground. The view factor to the indoor ground is divided between the ground and the canopy according to the leaf area index. Thus, according to the reciprocity rule and completeness of the view factor, as well as dimensions of the CSG cross-section, view factors between different surfaces can be obtained based on the algebraic analysis method. All the view factors, together with the corresponding area ratios, are listed in Table B.1.

The sky temperature is calculated according (Berdahl & Fromberg, 1982; Lawrence, 2005),

$$T_{sky} = {\varepsilon_{sky}}^{0.25} \cdot T_{out,K} - 273.15 \ [℃] \tag{4.47}$$

$$\varepsilon_{sky} = 0.741 + 0.0062 \cdot T_{dp} \ [-] \tag{4.48}$$

$$T_{dp} = T_{out} - 100 \cdot \left(\frac{1 - RH_{out}}{5}\right) \ [-] \tag{4.49}$$

where T_{sky} [℃] is the sky temperature, T_{dp} [℃] is dew point temperature of the outdoor air, T_{out} [℃] is the outdoor air temperature, $T_{out,K}$ [℃] is the outdoor air temperature in Kelvin, RH_{out} [-] is the relative humidity of the outdoor air.

4.2.2.5 Convective and conductive fluxes

Convective heat fluxes

Convective heat exchange occurs between the cover, soil, crop and the indoor air and between the cover and the outdoor air. As stated by Roy, Boulard, Kittas, and Wang (2002), the convective heat transfer process is influenced by both forced convection (due to wind pressure) and free convection (caused by temperature differences between solid surfaces and air). The dominant convection mode depends on the type of greenhouse, outdoor climate, and ventilation conditions. In well-ventilated greenhouses, forced convection is the primary mode due to strong air movement. And in closed greenhouses with low indoor air velocity, free convection dominates the process. As the convective heat flux density is proportional to the temperature difference, its description in the CSG climate model is given as,

$$C_{1\_2} = \sigma_{area} \cdot h_{1\_2} \cdot (T_1 - T_2) \ \ [\mathrm{W\ m^{-2}\ (gro)}] \tag{4.50}$$

where C_{1_2} [W m^{-2} (gro)] is the convective heat flux from object 1 to object 2; for objects 1 and 2 in convections, one is a solid surface while the other is a fluid. h_{1_2} [W m^{-2} °C^{-1}] is the convective heat transfer coefficient between object 1 and object 2, T_1 and T_2 are the temperatures of object 1 and object 2, respectively.

Convective heat transfer coefficients are presented in the form of empirical formulas. They are typically deduced from the appropriate Nusselt number that depends on convection modes and flow types (laminar or turbulent), with parameters fitted through experiments (Roy et al., 2002). Until now, no experimental study has determined convective heat transfer coefficients specific to CSGs. However, existing empirical formulas exhibit strong generality and can help achieve good performance of current CSG thermal climate models (R. Liu et al., 2021; Meng et al., 2009; Tong et al., 2009). In the model of this study and most others, the energy gain of CSG air is entirely from convections. Therefore, it is crucial to select appropriate convection coefficients. The challenge lies in the lack of criteria

description for selecting these coefficients in the developed CSG models, leading to confusion in calculating convections. The final result is that other researchers cannot reference convection formulas in present CSG models. To address this issue, R. Liu et al. (2021) categorized convective coefficients for four surface types, including the external and internal surfaces of the opaque wall and the transparent roof. However, this is not enough for climate models that fully depict crops and controls.

In choosing convective heat transfer coefficients, we consider the following points: (1) Vent openings affect the convection coefficients between the north wall, north roof, south roof, and the indoor air. In closed CSGs, only free convection exists. When the roof vent is opened, it switches to mixed convection, combining free convection and forced convection by turbulent airflow. Additionally, the indoor air velocity is assumed to be 0.5 m s^{-1} under natural ventilation. (2) Coefficient determination differs between transparent and opaque greenhouse covers. However, the influence of controls on the external thermal blanket will not be involved due to the similar properties between the south roof film and the surface layer of the thermal blanket. (3) The convection coefficient between indoor ground and air is affected by the leaf area index of the crop, considering only buoyancy-driven natural convection. Moreover, it does not distinguish between bare soil floor and that covered with fabric cloth. (4) The coefficient between crops and indoor air is calculated at the leaf level, responding simultaneously to temperature difference and indoor air velocity. In closed CSGs, the airflow velocity is 0.09 m s^{-1} (Van Ooteghem, 2010), consistent with the assumption in the crop model. (5) All convections of the cover external surfaces are considered mixed mode, with constants representing the buoyancy effect in formulas of convective coefficients. The constants are used to address low wind speed situations. Based on these criteria and assumptions, all convective heat transfer coefficients and area ratio factors involved in this model are given in Table B.2.

Conductive heat fluxes

Heat conductions occur in the CSG envelope and indoor soil. First, they occur between

adjacent layers for greenhouse objects with heat storage capacity, requiring artificial stratification and layer-by-layer temperature descriptions. In this scenario, the two layers involved in the heat conduction have thicknesses, with the centre point of the thickness representing each layer, and the temperature within the layer is considered uniform. Second, for the greenhouse object that can be considered to have no heat storage capacity, only heat conduction between the inner and outer surface layers of the object needs to be described, thus allowing heat transfer span across multiple layers. Conductive heat flux flows between the centre points of the two tangible layers or the two virtual surfaces, of which the thermal resistance is the sum of resistances along the heat conduction distance. The following equation can describe all conductive heat fluxes within the CSG:

$$D_{1\_2} = \begin{cases} \sigma_{area} \cdot \dfrac{1}{\dfrac{0.5\delta_1}{\lambda_1} + \dfrac{0.5\delta_2}{\lambda_2}} \cdot (T_1 - T_2), & between\ adjacent\ layers \\ \sigma_{area} \cdot \dfrac{1}{\dfrac{\delta_1}{\lambda_1} + \sum \dfrac{\delta_i}{\lambda_i} + \dfrac{\delta_2}{\lambda_2}} \cdot (T_1 - T_2), & across\ multiple\ layers \end{cases} \quad [\mathrm{W\ m^{-2}\ (gro)}] \tag{4.51}$$

where D_{1_2} [W m^{-2} (gro)] is the conductive heat flux from object 1 to object 2, and objects 1 and 2 in conductions are layers of greenhouse cover and indoor soil. δ_1, δ_2, and δ_i [m] are the thickness of object 1, object 2, and a specific layer between objects 1 and 2, respectively. λ_1, λ_2, and λ_i [W m^{-1} °C^{-1}] are, respectively, the heat conductivity coefficient of object 1, object 2, and a specific layer between objects 1 and 2, depending on the CSG materials.

For the special case of south roof, the conductive heat flux from the internal surface to the external surface can be described by,

$$D_{sr,in\_sr,e} = \frac{L_{sr}}{L_{gro}} \cdot \left(\frac{u_{ice} \cdot \delta_{ice}}{\lambda_{ice}} + \frac{\delta_{tc}}{\lambda_{tc}} + \frac{U_b \cdot \delta_b}{\lambda_b} \right)^{-1} \cdot \left(T_{sr,in} - T_{sr,e} \right) \ [\mathrm{W\ m^{-2}\ (gro)}] \tag{4.52}$$

where δ_{ice}, δ_{tc}, $\delta_{b,o}$ [m] are respectively the thickness of the ice layer, transparent covering, and the outermost layer of thermal blanket, λ_{ice}, λ_{tc}, and $\lambda_{b,o}$ [W m^{-1} °C^{-1}] are respectively the heat conductivity coefficient of the ice layer, transparent covering, and the outermost layer of thermal blanket, δ_b [m] is the total thickness of the thermal blanket, λ_b [W m^{-1} °C^{-1}] is the average thermal conductivity coefficient of the thermal blanket.

4.2.2.6 Latent heat fluxes

Conversion of sensible heat to latent heat is crucial in modelling CSG climate. The latent heat fluxes occur when water or water vapour undergoes phase changes. These phase change processes include crop transpiration, soil evaporation, and vapour condensation to the surfaces. This study assumes that all latent heat conversions exert the same amount of sensible heat on the solid objects that drive phase changes. The greenhouse air is considered not to participate in sensible heat transfer. For example, the required latent heat for soil evaporation is entirely supplied by the soil rather than directly absorbing heat from the surrounding air. Another example is that the heat released by condensation of indoor air to the inner surface of the south roof is entirely absorbed by the south roof. The latent heat flux is linear to the related vapour flux, expressed by the following general equation form.

$$L_{1\_2} = \lambda_v \cdot MV_{1\_2} \ [\mathrm{W\ m^{-2}\ (gro)}] \tag{4.53}$$

where L_{1_2} [W m^{-2} (gro)] is the latent heat flux from object 1 to object 2, MV_{1_2} [kg m^{-2} (gro) s^{-1}] is the vapour flux from object 1 to object 2. For objects 1 and 2 in latent conversions, one is the indoor air, while the other is the crop canopy or surface of the greenhouse cover or soil. If the latent heat flux points to the air, indicating the occurrence of evaporation or transpiration, the other object will lose sensible heat. Conversely, if the heat flux originates from the air, it indicates condensation and will lead to heat gain of the other object. λ_v [J kg^{-1}] is the latent heat of water vaporization, almost constant and about 2.45×10^6 J kg^{-1} for an air temperature of 20 °C (Stanghellini et al., 2019).

There is a particular case for quantifying the latent heat fluxes. When the temperature of the inner surface of the south roof film is lower than 0 ℃, condensation to this surface will switch to deposition. Then, the latent heat generated by the same water vapour flux will slightly increase due to the specific latent heat differences between condensation and deposition. Meanwhile, the description of water vapour flux remains unaffected. Therefore, a specific formula describing the latent heat flux to the south roof is as follows,

$$L_{air\_sr,in} = \begin{cases} \lambda_v \cdot MV_{air\_sr,in}, & T_{sr,in} \geq 0 \\ \lambda_{v,d} \cdot MV_{air\_sr,in}, & T_{sr,in} < 0 \end{cases} \ [\mathrm{W\ m^{-2}\ (gro)}] \tag{4.54}$$

where $L_{air\_sr,in}$ [W m^{-2} (gro)] is the latent heat flux from indoor air to the inner surface of the south roof film, $MV_{air\_sr,in}$ [kg m^{-2} (gro) s^{-1}] is the vapour flux from indoor air to the inner surface of the south roof film, $T_{sr,in}$ [℃] is the temperature of the inner surface of the south roof, $\lambda_{v,d}$ [J kg^{-1}] is the latent heat for water vapour deposition.

4.2.2.7 Vapour fluxes

The water vapour in the CSG air is away through condensations on the inner surface of the south roof and crop leaves and through air exchange. As the surface temperature is lower than the dew point temperature of the greenhouse air, water vapour will condense on the surface. The dew point temperature only depends on vapour pressure. Furthermore, the vapour exchange coefficient is linear to the convective heat transfer coefficient between the air and the condensation surface (Vanthoor, 2011). Hence, based on the study of F. He et al. (2009), we describe the condensation rate of the indoor water vapour using the following equation,

$$MV_{1\_2} = max\left\{0, \sigma_{area} \cdot \frac{h_{1\_2}}{\lambda_v \cdot \gamma} \cdot \left(e_{air} - e_{s,2}\right)\right\} \ [\mathrm{kg\ m^{-2}\ (gro)\ s^{-1}}] \tag{4.55}$$

$$e_{air} = e_{s,air} \cdot X_h \ [\mathrm{Pa}] \tag{4.56}$$

where MV_{1_2} [kg m^{-2} (gro) s^{-1}] is the vapour flux from object 1 to object 2. For objects 1 and 2 in condensation processes, object 1 represents greenhouse air, and object 2 represents the inner surface of CSG south roof or crop leaves. γ [Pa ℃$^{-1}$] is the psychrometric constant, $e_{s,2}$ [Pa] is the saturated vapour pressure of object 2 at its temperature, $e_{s,air}$ [Pa] is the saturated vapour pressure of greenhouse air (see detailed calculation formula in Chapter 3). Eq. (4.55) asserts that condensation only occurs when the saturated vapour pressure at the surface temperature is lower than the vapour pressure of the greenhouse air.

The water vapour flux generated by air exchange stems from the different water vapour content between the two exchanged air masses. Introducing absolute humidity (vapour concentration) is the most straightforward approach to quantify this vapour flux.

$$\begin{aligned} MV_{air\_out} &= g_{ae} \cdot (\chi_{air} - \chi_{out}) \\ &= g_{ae} \cdot \frac{M_v}{R_g} \cdot \left(\frac{e_{air}}{X_{t,K}} - \frac{e_{out}}{T_{out,K}} \right) \ [\text{kg m}^{-2}\ (\text{gro})\ \text{s}^{-1}] \end{aligned} \tag{4.57}$$

where MV_{air_out} [kg m^{-2} (gro) s^{-1}] is the vapour flux from indoor air to outdoor air, accompanying air exchange. χ_{air} and χ_{out} [kg m^{-3}] are the absolute humidity of indoor and outdoor air, respectively, g_{ae} [m^3 m^{-2} (gro) s^{-1}] is the total air exchange rate of the CSG, e_{out} [Pa] is vapour pressure of outdoor air.

The source vapour fluxes of the CSG air, including crop transpiration and soil evaporation, will be described in other sections.

4.2.2.8 CO_2 fluxes

The CO_2 concentration of the greenhouse air is influenced by crop and soil activities, as well as air exchange. Similar to the vapor flux accompanying ventilation, the CO_2 flux generated by air exchange can be expressed as follows:

$$MC_{air\_out} = g_{ae} \cdot \sigma_{CO2} \cdot (X_c - CO2_{out}) \ [\text{kg m}^{-2}\ \text{(gro)}\ \text{s}^{-1}] \quad (4.58)$$

where $CO2_{out}$ [μmol mol^{-1}] is the CO_2 concentration of the outdoor air. The CO_2 flux from the crop to indoor air is the result of the combined effects of crop photosynthesis and respiration, and that from the soil to indoor air is induced by soil respiration. These processes will be described in crop and soil activities.

4.2.2.9 Air exchange

The air exchange of the CSG that only has roof and side vents for ventilation is induced by natural ventilation and air infiltration. Its air exchange rate is described as

$$g_{ae} = g_{nv} + g_{inf} \ [\text{m}^3\ \text{m}^{-2}\ \text{(gro)}\ \text{s}^{-1}] \quad (4.59)$$

where g_{ae} [m^3 m^{-2} (gro) s^{-1}] is the total air exchange rate of the CSG, g_{nv} [m^3 m^{-2} (gro) s^{-1}] is the CSG natural ventilation rate, g_{inf} [m^3 m^{-2} (gro) s^{-1}] is the air exchange rate due to infiltration.

Then, the sensible heat fluxes due to the air exchange E_{air_out} can be described as,

$$E_{air\_out} = \rho_a \cdot c_{p,a} \cdot g_{ae} \cdot (X_t - T_{out}) \ [\text{W m}^{-2}\ \text{(gro)}] \quad (4.60)$$

Natural ventilation

A standard CSG has roof and side vents to remove excess heat, decrease humidity, and supplement CO_2. In practice, growers tend to only open roof vents during winter. Compared to solely opening side vents, the roof ventilation mode can achieve more uniform distributions of CSG air temperature and humidity, as well as alleviate direct exposure of

crops to cold winds (Fang et al., 2015; Zheng et al., 2023). In warmer seasons, the side vent is activated and combined with the roof vent for ventilation and cooling. Under this scenario, the cold outdoor air mainly gets into CSG through the side vent, while the warm indoor air is discharged to the outside through the roof vent, enhancing the air exchange rate and cooling effect (Fang et al., 2015; Zheng et al., 2023). In addition, it is uncommon to use side ventilation alone in practical CSG production. The roof and side vents are respectively opened at the top and bottom of the south roof with film covering, extending continuously in the east-west direction. Their opening or closing operations are achieved by rolling or pulling the film, with openings being rectangular in shape. Insect screens are generally installed with the vents to prevent pests from entering the greenhouse.

The description of the natural ventilation rate is indispensable for developing the CSG climate model. Natural ventilation is driven by two main forces: the wind effect and the buoyancy effect. The wind action results in a pressure field around the vents; the buoyancy effect, which is linked to gradients of air temperature and air density between inside and outside, leads to the vertical distribution of pressure (Thierry Boulard & Baille, 1995). Generally, when the outdoor wind velocity is higher than 1.5 m s^{-1}, or if the temperature difference between indoor and outdoor air is low, the wind effect will dominate the natural ventilation (Thierry Boulard & Baille, 1995; Kittas, Boulard, Mermier, & Papadakis, 1996). The buoyancy effect can be neglected when the wind velocity exceeds 2.5 m s^{-1} (Fang et al., 2016). Natural ventilation rate is influenced by various factors such as wind and buoyancy strength and distribution, greenhouse geometry, and vent size, shape, and arrangement (Jingfu Zhang et al., 2022). In addition, the usage of insect screens imposes significant resistance to greenhouse ventilation, causing a reduction in natural ventilation rate by 33%-87% (Baeza et al., 2009; Katsoulas, Bartzanas, Boulard, Mermier, & Kittas, 2006; Pérez Parra, Baeza, Montero, & Bailey, 2004).

The existing natural ventilation sub-models for CSG are derived from the Bernoulli equation and theories of fluid mechanics and thermodynamics, not fully considering the specific CSG structure, dimensions, and materials. So is the determination of the ventilation model

parameters that empirical values or values borrowed from other greenhouse types are used due to the lack of field experiments (R. Liu et al., 2021; Jingfu Zhang et al., 2022). Fang et al. (2016) applied the first-order assumption to model the ventilation rate of the CSG roof vent and used the CO_2 gas tracing technique to identify parameters. The discharge coefficient was estimated to be 0.78, 0.60, and 0.44, and the wind effect coefficient was estimated to be 0.04, 0.05, and 0.07 for the roof vent in width of 15, 25, and 35 cm, respectively. This study contributes to the parametrisation of the roof ventilation model specific to the CSG, but the model only applies to specific open widths of the roof vent and does not cover the scenario of using roof and side vents in conjunction.

This model focuses on the two ventilation modes of only the roof vent being open and the roof and side vents being open. The CSG natural ventilation, considering the resistance of insect screens to ventilation (Pérez Parra et al., 2004), is described as follows,

$$g_{nv} = \begin{cases} \eta_{inss} \cdot g_{vent,r}, & U_{vent,s} = 0 \\ \eta_{inss} \cdot g_{vent,rs}, & U_{vent,s} > 0 \cap U_{vent,r} > 0 \end{cases} \quad [\mathrm{m^3\ m^{-2}\ (gro)\ s^{-1}}] \quad (4.61)$$

$$\eta_{inss} = \varepsilon_{inss} \cdot (2 - \varepsilon_{inss}) \ [-] \quad (4.62)$$

where $g_{vent,r}$ [m^3 m^{-2} (gro) s^{-1}] is the natural ventilation rate when only the roof vent is opened, $g_{vent,rs}$ [m^3 m^{-2} (gro) s^{-1}] is the natural ventilation rate when both roof and side vents are opened, $U_{vent,r}$ [-] is the control of aperture of the roof vent, ranging from 0 to 1, $U_{vent,s}$ [-] is the control of aperture of the side vent, ranging from 0 to 1, η_{inss} [-] is the ratio between the ventilation rate with and without an insect screen, ε_{inss} [-] is porosity of the insect screen that mainly depends on the mesh count. Generally, the porosity decreases along with the increase in mesh count. The model requires insect screens installed for CSG vents to have the same ventilation resistance coefficient, and η_{inss} = 1 if insect screens are not installed.

The CSG south roof is curved, so the vents are not entirely horizontal and vertical. The roof vent has a practical dimension in the vertical direction, which can be significant in some

CSGs. Thus, the natural ventilation rate due to the roof vent $g_{vent,r}$, induced by the combined wind and buoyancy effects, can be described by (Thierry Boulard & Baille, 1995; Fang et al., 2016),

$$g_{vent,r} = \frac{A_{vent,r,U} \cdot c_d}{2 \cdot A_{gro}} \cdot \left(\frac{g \cdot H_{vent,r}}{2} \cdot \frac{X_t - T_{out}}{T_{out} + T_{0,K}} + c_{w,r} \cdot {v_e}^2 \right)^{0.5} \quad (4.63)$$

$$[\mathrm{m^3\ m^{-2}\ (gro)\ s^{-1}}]$$

where $A_{vent,r,U}$ [m^2] is the controlled opening area of the CSG roof vent, $H_{vent,r}$ [m] is the vertical dimension of the CSG roof vent, g [m s^{-2}] is the acceleration of gravity, $T_{0,K}$ [K] is the 0 °C in Kelvin, v_e [m s^{-1}] is outdoor wind speed, c_d [-] is the discharge coefficient of CSG vent openings, and the roof and side vents share the same discharge coefficient in this model, $c_{w,r}$ [-] is the wind pressure coefficient of the CSG roof vent. Eq. (4.63) assumes that the wind-induced and buoyancy-induced ventilation are independent. This equation can also be used to calculate the natural ventilation rate when only the side vent is open.

As recommended by Jingfu Zhang et al. (2022), the displacement ventilation model of CSG can follow the equation logic that the wind-induced ventilation considers the wind pressure coefficient difference between inlet and outlet vents. This assertion should be reasonable since the roof and side vents are located on a greenhouse roof facing south, and they are always in the same windward or leeward conditions, generating two offsetting wind effects on displacement ventilation (Chengwei Ma, Wang, Ding, Hou, & Han, 2008). The CSG climate model by F. He et al. (2009) adopted this assertion. However, the coefficient difference mentioned above is significantly influenced by wind directions despite its square root being fitted as a fixed value of 0.84 (Tian, 2021). This model does not involve wind direction inputs and cannot distinguish windward and leeward greenhouse sides. Thus, we describe the natural ventilation rate through both roof and side vents as follows (Dong, 2005; Kittas, Boulard, & Papadakis, 1997; PRC, 2018),

$$g_{vent,rs} = \frac{c_d}{A_{gro}} \cdot \left(\frac{{A_{vent,r,U}}^2 \cdot {A_{vent,s,U}}^2}{{A_{vent,r,U}}^2 + {A_{vent,s,U}}^2} \cdot \left(2 \cdot g \cdot \frac{X_t - T_{out}}{\frac{T_{out} + X_t}{2} + T_{0,K}} \cdot H_{vent,rs} \right) + \left(\frac{A_{vent,r,U} + A_{vent,s,U}}{2} \right)^2 \cdot c_{w,rs} \cdot {v_e}^2 \right)^{0.5} \quad (4.64)$$

$$\left(A_{vent,s} > 0\right) \ [\mathrm{m^3\ m^{-2}\ (gro)\ s^{-1}}]$$

where $A_{vent,s,U}$ [m^2] is the controlled opening area of the CSG side vent, $H_{vent,rs}$ [m] is the vertical distance between the mid-points of the CSG roof and side vents, $c_{w,rs}$ [-] is the global wind pressure coefficient of CSG vent openings.

$A_{vent,r,U}$ and $A_{vent,r,U}$ are described by the following equations,

$$A_{vent,r,U} = U_{vent,r} \cdot A_{vent,r} \ [\mathrm{m^2}] \quad (4.65)$$

$$A_{vent,s,U} = U_{vent,s} \cdot A_{vent,s} \ [\mathrm{m^2}] \quad (4.66)$$

where $A_{vent,r}$ and $A_{vent,s}$ [m^2] are the maximum opening areas of the CSG roof vent and side vent, respectively.

Air infiltration

The impact of air infiltration on greenhouse climate cannot be ignored. In well-insulated greenhouses, the heating demand resulting from cold air infiltration can account for up to 44% of the total demand (Weituo Sun et al., 2022). In closed CSGs, air infiltration along the edges of the soil and north wall results in the absorption of more than 30% of the solar energy

(Tong et al., 2018). The key to quantifying air exchange by infiltration lies in determining the air infiltration rate in units of h^{-1}. Tong, Che, Bai, and Yamaguchi (2008) used thermal balance method to calculate air infiltration rate in winter, revealing rate differences between daytime and nighttime, with rates of 0.28-2.31 h^{-1} during the day and 0.13-0.20 h^{-1} at night. Other researchers quoted by Tong et al. (2008) determined the infiltration rate to be 0.33-0.41 h^{-1} using the CO_2 gas tracing method and 0.96 h^{-1} by a simple method. Most current CSG climate models are developed and validated using these fixed air infiltration rates, which might be adjusted slightly based on greenhouse age and sealing performance. For instance, the value of the infiltration rate is set to be 0.8 in the model by Y. Zhang et al. (2020), 0.5 by Ahamed, Guo, and Tanino (2020), 0.33-0.41 by Meng et al. (2009), and 0.4 by Weituo Sun et al. (2022).

However, there is a linear dependency between air infiltration rate and wind velocity and temperature (Bakker et al., 1995). Ignoring these correlations might cause significant simulation errors and result in inefficient control. Thus, starting from the research of M S Ahamed et al. (2018), three models have described air exchange rate through infiltration that considers wind speed and temperature difference between indoor and outdoor air (R. Liu et al., 2021; J. Xiao et al., 2023), borrowing from the study of Jolliet, Danloy, Gay, Munday, and Reist (1991). Based on this air infiltration description, we introduce the control of the thermal blanket to modify the cover tightness. This gives rise to the following equation,

$$N_{inf} = \frac{3600}{V_{gh}} \cdot A_{cov} \cdot \eta_{inf} \cdot (1 - p_b \cdot U_b) \cdot \left({c_{w,cd}}^2 \cdot {v_e}^2 + {c_T}^2 \cdot (X_t - T_{out}) \right)^{0.5} \quad [h^{-1}] \tag{4.67}$$

where N_{inf} [h^{-1}] is the air infiltration rate of the CSG, V_{gh} [m^3] is the CSG volume, A_{cov} [m^2] is the surface area of the CSG cover or envelope, U_b [-] is the control of the position of the CSG thermal blanket, ranging from 0 to 1, c_T [m s^{-1} $K^{-1/2}$] is the temperature difference factor, η_{inf} [-] is the characterization of the tightness of the cover to air infiltration, and it takes 5×10^{-4} for well-maintained CSGs and 10×10^{-4} to 20×10^{-4} for leaky covers with cracks or holes, p_b

[-] is the reduction fraction of the external thermal blanket to η_{inf}.

Then the air exchange rate due to infiltration g_{inf} can be calculated by

$$g_{inf} = \frac{N_{inf} \cdot H_{gh}}{3600} \ [\mathrm{m^3\ m^{-2}\ s^{-1}}] \tag{4.68}$$

4.2.2.10 Crop activities

Crop photosynthesis and respiration

Crop photosynthesis assimilates CO_2 inside the greenhouse, while maintenance respiration releases CO_2 into the greenhouse air. These two crop growth activities influence the variation of CO_2 concentration inside CSGs. Few CSG climate models describe crop photosynthesis and respiration since they mainly focus on simulating light and thermal environments. Bi et al. (2010) developed a forecasting model of CO_2 concentration inside the CSG, describing crop photosynthesis and respiration based on the widely recognized crop models by Farquhar et al. (1980); Goudriaan and Van Laar (1994); Egbert Heuvelink (1996). However, the type of crop targeted by these referenced crop models is inconsistent with the cultivated lettuce crop in the model validation experiments performed by Bi et al. (2010). A greenhouse climate model with practical significance and precision should specify the crop when describing crop activities. This study aims to develop a climate model of the CSG for lettuce cultivation; thus, we adopt the photosynthesis and respiration sub-models from the developed lettuce growth model in Chapter 3, which the following equations can summarize,

$$A_C = f(LAI, X_t, X_h, X_c, I, T_{can}) \ [\mathrm{kg\ (CO_2)\ m^{-2}\ (gro)\ s^{-1}}] \tag{4.69}$$

$$R_d = f(X_d, T_{can}, \rho_c) \ [\mathrm{kg\ (CH_2O)\ m^{-2}\ (gro)\ s^{-1}}] \tag{4.70}$$

where A_C [kg (CO_2) m^{-2} (gro) s^{-1}] is the gross canopy assimilation rate, R_d [kg (CH_2O) m^{-2}

(gro) s^{-1}] is the crop maintenance respiration rate, LAI [m^2 (leaf) m^{-2} (gro)] is the leaf area index, ρ_c is plant density, plants m^{-2} (gro). See Chapter 3 for detail descriptions.

Since our lettuce growth model defaults to an effective cultivation area-based, instead of an arbitrary ground area-based, plant density, A_c and R_d cannot be directly coupled to the climate model. The crop photosynthesis and respiration at the whole greenhouse level should consider the ratio of the effective cultivated area to the indoor ground area.

$$A_{C,gh} = \frac{A_{cul}}{A_{gro}} \cdot A_C \ \ [\mathrm{kg\ (CO_2)\ m^{-2}\ (gro)\ s^{-1}}] \tag{4.71}$$

$$R_{d,gh} = \frac{A_{cul}}{A_{gro}} \cdot \frac{1}{c_\alpha} \cdot R_d \ \ [\mathrm{kg\ (CO_2)\ m^{-2}\ (gro)\ s^{-1}}] \tag{4.72}$$

where c_α [-] is the factor converts assimilated CO_2 into sugar equivalents in the photosynthesis process, A_{cul} [m^2] is the effective cultivated area of the greenhouse.

It should be noted that, in greenhouse climate models, the crop growth indicators, such as biomass and LAI based on the effective cultivated area, are the known model inputs. Certainly, the crop-related thermophysical states belong to the state variables of the climate model. Furthermore, canopy assimilation might be inhibited depending on the buffer storage. However, the buffer status cannot be measured, and thus, crop photosynthesis inhibition cannot be involved in the CSG climate model. This might lead to overestimating photosynthesis, further underestimating the CO_2 concentration inside the CSG. In addition, LAI based on the effective cultivated area should be used in simulating crop activities. However, to avoid differentiating between cultivated and non-cultivated areas in CSG climate modelling, which considers the CSG as a perfectly stirred tank, the model adopts an LAI at the whole greenhouse level to address the impact of crops.

$$LAI_{gh} = \frac{A_{cul}}{A_{gro}} \cdot LAI \ \ [\mathrm{m^2\ (leaf)\ m^{-2}\ (gro)}] \tag{4.73}$$

Crop transpiration

A wide range of methods to quantify greenhouse crop transpiration have been developed for irrigation scheduling and greenhouse climate control (Katsoulas & Stanghellini, 2019). The description of crop transpiration in most CSG climate models, such as the models by F. He et al. (2009); R. Liu et al. (2021), is based on the Penman-Monteith formula (Monteith, 1965). The Penman-Monteith formula describes the latent heat of evaporation from a leaf and is primarily used for predicting evapotranspiration of crops grown in open field conditions (Katzin et al., 2022; Villarreal-Guerrero et al., 2012). Stangheilini (1987) optimised the Penman-Monteith equation for greenhouse crops, including adding a factor of leaf area index, revising the calculation method for aerodynamic conductance, and linking stomatal conductance with all four greenhouse climate attributes. Compared with the Penman-Monteith model, the crop transpiration model by Stangheilini (1987) can have higher prediction accuracy and better overall performance in cases of greenhouse production (Villarreal-Guerrero et al., 2012). Thus, the Stangheilini model is utilized in this CSG climate model, which remains consistent with our crop model descriptions. The crop transpiration rate E_c [kg m^{-2} s^{-1}] is described by,

$$E_c = \frac{\Delta \cdot R_n + 2 \cdot LAI \cdot \rho_a \cdot c_{p,a} \cdot e_{c,a} \,/\, r_{bv}}{\lambda_v \cdot \left(\Delta + \gamma \cdot (1 + r_{sv} \,/\, r_{bv})\right)} \ \text{[kg m}^{-2}\text{ (gro) s}^{-1}\text{]} \qquad (4.74)$$

where Δ [Pa °C^{-1}] is the slope of the saturation curve of the psychrometric chart, R_n [W m^{-2}] is the net radiation of the crop, $e_{c,a}$ [Pa] is leaf to air vapour pressure difference, equal to vapour deficit of indoor air, r_{bv} [s m^{-1}] is boundary layer resistance to diffusion of H_2O, r_{sv} [s m^{-1}] is the stomatal resistance to diffusion of H_2O.

The two air temperature dependency parameters Δ and λ_v are described by the following formulas (Acquah et al., 2018; F. He et al., 2009; Villarreal-Guerrero et al., 2012),

$$\Delta = 41.45 \cdot e^{0.061 \cdot X_t} \ [\text{Pa °C}^{-1}] \tag{4.75}$$

$$\lambda_v = 1000 \cdot (2500.8 - 2.3668 \cdot X_t) \ [\text{J kg}^{-1}] \tag{4.76}$$

The net radiation of the crop R_n is the balance of intercepted and reflected solar radiation plus the balance of incoming and outgoing long-wave radiation. To distinguish it from the absorbed shortwave radiation by the canopy I_{can} defined in the lettuce growth model, R_n is described by (Stanghellini et al., 2019),

$$R_n = 0.86 \cdot (1 - e^{-0.7 \cdot LAI}) \cdot I \ [\text{W m}^{-2}] \tag{4.77}$$

The descriptions of stomatal and boundary layer resistances to vapour diffusion are derived from the lettuce growth model and the research of (Jarvis, 1976; Stangheilini, 1987; Van Ooteghem, 2010),

$$r_{sv} = r_{H2O,min} \cdot f_{I,s} \cdot f_{Tcan,s} \cdot f_{Xc,s} \cdot f_{Xh,s} \tag{4.78}$$

$$r_{bv} = {Le_v}^{0.67} \cdot r_{bh} \tag{4.79}$$

$$r_{bh} = \frac{1174 \cdot {l_f}^{0.5}}{\left(l_f \cdot |T_{can} - X_t| + 207 \cdot {v_a}^2\right)^{0.25}} \tag{4.80}$$

where $r_{H2O,min}$ [s m^{-1}] is the minimum possible internal crop resistance to H_2O, r_{bh} [s m^{-1}] is the boundary layer resistance or aerodynamic resistance to convective heat transfer, Le_v [-] is the Lewis number for water vapour in air. ${Le_v}^{0.67}$ represents the ratio of boundary layer resistance for H_2O diffusion to that for forced heat convection. Detailed definitions of all other parameters and auxiliary variables of Eq. (4.78) and Eq. (4.80) can be found in the lettuce growth model, which are not reiterated here.

Similarly, the crop transpiration rate at the whole greenhouse level $E_{c,gh}$ is described by,

$$E_{c,gh} = \frac{A_{cul}}{A_{gro}} \cdot E_c \ \ [\text{kg m}^{-2}\ \text{(gro)}\ \text{s}^{-1}] \tag{4.81}$$

4.2.2.11 Soil activities

Soil microbial respiration

CO_2 is released from the soil through soil respiration, which primarily includes microbial respiration and root respiration. Rastogi, Singh, and Pathak (2002) summarised that factors such as soil temperature, moisture, organic matter content, and fertiliser application influence CO_2 production and emission from the soil. While the crop growth model has covered root respiration, this description will only focus on soil microbial respiration rate R_{sm}, adapted from an empirical formula (PRC, 2018; Q. Yang, Wei, & Yu, 2004).

$$R_{sm} = 0.5 \cdot \lambda_{sm} \cdot R_{so,0} \cdot Q_{10,Rso}^{\frac{T_{gro}}{10}} \ \ [\text{kg m}^{-2}\ \text{(gro)}\ \text{s}^{-1}] \tag{4.82}$$

where R_{sm} [kg (CO_2) m^{-2} (gro) s^{-1}] is the soil microbial respiration rate inside the greenhouse, $R_{so,0}$ [kg (CO_2) m^{-2} (gro) s^{-1}] is the soil respiration rate at a reference temperature of 0 °C, $Q_{10,Rso}$ [-] is the Q_{10} value for soil respiration, λ_{sm} [-] is the correction factor for soil microbial respiration, which can be different for general soils and organic matter soils. The coefficient of 0.5 indicates that R_{sm} is assumed to contribute half of the soil respiration rate (Zhu, Cai, Song, & Chen, 2017). For bare soil conditions, 90% of the soil CO_2 is produced within a soil depth of 50 mm (X. Xiao, Kuang, Sauer, Heitman, & Horton, 2015). Therefore, the temperature of indoor ground layer is selected to calculate the soil respiration rate. In addition, if the ground inside the CSG is the hardened ground or covered with the ground fabric, soil microbial respiration will be negligible.

Soil evaporation

The soil evaporation process is influenced by soil moisture content, surrounding environment, as well as soil structure and physicochemical properties (Tang, Shi, & Gu, 2011). In greenhouse climate models, the term soil evaporation is often neglected due to the hardening or covering of greenhouse floors (Katzin et al., 2020) or for model simplification (T Boulard & Baille, 1993). Most CSGs employ soil cultivation. Soil evaporation cannot be ignored for accurately simulating indoor humidity changes, particularly during stages with low leaf area index. Existing CSG climate models vary in their descriptions of soil evaporation. Z. Guo and Yu (2012) addressed soil surface evaporation as a certain proportion of crop transpiration, which depends on the leaf area index and time of day, considering that transmitted solar radiation is firstly intercepted by the canopy and then the remaining reaches the ground. Bi and Wu (2012) and Deng (2021) determined soil evaporation based on greenhouse climate and soil thermal properties. F. He et al. (2009) further introduced a coefficient to characterize the level of soil surface moisture. Sufficient water and nutrients are supplied in both practical greenhouse production and assumptions for simulating the greenhouse crop production process. Soil water content in the 0-100 mm depth soil layer ranges from 17% to 28% during irrigation cycles (J. Li, Wang, Su, & Ji, 2016); thus, the indoor soil surface can be considered moist instead of as open water. Based on the research by F. He et al. (2009) and Tiwari (2003), we integrate the effects of greenhouse climate and specific moisture levels of greenhouse soil on evaporation, resulting in the following equation:

$$E_{so} = \beta_{sml} \cdot \frac{\Delta \cdot I_{gro} + h_{air\_gro} \cdot e_{s,air} \cdot (1 - X_h)}{\lambda_v \cdot (\Delta + \gamma)} \ [\text{kg m}^{-2}\ (\text{gro})\ \text{s}^{-1}] \qquad (4.83)$$

where E_{so} [kg m^{-2} s^{-1}] is the soil evaporation rate inside the greenhouse, β_{sml} [-] is the coefficient to characterize the level of soil surface moisture inside CSGs, h_{air_gro} [W m^{-2} °C^{-1}] is the convective heat transfer coefficient between greenhouse air and ground.

4.2.3 Model parameterization

The greenhouse structure is the input of the CSG climate model. However, structural parameters are constant for a given CSG. In this study, the model parameters are divided into two categories: general parameters and those dependent on the simulated CSG. Before using this model, these parameters need to be determined. Table 4.1 provides the values and sources for the general parameters of the CSG climate model. Table 4.2 presents the CSG-dependent parameters, including information on defining surfaces and layers. Next, the determination of some of the model parameters will be clarified.

Table 4.1 General parameters of the CSG climate model

Parameter	value	unit	source
c_d	0.65	-	(Dong, 2005; Fang et al., 2016)
$c_{p,a}$	1005	J kg^{-1} °C^{-1}	physical constant
$c_{p,L}$	4.0×10^{3}	J kg^{-1} °C^{-1}	estimated from measurement
c_T	0.16	m s^{-1} $K^{-1/2}$	(M S Ahamed et al., 2018)
$c_{w,cd}$	0.26	-	(Dong, 2005; R. Liu et al., 2021; PRC, 2018)
$c_{w,r}$	0.1	-	estimated from (Fang et al., 2016)
$c_{w,rs}$	0.16	-	estimated from (Dong, 2005; R. Liu et al., 2021; PRC, 2018)
c_α	0.68	-	physical constant
$c_{\delta\rho,1}$	0.076	plants m^{-2} (leaf)	Calibration
$c_{\delta\rho,2}$	0.924	kg m^{-2} (leaf)	Calibration
g	9.8	m s^{-2}	physical constant
k_I	0.48	-	(Van Ooteghem, 2010)
k_R	0.94	-	(De Zwart, 1996)
Le_v	0.89	-	(Monteith & Unsworth, 2013)
M_v	18×10^{-3}	kg mol^{-1}	physical constant
p_b	0.7	-	estimated from (Weituo Sun et al., 2022)
$Q_{10,Rso}$	3	-	(Bi et al., 2010)
R_g	8.314	J mol^{-1} K^{-1}	physical constant
$r_{H2O,min}$	82	s m^{-1}	(Stangheilini, 1987)
$R_{so,0}$	0.01×10^{-6}	kg (CO_2) m^{-2} (gro) s^{-1}	estimated from (Bi et al., 2010; Dong, 2005; PRC, 2018; Q. Yang et al., 2004)
$T_{0,K}$	273.15	K	physical constant
$T_{so,cs}$	15	°C	(M S Ahamed et al., 2018; Weituo Sun et al., 2022)

γ	66	Pa °C^{-1}	physical constant
κ_{ice}	0.3	-	estimated from analysis
$\lambda_{v,d}$	2.83 ×10^{6}	J kg^{-1}	(Yau & Rogers, 1996)
π_a	1	-	(Kalogirou, 2022)
ρ_a	1.20	kg m^{-3}	physical constant
σ	5.67×10^{-8}	W m^{-2} K^{-4}	physical constant
σ_{CO2}	1.83×10^{-6}	kg m^{-3} (μmol mol^{-1})$^{-1}$	(Stanghellini et al., 2019)
τ_{ice}	0.6	-	estimated from analysis
δ_{ice}	0.0001	m	estimated from analysis
ε_{ice}	1	-	physical constant
λ_{ice}	2.2	W m^{-1} °C^{-1}	physical constant
ψ_{ice}	0	-	physical constant
α_{can}	0.78	-	(Goudriaan & Van Laar, 1994)
ε_{can}	1.0	-	(Stangheilini, 1987)

Table 4.2 Greenhouse dependent parameters of the CSG climate model

Parameter	value		unit
	CSG for Exp_1	CSG for Exp_3	
Greenhouse profile			
L_{gro}	7.500	7.550	m
H_{gh}	2.350	3.110	m
A_{gro}	585.0	651.6	m^2
A_{cov}	874.4	1099.9	m^2
V_{gh}	1374.8	2026.4	m^3
L_{c1}	3.078	4.307	m
L_{c2}	7.816	8.143	m
$L_{sr,c}$	7.442	7.458	m
θ_{ghz}	5 ° west of south	5 ° west of south	°
φ	39.62	39.62	°
North wall			
L_{nw}	2.200	3.050	m
θ_{nw}	90	90	°
$\delta_{nw,in}$	0.01	0.01	m
$\alpha_{nw,in}$	0.75	0.75	-
$\varepsilon_{nw,in}$	0.94	0.94	-
$\lambda_{nw,in}$	0.93	0.93	W m^{-1} °C^{-1}
$\rho_{nw,in}$	2100	2100	kg m^{-3}
$c_{p,nw,in}$	900	900	J kg^{-1} °C^{-1}

$\delta_{nw,e}$	0.05	0.1	m
$\varepsilon_{nw,e}$	0.94	0.94	-
$\lambda_{nw,e}$	0.40	0.072	W m^{-1} $°C^{-1}$
$\rho_{nw,e}$	1220	540	kg m^{-3}
$c_{p,nw,e}$	900	916	J kg^{-1} $°C^{-1}$
$\delta_{nw(j)}$	$\delta_{nw(1)}$ - $\delta_{nw(3)}$: 0.123	$\delta_{nw(1)}$ - $\delta_{nw(3)}$: 0.135	m
$\lambda_{nw(j)}$	$\lambda_{nw(1)}$ - $\lambda_{nw(3)}$: 0.35	$\lambda_{nw(1)}$ - $\lambda_{nw(3)}$: 0.35	W m^{-1} $°C^{-1}$
$\rho_{nw(j)}$	$\rho_{nw(1)}$ - $\rho_{nw(3)}$: 1000	$\rho_{nw(1)}$ - $\rho_{nw(3)}$: 1000	kg m^{-3}
$c_{p,nw(j)}$	$c_{p,nw(1)}$ - $c_{p,nw(3)}$: 900	$c_{p,nw(1)}$ - $c_{p,nw(3)}$: 900	J kg^{-1} $°C^{-1}$
North roof			
L_{nr}	1.055	1.690	m
θ_{nr}	49	39	°
$\alpha_{nr,in}$	0.75	0.75	-
$\varepsilon_{nr,in}$	0.94	0.94	-
$\varepsilon_{nr,e}$	0.94	0.94	-
$\delta_{nr(i)}$	$\delta_{nr\,(1)}$, $\delta_{nr\,(5)}$: 0.002	$\delta_{nr\,(1)}$, $\delta_{nr\,(5)}$: 0.002	m
	$\delta_{nr\,(2)}$, $\delta_{nr\,(4)}$: 0.05	$\delta_{nr\,(2)}$, $\delta_{nr\,(4)}$: 0.05	
	$\delta_{nr\,(3)}$: 0.08	$\delta_{nr\,(3)}$: 0.08	
$\lambda_{nr(i)}$	$\lambda_{nr\,(1)}$, $\lambda_{nr\,(5)}$: 0.93	$\lambda_{nr\,(1)}$, $\lambda_{nr\,(5)}$: 0.93	W m^{-1} $°C^{-1}$
	$\lambda_{nr\,(2)}$, $\lambda_{nr\,(4)}$: 0.04	$\lambda_{nr\,(2)}$, $\lambda_{nr\,(4)}$: 0.04	
	$\lambda_{nr\,(3)}$: 1.20	$\lambda_{nr\,(3)}$: 1.20	
Indoor floor and soil			
λ_{sm}	1.0	1.0	-
β_{sml}	0.45	0.65	-
δ_{gro}	0.01	0.01	m
α_{gro}	0.92	0.92	-
ε_{gro}	0.96	0.96	-
λ_{gro}	1.0	1.0	W m^{-1} $°C^{-1}$
ρ_{gro}	1400	1400	kg m^{-3}
$c_{p,gro}$	1500	1500	J kg^{-1} $°C^{-1}$
$\delta_{so,cs}$	0.001	0.001	m
$\lambda_{so,cs}$	1.0	1.0	W m^{-1} $°C^{-1}$
$\delta_{so(i)}$	$\delta_{so(1)} - \delta_{so(2)}$: 0.245	$\delta_{so(1)} - \delta_{so(2)}$: 0.245	m
	$\delta_{so(3)}$: 0.5	$\delta_{so(3)}$: 0.5	
	$\delta_{so(4)}$: 2.0	$\delta_{so(4)}$: 2.0	
$\lambda_{so(i)}$	1.0	1.0	W m^{-1} $°C^{-1}$
$\rho_{so(i)}$	1400	1400	kg m^{-3}
$c_{p,so(i)}$	1500	1500	J kg^{-1} $°C^{-1}$
South roof			
L_{sr}	7.955	8.005	m

θ_{sr}	24	33	°
π_{tc}	1.5	1.5	-
δ_{tc}	0.08×10^{-3}	0.08×10^{-3}	m
ε_{tc}	0.15	0.15	-
λ_{tc}	0.13	0.13	W m^{-1} $°C^{-1}$
τ_{tc}	0.80	0.80	-
κ_{tc}	0.05	0.05	-
ψ_{tc}	0.75	0.75	-
$\alpha_{b,o}$	/	0.35	-
$\varepsilon_{b,o}$	/	0.85	-
δ_b	/	0.021	m
λ_b	/	0.04	W m^{-1} $°C^{-1}$
Vents			
$A_{vent,r}$	31.2	34.5	m^2
$A_{vent,s}$	78.0	86.3	m^2
$H_{vent,r}$	0.018	0.049	m
$H_{vent,rs}$	2.348	3.366	m
ε_{inss}	0.54	0.54	-
η_{inf}	15×10^{-4}	5×10^{-4}	-
Crops			
A_{cul}	261.4	368.8	m^2
ρ_c	11.71	11.52	plants m^{-2} (gro)

4.2.3.1 General model parameters

For simplification in this model, both air density (ρ_a) and specific heat capacity of air at constant pressure ($c_{p,a}$) were assumed to be constant by assuming at a temperature of 20 °C and under a standard atmospheric pressure of 101.325 kPa. Therefore, the ρ_a was taken as 1.20 kg m^{-3} and $c_{p,a}$ was taken as 1005 J kg^{-1} $°C^{-1}$. The latent heat for water vapour deposition ($\lambda_{v,d}$), which is almost constant in the temperature range from -40 to 0 °C (Yau & Rogers, 1996), took the value of 2.83×10^6 J kg^{-1}.

The ice layer that forms on the inner side of the transparent covering is rough and not entirely transparent. The incident solar radiation is scattered and deflected in many directions, leading to an increase in reflectivity and a decrease in transmissivity. Thus, the transmissivity of the ice layer to shortwave radiation from the transparent covering (τ_{ice}) was assumed to

be 0.6, and the reflectivity of the ice layer to shortwave radiation from the transparent covering (κ_{ice}) was assumed to be 0.3 in this model.

For calculating the natural ventilation rate through both roof and side vents, the global wind pressure coefficient of CSG vent openings ($c_{w,rs}$) was estimated to be 0.16 by ${c_{w,cd}}^2/{c_d}^2$, where $c_{w,cd} = 0.26$ is the combined wind pressure coefficient for empirically describing wind effect ventilation rate (Dong, 2005; R. Liu et al., 2021; PRC, 2018).

In the context of CSG production, the soil respiration rate at a reference temperature of 0 °C ($R_{so,0}$) ranges from 0.01 to 0.04×10^{-6} kg (CO_2) m^{-2} (gro) s^{-1} (Bi et al., 2010; Dong, 2005; PRC, 2018; Q. Yang et al., 2004). In this model, $R_{so,0}$ was set at 0.01×10^{-6} kg (CO_2) m^{-2} (gro) s^{-1} after considering the introduction of the correction factor for soil microbial respiration (λ_{sm}).

The average water content of the lettuce heads was found to be 93.8% across all validation experiments. Hence, it is reasonable to assume that the specific heat capacity of the lettuce crop leaves ($c_{p,L}$) is close to that of water, estimated at 4.0×10^3 J kg^{-1} $°C^{-1}$ for this study. While the available data do not allow for determining the average thickness of the crop leaves (δ_L) and the density of crop leaves (ρ_L) independently, they do enable the calculation of their product, $\delta_L \cdot \rho_L$, which denotes the fresh leaf weight per unit leaf area. This value can be determined using the data of shoot fresh weight and leaf area at an individual plant level. However, it is not constant and exhibits a logarithmic relationship with the individual plant dry weight (Figure 4.2). Therefore, $\delta_L \cdot \rho_L$ was calculated by the following fitting equation,

$$\delta_L \cdot \rho_L = c_{\delta\rho,1} \cdot ln\left(\frac{X_d}{\rho_c}\right) + c_{\delta\rho,2} \quad [\text{kg m}^{-2}\text{ (leaf)}] \tag{4.84}$$

where $c_{\delta\rho,1}$ [plants m^{-2} (leaf)] and $c_{\delta\rho,2}$ [kg m^{-2} (leaf)] are fit coefficients for describing the fresh leaf weight per unit leaf area. They are respectively fitted to be 0.076 plants m^{-2} (leaf) and 0.924 kg m^{-2} (leaf), with $R^2 = 0.734$ and $RMSE = 0.074$ kg m^{-2} (leaf).

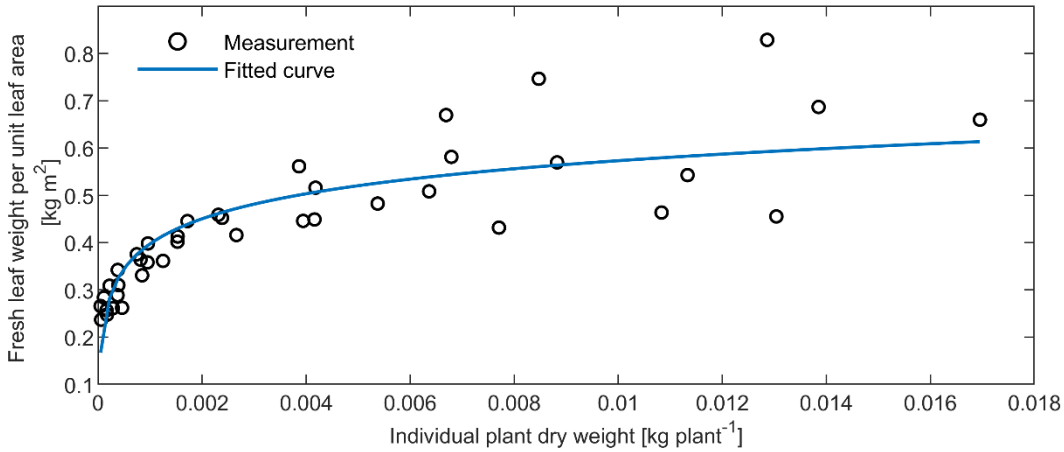

Figure 4.2 Variation of the fresh leaf weight per unit leaf area along with the individual plant dry weight for the lettuce crop. R^2 = 0.734, *RMSE* = 0.074 kg m^{-2} (leaf).

4.2.3.2 Greenhouse dependent parameters

The CSGs in both experiments were equipped with a 40-mesh insect screen with a wire diameter of 0.17 mm at the vents. The porosity of the insect screen (ε_{inss}) was estimated to be 54%. The CSG in Exp_3 was well-maintained and used for overwinter production of vegetables, and its characterization of the tightness of the cover to air infiltration (η_{inf}) was set to be 5×10^{-4}. In comparison, η_{inf} of the CSG in Exp_1 was set to be 15×10^{-4} due to its leaky covers. To facilitate the calculation of the heat conduction processes of the north roof, layering was also performed for north roof but without any thickness limitations.

In the absence of specific data, τ_{tc} can take 80-90% for new plastic films and 55-75% for old and dirty films; κ_{tc} can take 5% for new plastic films and 10-25% for old and dirty films. The reduction in transmissivity is primarily attributed to an increase in absorption for aged films, while for dirty films, it is more likely due to an increase in reflection and scattering.

An assumption underlying this model is that the water supply is sufficient for crop growth, and therefore, the soil surface is considered moist. According to the research by (F. He et al.,

2009), the coefficient to characterize the level of soil surface moisture inside CSGs (β_{sml}) was assigned a value of 0.45 in Exp_1, and 0.65 in Exp_3.

4.3 Results and discussion

Figure 4.3 to Figure 4.8 comprehensively present the inputs of the CSG climate model, including outdoor weather, greenhouse controls and crop states, for model validation, alongside the dynamic curves of the simulated and measured indoor climates. The assessment of model performance includes qualitatively comparing the dynamic trends of simulated and measured climate values, and quantitatively evaluating simulations across the entire crop growth cycle using *RMSE* and *RRMSE*. The validation data for the model were derived from experiments Exp_1 and Exp_3, covering two CSGs with different structural parameters and involving both warm and cold seasons. During the two experiments, the lettuce crop was cultivated in soil inside CSGs, with the growth periods being 35 and 45 days, respectively. The model simulations spanned these growth periods. The differential equations were solved using the ODE45 solver in MATLAB, in which the ‘fsolve’ function was employed to address certain energy balance equations.

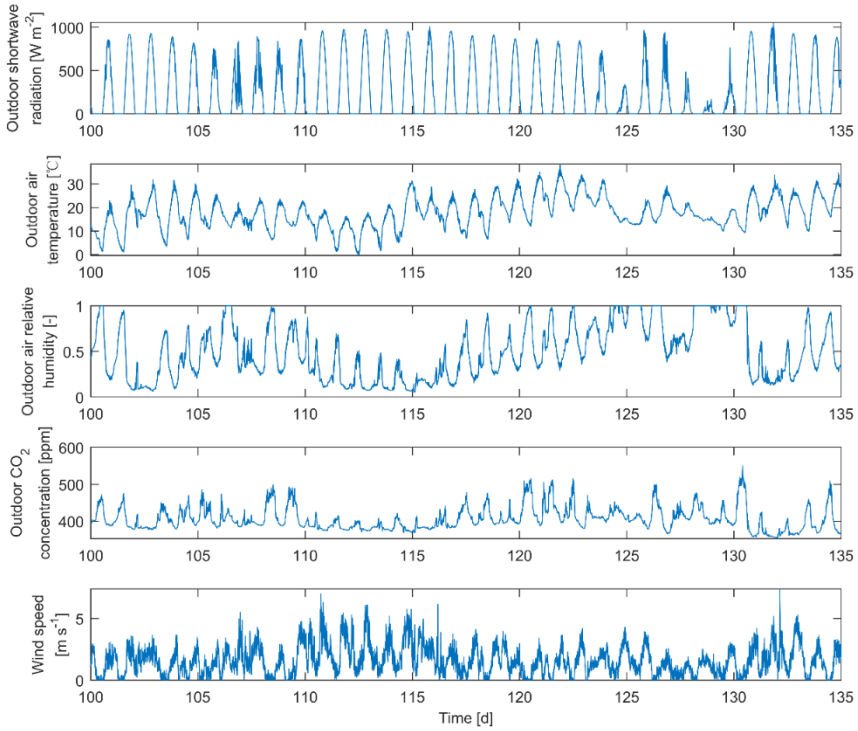

Figure 4.3 Outdoor climate used as model inputs in Exp_1 (17:00, 9 April 2020 – 17:00, 14 May 2020).

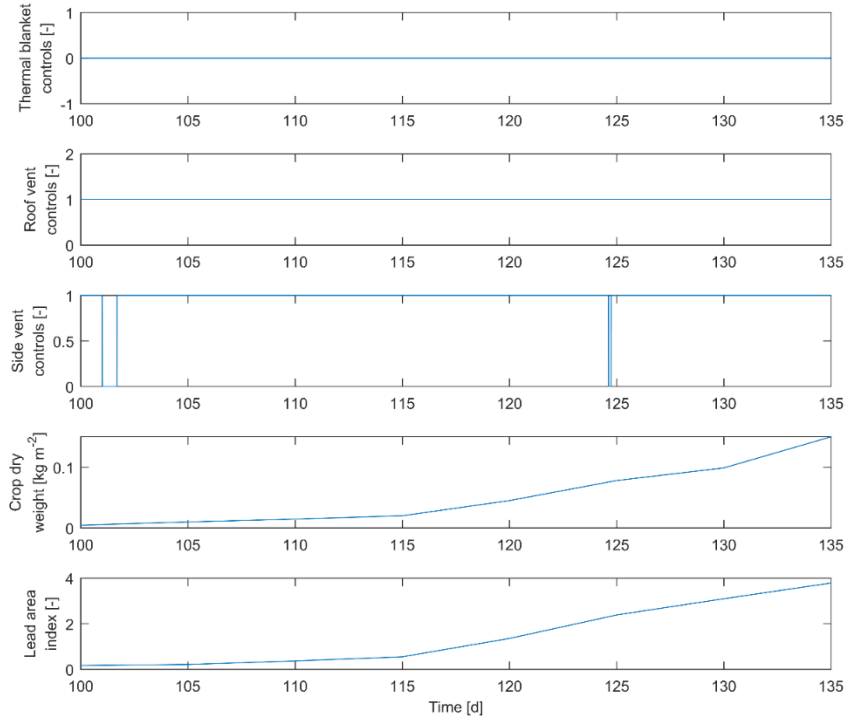

Figure 4.4 Greenhouse controls and crop states as model inputs in Exp_1 (17:00, 9 April 2020 – 17:00, 14 May 2020).

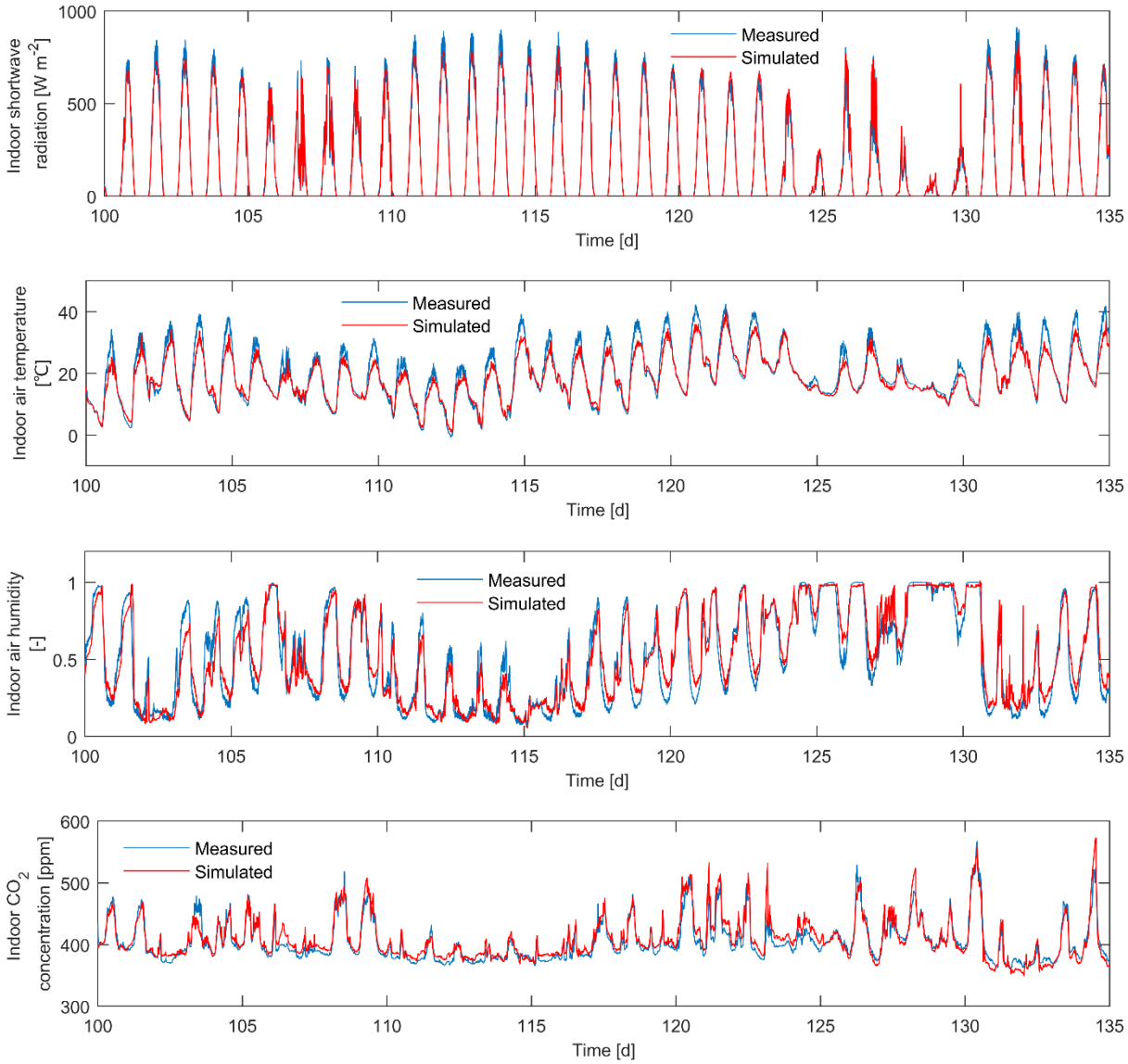

Figure 4.5 Comparison between the simulated and measured climate trajectories inside the CSG during Exp_1 (17:00, 9 April 2020 – 17:00, 14 May 2020). *RMSE* = 38.8 W m^{-2} and *RRMSE* = 12.6% for prediction of shortwave radiation at the top of the canopy. *RMSE* = 2.9 °C and *RRMSE* = 14.5% for prediction of indoor air temperature. *RMSE* = 0.09 and *RRMSE* = 17.7% for prediction of indoor relative humidity. *RMSE* = 12 ppm and *RRMSE* = 3.0% for prediction of indoor CO_2 concentration.

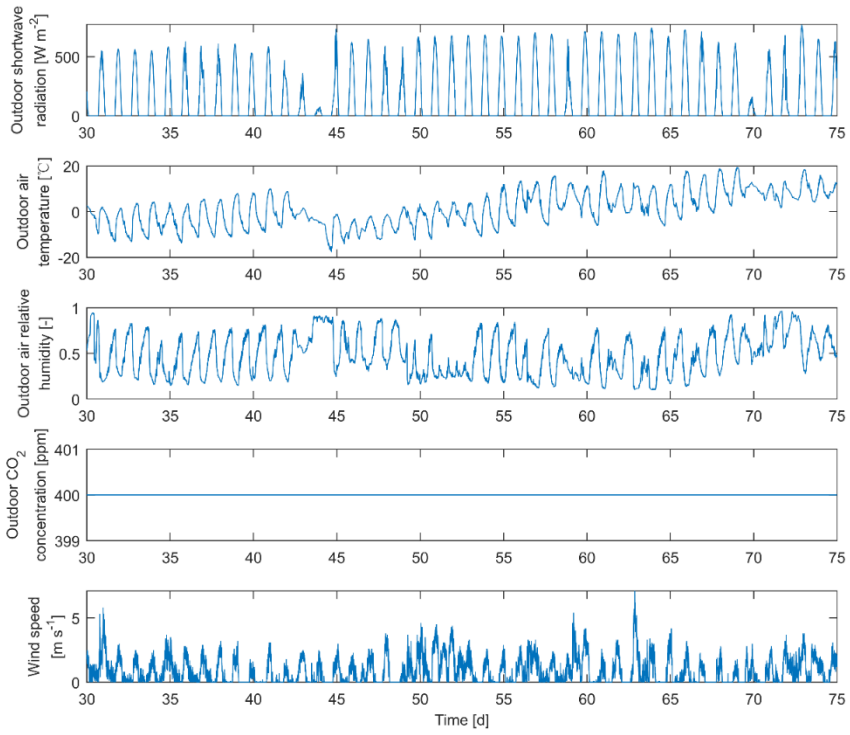

Figure 4.6 Outdoor climate used as model inputs in Exp_3 (15:00, 30 January 2022 – 15:00, 16 March 2022).

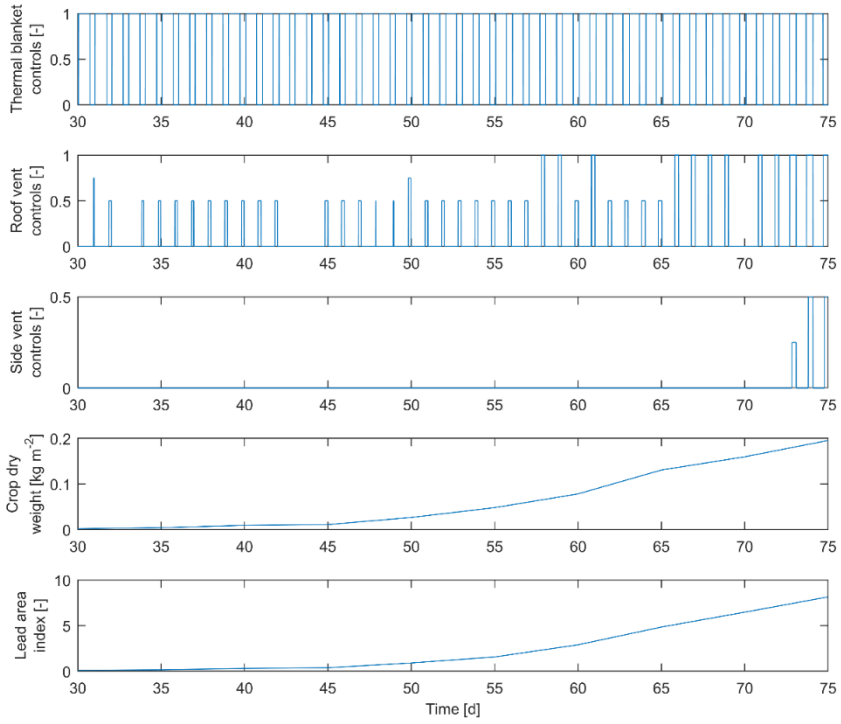

Figure 4.7 Greenhouse controls and crop states as model inputs in Exp_3 (15:00, 30 January 2022 – 15:00, 16 March 2022).

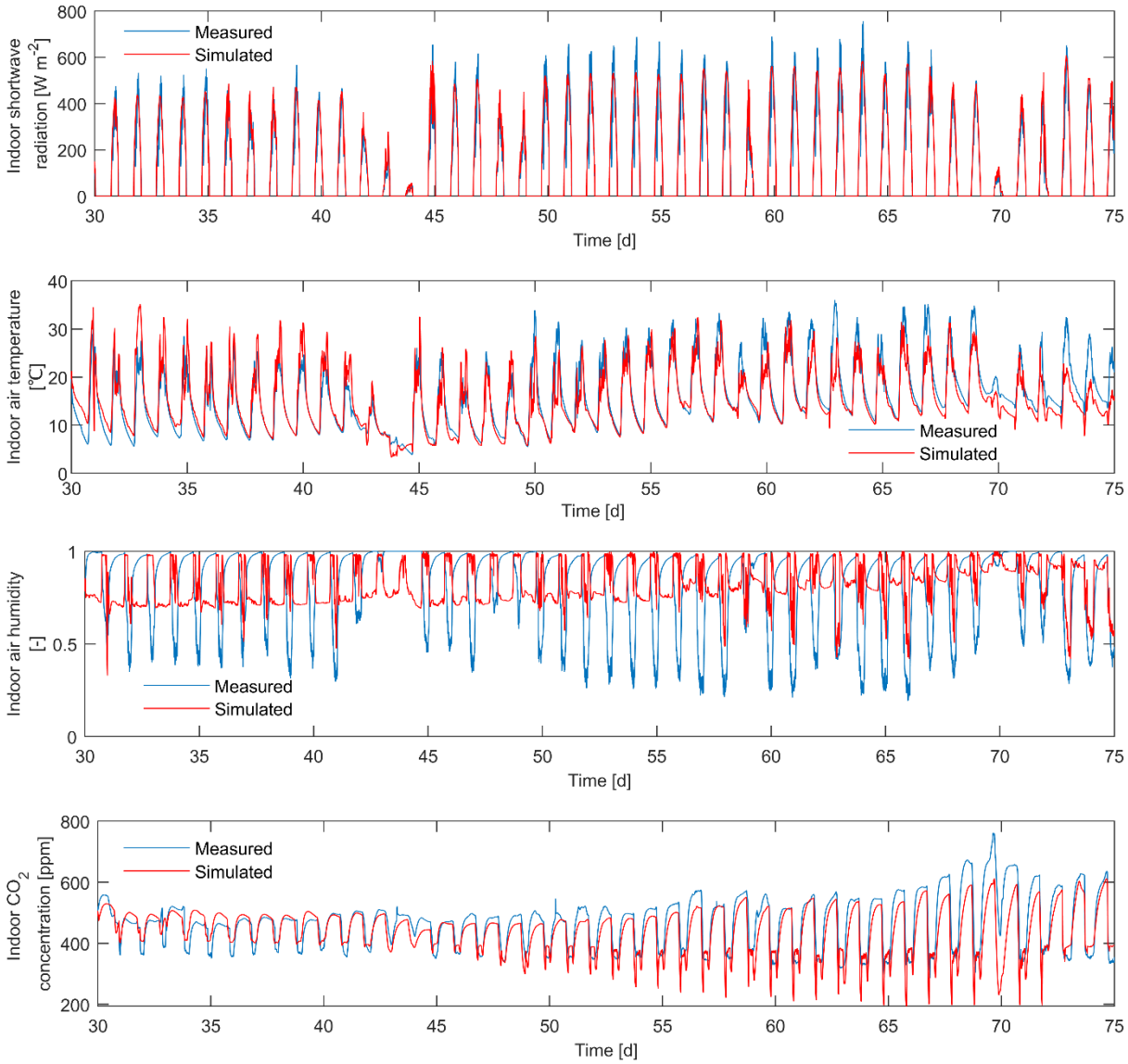

Figure 4.8 Comparison between the simulated and measured climate trajectories inside the CSG during Exp_3 (15:00, 30 January 2022 – 15:00, 16 March 2022). *RMSE* = 64.9W m^{-2} and *RRMSE* = 23.0% for prediction of shortwave radiation at the top of the canopy. *RMSE* = 3.3 ℃ and *RRMSE* = 21.1% for prediction of indoor air temperature. *RMSE* = 0.25 and *RRMSE* = 30.8% for prediction of indoor relative humidity. *RMSE* = 58 ppm and RRMSE = 12.4% for prediction of indoor CO_2 concentration.

4.3.1 Performance in predicting shortwave radiation

The horizontal solar radiation at the top of the canopy was selected to represent the radiation condition inside the CSG since the crop model takes it as a model input. It can be directly used to calculate the shortwave radiation absorbed by the canopy and indoor ground, as well as by internal surfaces of the CSG envelop through trigonometric transformation. Also, the validation experiments measured this value located at the mid-span of the greenhouse. As illustrated in Figure 4.5 and Figure 4.8, the simulated shortwave radiations closely agreed with the measured values across both validation experiments. Depending on the specific experiment and the time of day, the model exhibited different estimations for predicting shortwave radiation at the top of the canopy inside CSGs. Overall, the model tended to underestimate shortwave radiation around noon. Throughout the entire growth cycles of the lettuce crop in Exp_1 and Exp_3, the radiation predictions yielded *RMSE* of 38.8 and 64.9 W m^{-2} and *RRMSE* of 12.6% and 23.0%, respectively, demonstrating good model performance.

In Exp_1 and Exp_3, the average difference between simulated and measured indoor radiations during the daytime was respectively 1.0 and 21.8 W m^{-2}, indicating minimal discrepancies. The model tended to underestimate shortwave radiation around noon, which was consistent with the solar radiation model by H. Xu et al. (2019). This underestimation might be attributed to the simplification of the CSG south roof and the lack of distinction between direct and diffuse shortwave radiations. Firstly, the model simplifies the curved south roof to an inclined plane with a fixed slope angle. Compared to the time near sunrise and sunset, the solar rays reaching the top of the canopy around noon have a smaller incidence angle and higher transmissivity for the south roof (Figure 4.9), suggesting that the model should overestimate the radiation during this period. However, the actual south roof surface is curved, with its tangent angle increasing from top to bottom of the roof. As the solar altitude is low around noon during winter days, the incident solar radiation at the measurement point might pass through a point on the south roof surface with a greater slope angle than that of the inclined plane. This leads to a smaller actual incident angle and,

consequently, a higher transmittance and indoor radiation than the simulated values. It is important to note that the estimation errors around noon caused by the roof simplification have spatial variability, presenting both overestimations and underestimations at the same time. Secondly, the model does not differentiate between direct and diffuse shortwave radiation, and it analyses global solar radiation solely based on the optical properties of the direct part. A study conducted by Huang et al. (2020) found that the ability of transparent material to transmit diffused radiation is related to the angle of its surface slope. As the angle increases from 0 to 90 °, the transmissivity decreases gradually. Furthermore, in different seasons, the equivalent transmissivity of a typical south roof transparent covering to scattered radiation is much greater than for beam radiation at solar noon, though this difference was also reported to be only 2% (Han et al., 2014). As a result, the actual normal incident solar radiation, which includes diffuse components, has a considerable potential to have higher transmissivity than that of the single direct radiation assumed in the model. These may cause the model to underestimate the indoor radiation.

The transmissivity of the south roof to shortwave radiation decreases with an increase in the solar incidence angle for the south roof, and the rate of decrease gradually accelerates (Figure 4.9). According to the model description, for a given CSG, its base transmittance, south roof angle, and the greenhouse azimuth are fixed, with the local latitude also known. The transmissivity of the south roof transparent covering depends on the incidence angle, which in turn is determined by the solar altitude and azimuth angles, ultimately depending only on the day of the year and the time of day. On 21 February 2022, which was the 52nd day of the year, the solar altitude angle reached its maximum value of 39.2 ° at local solar noon, with an azimuth angle of 0 ° (Figure 4.9b). Due to the presence of the greenhouse azimuth angle (5 ° west of south), the minimum incidence angle for the south roof (17.9 °) and the maximum transmissivity (0.78) were delayed by the solar hour angle of 2.65 ° and by the period of 636 s. The thermal blanket was rolled up after sunrise and covered before sunset. The north wall was slightly shaded by the north roof around noon, with a duration of 0.6 h and a maximum shading ratio of 0.002. However, as the solar altitude angle increased, the issue of shading became increasingly severe, with a duration of 5.0 h and a maximum

shading ratio of 0.33 on 1 May 2020 (Figure 4.9a), which was the 122nd day of the year. In the two experiments, the days with shading respectively accounted for 100% and 53% of each crop production period (Figure 4.10), indicating that shading for the north wall cannot be ignored. Furthermore, as the available solar altitude angle increases, both the maximum shading ratio and the duration of shading throughout the day increase.

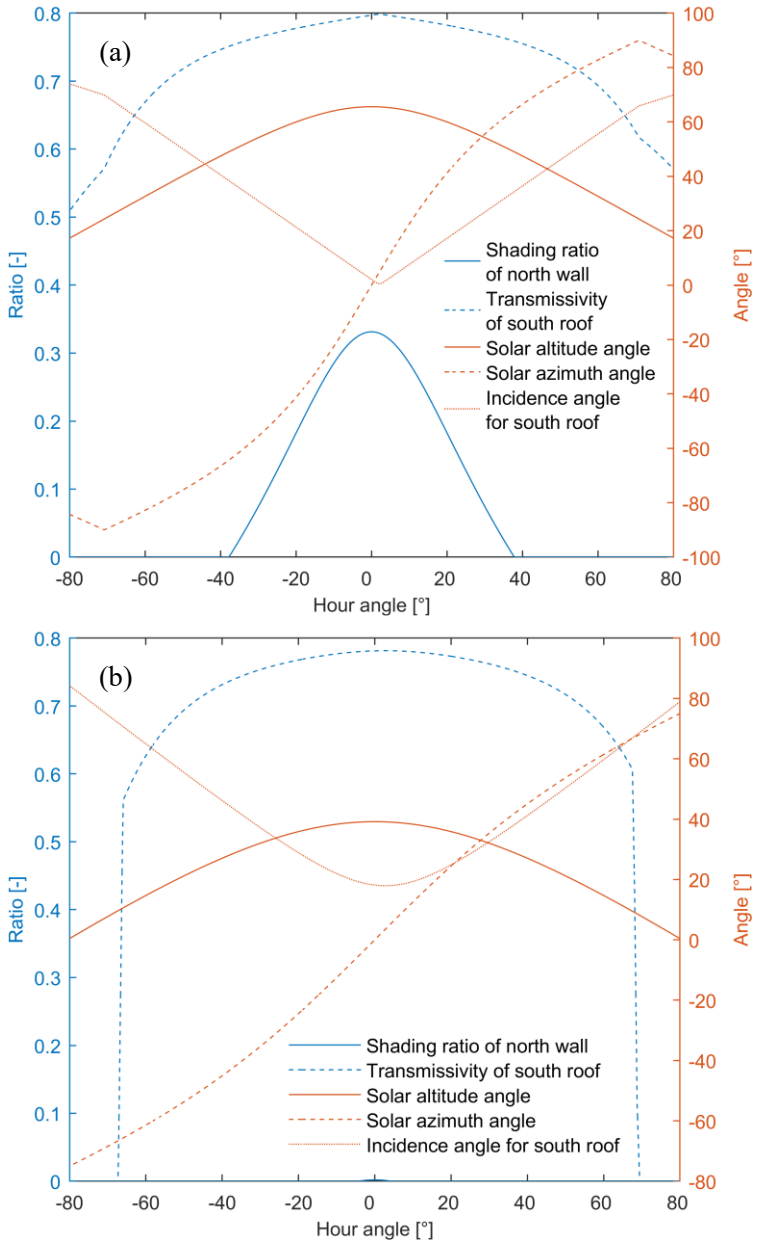

Figure 4.9 Optical characteristics of the shortwave radiation fluxes. (a) Analysis for the day of 1 May 2020 during Exp_1. (b) Analysis for the day of 21 February 2022 during Exp_3.

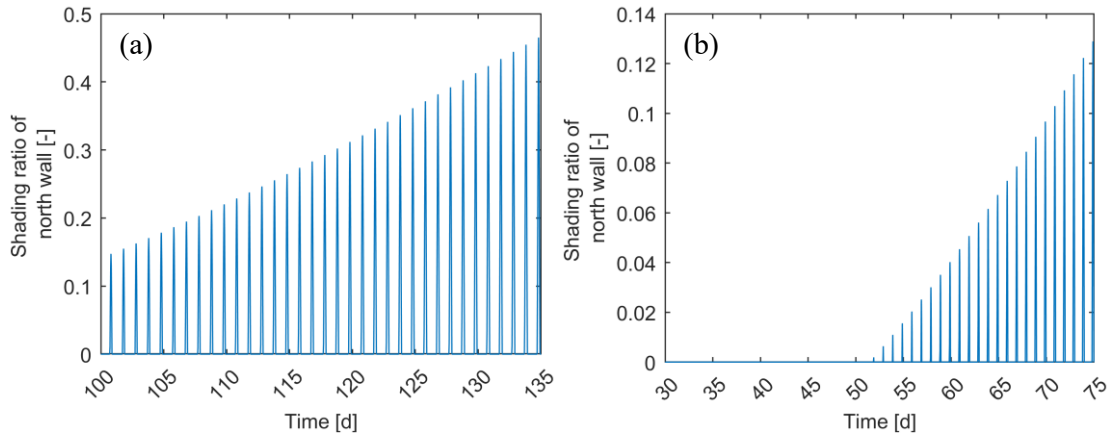

Figure 4.10 Occurrences of shading for the north wall in the three validation experiments (a: Exp_1; b: Exp_3)

4.3.2 Performance in predicting temperature

As illustrated in Figure 4.5 and Figure 4.8, the simulated CSG air temperatures closely mirrored the measured values across both validation experiments. The model demonstrated varied performance in simulating air temperatures during different simulation periods. In Exp_3, where the thermal blanket was used in a timely manner, and the CSG production scenario was the most representative, the model overestimated the indoor air temperature during nighttime at the initial stage of the simulation. Around noon, the model tended to overestimate temperatures in the early stages of the simulation and underestimate them in the later stages. In Exp_2, characterized by warm outdoor weather without the use of the thermal blanket, the simulations provided a perfect fit at night but consistently underestimated the temperature around noon. Throughout the entire growth cycles of the lettuce crop in Exp_1 and Exp_3, the *RRMSE* for indoor air temperature predictions was 14.5% and 21.1%, respectively, with the *RMSE* being 2.9 and 3.3 °C, indicating good model performance.

According to our simulation attempts, the primary reason for the overestimation of nighttime temperatures at the initial stage of the simulation is that the initial layer temperatures of the

north wall and indoor soil, which have heat storage capabilities, were overestimated. As the simulation progressed, this overestimation gradually disappeared. By comparing the simulated results across the two experiments, it can be inferred that the thermal blanket usage might also have been a potential cause of the overestimation. The use of the thermal blanket affects radiation, conduction, and infiltration processes. The model assumed a reduction fraction of 0.7 for the usage of the thermal blanket to modify air infiltration. Reducing this value could increase the infiltration rate. However, it might lower the simulated values of indoor air humidity at night, making them deviate further from the measurements (Figure 4.5 and Figure 4.8). Comparatively, in practical application, carefully assessing the actual status of the thermal blanket and appropriately selecting a comprehensive thermal conductivity can be a direction for improving model accuracy.

In both experiments, as found in Section 4.1, the indoor radiation around noon was underestimated, which can explain the underestimation of indoor air temperatures in Exp_1. However, in Exp_3, indoor air temperatures were overestimated around noon in the early stages of the simulation, indicating that the errors during the day were not solely due to the shortwave radiation at the top of the canopy. Another factor could be related to changes in the crop growth stage. In the early stages of crop growth, the indoor ground absorbs more solar radiation and exchanges heat with indoor air dominantly compared to the crop canopy. If the description of soil evaporation rate is lower than the actual value, or if the convective coefficient between indoor ground and air is higher than the actual value, the temperature of indoor ground will be overestimated, leading to an overestimation of CSG air temperatures in the early stages of crop growth. As the LAI increases, the temperature overestimation brought about by soil interactions becomes negligible, and the underestimated radiation dominates the temperature estimation errors. Although the crop transpiration in this model is derived from the study on tomatoes by Stangheilini (1987), its model components have been validated in the developed lettuce growth model. Therefore, transpiration can be considered as not significantly contributing to estimation errors of CSG air temperatures.

Figure 4.11 illustrates the heat fluxes that determine the air temperature dynamics inside the

CSG. Convective heat fluxes between indoor air and the canopy C_{can_air}, indoor ground C_{gro_air}, and the internal surface of the north wall C_{nw,in_air} consistently acted as incoming energy flows for indoor air. Among these, owing to a significant amount of solar radiation absorbed by the indoor ground, C_{gro_air} contributed the most to the heat gain of indoor air during warm seasons, with the proportion reaching 56.1%, and achieved 29.3% during cold seasons. Another major source was C_{nw,in_air}, which contributed the most during cold seasons, reaching 57.6%, while in warm seasons, it accounted for 14.3%. The contribution of C_{can_air} was relatively small, accounting for 3.4% and 13.2% of the total heat gain during Exp_1 and Exp_3, respectively. The magnitude relationship between the canopy temperature and surrounding air temperature is dynamically changing (Jackson, Idso, Reginato, & Pinter Jr, 1981). For lettuce cultivation inside CSGs, the average temperature differences between the canopy and greenhouse air based on the simulated results are summarized in Table 4.3. They ranged from -1.6 to 1.4 ℃ under different greenhouse scenarios. Generally, depending on the temperature differences, C_{can_air} tended to provide heat to the indoor air when the greenhouse was closed at night and under natural ventilation conditions during the daytime, while removing heat under natural ventilation conditions at night and when the greenhouse was closed during the daytime.

On the other hand, convective heat exchange between indoor air and the internal surface of the north roof C_{nr,in_air}, as well as the sensible heat exchange caused by air exchange E_{air_out} consistently acted as outgoing energy flows for indoor air. In both experiments, E_{air_out} served as the largest outgoing heat flux, constituting 95.3% and 62.0% of the total heat loss, respectively. The proportion of C_{nr,in_air} was relatively lower, at 4.7% in Exp_1 and 1.5% in Exp_3, aligning with the role of the north roof in thermal insulation. Furthermore, during the cold seasons, C_{nr,in_air} achieved a lower average heat flux since the north roof inner surface could receive solar radiation over a longer period at lower solar altitudes. An exception is the convective heat exchange between indoor air and the internal surface of the south roof C_{sr,in_air}, which represented a significant outgoing heat flux during the cold seasons, at 36.5%. However, it acted as a heat source that contributed 26.2% of the total heat gain during warm seasons. This was induced by the high outdoor temperatures that the south

roof could have a higher internal surface temperature than indoor air after absorbing solar radiation. Additionally, note that there was a minimal difference between the sums of incoming and outgoing energy flows, which applies to the mass flows as well.

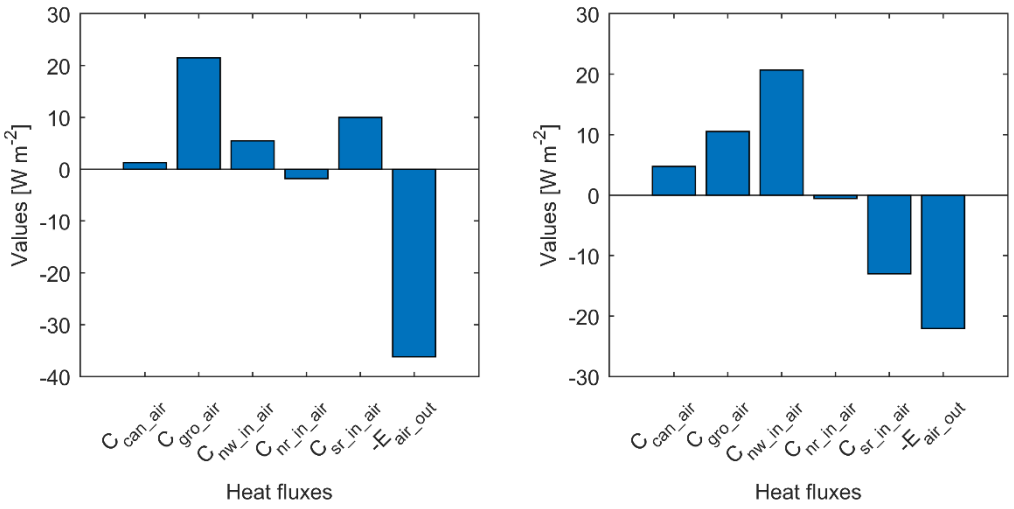

Figure 4.11 The average of heat fluxes that determine the CSG air temperature dynamics during the entire crop growth cycle (a: Exp_1; b: Exp_3)

Table 4.3 Average temperature differences between the crop canopy and greenhouse air

Greenhouse scenarios	Temperature difference between the canopy and greenhouse air	
	Exp_1	Exp_3
Closed greenhouse at night	/	0.8
Ventilated greenhouse at night	-1.6	/
Closed greenhouse in the daytime	/	-0.9
Ventilated greenhouse in the daytime	1.1	1.4

4.3.3 Performance in predicting humidity

As illustrated in Figure 4.5 and Figure 4.8, the simulated indoor air humidity levels closely matched the measurements in both Exp_1 and Exp_3. Throughout the entire growth cycle of the lettuce crop, the *RRMSE* for relative humidity predictions was 17.7% in Exp_1 and

30.8% in Exp_3, with the *RMSE* values being 0.09 and 0.25, respectively, indicating acceptable model performance. In cold seasons, the estimation errors in predicting humidity were significantly affected by greenhouse controls. The indoor air humidity was generally underestimated when the CSG was covered by the thermal blanket and overestimated when it was uncovered; this overestimation became more pronounced upon the activation of roof ventilation. When combining the analysis of the simulation results for indoor temperature, it becomes clear that the accuracy improvement for humidity predictions under non-radiative conditions should consider the potential underestimation of soil evaporation and overestimation of vapour condensations on the south roof inner surface and the canopy. Under radiative conditions, the natural ventilation through the roof vent was likely underestimated.

Figure 4.12 shows the vapour fluxes that determine the air humidity dynamics inside the CSG. Crop transpiration $E_{c,gh}$ and soil evaporation E_{so} always acted as source vapour fluxes, contributing to 34.2% and 65.8% of the total vapour gain of indoor air in Exp_1, and 46.5% and 53.5% in Exp_3, respectively. The removal of water vapour from the CSG air occurred through condensations on the inner surface of the south roof $MV_{air\_sr,in}$ and crop leaves MV_{air_can}, as well as through air exchange MV_{air_out}. Analogous to the heat loss from indoor air, MV_{air_out} served as the largest outgoing vapour flux, constituting 99.5% and 83.4% of the total vapour loss, respectively. $MV_{air\_sr,in}$ and MV_{air_can} primarily occurred in cold seasons, with a proportion of 14.5% and 2.1%, whereas in warm seasons, their contributions to vapour loss were limited to 0.1% and 0.4%, respectively.

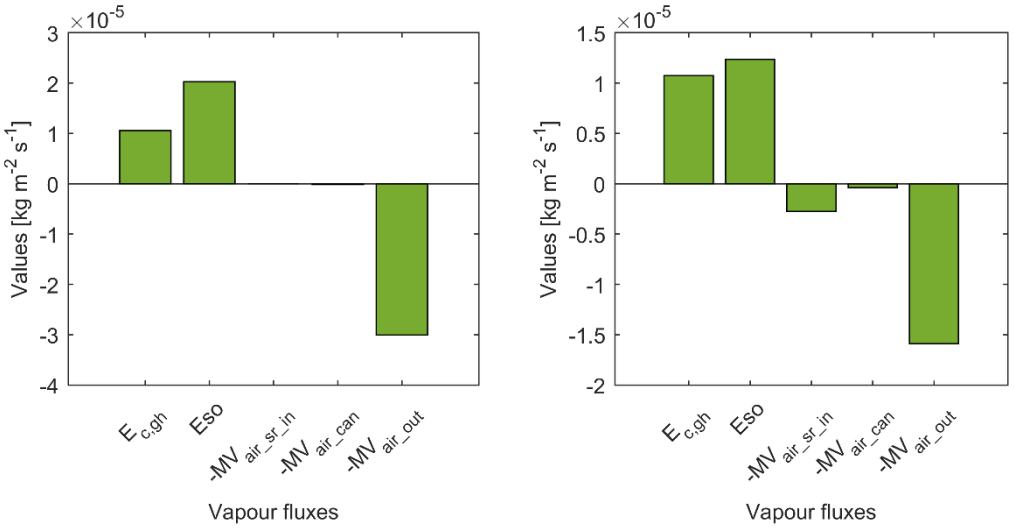

Figure 4.12 The average of vapour fluxes that determine the CSG air humidity dynamics during the entire crop growth cycle (a: Exp_1; b: Exp_3)

4.3.4 Performance in predicting CO_2 concentration

As depicted in Figure 4.5 and Figure 4.8, the simulated indoor air CO_2 concentrations closely matched the measured values in both validation experiments. Throughout the entire growth cycles of the lettuce crop in Exp_1 and Exp_3, the predictions of CO_2 concentration yielded *RMSE* values of 12 and 58 ppm, and *RRMSE* of 3.0% and 12.4%, respectively, demonstrating excellent model performance. Among all CSG climate attributes, the model exhibited the best predictive performance for CO_2 concentration. This is because the key components of the sub-model describing CO_2 dynamics, including canopy assimilation and respiration, were derived from an already developed and validated lettuce growth model. Additionally, the model should have accurately described soil microbial respiration and the CO_2 flux generated by air exchange. The model had a poorer performance in Exp_3 due to the lack of measured outdoor CO_2 concentrations in Exp_3, which instead utilized an assumed value of 400 ppm (Figure 4.6). However, there were discrepancies between the assumed and the actual measured values (Figure 4.3).

In both experiments (Figure 4.13), soil microbial respiration R_{sm} accounted for the largest

proportion of the source CO_2 fluxes, comprising 93.5% in Exp_1 and 46.6% in Exp_3, with average rates of 1.39×10^{-7} and 0.46×10^{-7} kg m^{-2} s^{-1}, respectively. R_{sm} exhibited larger rates in warm seasons primarily due to higher soil temperatures. Organic base fertilizers were used in both validation tests, which allowed soil respiration to release more CO_2, and the correction factor for soil microbial respiration λ_{sm} was set to 1.0. Thus, for the general soil, this greenhouse dependent parameter may need to be less than 1.0. Crop maintenance respiration $R_{d,gh}$, as another source CO_2 flux, had significantly lower average rates compared to R_{sm}, at 0.96×10^{-8} and 1.06×10^{-8} kg m^{-2} s^{-1}, respectively. The canopy assimilation $A_{C,gh}$ was always the main CO_2 consumer. The CO_2 flux induced by air exchange MC_{air_out} represented a special case. In cold seasons, it supplemented CO_2 for the CSG, constituting 42.6% of the total CO_2 sources, while in well-ventilated greenhouses during warm seasons, it transformed into an outgoing flux, accounting for 54.5% of the total CO_2 losses.

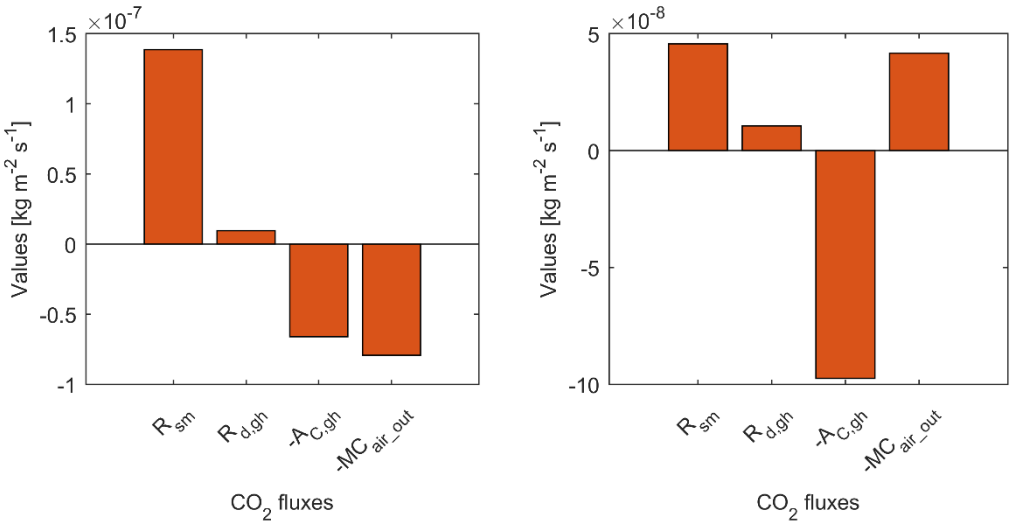

Figure 4.13 The average of CO_2 fluxes that determine the CO_2 concentration dynamics of CSG air during the entire crop growth cycle (a: Exp_1; b: Exp_3)

4.3.5 Heat fluxes inside the north wall and indoor soil

Layering and surface definition were conducted to describe the temperature dynamics of the north wall and indoor soil. Their temperatures across different layers in selected two days

are respectively illustrated in Figure 4.14 and Figure 4.15. It can be observed that the temperature fluctuations of the outer and inner surfaces of the north wall were significant, while the fluctuations in the interlayers were relatively smaller. During each day, there was at least one pair of adjacent layers whose temperature curves intersected, and on the day from the warm seasons, all four pairs of adjacent layers experienced intersections. This indicated that at different times of the day, there was at least one pair of adjacent layers where the relationship between their temperatures changed, leading to a reversal in the direction of the heat flux. That is, the direction of heat fluxes within the north wall was not always from inside to outside, which supported previous studies (M. Li et al., 2015; C Ma et al., 2010; Tong & Christopher, 2019). The thermal storage capacity of the north wall was also manifested in this manner. For example, at 21:00, 1 May 2020, the first layer of the north wall supplied heat to its internal surface to warm the greenhouse, and it also released heat to the second layer. Therefore, for the north wall, which has storage capacity and is considered to have internal heat sources, it is not appropriate to employ algebraic equations to calculate its states, and layering is undoubtedly necessary. On the two selected days, there was at least one pair of adjacent layers in the indoor soil whose temperature curves intersected, indicating that layering is also necessary for indoor soil. According to the simulated results, daily soil temperature fluctuations mainly occur in the indoor ground, and the first and second layers, that is within 0.5 m depth, consistent with measurements (Deng, 2021; Huang, 2021; Weituo Sun et al., 2015). This also proves the rationality of layering for indoor soil.

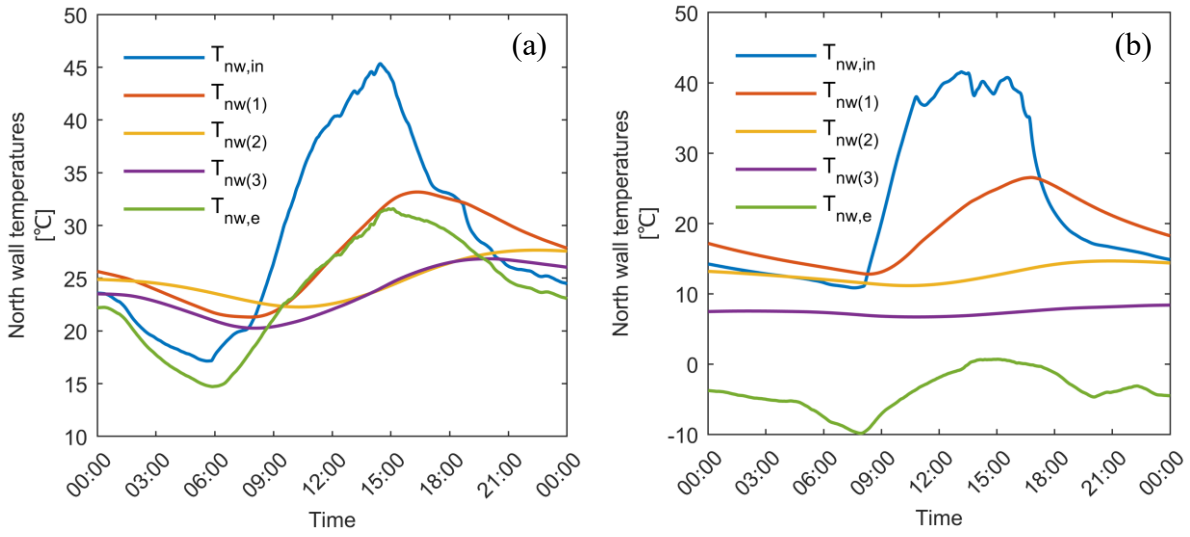

Figure 4.14 Temperature trajectories of the north wall surfaces and internal layers. (a) Analysis for the day of 1 May 2020 during Exp_1. (b) Analysis for the day of 21 February 2022 during Exp_3.

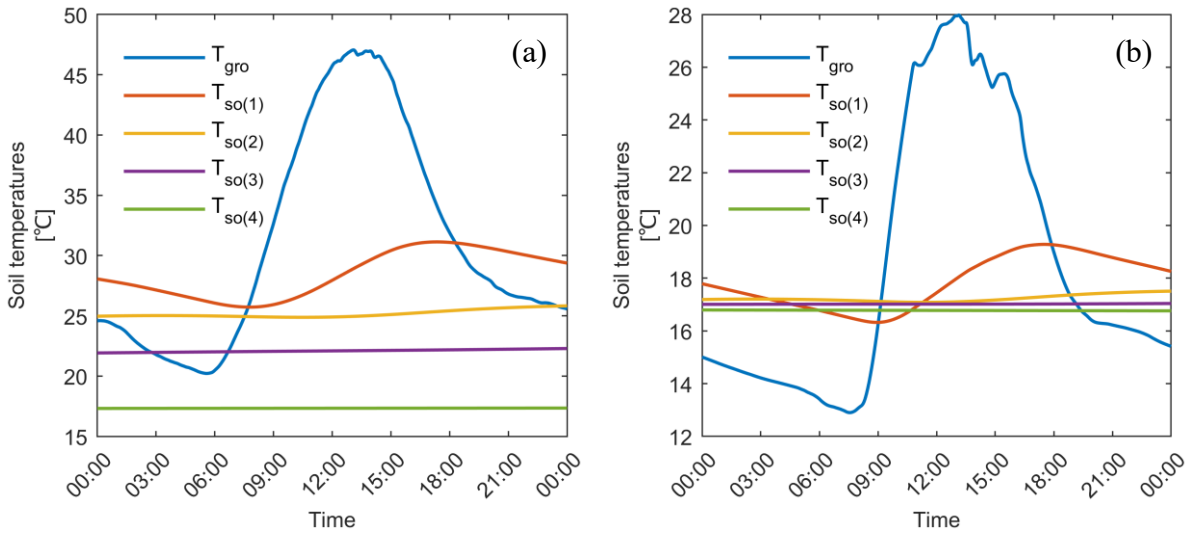

Figure 4.15 Temperature trajectories of indoor ground and soil layers. (a) Analysis for the day of 1 May 2020 during Exp_1. (b) Analysis for the day of 21 February 2022 during Exp_3.

4.3.6 Ice layer formation

Ice layer formation ultimately depends on the indoor air temperature and humidity, as well

as the temperature of the internal surface of the south roof. It was observed in Exp_3, which was conducted during the cold seasons (Figure 4.16). The ice layer formed on the internal surface of the south roof during periods when the CSG was closed, accompanied by low temperatures and high humidity levels of indoor air, as well as extremely low outdoor temperatures. Throughout the experiment, the duration of the ice layer formation accounted for only about 0.14% of the condensation time. However, it is foreseeable that this proportion would increase further in colder seasons (e.g. up to 1.2% in Exp_2, where, as anticipated, deposition frequently occurred after rolling up the thermal blanket). Ice layer formation directly impacts the heat fluxes of shortwave radiation, longwave radiation, conduction, and latent heat conversion. Therefore, incorporating a description of condensation switching to deposition is necessary to enhance the comprehensiveness and accuracy of the CSG climate model.

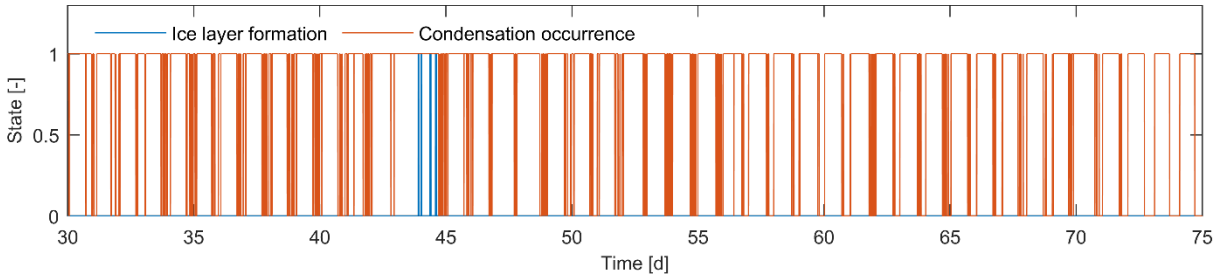

Figure 4.16 Ice layer formation and Condensation occurrence in Exp_3. 0 represents 'not formed/ not occurred', and 1 represents 'formed/ occurred'.

4.3.7 Universality, limitations, and perspective

The full-scale CSG climate model developed in this study, which is based on detailed process descriptions, can be used to simulate indoor climate attributes of shortwave radiation, air temperature, humidity, and CO_2 concentration, as well as other CSG object states for any standard CSG at any geographical location. It describes crop activities with lettuce as the target crop, but most of the knowledge can be extended to CSGs cultivating other crops. The CSG climate model can be incorporated with the crop growth model to simulate the CSG

production process since its outputs cover almost all the climate inputs of the current crop models for potential situations. The model has been validated to have acceptable performance during both warm and cold seasons. When Compared with other process-based models, such as those for Venlo-type greenhouses by Vanthoor, Stanghellini, Van Henten, and De Visser (2011) and Katzin et al. (2020), as well as the temperature and humidity prediction models for CSG by R. Liu et al. (2021), this model performs better on CO_2 concentration predictions but shows poorer performance in temperature and humidity predictions. In addition, it exhibited comparable performance in simulating shortwave radiation to the CSG radiation model by H. Xu et al. (2019). Thus, the developed CSG climate model can be deemed sufficiently accurate for control, considering that the CSG system is much more complex than the Venlo-type greenhouse in heat and mass transfers, the lack of CSG construction standards makes it difficult to precisely determine structural parameters and material properties, and the model is highly integrated, and its evaluation was performed over the entire crop growth cycles.

Another indicator used to measure greenhouse air humidity is VPD, which represents the amount of vapour the air can still hold before reaching saturation. VPD can more directly reflect the crop transpiration demand, making it a preferred metric among growers in some regions when discussing greenhouse climate (Stanghellini et al., 2019). Although VPD was entirely determined by air temperature and relative humidity in the developed CSG climate model, the VPD of CSG air did not achieve an acceptable *RRMSE* in our simulation tests. Therefore, future model optimization will focus on improving the description of humidity-related processes, particularly soil evaporation, vapour condensation, and natural ventilation.

Computational efficiency is another crucial metric for control-oriented models, especially when used for online control. It is closely related to how surfaces are defined in the CSG climate model. Based on our programming tests, increasing the thickness and thermal capacity of the internal surface of the north wall and the indoor floor could make their states less sensitive to variations in heat flow, improving the efficiency of solving differential equations and saving computation time. However, this adjustment also caused the model to

exhibit varying degrees of lag in predicting indoor air temperatures during both the rise and fall processes. This time lag could lead to overestimation or underestimation of the state variables, thereby significantly reducing the model's accuracy. For example, changing the inner surface thickness of the north wall from the current 10 mm to 50 mm resulted in an oversized thermal capacity. Consequently, the wall surface warmed up more slowly than the actual rate, correspondingly leading to a slower increase in indoor air temperature due to the convective interactions. Meanwhile, due to the larger thermal capacity, the maximum temperature that the wall surface could reach might be lower than the actual value, and this maximum temperature would be reached later at lower levels of indoor radiation. According to the same logic, the indoor air temperature also dropped more slowly in the afternoon. These generated the time lag issue in predicting indoor air temperatures, and the *RRMSE* increased from 21.1% to 26.7% in Exp_3. One should be aware of the distinction between the time lag issue in simulations and the expected thermal inertia and time delay effects of the greenhouse system.

Adjusting the surface definition to improve computational efficiency will sacrifice model accuracy. Meanwhile, thinner surface layers risk making their state dynamics overly sensitive, reducing the efficiency of solving differential equations and posing challenges for using common numerical simulation methods. Employing switch functions to smooth out the conditional 'if/else' statements in the model and greenhouse control inputs is a way to enable the model to tolerate lower thermal capacities. It can improve computational efficiency under the current surface definition. This approach also benefits optimal control. Firstly, gradient-based optimization algorithms require that differential equations be written in a continuously differentiable form. Secondly, although the operation of the thermal blanket is modelled as being instantaneously completed, its actual movement typically takes longer. By using switch functions, this movement can be fully identified by the model, thereby enhancing control efficiency. The construction of switch functions will be addressed in subsequent research.

4.4 Summary

A full-scale climate model of the CSG has been developed and evaluated. This model, designed for greenhouse climate control, is based on detailed process descriptions. It describes the effects of outdoor weather, greenhouse structure, crop states, and greenhouse controls on the indoor climate of a standard CSG. Full-scale is reflected in both inputs and outputs of the model. For a given CSG, inputs mainly include the external weather of horizontal solar radiation, air temperature, relative humidity, CO_2 concentration, and wind speed, the crop growth states of crop dry weight and leaf area index, as well as the controls of the thermal blanket, side vent, and roof vent. All four indoor climate attributes of shortwave radiation, air temperature, relative humidity, and CO_2 concentration, along with other CSG object states, can be integratively simulated.

The model was designed by detailing the following eleven subsections, introducing novelties and new insights: state variables, definition of layers and surfaces, capacities of CSG objects, radiative fluxes, convective and conductive fluxes, latent heat fluxes, vapour fluxes, CO_2 fluxes, air exchange, crop activities, and soil activities. Parameterisation of the model was achieved by classifying parameters into general parameters and those dependent on the simulated CSG. The model describes crop activities specifically targeting lettuce and was thoroughly evaluated in scenarios of lettuce production involving two different CSG structures across both warm and cold seasons.

The model demonstrated acceptable performance. Simulated CSG climates closely mirrored the measured values throughout crop growth cycles, with the *RRMSE* being 12.7-23.0% for shortwave radiation, 17.5-21.1% for air temperature, 22.7-30.8% for relative humidity, and 3.0-12.4% for CO_2 concentration predictions. Potential directions for enhancing model accuracy, as well as the contributions of energy and mass fluxes to the temperature, humidity, and CO_2 dynamics, were analysed. Layering was proved to be necessary to describe the temperature dynamics of the north wall and indoor soil. Seasonal variations in the shading of the north wall by the north roof and ice layer formation were noted; incorporating these

processes could improve the model descriptions.

The developed CSG climate model, which can be integrated with the crop growth model to simulate the CSG production process, can serve as a basis for optimal control of the CSG climate, considering its high computational efficiency, strong generalisation, and sufficient accuracy. Further research will focus on the optimisation of the surface definition and the development of switch functions to enhance the efficiency of computations.

Chapter 5

An integrated model of Chinese solar greenhouse climate and crop growth for control

This chapter develops an integrated CSG climate-crop growth model that describes the entire CSG lettuce production process by combining the two models presented in Chapters 3 and 4, supported by thorough validation. Meanwhile, exploratory modelling and model smoothing are performed.

5.1 Introduction

To implement optimal control theory or model predictive control in practical CSG production, an integrated model with acceptable accuracy, high computational efficiency, and robust generalisation is required. However, integrated models of greenhouse climate and crop growth specifically for CSGs are currently unavailable, let alone models with crop growth components that respond accurately to a wide range of greenhouse climates and CSG climate components capable of simulating these indoor climates synthetically. Existing integrated greenhouse-crop models are scarce and primarily designed for modern multi-span greenhouses (Gijzen et al., 1997). A representative model is the one developed by Van Henten (1994a), which couples the predictions of greenhouse climate and lettuce growth for optimal climate control. In a pilot study by Dan Xu et al. (2018), which applied two time-scale receding horizon optimal control to a high-tech CSG for lettuce cultivation, the basic CSG-crop model was adapted from the model of Van Henten (1994a) and is challenging to depict the actual CSG production scenarios. Also for the purpose of real-time optimal control, Tap (2000) designed, calibrated, and validated an comprehensive model describing the greenhouse tomato crop production based on existing greenhouse and crop models, e.g. the tomato model by de Koning (1994). Another significant model by Vanthoor (2011) integratively simulated the greenhouse climate and tomato growth dynamics for optimal greenhouse design. This model was later extended to include additional climate conditioning techniques, such as artificial lights, a secondary heating system, and heat harvesting for year-round production by Righini et al. (2020).

In our previous research, a lettuce growth model responding to a broad range of greenhouse climates and a full-scale climate model of the CSG were developed. These models were designed to meet the requirements for model predictive control or optimal control of the CSG climate, facilitating seamless integration. In this study, we aim to integrate these two models to establish a unified greenhouse-crop model for CSG lettuce production. While both models have demonstrated strong individual performance, their integrated performance needs to be specifically tested using the experimental data.

The performance of optimal control systems is sensitive to errors in the system model (Van Henten, 2003). Therefore, to generate an efficient optimal control system for CSG climate, model accuracy must be ensured. This typically implies that the integrated model needs to describe more processes, thereby making the model sophisticated. Although mechanistic models inherently possess high computational efficiency, significant improvement is still required, particularly for optimal control in on-line applications. One method to enhance computational efficiency is by employing differentiable switch functions to smooth out the conditional 'if/else' statements in the model and greenhouse control inputs (Vanthoor, 2011), enabling the model to minimise abrupt changes in output, have higher stability, and tolerate lower thermal capacities. This approach also benefits optimal control in terms of requirements of gradient-based optimisation algorithms, as well as the identification of movements of controllable structural components. In the model of Vanthoor (2011), all the switch functions featured steep flanks approaching the conditional 'if/else' statements, allowing greenhouse controls, including the operation of thermal screens, to be executed instantaneously. Similarly, in our developed CSG climate model, the rolling up and covering of the thermal blanket were also modelled as instantaneous events. However, in practice, these movements generally take 10-15 minutes to complete. Compared to the assumed instantaneous operation, fully capturing movements of the thermal blanket could enhance model accuracy and improve control efficiency. The use of switch functions to identify movements of greenhouse controls is a new concept and requires detailed study to understand its implementation and the impact on model performance.

In conclusion, a well-designed and thoroughly validated integrated model of Chinese solar greenhouse climate and crop growth for control is currently unavailable. The objective of this study is to establish and evaluate such an integrated greenhouse climate-crop growth model for CSG lettuce production by combining the lettuce growth model and the CSG climate model developed in Chapter 3 and Chapter 4, respectively. This integrated model describes the effects of outdoor climate, greenhouse structure, and greenhouse controls on the indoor climate and crop state dynamics. First, the model will be validated in terms of

predictions of shortwave radiation, air temperature, relative humidity, and CO_2 concentration inside the CSG, as well as the crop dry weight and leaf area index (LAI) of the cultivated lettuce. Second, the validated model will be used for exploratory modelling on practical control scenarios, to address the following research question: how much influence do current differentiating climate control scenarios in practice have on net economic return in standard CSG cultivation? Third, to further enhance computational efficiency, the integrated model will be optimised by employing differentiable switch functions to smooth out the conditional 'if/else' statements in the model and identify movements of greenhouse controls. Finally, the processed model after smoothing will be evaluated again. This study will provide an integrated CSG climate-crop growth model and its smoothed form for model-based climate management of CSG cultivation, with the latter possessing higher adaptability and computational efficiency.

5.2 Model synthesis and processing

5.2.1 Model integration

In the previous chapters, dynamic models that describe the lettuce growth and the CSG climate have been developed and evaluated individually. Combination of the two models results in an integrated CSG climate-crop growth model for lettuce production. As shown in Figure 5.1, this integrated model describes the effects of outdoor climate, greenhouse structure, and greenhouse controls on the indoor climate and crop state dynamics, determining the final output of the CSG crop production process. The model can be represented by the following general equations.

$$\frac{dX}{dt} = f(X, Y, U, D, P, t) \tag{5.1}$$

$$Y = g(X, Y, U, D, P, t) \tag{5.2}$$

where X is the vector of model state variables determined by numerically solving differential equations, including crop dry weight, LAI, buffer storage, indoor air temperature, relative humidity, CO_2 concentration, canopy temperature, indoor ground temperature, temperatures of soil layers, and temperatures of surfaces and layers of north wall; Y is the vector of model state variables obtained through analytical solutions or described by algebraic equations, including the shortwave radiation at the top of canopy, shortwave radiation absorbed by indoor ground, canopy, and surfaces of the CSG envelope, as well as temperatures of the north roof and south roof surfaces; U is the vector of greenhouse controls, including controls of the thermal blanket, roof vent, and side vent, and ranging from 0 to 1; D is the vector of external weather, including outdoor horizontal shortwave radiation, air temperature, relative humidity, CO_2 concentration, and wind speed; P is the vector of model parameters, including the constant parameters, greenhouse dependent parameters, effective cultivated area, and plant density; t is the vector of the time, including the nth day of the year and the local time, as well as the simulation timing.

More specifically, the generation of the integrated model integrates all state variables from the lettuce growth model and the CSG climate model into a unified description, directly merging their equations while retaining their constant parameters.

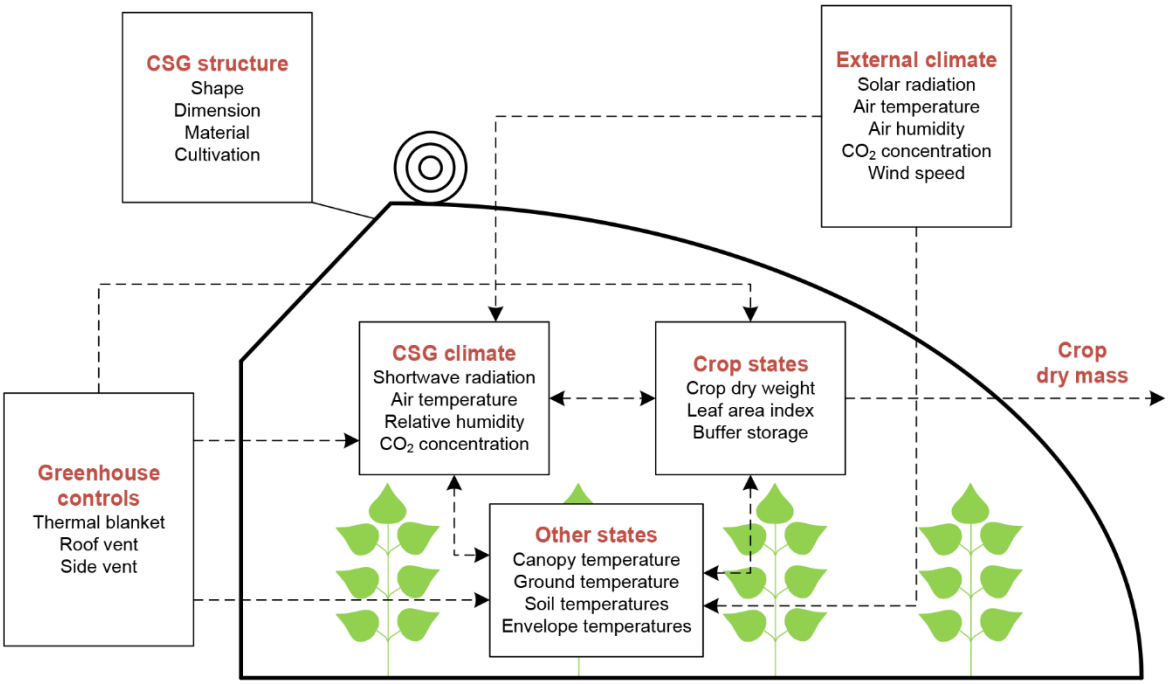

Figure 5.1 A schematic diagram of the integrated CSG climate-crop growth model. Elements outside the contour of the CSG serve as inputs of the model, while elements within the contour are outputs. Dashed lines indicate the flows of information. The crop dry mass is used to represent the final output of the CSG crop production process.

5.2.2 Model smoothing

5.2.2.1 Smoothed equations

In this research, the sigmoid function, known for its smooth and continuously differentiable properties, was used to improve the smoothness of model descriptions, particularly in the implementation of conditional statements and in managing inputs of greenhouse controls. The general form of the sigmoid function is $f(x) = \frac{1}{1+e^{-s\cdot(x-x_0)}}$, where x is the input variable, x_0 is the threshold or midpoint, and s is the slope of the differentiable switch function. The LogSumExp (LSE) function was used for the smooth approximation to the maximum and minimum functions, as well as the range of values. The general form of the

used LSE function is $\min(a,b) = -1/s \cdot \ln(e^{-s\cdot a} + e^{-s\cdot b})$, where a and b are the two values for which the smooth minimum is to be calculated. The absolute value functions were smoothly approximated by the function $f(x) = \sqrt{x^2 + z^2}$, where z is a small positive parameter introduced to ensure differentiability at the origin. Next, all formulas requiring smoothing in the integrated model will be processed into their smoothed versions.

The Eq. (3.2) that describes the buffer dependent inhibition function h_{buf} [-] can be smoothed as:

$$h_{buf} = \left(\frac{1}{1 + e^{-s_{h,buf,1}\cdot\left(\frac{C_{buf}}{C_{buf,max}} - 0.99\right)}}\right) \cdot \frac{-1}{s_{h,buf,2}} \cdot \ln\left(e^{-s_{h,buf,2}\cdot\frac{R_d + \frac{RGR_{max}\cdot X_d}{c_\beta}}{c_\alpha\cdot(A_C + z)}} + e^{-s_{h,buf,2}}\right) + \left(1 - \frac{1}{1 + e^{-s_{h,buf,1}\cdot\left(\frac{C_{buf}}{C_{buf,max}} - 0.99\right)}}\right) \cdot 1 \quad (5.3)$$

The Eq. (3.3) that describes the maximum relative growth rate RGR_{max} [s^{-1}] can be smoothed as:

$$RGR_{max} = \left(\frac{1}{1 + e^{-s_{RGR,max}\cdot(T_c - T_{c,RGR})}}\right) \cdot RGR_{max,20} \cdot Q_{10,gr}^{-\frac{T_c - 20}{10}} + \left(1 - \frac{1}{1 + e^{-s_{RGR,max}\cdot(T_c - T_{c,RGR})}}\right) \cdot RGR_{max,20} \cdot Q_{10,gr}^{\frac{T_c - 20}{10}} \quad (5.4)$$

The Eq. (A.6) that describes the light saturated net assimilation rate $A_{L,sat,n}$ [kg (CO_2) m^{-2} (leaf) s^{-1}] can be smoothed as:

$$A_{L,sat,n} = \frac{-1}{s_{A,L,sat,n}} \cdot \ln(e^{-s_{A,L,sat,n}\cdot A_{L,c,n}} + e^{-s_{A,L,sat,n}\cdot A_{L,mm}}) \quad (5.5)$$

The Eq. (3.16) that describes the temperature dependency of stomatal resistance $f_{Tc,s}$ [-] can be smoothed as:

$$f_{Tc,s} = \left(\frac{1}{1+e^{-s_{f,Tc,s}\cdot(I-3)}}\right)\cdot\left(1+2.3\cdot10^{-2}\cdot(T_c-24.5)^2\right) + \left(1-\frac{1}{1+e^{-s_{f,Tc,s}\cdot(I-3)}}\right)\cdot\left(1+0.5\cdot10^{-2}\cdot(T_c-33.6)^2\right) \quad (5.6)$$

The Eq. (3.17) that describes the CO_2 dependency of stomatal resistance $f_{Xc,s}$ [-] can be smoothed as:

$$f_{Xc,s} = \left(\frac{1}{1+e^{-s_{f,Xc,s,1}\cdot(I-3)}}\right)\cdot\left(\left(\frac{1}{1+e^{-s_{f,Xc,s,2}\cdot(X_c-1100)}}\right)\cdot1.5+\left(1-\frac{1}{1+e^{-s_{f,Xc,s,2}\cdot(X_c-1100)}}\right)\cdot\left(1+6.1\cdot10^{-7}\cdot(X_c-200)^2\right)\right)+\left(1-\frac{1}{1+e^{-s_{f,Xc,s,1}\cdot(I-3)}}\right)\cdot1 \quad (5.7)$$

The Eq. (3.21) that describes the saturated vapour pressure of the indoor air $e_{s,air}$ [Pa] can be smoothed as follows. The Eq. (5.8) also applies to the saturated vapour pressures at temperatures of the south roof inner surface, crop canopy, and outdoor air.

$$e_{s,air} = \left(\frac{1}{1+e^{-s_{e,s,air}\cdot X_t}}\right)\cdot10^{2.7857+\frac{7.5\cdot X_t}{237.3+X_t}} + \left(1-\frac{1}{1+e^{-s_{e,s,air}\cdot X_t}}\right)\cdot10^{2.7857+\frac{9.5\cdot X_t}{265.5+X_t}} \quad (5.8)$$

The Eq. (3.22) that describes the boundary layer resistance to CO_2 diffusion r_b [s m^{-1}] can be smoothed as:

$$r_b = Le^{0.67}\cdot\frac{1174\cdot {l_f}^{0.5}}{\left(l_f\cdot\left((T_c-X_t)^2+{z_{r,b}}^2\right)^{0.5}+207\cdot{v_a}^2\right)^{0.25}} \quad (5.9)$$

The Eq. (4.14) that describes the presence of the ice layer u_{ice} [-] can be smoothed as:

$$u_{ice} = \left(1 - \frac{1}{1 + e^{-s_{u,ice,1} \cdot T_{sr,in}}}\right) \cdot \left(\frac{1}{1 + e^{-s_{u,ice,2} \cdot (e_{air} - e_{s,sr,in})}}\right) \tag{5.10}$$

The Eq. (4.21) that describes the solar altitude angle θ_h [°] can be smoothed as follows:

$$\theta_h = \frac{1}{s_{\theta,h,2}} \cdot \ln\left(e^{s_{\theta,h,2} \cdot 0.1} + e^{s_{\theta,h,2} \cdot \frac{-1}{s_{\theta,h,1}} \cdot ln\left(e^{-s_1 \cdot 89.9} + e^{-s_{\theta,h,1} \cdot \theta'_h}\right)}\right) \tag{5.11}$$

$$sin\theta'_h = sin\varphi \cdot sin\delta_s + cos\varphi \cdot cos\delta_s \cdot cos\omega \tag{5.12}$$

where θ'_h [°] is the solar altitude angle without constraints in range.

The Eq. (4.41) that describes the shading ratio of the north wall due to the shading by north roof σ_{sha} [-] can be smoothed as:

$$\sigma_{sha} = \frac{1}{s_{\sigma,sha,2}} \cdot ln\left(1 + e^{\frac{-s_{\sigma,sha,2}}{s_{\sigma,sha,1}} \cdot ln\left(e^{-s_{\sigma,sha,1}} + e^{-s_{\sigma,sha,1} \cdot \frac{L_{nr}}{L_{nw}} \cdot \frac{cos(\theta_{nw} - \theta_h + \theta_{nr})}{sin(\theta_{nw} - \theta_h)}}\right)}\right) \tag{5.13}$$

The convective heat transfer coefficient between indoor ground and air h_{gro_air} [W m^{-2} °C^{-1}] listed in Table B.2 can be smoothed as:

$$h_{gro\_air} = \left(\frac{1}{1+e^{-s_{h,gro\_air}\cdot\left(LAI_{gh}-1\right)}}\right)\cdot 2.8 + \left(1-\frac{1}{1+e^{-s_{h,gro\_air}\cdot\left(LAI_{gh}-1\right)}}\right)\cdot 1.86 \cdot \left(\left(\left(T_{gro}-X_t\right)^2 + {z_{h,gro\_air}}^2\right)^{0.5}\right)^{0.33} \quad (5.14)$$

The convective heat transfer coefficient between the internal surface of the south roof and indoor air h_{sr,in_air} [W m^{-2} °C^{-1}] listed in Table B.2 can be smoothed as:

$$h_{sr,in\_air} = \left(\frac{1}{1+e^{-s_{h,sr,in\_air}\cdot\left(U_{vent,r}-0.1\right)}}\right)\cdot\left(0.95+6.76\cdot {v_a}^{0.49}\right) + \left(1-\frac{1}{1+e^{-s_{h,sr,in\_air}\cdot\left(U_{vent,r}-0.1\right)}}\right) \cdot\left(2.21\cdot\left(\left(\left(T_{sr,in}-X_t\right)^2 + {z_{h,sr,in\_air}}^2\right)^{0.5}\right)^{0.33}\right) \quad (5.15)$$

The convective heat transfer coefficient between the internal surface of the south roof and indoor air h_{nw,in_air} [W m^{-2} °C^{-1}] listed in Table B.2 can be smoothed as:

$$h_{nw,in\_air} = \left(\frac{1}{1+e^{-s_{h,nw,in\_air}\cdot\left(U_{vent,r}-0.1\right)}}\right)\cdot\left(7.2+3.84\cdot v_a\right) + \left(1-\frac{1}{1+e^{-s_{h,nw,in\_air}\cdot\left(U_{vent,r}-0.1\right)}}\right) \cdot\left(3.4\cdot\left(\left(\left(T_{nw,in}-X_t\right)^2 + {z_{h,nw,in\_air}}^2\right)^{0.5}\right)^{0.33}\right) \quad (5.16)$$

The convective heat transfer coefficient between the internal surface of the south roof and indoor air h_{nr,in_air} [W m^{-2} °C^{-1}] listed in Table B.2 can be smoothed as:

$$h_{nr,in\_air} = \left(\frac{1}{1+e^{-s_{h,nr,in\_air}\cdot\left(U_{vent,r}-0.1\right)}}\right)\cdot\left(7.2+3.84\cdot v_a\right) + \left(1-\frac{1}{1+e^{-s_{h,nr,in\_air}\cdot\left(U_{vent,r}-0.1\right)}}\right) \cdot\left(3.4\cdot\left(\left(\left(T_{nr,in}-X_t\right)^2+{z_{h,nr,in\_air}}^2\right)^{0.5}\right)^{0.33}\right) \tag{5.17}$$

The Eq. (4.54) that describes the latent heat flux to the south roof $L_{air\_sr,in}$ [W m^{-2} (gro)] can be smoothed as:

$$L_{air\_sr,in} = \left(\frac{1}{1+e^{-s_{L,air\_sr,in}\cdot T_{sr,in}}}\right)\cdot\left(\lambda_v\cdot MV_{air\_sr,in}\right) + \left(1-\frac{1}{1+e^{-s_{L,air\_sr,in}\cdot T_{sr,in}}}\right)\cdot\left(\lambda_{v,d}\cdot MV_{air\_sr,in}\right) \tag{5.18}$$

The Eq. (4.55) that describes the condensation rate of the indoor water vapour MV_{1_2} [kg m^{-2} (gro) s^{-1}] can be smoothed as follows. The Eq. (5.19) is preferred in warm seasons, and the Eq. (5.20) is preferred during the cold seasons.

$$MV_{1\_2} = \frac{1}{s_{MV,1\_2}}\cdot\ln\left(e^{s_{MV,1\_2}\cdot\sigma_{area}\cdot\frac{h_{1\_2}}{\lambda_v\cdot\gamma}\cdot\left(e_{air}-e_{s,2}\right)}+1\right) \tag{5.19}$$

$$MV_{1\_2} = \sigma_{area}\cdot\frac{h_{1\_2}}{\lambda_v\cdot\gamma}\cdot\left(e_{air}-e_{s,2}\right)+\frac{1}{s_{MV,1\_2}} \cdot\ln\left(e^{-s_{MV,1\_2}\cdot\sigma_{area}\cdot\frac{h_{1\_2}}{\lambda_v\cdot\gamma}\cdot\left(e_{air}-e_{s,2}\right)}+1\right) \tag{5.20}$$

The Eq. (4.61) that describes the CSG natural ventilation rate g_{nv} [m^3 m^{-2} (gro) s^{-1}] can be smoothed as:

$$g_{nv} = \left(\frac{1}{1 + e^{-s_{g,nv}\cdot(U_{vent,s}-0.1)}}\right)\cdot\left(\eta_{inss}\cdot g_{vent,rs}\right) + \left(1 - \frac{1}{1 + e^{-s_{g,nv}\cdot(U_{vent,s}-0.1)}}\right)\cdot\left(\eta_{inss}\cdot g_{vent,r}\right) \tag{5.21}$$

The Eq. (4.64) that describes the natural ventilation rate through both roof and side vents $g_{vent,rs}$ [m^3 m^{-2} (gro) s^{-1}] can be smoothed as:

$$g_{vent,rs} = \frac{c_d}{A_{gro}} \cdot \left(\frac{{A_{vent,r,U}}^2 \cdot {A_{vent,s,U}}^2}{{A_{vent,r,U}}^2 + {A_{vent,s,U}}^2 + {z_{g,vent,rs}}^2} \cdot \left(2\cdot g\cdot\frac{X_t - T_{out}}{\frac{T_{out}+X_t}{2} + T_{0,K}}\cdot H_{vent,rs}\right) + \left(\frac{A_{vent,r,U} + A_{vent,s,U}}{2}\right)^2 \cdot c_{w,rs}\cdot {v_e}^2\right)^{0.5} \tag{5.22}$$

The Eq. (4.80) that describes the boundary layer resistance or aerodynamic resistance to convective heat transfer r_{bh} [s m^{-1}] can be smoothed as:

$$r_{bh} = \frac{1174\cdot {l_f}^{0.5}}{\left(l_f\cdot\left((T_c - X_t)^2 + {z_{r,bh}}^2\right)^{0.5} + 207\cdot {v_a}^2\right)^{0.25}} \tag{5.23}$$

In the initial integrated model, greenhouse controls were assumed to be completed instantaneously. The moments of greenhouse control actions in the model validation experiments were recorded using the initial time of controls. Meanwhile, the control input data for simulations were provided at 5-minute intervals aligning with the external weather data, and the model program determined control values at integration moments based on the commonly used linear interpolation method. As a result, the covering and rolling up

processes of the thermal blanket were prematurely started in the model simulations and completed within a shorter time frame in comparison to the actual situation. This would affect the daylighting and insulation conditions of the CSG and, consequently, might reduce the model performance. Additionally, greenhouse controls, including those of the thermal blanket and roof and side vents, have a significant impact on the indoor climate, and smoothing them can enhance the stability of the model simulation. In practical CSG systems, the movements of the thermal blanket generally take 10-15 minutes. The controls of the thermal blanket U_b [-] in the smoothed integrated model are described as follows:

$$U_b = \frac{1}{1 + e^{-s_{U,b} \cdot (t - t_{cover}) \cdot (t - t_{uncover})}} \tag{5.24}$$

where t_{cover} [s] is the covering time of the thermal blanket, specifically located at the midpoint of its movement, $t_{uncover}$ [s] is the time for rolling up the thermal blanket, also specifically located at the midpoint of its movement.

Similarly, the controls of the roof vent $U_{vent,r}$ [-] and side vent $U_{vent,s}$ [-] in the smoothed integrated model are described as follows:

$$U_{vent,r} = \frac{1}{1 + e^{s_{U,vent,r} \cdot (t - t_{vent,r,on}) \cdot (t - t_{vent,r,off})}} \tag{5.25}$$

$$U_{vent,s} = \frac{1}{1 + e^{s_{U,vent,s} \cdot (t - t_{vent,s,on}) \cdot (t - t_{vent,s,off})}} \tag{5.26}$$

where $t_{vent,r,on}$ and $t_{vent,s,on}$ [s] are the opening times of the roof vent and side vent, respectively, $t_{vent,r,off}$ and $t_{vent,s,off}$ [s] are the closing times of the roof vent and side vent, respectively. These time points specifically correspond to the midpoints of the CSG vent movements and may vary daily.

5.2.2.2 Parameterisation for model smoothing

The slope of the differentiable switch function for each model equation might be different, primarily depending on the desired range of input variables over which the model description intends the switch function to complete the transition between 0 and 1. Additionally, the selection of these values must also consider the effectiveness of numerical simulations within the program. For the model smoothing process, all introduced parameters and their values are summarised in Table 5.1. The parameter selection methods and curve patterns of the smooth functions are illustrated with the following examples.

The movement of the thermal blanket, including both covering and uncovering processes, was assumed to be a constant 10 minutes. The curve patterns of the smoothed controls of the thermal blanket are illustrated in Figure 5.2a, where transitions between 0 and 1 are completed within 600 s, and the midpoint of the movements corresponds to a control state of 0.5. Note that in the simulations of the smoothed integrated model, the values for t_{cover} and $t_{uncover}$ should be set 5 minutes later than the initial time of the control actions. The control trajectory of the thermal blanket within a day is shown in Figure 5.2b, starting to uncover the south roof at 07:55 and being rolled up at 16:55. Additionally, the movements of both the roof and side vents, for switches between any positions, were assumed to be 60 s, with a control smoothing mechanism similar to that used for the thermal blanket.

In Equation 5.3, the threshold of 0.99 was defined to ensure that the calculation of h_{buf} could be based entirely on the formula applicable when $C_{buf} = C_{buf,max}$. The patterns of the switching function and the smooth minimum for h_{buf} are depicted in Figure 5.2c and Figure 5.2d, respectively. Similarly, in Equation 5.21, the selection of the threshold of 0.1 was aimed at clearly differentiating between the two ventilation modes of only the roof vent being open and both the roof and side vents being open.

Table 5.1 Introduced parameters for smoothing the integrated CSG climate-crop growth model

Notation	Meaning	Value	Unit
$s_{h,buf,1}$	Slope of the differentiable switch function for h_{buf}	1000	-
$s_{h,buf,2}$	Sharpness parameter of the smooth minimum for h_{buf}	100	-
$z_{h,buf}$	Auxiliary parameter to prevent A_C from being zero in the denominator of h_{buf}	1×10^{-12}	kg (CO_2) m^{-2} (gro) s^{-1}
$s_{RGR,max}$	Slope of the differentiable switch function for RGR_{max}	10	$°C^{-1}$
$s_{A,L,sat,n}$	Sharpness parameter of the smooth minimum for $A_{L,sat,n}$	1×10^{8}	-
$s_{f,Tc,s}$	Slope of the differentiable switch function for $f_{Tc,s}$	10	$m^2\ W^{-1}$
$s_{f,Xc,s,1}$	Slope of the radiation dependent differentiable switch function for $f_{Xc,s}$	10	$m^2\ W^{-1}$
$s_{f,Xc,s,2}$	Slope of the CO_2 dependent differentiable switch function for $f_{Xc,s}$	0.5	(μmol (CO_2) mol^{-1} (air))$^{-1}$
$s_{e,s,air}$	Slope of the differentiable switch function for $e_{s,air}$	10	$°C^{-1}$
$z_{r,b}$	Auxiliary parameter to smooth the absolute value function for r_b	1×10^{-4}	°C
$s_{u,ice,1}$	Slope of the temperature dependent differentiable switch function for u_{ice}	10	$°C^{-1}$
$s_{u,ice,2}$	Slope of the vapour pressure dependent differentiable switch function for u_{ice}	0.5	Pa^{-1}
$s_{\theta,h,1}$	Sharpness parameter of the smooth minimum for θ_h	5	-
$s_{\theta,h,2}$	Sharpness parameter of the smooth maximum for θ_h	5	-
$s_{\sigma,sha,1}$	Sharpness parameter of the smooth minimum for σ_{sha}	50	-
$s_{\sigma,sha,2}$	Sharpness parameter of the smooth maximum for σ_{sha}	50	-
s_{h,gro_air}	Slope of the differentiable switch function for h_{gro_air}	50	-
z_{h,gro_air}	Auxiliary parameter to smooth the absolute value function for h_{gro_air}	1×10^{-4}	°C
s_{h,sr,in_air}	Slope of the differentiable switch function for h_{sr,in_air}	100	-
z_{h,sr,in_air}	Auxiliary parameter to smooth the absolute value function for h_{sr,in_air}	1×10^{-4}	°C
s_{h,nw,in_air}	Slope of the differentiable switch function for h_{nw,in_air}	100	-
z_{h,nw,in_air}	Auxiliary parameter to smooth the absolute value function for h_{nw,in_air}	1×10^{-4}	°C
s_{h,nr,in_air}	Slope of the differentiable switch function for h_{nr,in_air}	100	-
z_{h,nr,in_air}	Auxiliary parameter to smooth the absolute value function for h_{nr,in_air}	1×10^{-4}	°C

$s_{L,air\_sr,in}$	Slope of the differentiable switch function for $L_{air\_sr,in}$	10	$°C^{-1}$
$s_{MV,1\_2}$	Sharpness parameter of the smooth maximum for MV_{1_2}	0.5×10^{7}	-
$s_{g,nv}$	Slope of the differentiable switch function for g_{nv}	100	-
$z_{r,bh}$	Auxiliary parameter to smooth the absolute value function for r_{bh}	1×10^{-4}	°C
$s_{U,b}$	Slope of the differentiable switch function for U_b	6×10^{-7}	s^{-2}
$s_{U,vent,r}$	Slope of the differentiable switch function for $Uvent,r$	6×10^{-6}	s^{-2}
$s_{U,vent,s}$	Slope of the differentiable switch function for $Uvent,s$	6×10^{-6}	s^{-2}
$z_{g,vent,rs}$	Auxiliary parameter to address the scenario where both $A_{vent,r,U}$ and $A_{vent,r,U}$ are zero for determining $g_{vent,rs}$	1×10^{-5}	m^2

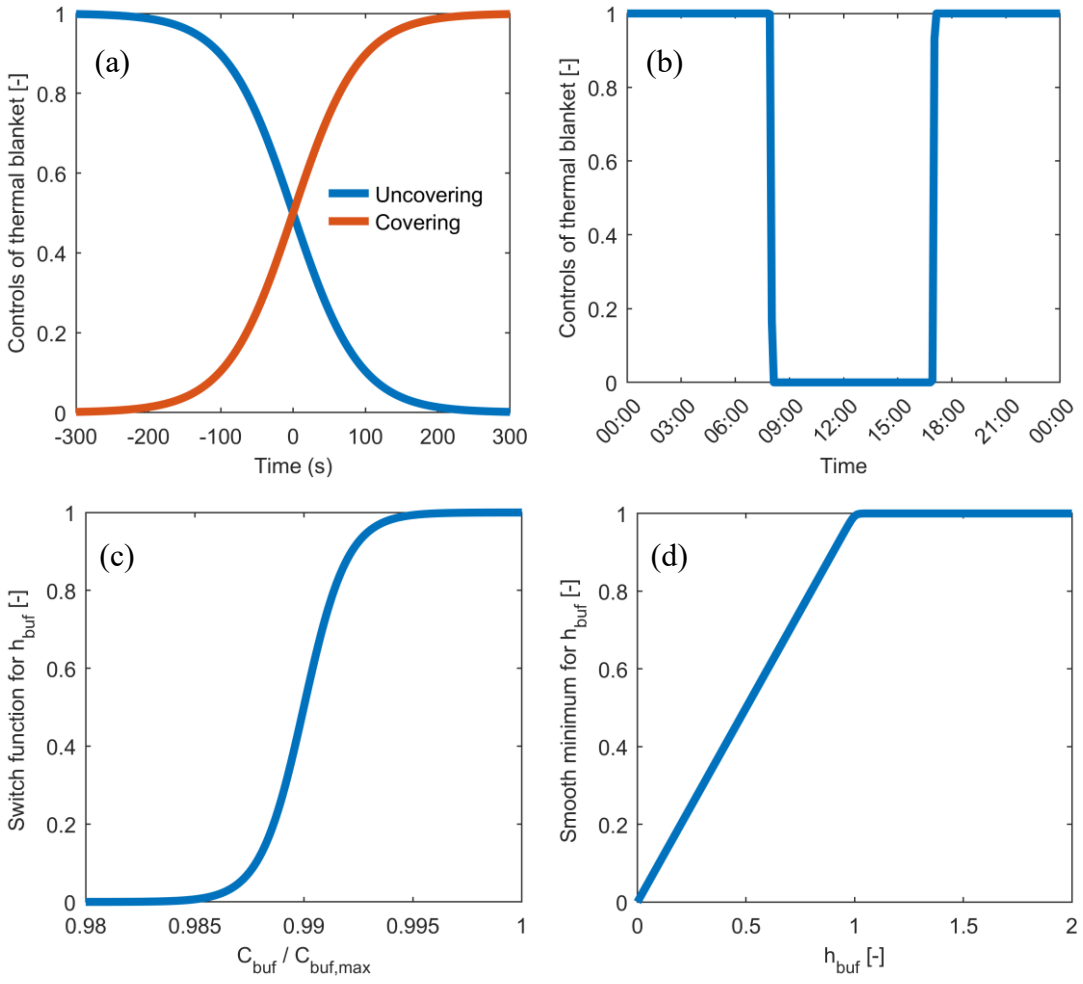

Figure 5.2 Curve patterns of the model smoothing on controls of the thermal blanket and the buffer dependent inhibition function.

5.3 Results and discussion

5.3.1 Validation of the initial integrated model

The integrated CSG climate-crop growth model was validated using data collected in three experiments (Exp_1, Exp_2, and Exp_3), which covered three different seasons, two CSGs with different structural parameters, and three lettuce cultivation scenarios. Figure 5.3 and Figure 5.4 display the measured model input data from Exp_2, including outdoor climate and greenhouse controls. Model inputs from Exp_1 and Exp_3 are detailed in previous chapters. To exclude the potential impact of crop senescence, which is beyond the scope of this study, data from the last five days of all experiments were uniformly discarded. All the constant parameters of the integrated model were consistent with those defined in the individual lettuce growth model and the CSG climate model. The greenhouse dependent parameters from Exp_1 and Exp_3 were also consistent with those used in the validation of the CSG climate model. All the parameters required by the integrated CSG-crop model, including the newly added greenhouse dependent parameters from Exp_2, are summarised in Table 5.2 and Table 5.3.

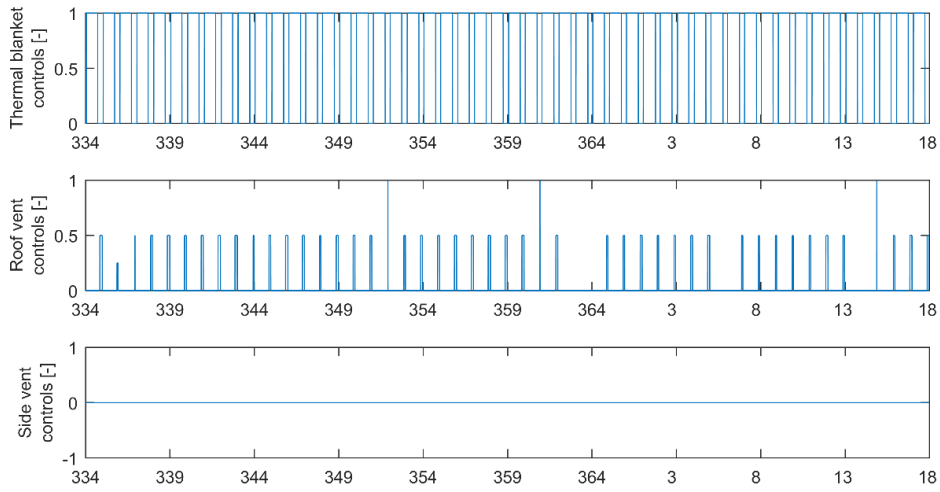

Figure 5.3 Greenhouse controls as model inputs in Exp_2 (15:00, 29 November 2020 – 15:00, 18 January 2021).

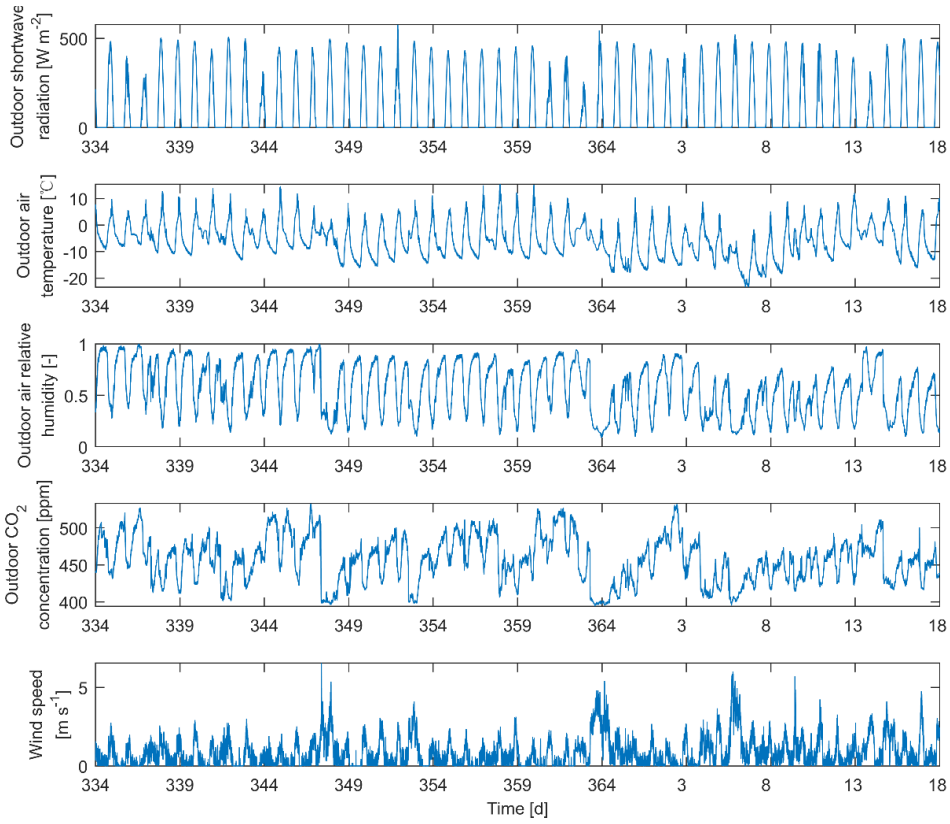

Figure 5.4 Outdoor climate used as model inputs in Exp_2 (15:00, 29 November 2020 – 15:00, 18 January 2021).

Table 5.2 Constant parameters of the integrated CSG climate-crop growth model

Parameter	value	unit
c_H	2.2×10^{5}	J mol^{-1}
$c_{r,I}$	0.22	-
$c_{r,PAR}$	0.07	-
$c_{rc,1}$	0.315	m s^{-1} $°C^{-2}$
$c_{rc,2}$	-27.35	m s^{-1} $°C^{-1}$
$c_{rc,3}$	790.7	m s^{-1}
$c_{Rd,25,r}$	1.16×10^{-7}	kg (CH_2O) kg (dry matter) s^{-1}
$c_{Rd,25,sh}$	3.47×10^{-7}	kg (CH_2O) kg (dry matter) s^{-1}
c_S	710	J mol^{-1} K^{-1}
c_α	0.68	-
c_β	0.8	-

c_{ζ}	1.6	-
$c_{\sigma r,1}$	-0.026	plants kg^{-1}
$c_{\sigma r,2}$	-0.076	-
E_J	3.7×10^{4}	J mol^{-1}
$I_{a,L,ref}$	50.3	W m^{-2} (leaf)
$J_{max,25}$	210.15	µmol (e^-) m^{-2} (leaf) s^{-1}
k_I	0.48	-
k_{PAR}	0.9	-
Le	1.47	-
l_f	0.1	m
M_{CO2}	44×10^{-3}	kg mol^{-1}
$Q_{10,gr}$	1.6	-
$Q_{10,Rd}$	2	-
$Q_{10,\Gamma}$	2	-
R_g	8.314	J mol^{-1} K^{-1}
$RGR_{max,20}$	1.54×10^{-6}	s^{-1}
$r_{H2O,min}$	82	s m^{-1}
r_t	50	s m^{-1}
SLA_{rf}	47.93	m^2 (leaf) kg^{-1} (leaf)
$T_{c,RGR}$	25	°C
v_a	0.09	m s^{-1}
$X_{h,ref}$	0.75	-
β_I	-4.74×10^{-3}	m^2 (leaf) W^{-1}
β_{Xh}	0.912	-
ε_0	17×10^{-9}	kg (CO_2) J^{-1}
$\rho_{CO2,T0}$	1.98	kg m^{-3}
σ_{buf}	0.2	-
σ_{PAR}	0.5	-
Γ_{T20}	40	µmol (CO_2) mol^{-1} (air)
c_d	0.65	-
$c_{p,a}$	1005	J kg^{-1} °C^{-1}
$c_{p,L}$	4.0×10^{3}	J kg^{-1} °C^{-1}
c_T	0.16	m s^{-1} $K^{-1/2}$
$c_{w,cd}$	0.26	-
$c_{w,r}$	0.1	-

$c_{w,rs}$	0.16	-
c_{α}	0.68	-
$c_{\delta\rho,1}$	0.076	plants m^{-2} (leaf)
$c_{\delta\rho,2}$	0.924	kg m^{-2} (leaf)
g	9.8	m s^{-2}
k_I	0.48	-
k_R	0.94	-
Le_v	0.89	-
M_v	18×10^{-3}	kg mol^{-1}
p_b	0.7	-
$Q_{10,Rso}$	3	-
R_g	8.314	J mol^{-1} K^{-1}
$r_{H2O,min}$	82	s m^{-1}
$R_{so,0}$	0.01×10^{-6}	kg (CO_2) m^{-2} (gro) s^{-1}
$T_{0,K}$	273.15	K
$T_{so,cs}$	15	°C
γ	66	Pa $°C^{-1}$
κ_{ice}	0.3	-
$\lambda_{v,d}$	2.83×10^{6}	J kg^{-1}
π_a	1	-
ρ_a	1.20	kg m^{-3}
σ	5.67×10^{-8}	W m^{-2} K^{-4}
σ_{CO2}	1.83×10^{-6}	kg m^{-3} (μmol mol^{-1})$^{-1}$
τ_{ice}	0.6	-
δ_{ice}	0.0001	m
ε_{ice}	1	-
λ_{ice}	2.2	W m^{-1} $°C^{-1}$
ψ_{ice}	0	-
α_{can}	0.78	-
ε_{can}	1.0	-

Table 5.3 Greenhouse dependent parameters of the integrated CSG climate-crop growth model from the three validation experiments

Parameter	value		unit
	CSG for Exp_1	CSG for Exp_2 and Exp_3	
Greenhouse profile			
L_{gro}	7.500	7.550	m
H_{gh}	2.350	3.110	m

A_{gro}	585.0	651.6	m^2
A_{cov}	874.4	1099.9	m^2
V_{gh}	1374.8	2026.4	m^3
L_{c1}	3.078	4.307	m
L_{c2}	7.816	8.143	m
$L_{sr,c}$	7.442	7.458	m
θ_{ghz}	5 ° west of south	5 ° west of south	°
φ	39.62	39.62	°
North wall			
L_{nw}	2.200	3.050	m
θ_{nw}	90	90	°
$\delta_{nw,in}$	0.01	0.01	m
$\alpha_{nw,in}$	0.75	0.75	-
$\varepsilon_{nw,in}$	0.94	0.94	-
$\lambda_{nw,in}$	0.93	0.93	W m^{-1} °C^{-1}
$\rho_{nw,in}$	2100	2100	kg m^{-3}
$c_{p,nw,in}$	900	900	J kg^{-1} °C^{-1}
$\delta_{nw,e}$	0.05	0.1	m
$\varepsilon_{nw,e}$	0.94	0.94	-
$\lambda_{nw,e}$	0.40	0.072	W m^{-1} °C^{-1}
$\rho_{nw,e}$	1220	540	kg m^{-3}
$c_{p,nw,e}$	900	916	J kg^{-1} °C^{-1}
$\delta_{nw(j)}$	$\delta_{nw(1)}$ - $\delta_{nw(3)}$: 0.123	$\delta_{nw(1)}$ - $\delta_{nw(3)}$: 0.135	m
$\lambda_{nw(j)}$	$\lambda_{nw(1)}$ - $\lambda_{nw(3)}$: 0.35	$\lambda_{nw(1)}$ - $\lambda_{nw(3)}$: 0.35	W m^{-1} °C^{-1}
$\rho_{nw(j)}$	$\rho_{nw(1)}$ - $\rho_{nw(3)}$: 1000	$\rho_{nw(1)}$ - $\rho_{nw(3)}$: 1000	kg m^{-3}
$c_{p,nw(j)}$	$c_{p,nw(1)}$ - $c_{p,nw(3)}$: 900	$c_{p,nw(1)}$ - $c_{p,nw(3)}$: 900	J kg^{-1} °C^{-1}
North roof			
L_{nr}	1.055	1.690	m
θ_{nr}	49	39	°
$\alpha_{nr,in}$	0.75	0.75	-
$\varepsilon_{nr,in}$	0.94	0.94	-
$\varepsilon_{nr,e}$	0.94	0.94	-
$\delta_{nr(i)}$	$\delta_{nr\,(1)}$, $\delta_{nr\,(5)}$: 0.002	$\delta_{nr\,(1)}$, $\delta_{nr\,(5)}$: 0.002	m
	$\delta_{nr\,(2)}$, $\delta_{nr\,(4)}$: 0.05	$\delta_{nr\,(2)}$, $\delta_{nr\,(4)}$: 0.05	
	$\delta_{nr\,(3)}$: 0.08	$\delta_{nr\,(3)}$: 0.08	
$\lambda_{nr(i)}$	$\lambda_{nr\,(1)}$, $\lambda_{nr\,(5)}$: 0.93	$\lambda_{nr\,(1)}$, $\lambda_{nr\,(5)}$: 0.93	W m^{-1} °C^{-1}
	$\lambda_{nr\,(2)}$, $\lambda_{nr\,(4)}$: 0.04	$\lambda_{nr\,(2)}$, $\lambda_{nr\,(4)}$: 0.04	
	$\lambda_{nr\,(3)}$: 1.20	$\lambda_{nr\,(3)}$: 1.20	
Indoor floor and soil			
λ_{sm}	1.0	1.4 (Exp_2)	-

		1.0 (Exp_3)	
β_{sml}	0.45	0.65	-
δ_{gro}	0.01	0.01	m
α_{gro}	0.92	0.92	-
ε_{gro}	0.96	0.96	-
λ_{gro}	1.0	1.0	W m^{-1} °C^{-1}
ρ_{gro}	1400	1400	kg m^{-3}
$c_{p,gro}$	1500	1500	J kg^{-1} °C^{-1}
$\delta_{so,cs}$	0.001	0.001	m
$\lambda_{so,cs}$	1.0	1.0	W m^{-1} °C^{-1}
$\delta_{so(\mathrm{i})}$	$\delta_{so(1)} - \delta_{so(2)}$: 0.245	$\delta_{so(1)} - \delta_{so(2)}$: 0.245	m
	$\delta_{so(3)}$: 0.5	$\delta_{so(3)}$: 0.5	
	$\delta_{so(4)}$: 2.0	$\delta_{so(4)}$: 2.0	
$\lambda_{so(\mathrm{i})}$	1.0	1.0	W m^{-1} °C^{-1}
$\rho_{so(\mathrm{i})}$	1400	1400	kg m^{-3}
$c_{p,so(\mathrm{i})}$	1500	1500	J kg^{-1} °C^{-1}
South roof			
L_{sr}	7.955	8.005	m
θ_{sr}	24	33	°
π_{tc}	1.5	1.5	-
δ_{tc}	0.08×10^{-3}	0.08×10^{-3}	m
ε_{tc}	0.15	0.15	-
λ_{tc}	0.13	0.13	W m^{-1} °C^{-1}
τ_{tc}	0.80	0.75 (Exp_2)	-
		0.80 (Exp_3)	
κ_{tc}	0.05	0.15 (Exp_2)	-
		0.05 (Exp_3)	
ψ_{tc}	0.75	0.75	-
$\alpha_{b,o}$	/	0.35	-
$\varepsilon_{b,o}$	/	0.85	-
δ_b	/	0.021	m
λ_b	/	0.04	W m^{-1} °C^{-1}
Vents			
$A_{vent,r}$	31.2	34.5	m^2
$A_{vent,s}$	78.0	86.3	m^2
$H_{vent,r}$	0.018	0.049	m
$H_{vent,rs}$	2.348	3.366	m
ε_{inss}	0.54	0.54	-
η_{inf}	15×10^{-4}	5×10^{-4}	-
Crops			

A_{cul}	261.4	351.5 (Exp_2) 368.8 (Exp_3)	m^2
ρ_c	11.71	11.31 (Exp_2) 11.52 (Exp_3)	plants m^{-2} (gro)

Based on the simulation results presented in Figure 5.5, Figure 5.6, and Figure 5.7, the integrated CSG climate-crop growth model generally exhibited satisfactory simulation accuracy. The *RMSE* ranged from 38.9 to 66.3 W m^{-2}, with the *RRMSE* of 13.0-24.2%, for predicting shortwave radiation at the top of the canopy. The *RMSE* ranged from 2.7 to 3.2 ℃, with the *RRMSE* of 14.2-26.6%, for predicting indoor air temperature. The *RMSE* ranged from 0.09 to 0.26, with the *RRMSE* of 17.8-32.0%, for predicting relative humidity of indoor air. The *RMSE* ranged from 12 to 100 ppm, with the *RRMSE* of 3.0-17.7%, for predicting CO_2 concentration of indoor air. The *RMSE* ranged from 0.0108-0.0158 kg m^{-2} (gro), with the *RRMSE* of 25.1-40.7%, in simulating the crop dry weight of the lettuce. The *RMSE* = 0.7989-1.3507 (leaf) m^{-2} (gro), with the *RRMSE* of 58.5-98.4% in simulating the leaf area index of the lettuce. The model demonstrated excellent to acceptable performance in predicting the four key climate attributes directly regulated by greenhouse controls, as well as the crop biomass that constitutes the final output of the greenhouse production process, across most CSG cultivation scenarios. Therefore, this model is considered suitable for use in optimal management of the CSG climate.

The integrated model exhibited varying performance in simulating different states and the same states under different scenarios. In terms of greenhouse climate simulation, the integrated model performed better in the CSG production scenario of Exp_1 compared to Exp_2 and Exp_3, across all four climate variables. Apart from the model descriptions discussed in Chapter 4 as potential directions for improving accuracy, several other factors may explain this difference. First, greenhouse controls in the experiments were manually operated and recorded by the growers. While Exp_2 and Exp_3 involved daily control actions, Exp_1 did not use the thermal blanket, with the roof and side vents remaining open unless extreme weather occurred, which helped reduce errors from control inputs. Second, Exp_2 and Exp_3 were conducted in the same CSG, with structural parameters that differed

significantly from those of the CSG used for Exp_1. Since the model includes many greenhouse-dependent parameters, such values used in Exp_1 may have been closer to actual conditions.

The simulated CSG climates did not show significant differences compared to the simulated results of the CSG climate model presented in Chapter 4, which was consistent with the research conducted by Van Henten (1994a). In the evaluation of the CSG climate model, measured crop states were used as inputs, whereas in the integrated model, they acted as outputs. Meanwhile, during the later stages of crop growth, the simulated crop states showed significant positive deviations from the measurements, especially in terms of the leaf area index. This indicates that the outputs and overall performance of the CSG climate simulations are not highly sensitive to disturbances in crop inputs, which may explain why most greenhouse climate models set crop status as a fixed value (R. Liu et al., 2021; Vanthoor, Stanghellini, et al., 2011).

Conversely, compared to the individual lettuce growth model, the integrated model overestimated the biomass and leaf area index more severely in the later stages of crop growth. Obviously, the performance differences originated from prediction errors in the greenhouse climate (Figure 5.5, Figure 5.6, and Figure 5.7), more likely due to an overestimation of humidity levels that further influenced the specific leaf area of crop leaves. Unlike periodic changes in the greenhouse climate, crop growth accumulated these errors, leading to a decline in model performance in simulating crop dynamics. In addition, the integrated model showed similar performance trends to the crop model, achieving acceptable performance in simulating crop biomass in Exp_2 and Exp_3 conducted during the cold and cold-warm seasons. Crop production over cold seasons is the primary function of the CSG system and, naturally, the scenario that optimal climate control should focus on the most. Although the model slightly exceeded the pre-set acceptable range of performance during warm seasons, it remains usable. In practice, control algorithms that utilise receding horizon (D. Xu et al., 2018) and crop information feedback (Mao, Jin, & Chen, 2018) will further enhance the robustness of the model and control system.

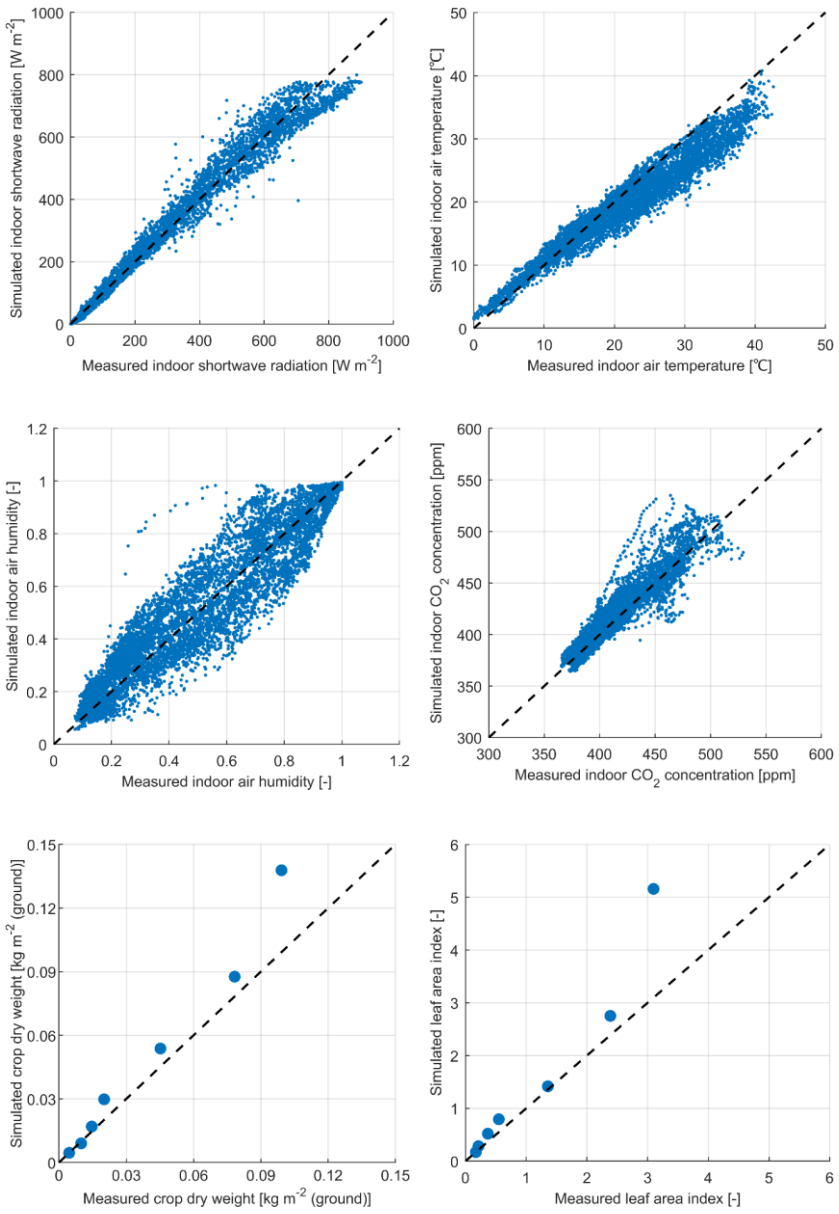

Figure 5.5 Five-minute averages of the indoor shortwave radiation, air temperature, relative humidity, and CO_2 concentration, as well as crop dry weight and leaf area index every five days, simulated by the integrated model versus the measured values during Exp_1. Data were selected from 17:00, 9 April 2020 to 17:00, 9 May 2020. *RMSE* = 38.9 W m^{-2} and *RRMSE* = 13.0% for prediction of shortwave radiation at the top of the canopy. *RMSE* = 2.7 ℃ and *RRMSE* = 14.2% for prediction of indoor air temperature. *RMSE* = 0.09 and *RRMSE* = 17.8% for prediction of indoor relative humidity. *RMSE* = 12 ppm and *RRMSE* = 3.0% for prediction of indoor CO_2 concentration. *RMSE* = 0.0158 kg m^{-2} (gro) and *RRMSE* = 40.7% in simulating the crop dry weight of the lettuce. *RMSE* = 0.7989 (leaf) m^{-2} (gro) and *RRMSE* = 68.7% in simulating the leaf area index of the lettuce.

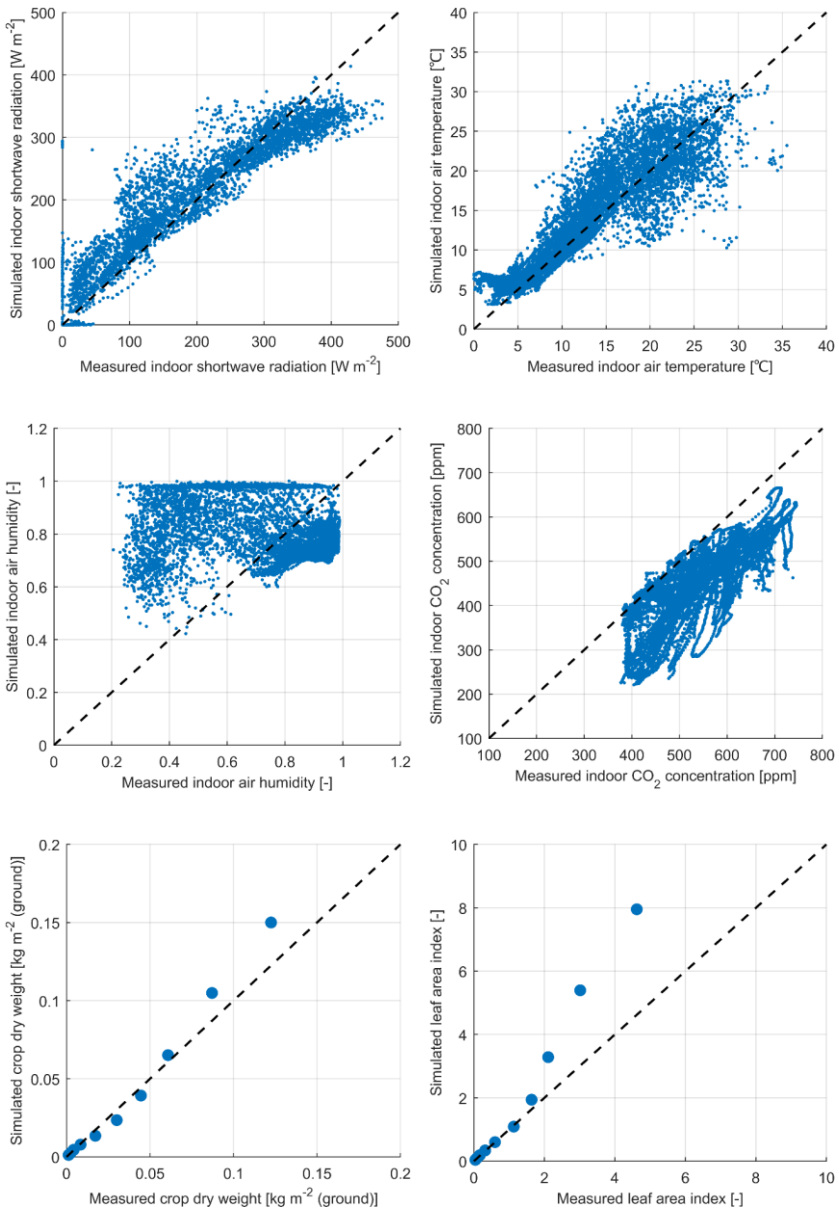

Figure 5.6 Five-minute averages of the indoor shortwave radiation, air temperature, relative humidity, and CO_2 concentration, as well as crop dry weight and leaf area index every five days, simulated by the integrated model versus the measured values during Exp_2. Data were selected from 15:00, 29 November 2020 to 15:00, 18 January 2021. *RMSE* = 48.8 W m^{-2} and *RRMSE* = 24.2% for prediction of shortwave radiation at the top of the canopy. *RMSE* = 2.8 ℃ and *RRMSE* = 26.6% for prediction of indoor air temperature. *RMSE* = 0.25 and *RRMSE* = 30.4% for prediction of indoor relative humidity. *RMSE* = 100 ppm and *RRMSE* = 17.7% for prediction of indoor CO_2 concentration. *RMSE* = 0.0108 kg m^{-2} (gro) and *RRMSE* = 28.6% in simulating the crop dry weight of the lettuce. *RMSE* = 1.3507 (leaf) m^{-2} (gro) and *RRMSE* = 98.4% in simulating the leaf area index of the lettuce.

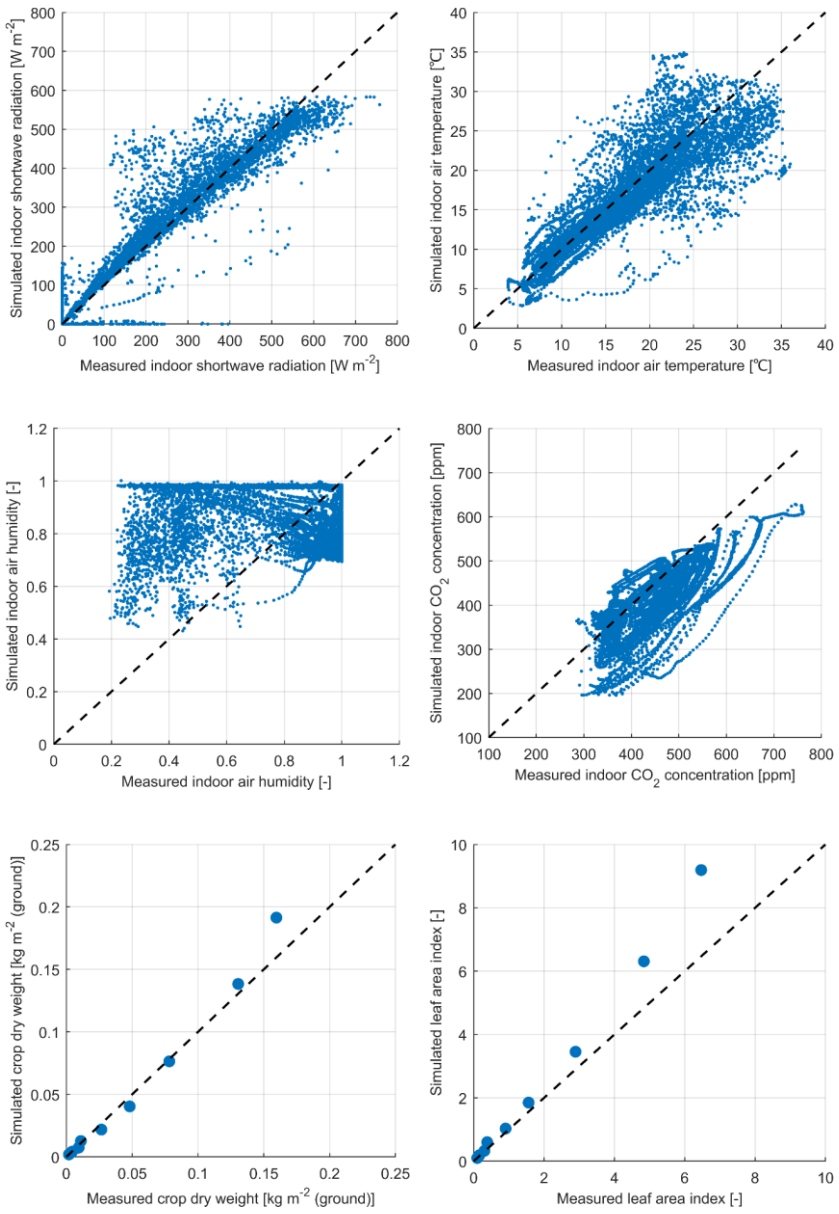

Figure 5.7 Five-minute averages of the indoor shortwave radiation, air temperature, relative humidity, and CO_2 concentration, as well as crop dry weight and leaf area index every five days, simulated by the integrated model versus the measured values during Exp_3. Data were selected from 15:00, 30 January 2022 to 15:00, 11 March 2022. *RMSE* = 66.3 W m^{-2} and *RRMSE* = 22.9% for prediction of shortwave radiation at the top of the canopy. *RMSE* = 3.2 ℃ and *RRMSE* = 20.5% for prediction of indoor air temperature. *RMSE* = 0.26 and *RRMSE* = 32.0% for prediction of indoor relative humidity. *RMSE* = 56 ppm and *RRMSE* = 12.0% for prediction of indoor CO_2 concentration. *RMSE* = 0.0131 kg m^{-2} (gro) and *RRMSE* = 25.1% in simulating the crop dry weight of the lettuce. *RMSE* = 1.1436 (leaf) m^{-2} (gro) and *RRMSE* = 58.5% in simulating the leaf area index of the lettuce.

5.3.2 Impact of control schemes on greenhouse production output

Before applying optimal control theory to CSG cultivation, it is necessary to investigate the potential for economic improvement by comparing control scenarios determined by different growers and controllers in practice. The integrated model developed in this study, as a comprehensive, science-based, dynamic model of the CSG-crop system, can conduct this work through simulation. The majority of present CSGs are low-tech and lack automatic control systems (Qi et al., 2017). Climate control in such standard CSGs is manually manipulated and relies on the grower's experience and even on his labour time. The controllers utilised in CSGs are simple, featuring primarily on-off and PI-like mechanisms (R. Cao et al., 2020; X. Yang, Zhu, Jiang, Huang, & Li, 2014). In contrast to multi-span greenhouses, where climate controllers manage all climate conditioning equipment through 24-hour setpoints of greenhouse climates and control constraints of equipment (Aaslyng, Lund, Ehler, & Rosenqvist, 2003; management, 2024; Priva, 2024), the CSGs have fewer controllable elements and typically directly set points for each device, employing a simpler control logic. Moreover, indoor temperature is the primary focus of CSG climate management, and humidity control not subject to temperature regulation is often completed within an extremely short time frame. Thus, four control schemes commonly used in practical CSG production, including the manual control, timer control, on-off control, and proportional control, were used to do the modelling exploratory. The aim was to assess the impact of different climate control scenarios on the outputs of the CSG cultivation.

To accomplish this, test scenarios were selected from a period of 10 consecutive days in the second half of Exp_3. This 10-day period was representative, covering a range of weather conditions from cold to warm, during which the thermal blanket and vents required daily operation. During this period, the crop status was also ideal, ensuring strong interactions between the greenhouse climate and crops, and allowing the integrated model to perform well in simulating lettuce growth. The control schemes are detailed as follows:

- Manual control: CSG climate control was supervised by the grower, with adjustments of the thermal blanket, roof and side vents achieved entirely by hand.

The manual control strategy used for comparative analysis originated from the actual operations conducted in Exp_3.

- Timer control: The roof vent was fully opened from 11:00 to 14:00, denoted as $U_{vent,r}$ = 1; during other times, it was completely closed, thus $U_{vent,r}$ = 0. The side vent remained continuously closed, thus $U_{vent,s}$ = 0. The thermal blanket fully covered the south roof from 16:30 to 08:00 the next day, indicated by U_b = 1; during other times, it was completely rolled up, thus U_b = 0.
- On-off control: When X_t > 27 °C, $U_{vent,r}$ = 1; when $X_t \leq$ 23 °C, $U_{vent,r}$ = 0; when 23 < $X_t \leq$ 27 °C, no actions. When X_t > 30 °C, $U_{vent,s}$ = 1; when $X_t \leq$ 25 °C, $U_{vent,s}$ = 0; when 25 < $X_t \leq$ 30 °C, no actions. When I_{out} > 50 W m^{-2}, U_b = 0; when $I_{out} \leq$ 50 W m^{-2}, U_b = 1.
- Proportional control: $U_{vent,r} = 0.25 \cdot (X_t - 25), 0 \leq U_{vent,r} \leq 1$; $U_{vent,s} = 0.5 \cdot (X_t - 32), 0 \leq U_{vent,s} \leq 1$; When $I_{out} \leq$ 10 W m^{-2}, or $I_{out} \leq$ 50 W m^{-2} $\cap$ $X_t \leq$ 20 °C, U_b = 1; otherwise, U_b = 0.

As shown in Figure 5.8, distinct differences existed in the daily average and accumulated values of indoor climate, as well as in the crop output, under different CSG climate control schemes over a 10-day period. The largest difference in daily averages of indoor air temperature reached 1.6 °C, corresponding to a maximum relative difference of 10%. For relative humidity, the maximum daily average difference was 0.08, also with a relative difference of up to 10%. The maximum difference in daily average CO_2 concentration was 37 ppm, with a relative difference of 9%, and the maximum difference in daily accumulated shortwave radiation was 0.6 MJ d^{-1}, with a relative difference of 6%. After ten days of differentiated greenhouse control, the maximum relative difference in the final crop dry mass reached 4%. For standard CSGs, without additional energy-consuming devices, the crop production output can serve as a measure of the net revenue from CSG cultivation. Therefore, different practical control schemes significantly affected the economic performance of crop production in standard CSGs. This emphasises the importance of optimising CSG climate management, even in standard CSGs where little seems to be controllable, motivating the implementation of optimal climate controls. It was also observed that the CSG system, when

supervised and manually controlled by the grower, yielded the highest crop output, while the dry weight of these crops was generally lower than those under other controls over most of the period. This indicates potential for further optimisation, both in manual control by experienced growers and in rule-based controller setpoints.

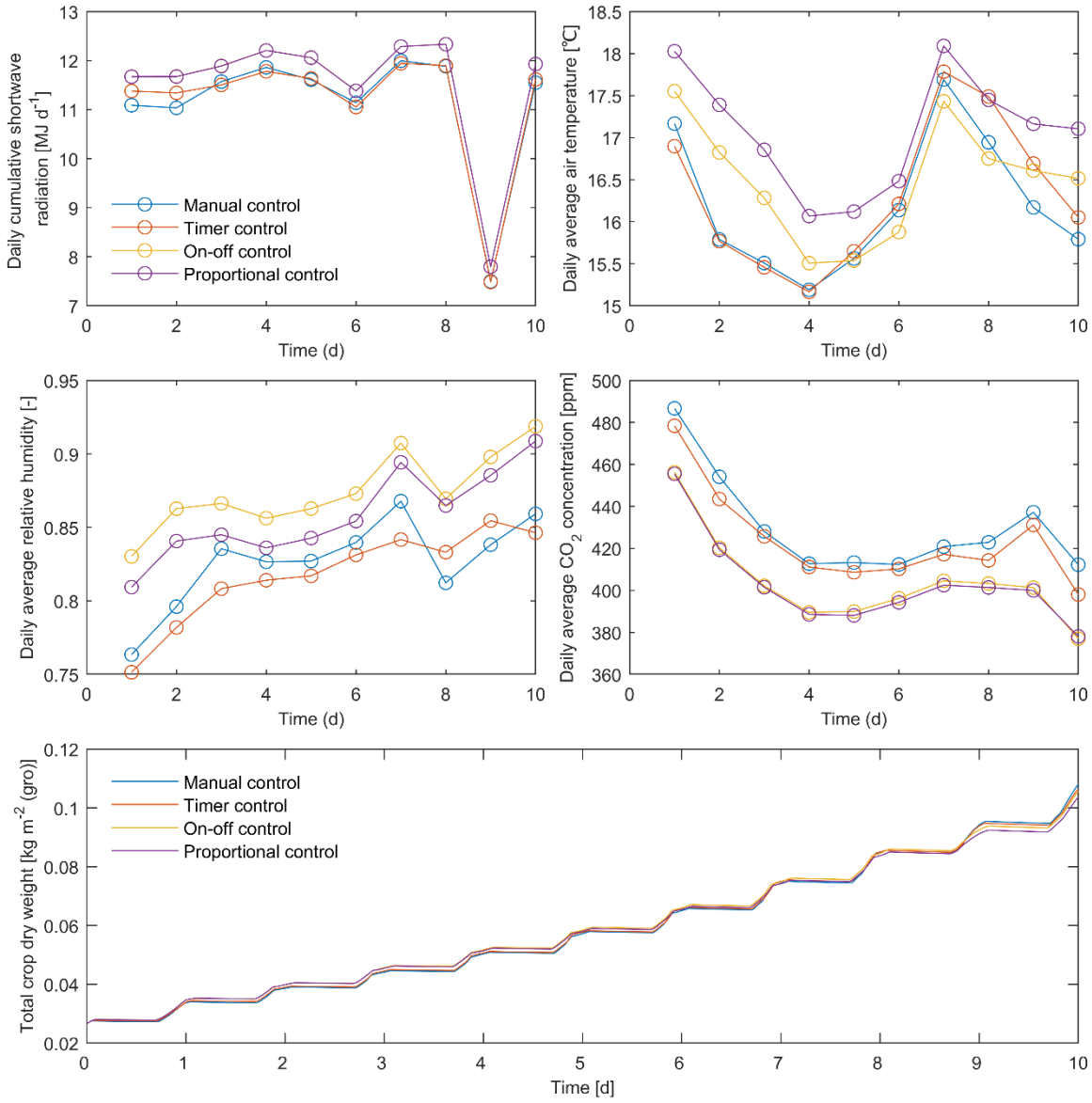

Figure 5.8 Comparison of indoor climates and crop production outputs under different CSG climate control schemes. The modelling exploratory was conducted based on the greenhouse production scenario of Exp_3 from 15:00, 19 February 2022, to 15:00, 1 March 2022.

5.3.3 Evaluation of the smoothed integrated model

The integrated CSG climate-crop growth model was smoothed by substituting the original formulas with the smoothed equations and introduced parameters in Section 5.2.2. The smoothed model was evaluated using the same outdoor climate data and constant and greenhouse-dependent parameters as those used in the integrated model. As detailed in Table 5.4, the smoothing not only enhanced the computational efficiency of the integrated model but also generally improved its predictive performance. This contrasts with the findings of Vanthoor, Stanghellini, et al. (2011), who reported no discrepancies in output between the initial and smoothed greenhouse climate models. Specifically, in Exp_1, compared to the initial model (Figure 5.5), the smoothed model maintained or slightly improved its prediction accuracy for the four greenhouse climate attributes and two crop states, a trend that was also observed in Exp_3 (Figure 5.7). In Exp_2, the smoothed model presented a slight performance decrease in predicting shortwave radiation and CO_2 concentration, as well as a minor increase for humidity and a substantial increase (with *RRMSE* being reduced from 26.6% to 23.6%) for temperature predictions (Figure 5.6). The most significant improvements were observed in the prediction of crop states, with the *RRMSE* for predicting the total crop dry weight decreasing from 28.6% to 18.7%.

Figure 5.9 presents a five-day sample from the simulation based on Exp_2, comparing the trajectories of the simulated CSG climates, crop states, and intermediate variables between the initial model and the smoothed model. The smoothed controls of the thermal blanket enabled the model to achieve higher accuracy in radiation simulations over a cumulative period of 30 minutes during the covering and rolling up events in comparison to controls in the initial model, which were assumed to be instantaneously completed and were managed through interpolation within the program. Differences in greenhouse air temperature and humidity arose due to the two kinds of thermal blanket controls but then disappeared quickly. Moreover, the smoothed model showed a slight overall increase in *RRMSE* for radiation predictions, likely due to the offsetting effects of other shortwave radiation related smoothing processes. However, these observations do not imply that capturing movements

of the thermal blanket is irrelevant to enhancing model performance, given that crop growth integrates instantaneous responses to climate dynamics.

The two models exhibited significant differences in the simulation of indoor air temperature and humidity during the latter parts of some nights; the initial model tended to overestimate these variables, whereas the smoothed model showed closer agreement with the measurements. This is most likely induced by the smoothing of the ice layer formation and the latent heat flux switches. Correspondingly, during these latter parts of the night, the simulated convective heat flux from the internal surface of the south roof to indoor air by the smoothed model exhibited lower levels and more stable change curves. The smoothing of model descriptions and control inputs finally led to differences in the simulation results for crop status between the two models, with the deviation increasing as the simulation progressed. The sample was selected from the first half of the lettuce growth cycle, during which the smoothed model simulated lower crop states. Based on the experience of model calibration in Chapter 3, suppressing crop growth appropriately during the early stages of the growth cycle has potential to improve the model accuracy at harvest and achieve a higher overall performance. As indicated by this empirical rule, the smoothed model performed substantially better in predicting crop states during Exp_2 (Table 5.4).

Table 5.4 *RRMSE* of the smoothed integrated model for predicting CSG climates and crop states across the three validation experiments.

Model states	*RRMSE*		
	Exp_1	Exp_2	Exp_3
I	12.9%	25.2%	23.5%
X_t	14.2%	23.6%	20.5%
X_h	17.8%	29.6%	31.9%
X_c	3.0%	18.0%	12.1%
X_d	40.4%	18.7%	24.1%
LAI	68.5%	82.2%	56.5%

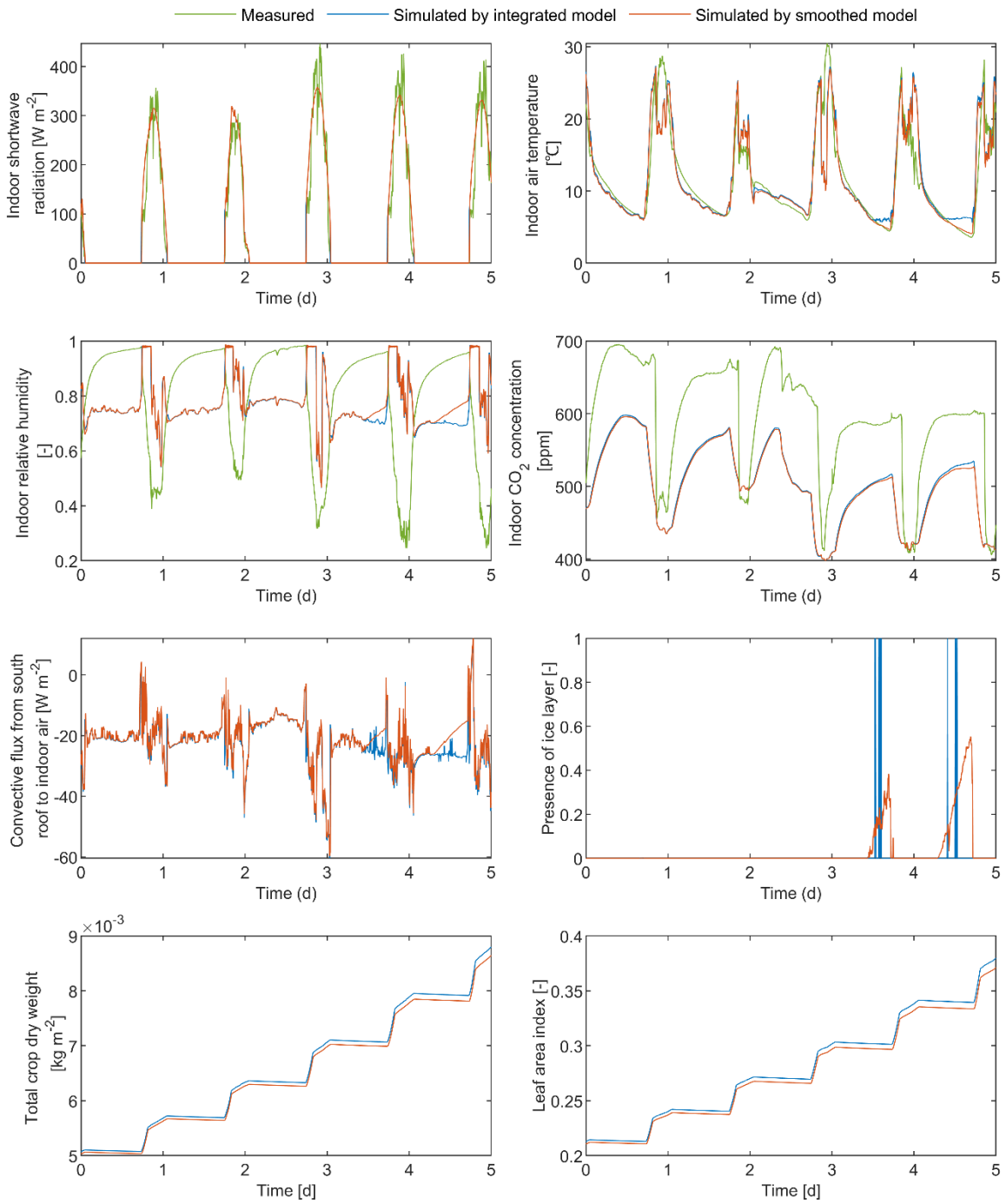

Figure 5.9 Sample of the simulated greenhouse climate, crop state and intermediate variable trajectories by the integrated mode and its smoothed version, along with the measured climate states. The sample simulations span from 15:00, 10 December 2020, to 15:00, 15 December 2020, during Exp_2.

5.3.4 Applicability, limitations, and improvement directions

This study developed an integrated CSG climate-crop growth model by combining the lettuce growth model and CSG climate model presented in previous chapters, accompanied by thorough validation. The model demonstrated satisfactory accuracy for optimal control and identified the opportunities for economic improvement of the standard CSG production systems. To further improve computational efficiency and adaptability, the model descriptions and control inputs were smoothed, resulting in enhanced performance. This represents the first instance of a process-based integrated model, as well as its smoothed version, that comprehensively simulates the CSG lettuce production process with acceptable accuracy and high computation efficiency for control purposes.

Similar to the lettuce growth model, the integrated model tended to overestimate biomass near harvest, but with greater deviations since it accumulated the effects of the greenhouse climate prediction errors. The potential directions for model accuracy improvement are as follows. First, the buffer dependent inhibition function for canopy assimilation needs to be optimised to remain effective at high dry matter levels. Second, since the performance in humidity predictions is notably poorer, and model smoothing has not led to a significant improvement, it is crucial to emphasise the optimisation of vapour flux descriptions. Zhou et al. (2023) employed a particle filter to calibrate five parameters of a process-based greenhouse climate-tomato model. This approach successfully reduced the *RRMSE* for air vapour pressure predictions from 40.7% to 16.4%, offering a potential method for model accuracy improvement. Third, distinguishing the crop growth responses to direct and diffuse radiations, while also differentiating these radiations in greenhouse climate simulations.

To further improve the universality of the model, one could consider converting the energy balance equations of the south and north roofs to differential equations. The computational efficiency losses caused by increased model dimensions can be compensated by defining appropriate surfaces and layers of the CSG objects. The smoothing process introduces numerous parameters into the model, which can lead to uncertainty in the predictions (Payne,

van Henten, & van Mourik, 2024) and must be carefully calibrated to boost accuracy and stability. Control inputs of the smoothed model will utilise data in the form of state switching points. Additionally, combining machine learning technology with process-based model development, especially in terms of model structure optimisation and parameter identification (Y. Guo, Zhao, Zhang, Wang, & Chow, 2021; Zhou et al., 2023), has considerable potential to improve the accuracy, computational efficiency, and generalisation of the model.

Although mechanistic models inherently possess high computational efficiency, it is favourable to work with a simpler yet relatively high-precision system model (Van Ooteghem, 2010), especially for on-line controls. Given that the developed integrated CSG-crop model already employs as few state variables and outdoor climate inputs as possible, and greenhouse control inputs are essential, the potential simplification of the integrated model should primarily focus more on modifying intermediate (auxiliary) variables based on sensitivity analysis. Setting some intermediate variables as constants can reduce the number of computational processes and further enhance simulation efficiency. The method for simplifying the integrated model, as well as its impact on model performance, will be explored in the future study.

5.4 Summary

An integrated model of CSG climate and crop growth for control, along with its smoothed version, has been meticulously developed and rigorously validated. The integrated CSG climate-crop growth model provides a comprehensive depiction of the entire CSG lettuce production process, elucidating the influence of outdoor climate, greenhouse structure, and greenhouse controls on the dynamics of indoor climate and crop state. Its formulation involved the amalgamation of the lettuce growth model and CSG climate model developed in previous chapters, harmonizing all their state variables into a cohesive and unified description.

The integrated model was validated using data from three different seasons, two CSGs with different structural parameters, and three lettuce cultivation scenarios. It demonstrated an overall satisfactory performance for optimal control, with *RRMSE* being 13.0-24.2% for predicting shortwave radiation at the top of the canopy, 14.2-26.6% for indoor air temperature, 17.8-32.0% for relative humidity, 3.0-17.7% for CO_2 concentration, and 25.1-40.7% for crop dry weight of the lettuce throughout the entire growth cycle. Exploratory modelling revealed that implementing different practical control schemes over a 10-day period could lead to a 4% difference in the final crop dry mass and net economic return in standard CSGs. This highlights potential for further optimisation in both manual control and controller setpoints and motivating the application of optimal control theory to the standard CSG cultivation.

To enhance computational efficiency and adaptability of the integrated model, model smoothing, particularly of conditional statements and control inputs, was performed. The smoothed model exhibited a general improvement in predictive performance, notably in predicting crop states, with the *RRMSE* for total crop dry weight being decreasing from the initial 28.6% to 18.7%. The integrated CSG-crop model, along with its smoothed version, will serve as a foundation for investigating the optimally controlled CSG systems.

Chapter 6

Event-driven receding horizon optimal control of Chinese solar greenhouse climate

Based on the opportunities for economic improvement in standard CSG cultivation identified in Chapter 5, this chapter presents an optimal climate control system for crop production in a standard CSG without a local controller. The control algorithm employs an event-driven receding horizon design with real-time feedback to enhance system robustness and ensure user-friendliness. Three optimal control approaches, along with grower-supervised control, will be evaluated through comparative simulation trials.

6.1 Introduction

In practical production, climate control for CSGs is mainly based on experience and implemented through manual operations or simple on-off and PI-like controllers (R. Cao et al., 2020; X. Yang et al., 2014). These control strategies have significant potential for optimisation. For example, in a CSG with standard configurations, adopting different practical control schemes can result in a 4% difference in net revenue within just 10 days (see Chapter 5). Given the enormous scale of CSG cultivation (see Chapter 4), any improvement in control efficiency can lead to substantial economic growth in the industry. Therefore, optimising greenhouse climate control is essential. Although the investigations into control optimisation can assume potential application scenarios, it is crucial for these approaches to be based on the current state of the industry, target specific greenhouse production systems, and consider user acceptance. Meeting these requirements can drive the practical application of optimised control approaches, ultimately benefiting the industry economically.

The greenhouse industry has explored numerous approaches for climate control, aiming to improve economic performance (Golzar, Heeren, Hellweg, & Roshandel, 2021), enhance energy efficiency (Körner & Van Straten, 2008; Lin et al., 2021), or optimise controller performance (Bennis, Duplaix, Enéa, Haloua, & Youlal, 2008). These approaches fall into different control theory classifications: classical control, such as proportional-integral-derivative (PID) control (Su, Yu, & Zeng, 2020); modern control, including optimal control (Van Straten et al., 2010) and model predictive control (MPC) (Lin et al., 2021); intelligent control, such as neural network method (Ido Seginer, 1997) and fuzzy control (Castañeda-Miranda, Ventura-Ramos, del Rocío Peniche-Vera, & Herrera-Ruiz, 2006); as well as hybrid control, for example neural networks based on PID control (Qu, Ning, Lai, Cheng, & Mu, 2011). Each method is designed to meet different automation control needs and controller design considerations. The sustainable development of the greenhouse industry lies in maximising the economic benefits of crop production. From the perspective of greenhouse climate management, this requires balancing the operational costs of the climate

conditioning equipment with the marketable crop product, which falls within the scope of optimal control. Greenhouse production systems are multi-input multi-output (MIMO) systems, where external weather and greenhouse controls influence greenhouse states, and the climate and crop states interact with each other. PID control, based on transfer functions, is suited for single-input single-output (SISO) systems and relies on the designer's experience for tuning, making it inadequate for handling complex greenhouse control problems (Su et al., 2020). In contrast, optimal control uses state-space methods with first-order differential equations to describe system dynamics and set optimisation goals, enabling effective MIMO system control. Furthermore, the theoretical framework of optimal control can integrate artificial intelligence algorithms during the optimisation phase (Jin et al., 2020) and utilise data-driven models for system description (Mahmood, Govindan, Bermak, Yang, & Al-Ansari, 2023), demonstrating strong compatibility. Compared to purely intelligent control algorithms, optimal control, typically employing process models, offers greater interpretability and generalisation capabilities in addressing control and optimisation problems. Meanwhile, it has a stronger capability to handle the constraints explicitly (Morcego et al., 2023). As a result, optimal control theory is highly favoured in greenhouse climate control and has seen significant development in recent years.

Compared to conventional control, optimal control can significantly improve the production efficiency of greenhouse systems. For instance, in greenhouse tomato production, optimal control can improve energy efficiency by 8% (Tap, 2000), reduce control costs by 20% (W.-H. Chen et al., 2022), and boost net economic returns by up to 27% (Chalabi et al., 2002a). Additionally, equipping greenhouses with more climate regulation devices can provide further opportunities for optimisation, improving net profits up to 32% in greenhouse lettuce production (Dan Xu et al., 2018). However, due to uncertainties in the system model and weather forecast, optimal control aiming to achieve the global optimum over the entire crop growth cycle cannot be directly applied in practice. This limitation has led to the development of various optimal control algorithms and systems for robust practical application. These algorithms implement feedback through a receding horizon to achieve closed loop control, known as suboptimal control or MPC. Both optimal control and MPC

aim to maximise or minimise control functionals based on models (Mayne, 2014; Van Straten et al., 2010), with the primary difference being the control horizon for optimisation. Their hierarchical relationship remains under discussion. This study proposes that MPC is a specific implementation of optimal control theory, where optimal control theory provides the fundamental mathematical framework and methods, while MPC applies this theory to practical prediction and control problems in the greenhouse crop production process.

Specifically, to put optimal control into practice, Van Beveren et al. (2015) developed an optimisation framework for greenhouse heating and cooling that allows growers to modify indoor climate bounds, potentially reducing energy consumption by 47% in heating and 15% in cooling, with a 10% reduction in CO_2 injection. W.-H. Chen et al. (2022) developed a novel nonlinear model predictive control framework for greenhouse climate control to minimise the total control cost mainly coming from energy use. In order to deal with rapidly fluctuating disturbances of external inputs, Van Henten and Bontsema (2009) proposed a two time-scale decomposition for the optimal control problem in greenhouse climate management based on singular perturbation theory. This hierarchical approach was also employed by Tap (2000) for tomato cultivation and extended by D. Xu et al. (2018) with online parameter estimation for generating an adaptive controller. In addition, Kuijpers et al. (2022) found that a receding horizon of 15 minutes contributed to the mitigation of the effect of weather prediction uncertainties on the performance of the optimally controlled greenhouses. However, these optimal control approaches primarily address the climate management of multi-span greenhouses, with limited research on CSGs that have significant differences in greenhouse structure and supporting equipment. In order to effectively apply optimal control theory to practical CSG cultivation, it is necessary to investigate optimal control systems of CSG climate based on models that explicitly describe the entire greenhouse crop production process specific to CSG and develop user-friendly optimal control algorithms that meet practical industry needs.

A pilot study on the optimal control system for CSG climate management was conducted by Dan Xu et al. (2018). They applied a two time-scale receding horizon optimal control to a

high-tech CSG cultivating lettuce. The study investigated the economic improvements by introducing an online controller in combination with the additional supply of heat, CO_2, ventilation, and artificial light. The CSG-crop model used in this study was adapted from Van Henten (2003). The main addition to the original scheme of Van Henten (1994a) was the introduction of the state of the north wall temperature as well as control inputs of the thermal blanket and artificial lighting. However, this study did not focus on the control optimisation of the standard CSG itself, which constitutes the majority of CSGs and typically involves only the thermal blanket and ventilation openings without a local controller. Thus, although this study contributes to the theoretical development of CSG optimal control, the developed control algorithm may not be applicable to most CSG production systems. Meanwhile, the potential for improving the economic performance of crop production inside standard CSGs by using optimal climate control remains to be explored.

The optimal control systems reported so far have not yet been implemented in commercial greenhouses (Van Beveren et al., 2015). This fact is partly due to the lack of corresponding hardware support for controllers. Another crucial factor is that growers lack confidence in optimal control or are reluctant to accept the decision support system (DSS) working modes, which mainly depend on control algorithms. For the development of an optimal climate control system tailored to standard CSGs, the optimal control algorithm is expected to possess the following characteristics:

1. Target CSGs lacking local controllers and reliant on manual control.
2. Designed for decision support, delivering grower-accepted and efficient guidance for climate control decision-making.
3. Focused on the grower, fully considering the grower's control objective, acceptable labour input, and available manual operations.
4. Ensure the robustness of the control system, even accommodating growers who sometimes choose not to follow the control action advice.

In summary, a user-friendly optimal climate control system for crop production in a standard CSG without the local controller is currently unavailable. The objective of this chapter is to

develop, analyse, and evaluate such a system. The process-based integrated model of CSG climate and crop growth presented in Chapter 5 demonstrated acceptable simulation accuracy and high computation efficiency, making it a suitable basis for the optimal control system. Consequently, the system development will focus on formulating the optimal control algorithm. This algorithm employs an event-driven receding horizon design with real-time feedback to enhance system robustness while ensuring user-friendliness. Next, a comparative study will be conducted between three control approaches: ideal optimal control, open loop optimal control, and control based on the grower's experience. These comparative simulations aim to address the research question: What is the potential economic improvement of a standard CSG using optimal control compared to conventional control supervised by the grower? The feasibility of implementing closed-loop optimal control will be investigated, addressing the following research question: To what extent can the efficiency of CSG production achieved by optimal control be realised in practical production? Finally, the study will discuss the simplification of the system model, methods for solving the optimal control problem, limitations of the research outputs, and future research prospects. This study will provide an optimisation framework for the efficient climate management of standard CSGs, promoting the application of optimal control theory in practical CSG production.

6.2 Optimal control system formulation

The optimal control system developed in this study is designed for climate management during the crop production process of a standard CSG without the local controller. Using an event-driven receding horizon design incorporated with real-time feedback, it functions as a DSS for growers (Figure 6.1). The system does not replace the current manual control in CSG cultivation but provides growers with more efficient, grower-accepted advice for climate control decision-making. The development of this system integrates the system model with the optimal control algorithm. The optimal control algorithm, consisting of optimal control problem definition and the overall control process planning (controller design), is centred around the grower, fully considering the grower's greenhouse production

objective, acceptable labour input, and the accuracy of manual operations.

To conduct comparative research and thoroughly explore the economic performance of CSG crop production using optimal climate control theory, this study will involve four control algorithms, defined as follows:

1. **Ideal optimal control**: Open loop optimal control where greenhouse control inputs are assumed to have continuous adjustment without restriction on operation frequency. This approach aims to reveal the maximum potential of production performance in standard configuration CSGs.
2. **Open loop optimal control**: Open loop optimal control that employs the same problem definition as the event-driven receding horizon optimal control, with control inputs following the manual control practices of the grower. This approach explores the potential of production performance in standard CSGs without the local controller.
3. **Conventional control**: Climate control supervised by the grower.
4. **Closed loop optimal control**: Event-driven receding horizon optimal control with real-time feedback, also referred to as model predictive control or sub-optimal control.

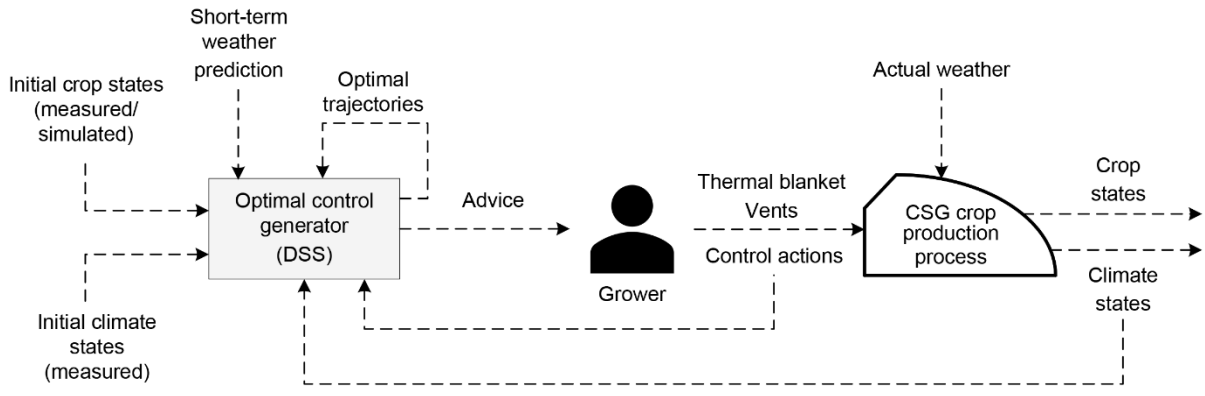

Figure 6.1 The event-driven receding horizon optimal control system designed for the CSG cultivation. The text blocks are design elements, and the dashed lines are information flows.

6.2.1 System model

The integrated CSG climate-crop growth model developed in Chapter 5 serves as the system model for the optimal control of this study. According to the model descriptions, the CSG lettuce production process is a MIMO system with numerous inputs and outputs. Among these, greenhouse controls, including the thermal blanket U_b, roof vent $U_{vent,r}$, and side vent $U_{vent,s}$, are the decision variables for the optimal control system. For a given CSG and a specific cultivation scenario where the greenhouse-dependent input parameters are fixed, the optimal control determines the optimal trajectories of greenhouse controls mainly based on external climate inputs.

6.2.2 Optimal control algorithm

6.2.1.1 Definition of optimal control problem

Control objective

The objective of the optimal control is to maximise the net economic return of CSG lettuce cultivation. However, the energy consumption for operating the thermal blanket and ventilation openings is negligible, and standard CSGs lack additional energy-consuming climate conditioning equipment. In this context, it is unnecessary for the control to continuously balance the benefits of crop production against the operating costs of the climate conditioning devices. As a result, the cost function can be simplified to focus solely on maximising the crop yield, specifically the fresh weight of the lettuce heads. It is possible to measure crop economic return by yield in the Chinese agricultural product market, especially when selling soil-cultivated lettuce in bulk. The fresh weight of the lettuce heads is assumed to be proportional to their dry weight, which can be described as

$$X_{hfw} = c_{hfw} \cdot X_d \cdot (1 - \sigma_r) \tag{6.1}$$

where X_{hfw} [kg m^{-2} (gro)] is the head fresh weight of the crop, c_{hfw} [-] is the ratio of head fresh weight to head dry weight of the lettuce crop. As reported in Chapter 4, in all three validation experiments conducted with soil cultivation, the average water content of the lettuce heads was 93.8%. Therefore, c_{hfw} takes 17.5 in this study, which is lower than the ratio of 22.5 measured by Van Henten (1994a) in hydroponic cultivation.

Then, the cost function described in Eq. (2.3) can be converted as

$$J(U) = X_{hfw}\left(X, Y, U, D, P, t, t_0, t_f\right) \tag{6.2}$$

Eq. (6.2) asserts that for the climate management of standard CSGs, maximising crop yield is equivalent to maximising net revenue of CSG crop production. Meanwhile, the problem definition does not take into account the risk of commercial value reduction of lettuce products due to excessive individual plant weight or aging. Before the initially anticipated crop harvest time, which is also the final time targeted by the optimisation, growers are allowed to terminate cultivation activity in a timely manner based on observed and simulated crop states. The problem can then be described as determining the open loop control strategy to maximise the crop yield within a fixed time frame. According to Eq. (3.24), there is a negative correlation between the root ratio and the crop dry weight. Consequently, referring to Eq. (6.1), the yield of the lettuce is positively correlated with its total dry weight. This implies that maximising the output (i.e., crop dry weight), yield, and net revenue of the CSG crop production process converge towards the same objective when solving the optimal control problem.

Control constraints

In ideal optimal control, the control variables are constrained by the following inequations:

$$0 \leq U_b(t) \leq 1 \tag{6.3}$$

$$0 \leq U_{vent,r}(t) \leq 1 \tag{6.4}$$

$$0 \leq U_{vent,s}(t) \leq 1 \tag{6.5}$$

In open loop optimal control and event-driven receding horizon optimal control, which are designed for manual control, the control inputs are subject to the grower's acceptable labour input and the accuracy of manual operations. The control actions for the thermal blanket are limited to twice per day and kept in fully opened or closed condition. Similarly, the vents are designed to be operated twice daily, with the roof vent opening before the side vent. The aperture of vents can be operated at five levels. A basic rule lies in that the thermal blanket and vents cannot be used simultaneously. The available control magnitudes are as follows:

$$U_b(t) = \{0,\ 1\} \tag{6.6}$$

$$U_{vent,r} = \left\{0,\ \frac{1}{4},\ \frac{2}{4},\ \frac{3}{4},\ 1\right\} \tag{6.7}$$

$$U_{vent,s} = \left\{0,\ \frac{1}{4},\ \frac{2}{4},\ \frac{3}{4},\ 1\right\} \tag{6.8}$$

State constraints

The developed lettuce growth model responds to a broad range of greenhouse climates, including air temperature with extreme conditions, humidity, CO_2 concentration, and shortwave radiation, and even works with sub-zero temperature inputs. The process model integrates this crop model, inheriting its characteristics and capabilities. It has been thoroughly validated across various seasons and can effectively address the occurrence of extreme greenhouse climates. On the other hand, as stated in Chapter 3, extreme climate conditions frequently occur in CSGs with inadequate climate conditioning, which cannot be avoided even with optimal controls. Thus, for most climate states, we set broad bounds that

comply with physical laws and only pay attention to high temperatures as the model demonstrated greater tolerance to them, allowing the system model to play a leading role in decision-making. These bounds for the optimal climate control of the CSG cultivation scenario in Exp_3 are shown in Table 6.1.

As mentioned in formulating the control objective, although the growers can advance or delay the harvest time during the practical production process supported by the optimal control system, the final time (harvest time) is fixed in solving the optimal control problem. The control system does not optimise the final time, and there are no constraints on the terminal crop state. Note that if the lettuce is required to be harvested after being fully grown with a fixed terminal crop dry weight, the problem will convert to one with free final time (Dan Xu et al., 2018), which would not bring convenience or improve yield to the process considered.

Table 6.1 Climate state constraints for optimisation

State variable	I [W m^{-2} (gro)]	X_t [°C]	X_h [-]	X_c [ppm]
Lower bound	0	3	0	0
Upper bound	1200	35	1	1500

6.2.1.2 Event-driven receding horizon optimal control

Open loop optimal control is not practical for direct application in actual greenhouse production due to the uncertainties in the underlying process model and weather forecasting. To address these prediction errors and enhance system robustness while ensuring user-friendliness, an optimal control algorithm employing an event-driven receding horizon design with real-time feedback was proposed (Figure 6.1). Unlike previous studies (Tap, 2000; Van Henten, 1994a; Van Ooteghem, 2010; Dan Xu et al., 2018), the horizon receding is triggered subjecting to the control actions of the thermal blanket, roof vent, and side vent,

rather than at fixed and relatively short time intervals, thereby making it event-driven. Furthermore, to prevent frequent updates to decision recommendations within a single day and enhance user-friendliness, a deviation assessment between simulated and measured CSG climates has been incorporated into the event-driven receding horizon trigger mechanism. A forced repetition of solving the optimal control problem must be performed before the last control action of the day to ensure control efficiency.

In this system, the closed loop is realised by performing the model based receding horizon optimal control. The initial climate states for solving the optimal control problem within the current control horizon are based on real-time climate measurements at the start of this horizon. Meanwhile, the initial crop state is derived from the simulated crop state, which is based on the measured crop state at the transplanting date and the measured climates from the beginning of the growth cycle to the start of the current horizon. Thus, the real-time feedback of greenhouse climates contributes to triggering the computational solving for the forward horizon receding and supports determining the initial states. Feedback endows the control system with solid robustness so that subsequent decisions can be effectively determined even if growers do not follow recommended control actions during some periods.

Figure 6.2 illustrates the specific steps taken in implementing the event-driven receding horizon optimal control with a closed loop. More information is provided below. The measured initial states at t_0 include indoor air temperature, relative humidity, CO_2 concentration, crop dry weight, and LAI, while other initial state variables are estimated. Weather predictions cover outdoor horizontal solar radiation, air temperature, relative humidity, CO_2 concentration, and wind speed. The default receding control horizon ΔH starts at 2-3 days and shortens near harvest. Control actions derived from the optimal control trajectories and to be executed are denoted as u_i, where i counts the actions actually executed from the start of the crop growth cycle. At the moment t_i, which should be prior to executing u_i and after executing u_{i-1}, a check is conducted for any significant deviations to determine whether an updated calculation should be performed. If triggered, this moment t_i becomes the starting point of the new control horizon.

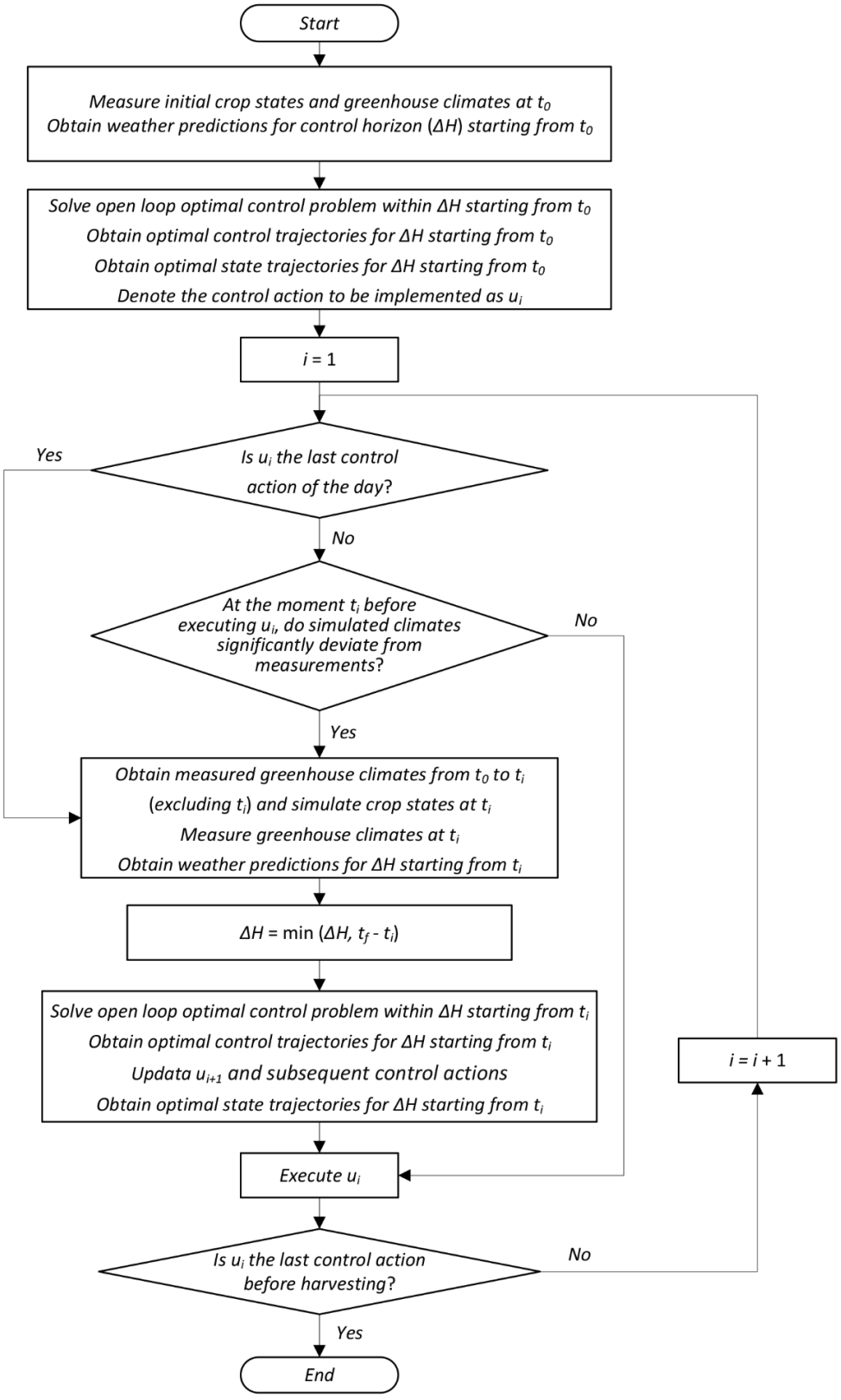

Figure 6.2 Overall control process planning of the event-driven receding horizon optimal control.

Indoor climate elements involved in the deviation judgment include air temperature, humidity, and CO_2 concentration. If the predicted value of any of these climates significantly deviates from the actual value, it triggers the horizon receding. The specific thresholds for deviation should, at the most basic level, accommodate the measurement accuracy of the sensors. For example, the thresholds can be set at 2 ℃ for temperature, 0.1 for humidity, and 100 ppm for CO_2. If the deviation does not exceed the threshold, then u_i is prepared for execution, and u_{i+1} is derived from the optimal control trajectory for the current control horizon starting from t_{i-1}. The control system solves the optimal control problem within ΔH starting from t_i, determining the optimal control trajectories for this horizon. The updated computation does not change the imminent control action u_i, but only updates u_{i+1} and its subsequent actions. This ensures that the grower can execute u_i at the scheduled time and accurately know the timing of u_{i+1} after the execution of u_i, thereby facilitating time management. The control system stops problem-solving after determining the last control action before harvesting.

The control system communicates updated climate control recommendations to the grower as part of a DSS. In most cases, the advice includes actions for managing the thermal blanket and vents within a single day, derived from the optimal control trajectories over the control horizon. Except for the optimal control trajectories generated at the initial time of the growth cycle, where only the first control action is guaranteed to be executed, the execution of the first two control actions from trajectories computed at subsequent times is guaranteed. All recommended control actions by the DSS occur during the day, with no actions are taken at night. The grower receives the decision advice for the next day in the evening, with the possibility of updates during the following day if necessary.

As stated above, the event-driven receding horizon optimal control follows the practices of growers and meets the requirement for manual control. It tries to trigger horizon receding in response to each control action, providing appropriate opportunities for updating the solution of the optimal control problem and ensuring control efficiency. Moreover, the event-driven mechanism reduces time intervals between the control actions to be updated, particularly

u_{i+1}, and the solving time. This enables optimal control trajectories to be generated based on more accurate weather predictions and less accumulation of system model errors, benefitting the optimality of updated control actions. The event-driven approach provides a balance between robustness and user-friendliness for applying receding horizon optimal control in CSG climate management.

6.3 Results

6.3.1 Ideal optimal control versus grower

In the ideal optimal control scenario, it was assumed that the thermal blanket and roof and side vents could be continuously adjusted and activated at any time, which can be achieved with a well-designed local controller paired with limiters. Additionally, there is no priority differentiation between roof and side ventilation openings to meet the potential need for rapid ventilation. Therefore, besides adhering to the path constraints and dynamics defined by the system model, the optimisation control solution must also address the rule that the thermal blanket and vents cannot be used simultaneously, as well as the constraints of the greenhouse climate states, especially for the indoor air temperature. In the following case studies, the ideal optimal control problems were solved within a control horizon of 24 hours, and the optimisation time step was set to 30 minutes.

Figure 6.3 depicts the control and state trajectories of CSG crop production under ideal optimal control and grower empirical control during a specific day in Exp_3, from 15:00 on 7 March 2022 to 15:00 on 8 March 2022. With ample biomass present in the crops, there was no opportunity for photosynthesis inhibition. Consequently, the ideal optimal control reduced the indoor air temperature as much as possible during the night to reduce respiration while ensuring it did not drop below the lower bound. Therefore, under the optimal control regime, natural ventilation was consistently executed from 15:00 to 17:00, with varying vent openings ranging from 6% to 100%. In contrast, the grower closed the vents entirely by 16:00. This disparity contributed to consistently lower night temperatures and higher

biomass in optimal control. Furthermore, increased ventilation facilitated the introduction of outdoor CO_2, thereby supporting photosynthesis. On the other hand, the grower completely covered the thermal blanket on the south roof from 17:05 until 7:50 the following day. In comparison, optimal control covered 51% at 17:30, 41% at 18:00, 2% at 18:30, and fully covered by 19:00, with complete uncovering at 8:00 the next day. Compared to the grower control, the optimal control allowed the crops about two additional hours of light exposure for photosynthesis around sunset. Since the control inputs at integration moments were obtained using linear interpolation in the program, the optimal control also tended to uncover the blanket earlier the next morning. All optimised greenhouse controls around sunset were scheduled to provide the crops with higher light intensity and CO_2 levels, as well as lower night temperatures, thereby enhancing photosynthesis, reducing respiration, and augmenting biomass.

During the photosynthetic period (Figure 6.3), the ideal optimal control employed longer ventilation times and simultaneously opened both roof and side vents around noon to enhance ventilation. As a result, the air temperature and humidity inside the optimally controlled CSG were lower than those in the grower controlled CSG for most of the day, with an average difference of 2.8 °C and 0.09, respectively. Meanwhile, the CO_2 concentration was higher, with an average difference of 28 ppm. These optimal control strategies and resulting indoor climate dynamics were efficient, leading to a sustained increase in crop production output difference. Timely CO_2 supplementation likely played a crucial role. Evidence for this is the rapid drop in CO_2 levels in both greenhouses after uncovering the thermal blanket, with optimal control gradually opening vents from 8:00, while the grower did so at 10:20, only opening the roof vents. Between 8:30 and 10:20, CO_2 levels in the grower controlled greenhouse dropped to a minimum of 203 ppm, indicating extreme deficiency, while the optimally controlled greenhouse received timely CO_2 supplementation. The output difference widened during this period, with an average growth rate difference reaching 24.8%. Throughout the day, ideal optimal control ultimately increased crop dry weight by 1.229×10^{-3} kg m^{-2}, resulting in a 0.7% improvement in crop dry weight and an 8.5% improvement in dry matter accumulation over grower-supervised

climate control. On a short time scale, such as a single day, comparing the changes in dry matter and yield is evidently more reasonable than directly comparing the terminal states. According to Eq. (6.1), the improvement in lettuce yield increment reached 8.6%. This means that, compared with conventional control, the maximum potential for improving the economic performance of a standard CSG by using optimal control can reach 8.6% during a single day.

It should be noted that when there is no photosynthesis inhibition the following day, or when the reduction in respiration offsets the increased photosynthesis inhibition due to lower nighttime temperatures, the optimal control system tends to lower the nighttime temperature, even leading to temperatures below 0 °C. Therefore, state constraints are essential as they can compensate for any inadequacies in the system model description.

In warm seasons, unless there were exceptional circumstances like rain, growers did not pay much attention to greenhouse climate control. They kept the roof and side vents fully open continuously (Figure 4.4). As shown in Figure 6.4, the efforts of optimal control yielded minimal results at night and mainly became effective after sunrise. Between 6:30 and 9:00, the ideal optimal control reduced window openings to increase air temperature and humidity inside the CSG, which also led to a slight decrease in indoor CO_2 concentration. This control strategy significantly improved the crop growth rate, with increased humidity likely being the dominant factor. These optimised controls laid a strong foundation for subsequent photosynthesis production, increasing dry matter accumulation by up to 12.5% during the photosynthetic period. However, the occurrence of photosynthesis inhibition considerably reduced the advantages of optimal control. In other words, the crop state itself, instead of its growing environment, was the limiting factor. The overall increase in dry matter accumulation due to optimal control throughout the day was found to be 0.8%, with an improvement of 0.8% in crop yield increment. Therefore, optimal control had a more significant impact in the later stages of crop growth. This does not mean that early-stage optimisation was not important, as these relatively small improvements would accumulate over time, and their impact would gradually amplify.

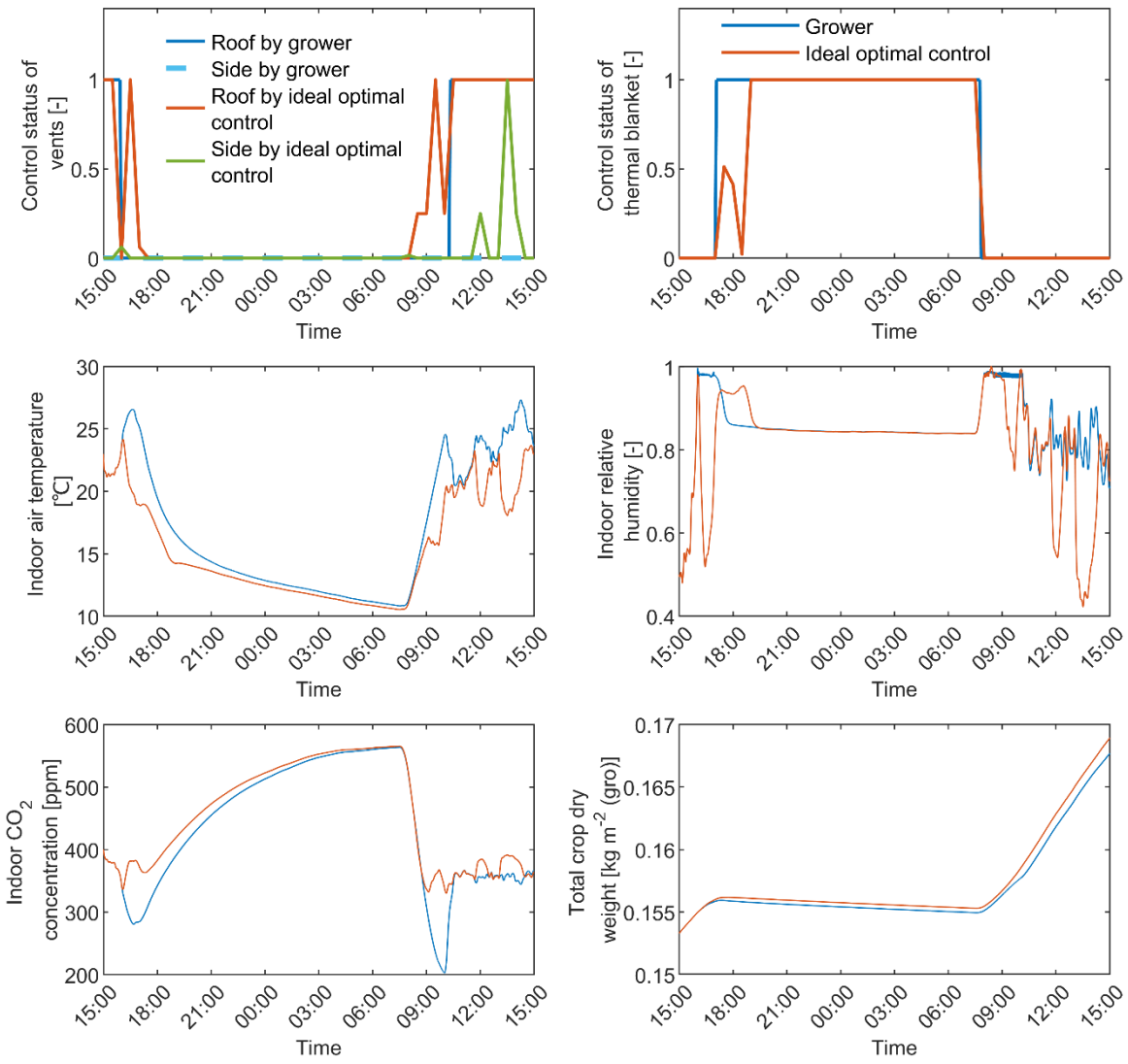

Figure 6.3 Control patterns and state trajectories of the CSG production process (without photosynthesis inhibition) using grower supervised control and ideal optimal control. This case study of control performance comparison was based on the data from 15:00, 7 March 2022, to 15:00, 8 March 2022, during Exp_3.

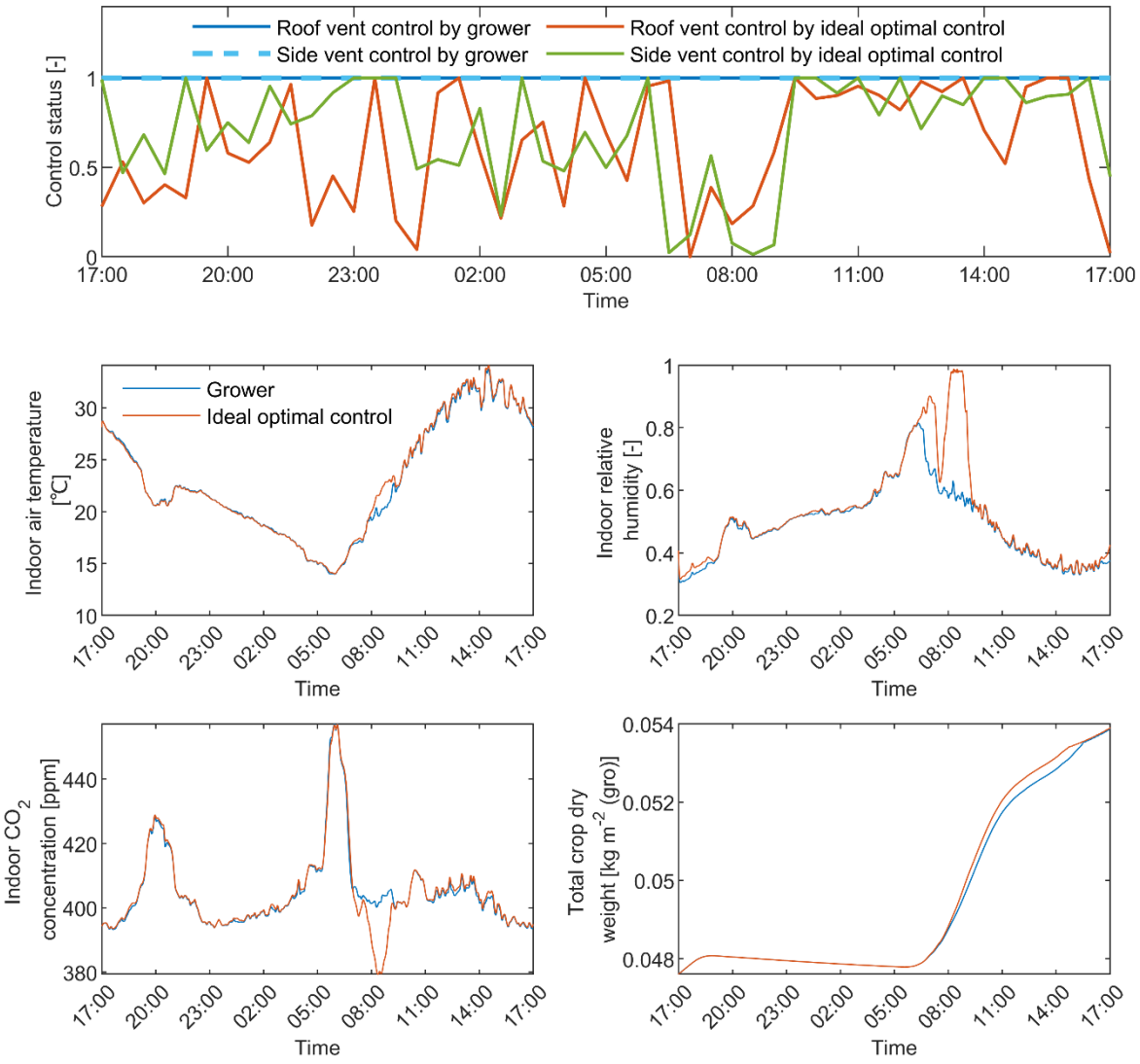

Figure 6.4 Control patterns and state trajectories of the CSG production process (with photosynthesis inhibition) using grower supervised control and ideal optimal control. This case study of control performance comparison was based on the data from 17:00, 28 April 2020, to 17:00, 29 April 2020, during Exp_1.

6.3.2 Open loop optimal control versus grower

In open loop control, considering the acceptance of growers, the number of state switches of the thermal blanket and vents was limited, and their positions were also fixed to specific levels. Therefore, the switching functions established for greenhouse controls in Chapter 5

presented an opportunity for efficient solutions to the optimal control problem. By using these functions, solving the dynamic control trajectories could be converted into determining a minimal number of daily switching time points and the corresponding opening coefficients. For example, in Exp_3, there were five optimisation objects for a single day, including the switching times of the thermal blanket and the roof vent, as well as the opening levels of the roof vent. To further improve computational efficiency, the state and control bounds of the optimal control problem were implemented through penalty functions in the program. In the following case studies, the open loop optimal control problems were also solved within a control horizon of 24 hours, and the optimisation time step was set to 30 minutes.

Figure 6.5 shows the control and state trajectories of CSG crop production under open loop optimal control and grower empirical control on a specific day in Exp_3, from 15:00, 19 February 2022, to 15:00, 20 February 2022. Similar to the ideal optimal control strategy, the open loop approach enhanced lighting by delaying the coverage of the thermal blanket and uncovering it earlier to enhance photosynthetic production. In terms of ventilation, to boost crop production output, the optimal control strategy closed the side vent earlier to raise indoor air temperature and humidity, which also resulted in a decrease in CO_2 concentration. Photosynthetic inhibition occurred around 10:40 and continued until the end of the day cycle. Compared with the climate control supervised by the grower, the open loop optimal control increased dry matter accumulation and crop yield increment by 1.8% each within a day. In the absence of photosynthesis inhibition, both increases reached 3.1% (Figure 6.6). Thus, subjecting to the acceptance of growers, the potential economic improvement of crop production inside a standard CSG using optimal control over a conventional control reached 1.8-3.1%.

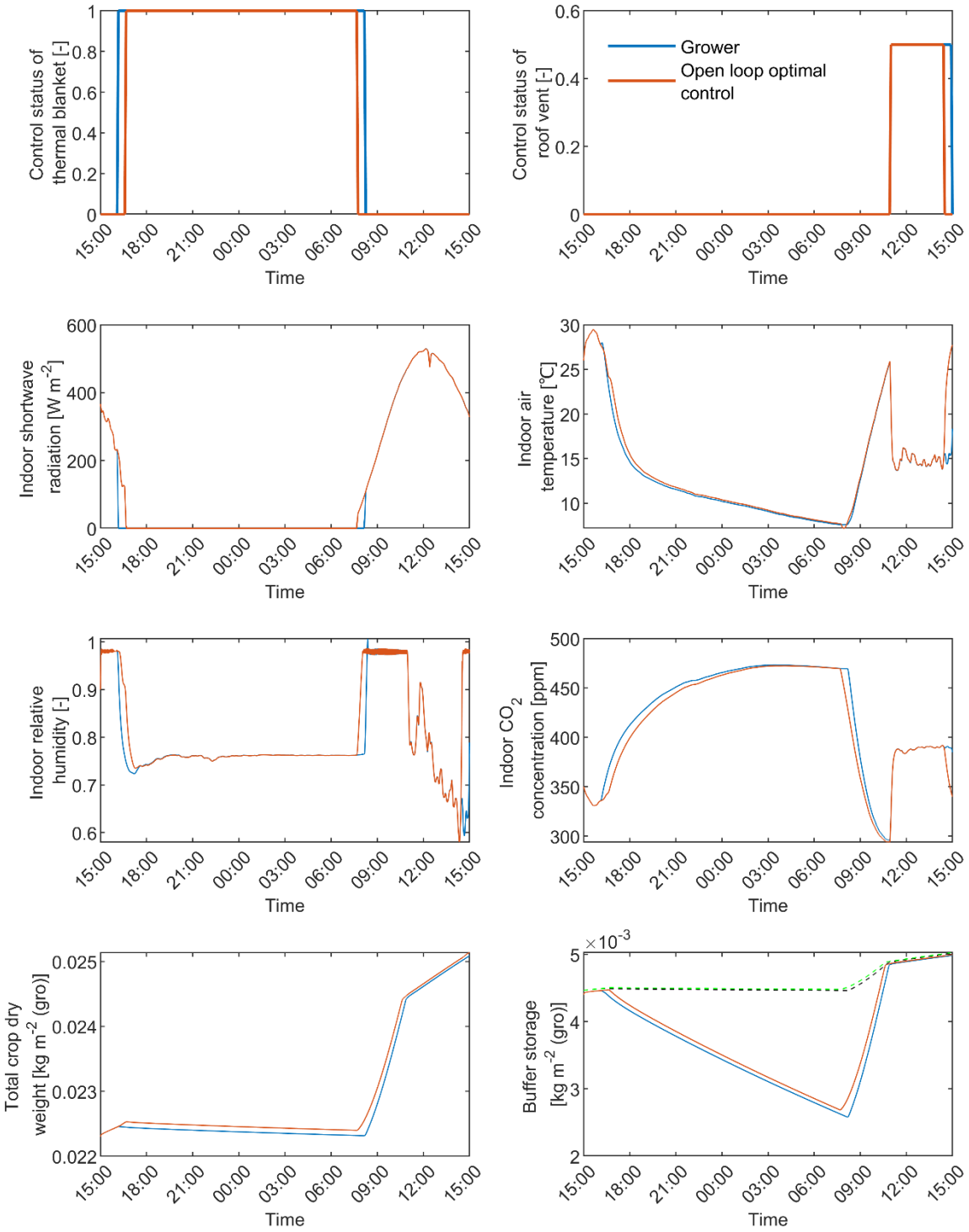

Figure 6.5 Control patterns and state trajectories of the CSG production process (with photosynthesis inhibition) using grower supervised control and open loop optimal control. This case study of control performance comparison was based on the data from 15:00, 19 February 2022, to 15:00, 20 February 2022, during Exp_3. The dashed black and green lines represent the upper limits of the buffer capacity for diurnal assimilate storage.

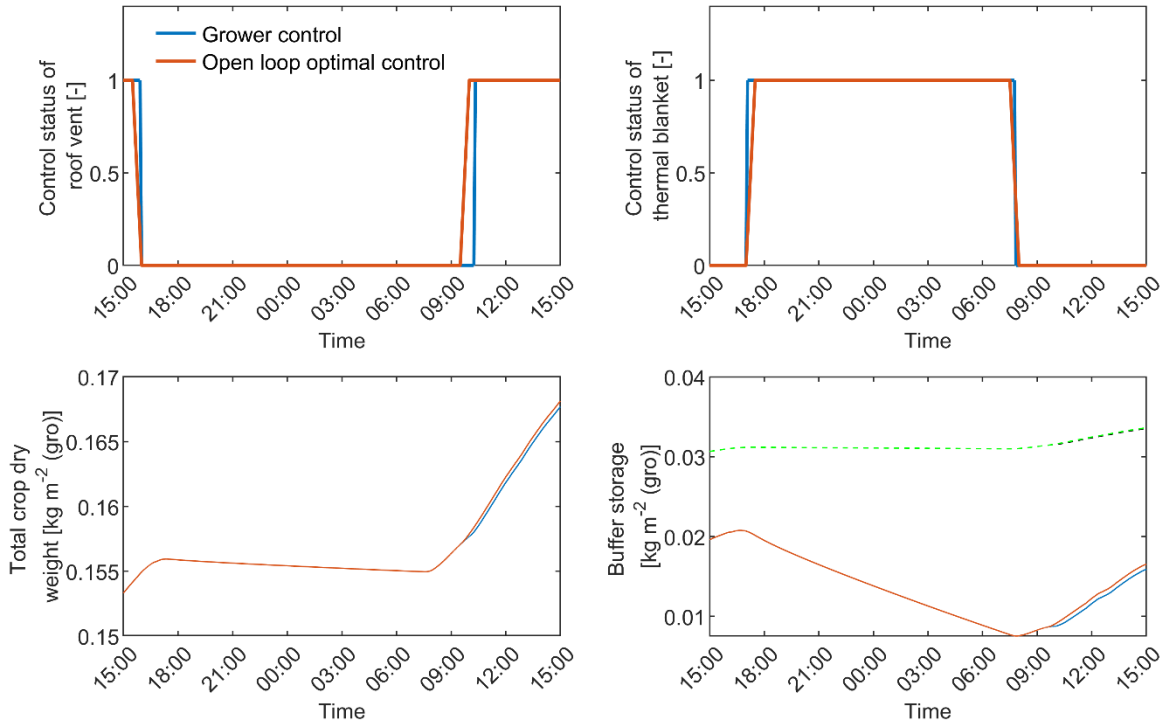

Figure 6.6 Control patterns and state trajectories of the CSG production process (without photosynthesis inhibition) using grower supervised control and open loop optimal control. This case study of control performance comparison was based on the data from 15:00, 7 March 2022, to 15:00, 8 March 2022, during Exp_3. The dashed black and green lines represent the upper limits of the buffer capacity for diurnal assimilate storage.

6.3.3 Feasibility of closed loop optimal control

The practical performance of the closed loop optimal control system needs field trials and support from a specially designed cloud service system, which is currently unavailable. Actually, determining what constitutes optimal climate control for an actual greenhouse production system is challenging due to uncertainties in the process model on which optimal control solutions are based. Previous studies assumed that the system model was perfectly accurate when exploring the potential of optimal control for economic improvement of greenhouse production. To test the event-driven receding horizon optimal control algorithm proposed in this study and investigate to what extent it can achieve optimal while maintaining grower-friendliness, we continued with this assumption and conducted

simulation comparison trials. Then, in these trials, the only source of uncertainties came from weather predictions.

As detailed in Section 6.2.1.2, the default receding control horizon for the closed loop optimal control system was set to 2-3 days. Running the algorithm across each receding horizon throughout the crop growth cycle entailed substantial computational costs. To facilitate the simulation trials for performance evaluation, we selected two consecutive days from Exp_2 as the target production scenario. Algorithm execution over this 2-day horizon served as a mapping of the computational process for the entire crop growth cycle, allowing for a feasibility assessment of the system. In addition, these two days featured cold outdoor weather and represented a typical scenario for CSG cultivation, where the thermal blanket and roof vent were used while the side vent remained closed. The control optimisation and external inputs spanned but did not exceed these days. During this period, the conditions for inhibiting photosynthesis were not present. This absence could reduce excessive temporal correlation in control strategy generation and ensure that the application effect of the horizon receding in the simulation trials closely approximates that of the controller design. The specific steps for conducting the simulation trials are outlined below:

1. Use the 'lazy man weather prediction' (Tap, 2000; Van Ooteghem, 2010) to obtain the outdoor climate at 5-minute intervals over the target two days. Specifically, it was assumed that the outdoor weather, except for shortwave radiation, during the next hour was the same as the weather during the past hour. In this way, uncertainties in weather predictions were generated with relatively reasonable errors.
2. Solve the optimal control problem within the two days based on the weather forecast to obtain the first control action to be taken, u_1 (i.e. covering the thermal blanket in this case study).
3. Repeat solving the optimal control problem at the first half-hour mark after executing u_1 (denoted as t_1), with the control horizon from t_1 to the end, to determine u_2. Both the initial climate and crop states were derived from simulations based on measured weather and executed controls from the initial time to t_1 (excluding t_1).

4. Repeat step 3 until the last control action within the 2 days was obtained.
5. Simulate and compare open and closed loop controls over the two days using actual weather conditions.

The differences from controller design of the event-driven receding horizon optimal control included using simulation instead sensors for feedback on greenhouse climate information. These trials also employed non-fixed receding control horizons, similar to the special situation near harvest, and triggered horizon receding without assessing indoor climate deviations. Additionally, calculations were updated after executing control actions to simplify the optimisation algorithm. Despite these differences, the simulation trials can still practice the controller design and explore its robustness in handling weather prediction uncertainties.

Figure 6.7 shows the control and state trajectories of CSG crop production under grower empirical control, closed loop optimal control, and open loop optimal control over two consecutive days in Exp_2, from 15:00 on January 10, 2021, to 15:00 on January 12, 2021. The initial crop dry weight was 0.1233 kg m^{-2}, and the final states reached 0.1417, 0.1427, and 0.1423 kg m^{-2}, respectively, under the grower, closed loop, and open loop controls. Using dry matter accumulation as the performance criterion, the closed loop optimal control achieved 98.1% of the efficiency by open loop optimal control, indicating strong robustness in handling weather forecast errors. Moreover, compared to grower control, the closed-loop optimal control system that can be used in practice increased dry matter accumulation and crop yield by 3.2%, resulting in a corresponding 3.2% increase in net revenue. Additionally, applying open loop optimal control continuously for two days resulted in a 5.2% increase in dry matter accumulation and yield increment of greenhouse crops compared to those in the grower-controlled greenhouse.

The event-driven receding horizon optimal control system was designed to focus on the grower and ensure user-friendliness. The event-driven mechanism reduces computational demand by performing calculations only when specific events trigger them, rather than at

regular intervals as in traditional receding horizon control. The system has demonstrated robustness in addressing uncertainties and can achieve higher efficiency in greenhouse crop production compared to conventional control methods. Therefore, the closed optimal control system is feasible for practical application in climate management of standard CSGs.

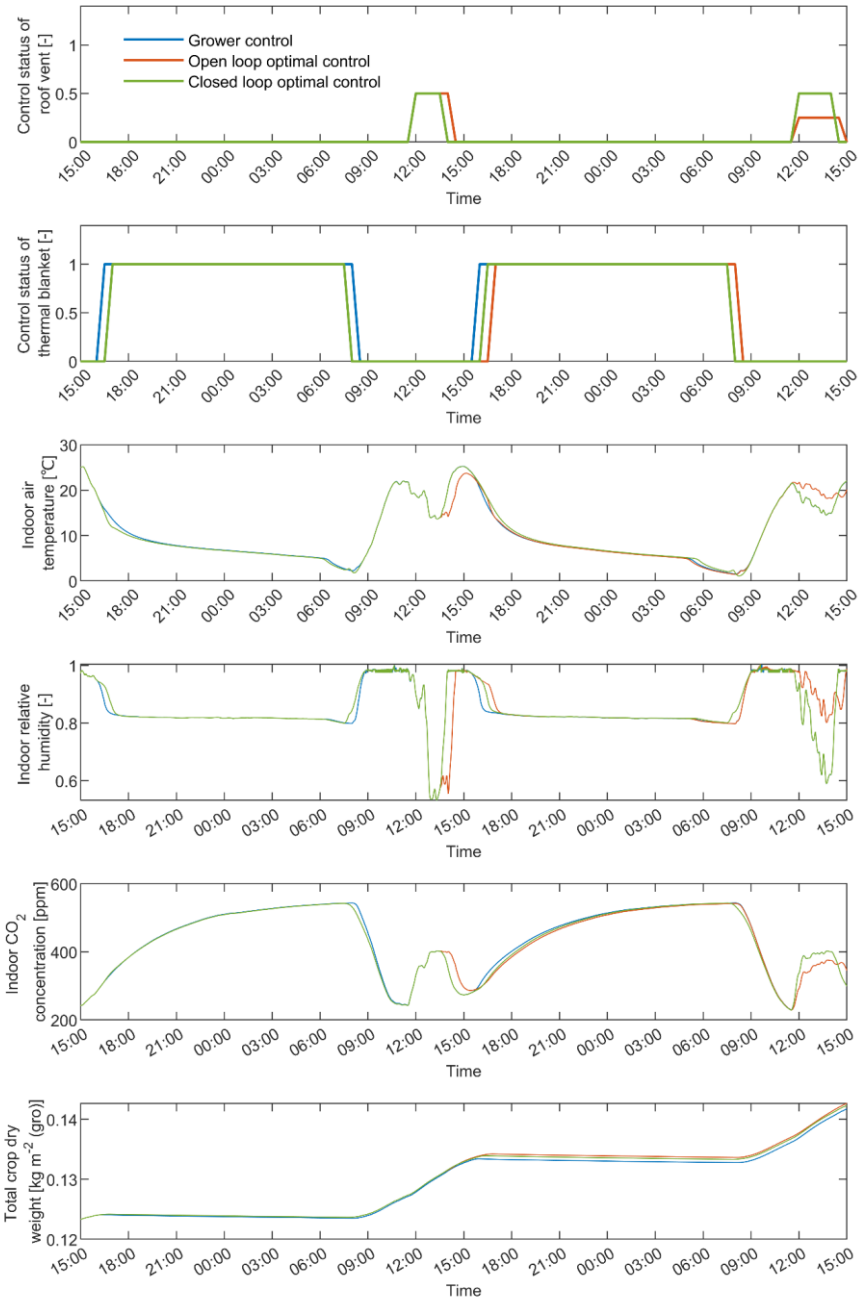

Figure 6.7 Control patterns and state trajectories of the CSG production process (without photosynthesis inhibition) using climate control supervised by the grower, closed loop optimal control, and open loop optimal control. This case study was based on the data f from 15:00, 10 January 2021, to 15:00, 12 January 2021, during Exp_2.

6.4 Discussion

Towards grower acceptance, this study investigated an optimal control system for climate management of the standard CSG without the local controller. The study makes two main contributions. On the one hand, it provides an optimal control model system and optimisation framework for manual control of CSGs. The optimal control algorithm employs an event-driven receding horizon design with real-time feedback, demonstrating that it could provide a balance between system robustness and user-friendliness. This system acts as a decision support system for growers, showing great potential for practical application. On the other hand, this study is the first to reveal the potential of optimal control for improving the production efficiency of standard CSGs and its feasibility in practice. The findings confirm that optimal control can enhance the production efficiency or economic performance of standard CSG cultivation.

6.4.1 Costs of deploying the proposed optimal control system

The observed crop production efficiency improvements in a standard CSG when using optimal control systems designed for practical applications are in the range of 1-3%. They occurred over a time scale of 1-2 days, and it is foreseeable that these daily gains will accumulate throughout the entire crop growth cycle, leading to considerable overall economic benefits. The development of optimal greenhouse climate control algorithms and systems typically aims to reduce energy consumption, increase crop yields, or improve net returns, while also enhancing the robustness of the control system. In addition, this study particularly emphasizes user-friendliness. However, evaluating the feasibility of algorithm and controller designs should also consider required hardware support. Different algorithms necessitate different levels of hardware resources, mainly involving computational power, sensors, local controllers, and weather forecasting services. The consideration of hardware support costs and the payback period in optimally controlling greenhouse climate has not been extensively studied. As intelligent control algorithms are gradually implemented in the greenhouse horticulture industry, this area will attract increasing attention.

Below an exploratory evaluation of the investment and payback period for the proposed closed-loop optimal control system will be conducted based on a hypothetical CSG production scenario (Table 6.2). In this scenario, the grower, operating an agricultural park with multiple CSGs, is the investor. All CSGs are assumed to have identical structural parameters and follow the same cultivation and management practices. With decision support for greenhouse climate management, the annual net revenue increase for a single CSG is calculated as 0.08×4200×10×5 = 16,800 CNY (Chinese Yuan). Since the decision advice is delivered directly to the grower for manual control, there is no need to install local controllers. Therefore, the costs of deploying the optimal control system primarily come from servers needed for system execution, climate sensors with remote communication capabilities installed in each CSG, and commercial weather forecasting services. According to survey data, the total cost of these components amounts to 60,000 CNY. In order to recover this investment within one year, the number of CSGs using the decision support system should be no less than eight, corresponding to a total cultivation area of approximately 5300 m^2.

Table 6.2 A hypothetical CSG production scenario using event-driven receding horizon optimal control.

Items	value
Cultivation area of a single CSG	667 m^2
Number of lettuce plants cultivated in a single CSG	4,200
Number of crop rotation cycles per year	5
Average duration of each crop growth cycle	45 days
Reference harvest weight of a single lettuce plant	0.2 kg
Increase ratio of lettuce yield at harvest	40%
Yield increase per lettuce plant	0.08 kg
Selling price of lettuce	10 CNY/kg
Cost of servers for deploying the optimal control system	30,000 CNY
Cost of sensors used in a single CSG	10,000 CNY
Annual fee for commercial weather forecasting services	20,000 CNY

6.4.2 Model processing and algorithm selection

To reduce the dimensionality of the model and avoid the excessive sensitivity caused by the thin south roof transparent covering, the temperature states of the south and north roofs were described using analytical equations. In the process model programming, the solution of these analytical equations was nested within the solution of differential equations. The roof temperatures, treated as analytical state variables, were determined based on the previous differential state values, such as indoor air temperature. These determined values were then used to compute those differential states at the current time step. While this approach achieved high accuracy in simulations, it incurred a relatively high computational cost. By expressing the south roof temperatures as simplified functions of the indoor and outdoor climates, a minor reduction in accuracy was observed, but computational efficiency increased approximately 10 times. These expressions, detailed in Table 6.3, were parameterised using the simulation results of the integrated CSG climate-crop growth model for Exp_3. The model simplification also ignored the convective interactions between roof surfaces and the air. Despite these simplifications, the integrated model provided a robust foundation for generating the optimal control strategy in this study.

Table 6.3 Simplified expressions for the surface temperatures of the south and north roofs.

Symbol	Expression	Unit
$T_{nr,in}$	X_t	℃
$T_{nr,e}$	T_{out}	℃
$T_{sr,in}$	$U_b \cdot (X_t - 4.77) + (1 - U_b) \cdot (0.89 \cdot X_t + 0.11 \cdot T_{out})$	℃
$T_{sr,e}$	$U_b \cdot (T_{out} - 4.80) + (1 - U_b) \cdot (T_{sr,in} - 0.16)$	℃

In solving optimal control problems, this study employed a genetic algorithm (GA). On the one hand, we implemented CSG controls at certain levels to account for the precision of manual operations. Genetic algorithms are effective for addressing discrete control problems.

On the other hand, we faced challenges when using sequential quadratic programming (SQP) and the pseudospectral collocation method. These issues may have been caused by an excessive number of state variables, making the problem unsolvable, or by the insensitivity to control objectives that results in ineffective solutions. In complex optimisation problems, providing one or more potential optimal solutions as part of the initial population can significantly speed up the convergence of a GA. For controlling the climate in standard CSGs, the grower's experiential control served as an excellent starting point. A good initial guess is equally essential in other optimisation algorithms, as it can prevent the risk of achieving local minima and reduce computation time. For example, a grid search method was implemented to provide a proper initial guess for the gradient search in solving the greenhouse climate control problem (Van Ooteghem, 2010). Additionally, the use of penalty terms to enforce control and state constraints seemed to improve computational efficiency.

Although the efficiency improvements introduced by the optimal control approaches were evaluated, they were based on a limited period and data. Future research will focus on optimising algorithms to solve optimal control problems of the complex greenhouse system using mathematical techniques (I Ioslovich et al., 2009). This includes utilising software like TOMLAB-PROPT, which supports both ordinary differential equations and differential algebraic equations for state-space descriptions (Rutquist & Edvall, 2010). The aim is to improve calculation efficiency further and achieve optimal solutions throughout the entire crop growth period.

6.5 Summary

A user-friendly optimal climate control system for crop production of a standard CSG without the local controller has been developed and evaluated. Its generation takes the integrated CSG climate-crop growth model presented in Chapter 5 as a basis and employs an event-driven receding horizon design with real-time feedback to enhance system robustness while ensuring user-friendliness. Event-driven means horizon receding is triggered subject to the control actions. The control system is expected to serve as a decision

support system and provide growers with user-accepted and more efficient advice for decision-making in CSG climate control.

Simulation trials were conducted to compare the ideal optimal control, open-loop optimal control, closed-loop optimal control, and grower empirical control, aiming to explore the crop production efficiency improvement of a standard CSG by using optimal control. Throughout a single day, ideal optimal control ultimately increased crop yield increment by 8.6% compared to grower-supervised climate control, representing the maximum potential for economic performance improvement. When following grower practices, the open loop optimal control increased dry matter accumulation and crop yield increment by 1.8-3.1% within a day. The occurrence of photosynthesis inhibition considerably reduced the advantages of optimal controls. Orienting to practical usage, the event-driven receding horizon optimal control achieved 98.1% of the optimal efficiency over two consecutive days, indicating strong robustness in handling weather prediction uncertainties. Meanwhile, the closed loop optimal control system demonstrated a 3.2% higher net revenue than conventional control. Therefore, optimal control can significantly enhance the production efficiency and economic performance of standard CSGs, and the closed loop optimal control system developed in this study is feasible for practical application.

Chapter 7

Conclusion

This chapter presents the conclusion and future outlook of this research project.

7.1 Conclusion

This project has generated an optimal climate control system for standard CSGs, incorporating the development of a required system model and an applicable control algorithm. The integrated CSG climate-crop growth model for optimal control, comprehensively simulating the CSG crop production process, was developed by combining a lettuce growth model responding to a broad range of greenhouse climates and a full-scale CSG climate model. This system model was thoroughly validated to have acceptable accuracy, with high computational efficiency and strong generalisation. The event-driven receding horizon optimal control algorithm was designed for standard CSGs without controllers, with a comprehensive focus on the grower, enabling the application of optimal control theory into practice. The control system, acting as a decision support system, resulted in higher net revenue in CSG cultivation over a conventional control supervised by the grower. Thus, the objective of this project has been successfully achieved.

Based on the models, control algorithm, and control system developed in this study, there is potential to develop a cloud service system for area-wide management of lettuce production in CSGs. By utilising weather forecast service in the region and installing climate sensors with remote communication capabilities within the target CSGs, the system can provide growers with grower-accepted and more efficient recommendations for decision-making in greenhouse climate control.

Below is the summary of the contributions and important findings of this study, organised by chapter:

In Chapter 1, we introduced the CSG properties and its standard configuration, challenges in production, limitations of conventional climate controls, and the prospect of employing optimal control. The motivation of this project was further clarified by comparing the current and desired situations, leading to the formulation of the research objective.

In Chapter 2, the methodologies, data, and codes that supported the whole research were illustrated. Three experiments of lettuce soil cultivation were conducted in two CSGs with differing structural parameters across cold, cold-warm, and warm seasons. The effective cultivated area, determining the implicit plant density in models, was defined by constraining the maximum ground area occupied by a single lettuce plant. The collected data, including crop growth indicators, greenhouse climate, outdoor climate, and greenhouse controls, were used for model calibration, validation, and control system evaluation in the following chapters. In order to ensure representative data and evaluation results, crop data were pre-processed, and outdoor climates during the three experiments were summarised. The selection of mechanistic model types and the phases of model development were outlined. Model performance was assessed by comparing measurements with simulation results using graphical interpretation and statistical metrics of *RMSE* and *RRMSE*. Local calibration used data from the lower integration level to parameterise the model by fitting, while global calibration was performed at a higher integration level to minimise the *RRMSE*. The basic methods for optimal control system development and problem solving were summarised. The initial states and programming for simulations were also presented.

In Chapter 3, we developed a mechanistic lettuce growth model that describes the effects of a broad range of greenhouse climates, including air temperature with extreme conditions, humidity, CO_2 concentration, and shortwave radiation on dynamics of the single state variable, structural crop dry weight. The proposed model framework performs two parallel sets of mass flows: dry matter accumulation and buffer evolution. The buffer carbohydrates flow to growth conversion based on the temperature-dependent sink strength. The inhibition of canopy assimilation occurs when the carbohydrate storage approaches the buffer capacity. The humidity effects are incorporated by describing stomatal resistance and specific leaf area of new leaves. The model was first calibrated at both sub-model and model levels and then validated against data collected in three experiments, covering a broad range of greenhouse climates. Results demonstrated that the model performance was good and acceptable; the simulated crop dry weights closely mirrored the measured values, with the *RRMSE* of 10.5-24.9% and the *RMSE* of 0.0070-0.0131 kg m^{-2}. The model predicted the leaf

area index with an *RRMSE* of 12.1-54.7% and performed well for the vegetative growth stage concerned by commercial production. The photosynthesis inhibition time accounted for 27-41% of the total photosynthesis time, indicating that the model framework and underlying hypothesis worked in simulations. The developed model, simulating instantaneous lettuce dynamics for the potential situation, can be applied to low-tech greenhouses with limited climate conditioning capacities and enables optimal control of all four climate factors.

In Chapter 4, a process based full-scale climate model of the CSG was developed and evaluated. It describes the effects of outdoor weather, greenhouse structure, crop states, and greenhouse controls on the indoor climate of a standard CSG, including shortwave radiation, air temperature, relative humidity, and CO_2 concentration, along with other CSG object states. The model description is divided into eleven subsections, and its parameters are classified into general parameters and those that depend on the simulated CSG. The model describes crop activities specifically targeting lettuce and was thoroughly evaluated in scenarios of lettuce production involving two different CSG structures across both warm and cold seasons. The model demonstrated acceptable performance. Simulated CSG climates closely mirrored the measured values throughout crop growth cycles, with the *RRMSE* being 12.7-24.2% for shortwave radiation, 17.5-26.7% for air temperature, 22.7-32.0% for relative humidity, and 3.0-10.7% for CO_2 concentration predictions. Layering was proved to be necessary to describe the temperature dynamics of the north wall and indoor soil. Seasonal variations in the shading of the north wall by the north roof and ice layer formation were noted. Incorporating these processes could improve the model descriptions. The developed CSG climate model can serve as a basis for optimal control because of its high computational efficiency, strong generalisation, and sufficient accuracy.

In Chapter 5, an integrated model of CSG climate and crop growth for control, as well as its smoothed version, were developed and thoroughly validated. The integrated CSG climate-crop growth model explicitly describes the entire CSG lettuce production process, detailing the effects of outdoor climate, greenhouse structure, and greenhouse controls on the

dynamics of indoor climate and crop state. Its generation combined the lettuce growth model and CSG climate model developed in Chapter 3 and 4. The integrated model was validated using data from three experiments. It demonstrated overall satisfactory performance for optimal control, with *RRMSE* being 13.0-24.2% for predicting shortwave radiation at the top of the canopy, 14.2-26.6% for indoor air temperature, 17.8-32.0% for relative humidity, 3.0-17.7% for CO_2 concentration, and 25.1-40.7% for crop dry weight of the lettuce throughout the entire growth cycle. Exploratory modelling revealed that implementing different practical control schemes over 10 days could lead to a 4% difference in the final crop production output in standard CSGs. This motivates the implementation of optimal climate controls in standard CSGs where little seems to be controllable. The model was smoothed, particularly on conditional statements and control inputs, to improve computational efficiency and adaptability further. The smoothed model turned out to have a generally better performance, especially in predicting crop states, with the *RRMSE* for crop dry weight being able to decrease from the initial 28.6% to 18.7%. The integrated CSG-crop model, along with its smoothed version, will serve as a basis for investigating the optimally controlled CSG system.

In Chapter 6, addressing practical industry needs, a user-friendly optimal climate control system for crop production of a standard CSG without the local controller was generated and evaluated. The control algorithm employs an event-driven receding horizon design with real-time feedback to enhance system robustness while ensuring user-friendliness. The control system acts as a decision support system and is expected to provide growers with user-accepted and more efficient advice for decision-making in CSG climate control. Simulation trials found that, compared with conventional control, the maximum potential for improving the economic performance of a standard CSG by using optimal control could reach 8.6% during a single day. When subjected to the acceptance of growers, the open loop optimal control increased dry matter accumulation and crop yield increment by 1.8-3.1% within a day. In terms of addressing weather prediction uncertainties, the event-driven receding horizon optimal control achieved 98.1% of the optimal efficiency over two consecutive days, indicating strong robustness. Meanwhile, the closed loop optimal control system

demonstrated a 3.2% higher net revenue than conventional control. Therefore, optimal control can significantly enhance the production efficiency and economic performance of standard CSGs, and the closed loop optimal control system developed in this study is feasible for practical application. This study provides an optimization framework for the efficient climate management of standard CSGs.

This thesis, for the first time, establishes a comprehensive modelling and algorithmic framework specifically for climate management in CSG cultivation scenarios, significantly advancing the field of process simulation and optimal control in greenhouse production. The developed lettuce growth model demonstrates high adaptability, enabling accurate simulations across low-tech and high-tech greenhouses, and even plant factories, with much of its underlying knowledge transferable to other crops. The developed full-scale CSG climate model is applicable across diverse CSG structures in various regions, including traditional brick- and soil-walled CSGs, as well as the increasingly popular ones covered with flexible insulation materials. The integrated CSG climate-crop growth model, describing the CSG lettuce production process from external weather to indoor crop biomass, allows for the substitution of crop growth components as needed. These mechanistic models not only provide a basis for climate control optimisation targeted in this thesis, but also support model-based greenhouse design, exploratory modelling, and system analysis. The developed optimal control algorithm is similarly applicable to greenhouse production scenarios managed manually or by simple controllers. The process-based models, industry-informed control algorithm, and the integrated optimal control system perform well overall, regarding prediction accuracy, generalisation, computational efficiency, robustness, and user-friendliness. Further improvements are anticipated by extending the effects of lettuce plant senescence, distinguishing between direct and diffuse radiation, refining vapour flux descriptions, conducting parameter calibration and model evaluation across more scenarios, incorporating data-driven approaches, simplifying process models, and enhancing the method for solving optimal control problems with complex system models.

Meanwhile, this thesis is the first to explore and demonstrate the substantial potential for

improving crop production efficiency and economic performance in manually controlled standard CSGs through optimising climate management. This output introduces a novel direction for enhancing greenhouse productivity in the CSG industry and boosts growers' confidence in adopting optimised control measures. While further evaluation of the benefits from optimal climate control throughout the entire crop growth cycle would strengthen the evidence, this research advances the implementation of modern and intelligent controls in practical CSG cultivation. The developed optimal climate control system does not require customised local controllers, is grower-centred, exhibits robustness, and provides efficient decision-making support, showing strong potential for practical application. However, further improvements in computational efficiency, along with considerations of hardware support costs and the payback period, remain critical areas requiring sustained effort. Moreover, deploying the developed models, algorithm, and control system in actual production settings will be essential to assess whether the models provide sufficient accuracy, whether the algorithm offers adequate robustness, the degree to which optimal control improves production efficiency, and the overall feasibility of the proposed system. At present, no technical barriers impede field testing of this system.

7.2 Future outlook

7.2.1 Model simplification based on sensitivity analysis

Optimal control systems, particularly those implemented online that frequently solve optimal control problems, require the system model to be simpler to achieve higher computational efficiency while still maintaining accuracy. Setting some intermediate variables as constants can be a direction for simplifying the integrated CSG climate-crop growth model presented in Chapter 5. A sensitivity analysis can serve as a basis for such model simplification (Van Henten, 1994a). In greenhouse horticulture science, sensitivity analysis, such as the first-order method (Van Henten, 2003), second-order method (Vanthoor, Van Henten, Stanghellini, & De Visser, 2011), or the Fisher information matrix (Van Ooteghem, 2010), is mainly used to reveal the relative importance of model elements to the

model outputs (Md Shamim Ahamed, Huiqing Guo, & Karen Tanino, 2018; Liang, Hu, Batchelor, Qin, & Li, 2018; Van Henten, 1994b; Vanthoor, Van Henten, et al., 2011) and the performance of control systems (Van Henten, 2003). The analysis results can then help identify which model parameters, external climates, greenhouse controls, and greenhouse structure design parameters need careful consideration. However, these studies have never advanced the model based on sensitivity analysis, such as through model optimisation, simplification, or reduction. The method for simplifying the integrated greenhouse-crop model for CSG lettuce production based on sensitivity analysis of intermediate variables, as well as its impact on model performance, remain to be explored.

7.2.2 Setpoint optimal control of high-tech CSGs

The generated optimal climate control system in this project is designed for standard CSGs, which have only the thermal blanket and vents as the controllable objects, with climate control being manually operated. These standard configurations may be insufficient for production activities requiring high standards for indoor climate conditions, such as seedling cultivation and flower production, in cold regions, or when aiming at year-round production. Currently, some newly constructed and commercially operated CSGs tend to be equipped with additional energy-consuming devices for light, heat, vapour, and/or CO_2 adjustments. In such high-tech CSGs, controllers are installed to comprehensively manage these devices, thereby increasing control efficiency and reducing labour costs. The high-tech CSG is a relative concept, which is extended from the standard CSG with extra on-off type and/or continuously adjustable equipment, as well as an automated controller. It has more opportunities for control actions than the standard CSG.

An optimal climate control system for high-tech CSGs, with potential for practical application, is expected to be designed and evaluated in future work. Firstly, the integrated model developed for standard CSGs will be extended for high-tech CSGs by incorporating descriptions of extra climate conditioning equipment, such as the heating system, fan-pad cooling system, artificial light, external shading screen, etc. Secondly, an optimal climate

setpoint control algorithm will be designed. The conventional optimal controller, such as the two time-scale receding horizon optimal control system developed for a high-tech CSG (Dan Xu et al., 2018), directly issues the control action commands to the local controller at specific moments. Instead, the setpoint optimal control system requires the local controller to set points for greenhouse climate attributes, along with equipment constraints, enabling the system to have lower operational risk and higher applicability. This is because when the optimal control generator fails or if there is a disruption in equipment communication, the grower will take over control. Compared to local controllers that directly set points for equipment, those with setpoints for climate factors and control constraints for equipment are more capable of handling the integrated management of various devices. Meanwhile, these controllers have become the most commonly used in high-tech greenhouses (Aaslyng et al., 2003; Stanghellini et al., 2019).

Then, the optimal control problem will be defined with the objective of maximising net economic return based on the final time. Receding horizon optimal control will be introduced to decrease the impact of uncertainties in parameters, weather predictions and measurements. In order to save computation time, two time-scale decomposition within optimal control of greenhouse cultivation can be employed (Van Henten & Bontsema, 2009; D. Xu et al., 2019; Dan Xu et al., 2018). The fast climate states and slow crop growth states will be distinguished. For the equipment offering on-off switching outputs, the control algorithm design should avoid frequent on-off switchovers. Furthermore, solving the optimal control problem will fully invoke the control logic of the local controller. The economic performances of the optimally controlled high-tech CSG will be compared to that of the optimally controlled standard CSG, considering the depreciation of any additional equipment. The development of the setpoint optimal control system aims to achieve hosted control of high-tech CSGs but can also serve as a decision support system, depending on the specific algorithm designs.

7.2.3 Optimal control of CSG climate assisted by data-driven method

In Chapter 4, we provided an overview of data-driven approaches applied in CSG climate

simulations. In Chapter 5, we discussed the potential of data-driven methods, such as Bayesian inference and machine learning, in optimising the system model structure and parameters. With the advancement of big data and artificial intelligence technology, data-driven methods play an increasingly significant role in modelling and controlling the greenhouse crop production process (Zhou et al., 2023). However, the optimal control system generated in this study, based on mechanistic models, possesses irreplaceable advantages in interpretability, generalisation ability, and handling constraints (Morcego et al., 2023). Within the framework of this study, how to introduce data-driven methods to enhance model prediction accuracy, control performance, and computational efficiency should be an important future research topic.

Here, we propose three potential points of integration: (1) The performance of optimal control systems heavily relies on the accuracy of crop models. Although the receding horizon computation can mitigate the cumulative impact of climate prediction errors on crop growth simulation, the crop model itself, as reported in Chapter 3, also has prediction errors, especially around crop harvest periods. Therefore, incorporating a crop state feedback loop into the optimal control algorithm, where crop growth simulation can stand at the updated and measured initial states, can improve simulation accuracy and control performance. Thus, to implement optimal control theory in practical greenhouse cultivation, a low-cost method for capturing crop states (mainly morphology) in real-time and without damage is required. Image identification, which low-cost industrial cameras can support well, has enormous potential to be a solution for crop state acquisition oriented toward CSG climate management. Thus, future work is expected to establish and evaluate an optimal CSG climate control system assisted by low-cost image identification. (2) Optimising model parameterisation and process descriptions using data-driven methods, as well as exploring the possibility of fusing ‘knowledge’ and ‘data’ to improve computational efficiency. (3) Investigating and comparing the advantages and disadvantages of traditional mathematical optimisation methods and heuristic optimisation algorithms in solving optimal control problems of CSG climate.

Furthermore, we prefer to apply these data-driven method assisted optimal control approaches to CSGs for fruit-bearing crop production. This is because fruit-bearing crops, i.e. tomatoes, have longer growth cycles and more complex growth and development processes. Certainly, most of the knowledge gained in this study can be applied to the scenario of CSG tomato production.

Appendix A Supplementary description of the lettuce growth model

A.1 Photosynthesis-light response

The gross assimilation rate of individual leaves A_L [kg (CO_2) m^{-2} (leaf) s^{-1}] can be described by a negative exponential photosynthesis-light response curve (Goudriaan & Van Laar, 1994; Spitters et al., 1989; Van Ooteghem, 2010)

$$A_L = A_{L,sat} \cdot \left(1 - e^{-\frac{\varepsilon \cdot PAR_a}{A_{L,sat}}}\right) \quad \text{(A.1)}$$

where $A_{L,sat}$ [kg (CO_2) m^{-2} (leaf) s^{-1}] is the potential gross leaf assimilation rate at light saturation, ε [kg (CO_2) J^{-1} (absorbed)] is the light use efficiency by photorespiration, PAR_a [W m^{-2} (leaf)] is the absorbed photosynthetically active radiation (PAR).

On the basis of the photosynthesis-light response of individual leaves, the A_L in a specific leaf layer located by canopy depth l_i, that is $A_{L,li}$, is calculated by substituting PAR_a for the absorbed PAR by this specific leaf layer $PAR_{a,li}$. The $PAR_{a,li}$ [W m^{-2} (leaf)] is described by

$$PAR_{a,l_i} = k_{PAR} \cdot \left(1 - c_{r,PAR}\right) \cdot I \cdot \sigma_{PAR} \cdot \mathrm{e}^{-k_{PAR} \cdot l_i} \quad \text{(A.2)}$$

where $c_{r,PAR}$ [-] is the canopy reflection coefficient for PAR, I [W m^{-2} (gro)] is the shortwave radiation at the top of the canopy, σ_{PAR} [-] expresses the ratio of PAR to shortwave radiation, k_{PAR}, the extinction coefficient for PAR, is assumed to be constant. To save computing time, the direct and diffuse radiations, as well as the sunlit and shaded leaves, are not distinguished. Their influences on crop photosynthesis are not involved in this model.

The effect of photorespiration on the light use efficiency is described by (Van Henten, 1994a)

$$\varepsilon = \varepsilon_0 \cdot \frac{X_c - \Gamma}{X_c + 2 \cdot \Gamma} \quad \text{(A.3)}$$

where ε_0 [kg (CO_2) J^{-1} (absorbed)] is the light use efficiency at very high CO_2 concentration in the absence of photorespiration. X_c [µmol (CO_2) mol^{-1} (air)] is the CO_2 concentration of the indoor air. The CO_2 compensation point deals with photorespiration and dark respiration. For simplicity, dark respiration is assumed to be suppressed in the light. Then Γ [µmol (CO_2) mol^{-1} (air)] is the CO_2 compensation concentration in the absence of dark respiration, which accounts for photorespiration under high light levels.

Higher temperatures strongly stimulate photorespiration by a faster increase in the affinity of rubisco to oxygen than to CO_2. The Γ is affected by the canopy temperature T_c according to the following relation (Goudriaan & Van Laar, 1994)

$$\Gamma = \Gamma_{T20} \cdot Q_{10,\Gamma}^{\frac{T_c - 20}{10}} \quad \text{(A.4)}$$

where Γ_{T20} [µmol (CO_2) mol^{-1} (air)] is a reference value of the CO_2 compensation point at 20 °C, $Q_{10,\Gamma}$ [-] is a Q_{10} value for CO_2 compensation point.

The gross leaf assimilation rate at light saturation $A_{L,sat}$ is determined by adding the net leaf assimilation rate at light saturation $A_{L,sat,n}$ [kg (CO_2) m^{-2} (leaf) s^{-1}] and the leaf maintenance respiration,

$$A_{L,sat} = A_{L,sat,n} + \frac{1}{c_\alpha} \cdot \frac{R_d}{LAI} \quad \text{(A.5)}$$

The light saturated net assimilation rate $A_{L,sat,n}$ is described by a simple Blackman-type approach (Goudriaan & Van Laar, 1994),

$$A_{L,sat,n} = \min\left(A_{L,c,n}, A_{L,mm}\right) \quad \text{(A.6)}$$

where $A_{L,c,n}$ [kg (CO_2) m^{-2} (leaf) s^{-1}] is the net leaf assimilation rate only limited by CO_2 concentration, $A_{L,mm}$ [kg (CO_2) m^{-2} (leaf) s^{-1}] is the maximum endogenous photosynthetic capacity, representing the theoretical value of the net assimilation rate at both high levels of light and CO_2.

The $A_{L,c,n}$ is described by

$$A_{L,c,n} = \frac{\rho_{CO2} \cdot (X_c - \Gamma)}{r_{CO2}} \cdot 10^{-6} \quad \text{(A.7)}$$

where r_{CO2} [s m^{-1}] is the total leaf resistance to CO_2 diffusion, ρ_{CO2} [kg m^{-3}] is the CO_2 density.

The CO_2 density ρ_{CO2} at temperature $T_{c,K}$ is described by

$$\rho_{CO2} = \rho_{CO2,0} \cdot \frac{T_{0,K}}{T_{c,K}} \quad \text{(A.8)}$$

where $\rho_{CO2,0}$ [kg m^{-3}] is the CO_2 density at temperature of $T_{0,K}$ = 273.15 K, $T_{c,K}$ = (T_c + $T_{0,K}$) K is the canopy temperature in Kelvin.

The maximum endogenous photosynthetic capacity $A_{L,mm}$ [kg (CO_2) m^{-2} (leaf) s^{-1}] is defined by (Farquhar et al., 1980; Van Ooteghem, 2010)

$$A_{L,mm} = \frac{M_{CO2} \cdot J_{max}}{4} \cdot 10^{-6} \quad \text{(A.9)}$$

in which M_{CO2} [kg mol^{-1}] is molar mass of CO_2, and the maximum electron transport rate J_{max} [µmol (e-) m^{-2} (leaf) s^{-1}] is given by

$$J_{\max} = J_{\max,25} \cdot e^{E_J \cdot \frac{T_{c,K} - T_{25,K}}{T_{c,K} \cdot R_g \cdot T_{25,K}}} \cdot \frac{1 + e^{\frac{c_S \cdot T_{25,K} - c_H}{R_g \cdot T_{25,K}}}}{1 + e^{\frac{c_S \cdot T_{c,K} - c_H}{R_g \cdot T_{c,K}}}} \quad \text{(A.10)}$$

where $J_{max,25}$ [μmol (e^-) m^{-2} (leaf) s^{-1}] is the maximum electron transport rate at 25℃, E_J [J mol^{-1}] is the activation energy of the maximum electron transport rate, $T_{25,K} = (T_{0,K} + 25)$ K, R_g [mol^{-1} K^{-1}] is the gas constant, c_S and c_H are constants.

A.2 Respiration

Some carbohydrates generated are used in respiration to supply energy to sustain the current biostructures. The crop maintenance respiration rate R_d is described by

$$R_d = R_{d,25} \cdot Q_{10,Rd}^{\frac{T_c - 25}{10}} \quad \text{(A.11)}$$

where $R_{d,25}$ [kg (CH_2O) m^{-2} (gro) s^{-1}] is the leaf maintenance (dark) respiration rate at a reference temperature of 25 ℃, $Q_{10,Rd}$ [-] is a Q_{10} value for maintenance respiration.

Based on the typical values for the maintenance coefficients of various plant organs used by van Keulen et al. (1982), $R_{d,25}$ is described by

$$R_{d,25} = \left(c_{Rd,25,sh} \cdot (1 - \sigma_r) + c_{Rd,25,r} \cdot \sigma_r \right) \cdot X_d \quad \text{(A.12)}$$

where $c_{Rd,25,sh}$ and $c_{Rd,25,r}$ [kg (CH_2O) kg (dry matter) s^{-1}] are the maintenance coefficients for the shoot (leaf) and root at 25℃.

Appendix B Supplementary material for the Chinese solar greenhouse climate model

Table B.1 View factors and area ratios to calculate the longwave radiation heat fluxes of the CSG climate model

R_{l_2}, R_{l_sky} [W m^{-2} (gro)]	σ_{area} [-]		F_{l_2}, $F_{l,sky}$ [W m^{-2} °C^{-1}]
R_{gro_can}	1		$F_{gro\_can} = 1 - e^{-k_R \cdot LAI_{gh}}$
R_{nw,in_can}		$\frac{L_{nw}}{L_{gro}}$	$F_{nw,in\_can} = \frac{L_{nw} + L_{gro} - L_{c2}}{2L_{nw}} \cdot \left(1 - e^{-k_R \cdot LAI_{gh}}\right)$
R_{nr,in_can}		$\frac{L_{nr}}{L_{gro}}$	$F_{nr,in\_can} = \frac{L_{c1} + L_{c2} - L_{nw} - L_{sr}}{2L_{nr}} \cdot \left(1 - e^{-k_R \cdot LAI_{gh}}\right)$
R_{sr,in_can}		$\frac{L_{sr}}{L_{gro}}$	$F_{sr,in\_can} = \frac{L_{gro} + L_{sr} - L_{c1}}{2L_{sr}} \cdot \left(1 - e^{-k_R \cdot LAI_{gh}}\right)$
R_{can_sky}	1		$F_{can\_sky} = \frac{L_{gro} + L_{sr} - L_{c1}}{2L_{gro}} \cdot \left(1 - e^{-k_R \cdot LAI_{gh}}\right)$
R_{nw,in_gro}		$\frac{L_{nw}}{L_{gro}}$	$F_{nw,in\_gro} = \frac{L_{nw} + L_{gro} - L_{c2}}{2L_{nw}} \cdot e^{-k_R \cdot LAI_{gh}}$
$R_{nw,in\_nr,in}$		$\frac{L_{nw}}{L_{gro}}$	$F_{nw,in\_nr,in} = \frac{L_{nw} + L_{nr} - L_{c1}}{2L_{nw}}$
$R_{nw,in\_sr,in}$		$\frac{L_{nw}}{L_{gro}}$	$F_{nw,in\_sr,in} = \frac{L_{c1} + L_{c2} - L_{gro} - L_{nr}}{2L_{nw}}$
R_{nw,in_sky}		$\frac{L_{nw}}{L_{gro}}$	$F_{nw,in\_sky} = \frac{L_{c1} + L_{c2} - L_{gro} - L_{nr}}{2L_{nw}}$
R_{nw,e_sky}		$\frac{L_{nw}}{L_{gro}}$	1
R_{nr,in_gro}		$\frac{L_{nr}}{L_{gro}}$	$F_{nr,in\_gro} = \frac{L_{c1} + L_{c2} - L_{nw} - L_{sr}}{2L_{nr}} \cdot e^{-k_R \cdot LAI_{gh}}$
$R_{nr,in\_sr,in}$		$\frac{L_{nr}}{L_{gro}}$	$F_{nr,in\_sr,in} = \frac{L_{nr} + L_{sr} - L_{c2}}{2L_{nr}}$
R_{nr,in_sky}		$\frac{L_{nr}}{L_{gro}}$	$F_{nr,in\_sky} = \frac{L_{nr} + L_{sr} - L_{c2}}{2L_{nr}}$
R_{nr,e_sky}		$\frac{L_{nr}}{L_{gro}}$	1
R_{sr,in_gro}		$\frac{L_{sr}}{L_{gro}}$	$F_{sr,in\_gro} = \frac{L_{gro} + L_{sr} - L_{c1}}{2L_{sr}} \cdot e^{-k_R \cdot LAI_{gh}}$
R_{sr,e_sky}		$\frac{L_{sr}}{L_{gro}}$	1

R_{gro_sky}	1	$F_{gro\_sky} = \frac{L_{gro} + L_{sr} - L_{c1}}{2L_{gro}} \cdot e^{-k_R \cdot LAI_{gh}}$

Note: L_{c1} [m] is the length of connecting line between the roof ridge and the bottom angle of the north wall, and L_{c2} [m] is the length of connecting line between the bottom angle of the south roof and the apex of the north wall, L_{sr} [m] is the arc length of the south roof, k_R [-] is extinction coefficient for longwave radiation.

Table B.2 The convective heat fluxes and their convection coefficients and area ratio factors

C_{1_2} [W m^{-2} (gro)]	σ_{area} [-]	h_{1_2} [W m^{-2} °C^{-1}]	Source of $h_{1,2}$
C_{can_air}	$2 \cdot LAI_{gh}$	$h_{can\_air} = \frac{\rho_a \cdot c_{p,a}}{r_{bh}}$	(Roy et al., 2002; Stanghellini et al., 2019)
C_{gro_air}	1	$h_{gro\_air} = \begin{cases} 1.86 \cdot \lvert T_{gro} - X_t \rvert^{0.33}, & LAI_{gh} \le 1 \\ 2.8, & LAI_{gh} > 1 \end{cases}$	Adapted from (Roy et al., 2002; Sethi, 2009)
C_{sr,e_out}	$A_{sr}/A_{gro} = L_{sr}/L_{gro}$	$h_{sr,e\_out} = 0.95 + 6.76 \cdot {v_e}^{0.49}$	(Papadakis, Frangoudakis, & Kyritsis, 1992)
C_{sr,in_air}	$A_{sr}/A_{gro} = L_{sr}/L_{gro}$	$h_{sr,in\_air} = \begin{cases} 2.21 \cdot \lvert T_{sr,in} - X_t \rvert^{0.33}, & U_{vent,r} = 0 \\ 0.95 + 6.76 \cdot {v_a}^{0.49}, & U_{vent,r} > 0 \end{cases}$	Adapted from (Papadakis et al., 1992)
C_{nw,e_out}	$A_{nw}/A_{gro} = L_{nw}/L_{gro}$	$h_{nw,e\_out} = 7.2 + 3.84 \cdot v_e$	(Weituo Sun et al., 2022)
C_{nw,in_air}	$A_{nw}/A_{gro} = L_{nw}/L_{gro}$	$h_{nw,in\_air} = \begin{cases} 3.4 \cdot \lvert T_{nw,in} - X_t \rvert^{0.33}, & U_{vent,r} = 0 \\ 7.2 + 3.84 \cdot v_a, & U_{vent,r} > 0 \end{cases}$	(Weituo Sun et al., 2022)
C_{nr,e_out}	$A_{nr}/A_{gro} = L_{nr}/L_{gro}$	$h_{nr,e\_out} = 7.2 + 3.84 \cdot v_e$	(Weituo Sun et al., 2022)
C_{nr,in_air}	$A_{nr}/A_{gro} = L_{nr}/L_{gro}$	$h_{nr,in\_air} = \begin{cases} 3.4 \cdot \lvert T_{nr,in} - X_t \rvert^{0.33}, & U_{vent,r} = 0 \\ 7.2 + 3.84 \cdot v_a, & U_{vent,r} > 0 \end{cases}$	(Weituo Sun et al., 2022)

Bibliography

Aaslyng, J. M., Lund, J. B., Ehler, N., & Rosenqvist, E. (2003). IntelliGrow: a greenhouse component-based climate control system. Environmental Modelling Software, 18(7), 657-666. https://doi.org/10.1016/S1364-8152(03)00052-5

Acquah, S. J., Yan, H. F., Zhang, C., Wang, G. Q., Zhao, B. S., Wu, H. M., & Zhang, H. (2018). Application and evaluation of Stanghellini model in the determination of crop evapotranspiration in a naturally ventilated greenhouse. International Journal of Agricultural and Biological Engineering, 11(6), 95-103. https://doi.org/10.25165/j.ijabe.20181106.3972

Ahamed, M. S., Guo, H., & Tanino, K. (2018). Development of a thermal model for simulation of supplemental heating requirements in Chinese-style solar greenhouses. Computers and Electronics in Agriculture, 150, 235-244. https://doi.org/10.1016/j.compag.2018.04.025

Ahamed, M. S., Guo, H., & Tanino, K. (2018). Sensitivity analysis of CSGHEAT model for estimation of heating consumption in a Chinese-style solar greenhouse. Computers and Electronics in Agriculture, 154, 99-111. https://doi.org/10.1016/j.compag.2018.08.040

Ahamed, M. S., Guo, H., & Tanino, K. (2020). Modeling heating demands in a Chinese-style solar greenhouse using the transient building energy simulation model TRNSYS. Journal of Building Engineering, 29, 101114. https://doi.org/10.1016/j.jobe.2019.101114

Baeza, E. J., Pérez-Parra, J. J., Montero, J. I., Bailey, B. J., López, J. C., & Gázquez, J. C. (2009). Analysis of the role of sidewall vents on buoyancy-driven natural ventilation in parral-type greenhouses with and without insect screens using computational fluid dynamics. Biosystems engineering, 104(1), 86-96. https://doi.org/10.1016/j.biosystemseng.2009.04.008

Bai, Y., Liu, W., Wang, T., Tong, G., & Meng, S. (2003). Experimental research on environment and heat preservation effect of solar greenhouse: type Liaoshen Ⅰ. Transactions of the Chinese Society of Agricultural Engineering (Transactions of the CSAE), 19(5), 191-196. https://doi.org/10.3321/j.issn:1002-6819.2003.05.038

Bakker, J. C. (1991). Analysis of humidity effects on growth and production of glasshouse fruit vegetables. Wageningen University and Research, The Netherlands.

Bakker, J. C., Bot, G. P. A., Challa, H., & van de Braak, N. J. (1995). Greenhouse climate control: an integrated approach. Wageningen: Wageningen Academic Publishers.

Bennis, N., Duplaix, J., Enéa, G., Haloua, M., & Youlal, H. (2008). Greenhouse climate modelling and robust control. Computers and Electronics in Agriculture, 61(2), 96-107. https://doi.org/10.1016/j.compag.2007.09.014

Berdahl, P., & Fromberg, R. (1982). The thermal radiance of clear skies. Solar Energy, 29(4), 299-314. https://doi.org/10.1016/0038-092X(82)90245-6

Bi, Y., Ma, S., Cong, H., & Zhu, J. (2010). Forecasting model of CO2 concentration of solar greenhouse in the northern drought cold area and experimental verification in winter. Transactions of the Chinese Society of Agricultural Machinery, 41(12), 183-189. https://doi.org/10.3969/j.issn.1000-1298.2010.12.038

Bi, Y., & Wu, P. (2012). Simulation of humidity model in Chinese solar greenhouse and experiment. Journal of Inner Mongolia Agricultural University, 33(2), 136-140. https://doi.org/10.16853/j.cnki.1009-3575.2012.02.030

Bot, G. P. A. (1983). Greenhouse climate: from physical processes to a dynamic model. Wageningen University and Research, The Netherlands.

Boulard, T., & Baille, A. (1993). A simple greenhouse climate control model incorporating effects of ventilation and evaporative cooling. Agricultural and Forest Meteorology, 65(3), 145-157. https://doi.org/10.1016/0168-1923(93)90001-X

Boulard, T., & Baille, A. (1995). Modelling of air exchange rate in a greenhouse equipped with continuous roof vents. Journal of Agricultural Engineering Research, 61(1), 37-47.

Bournet, P.-E., & Rojano, F. (2022). Advances of Computational Fluid Dynamics (CFD) applications in agricultural building modelling: Research, applications and challenges. Computers and Electronics in Agriculture, 201, 107277. https://doi.org/10.1016/j.compag.2022.107277

Bradbury, M., & Ahmad, R. (1996). Effect of humidity on growth of lettuce (Lactuca sativa, var. Great Lakes) under saline condition. Pakistan Journal of Botany, 28(1), 97-102.

Cao, K., Xu, H., Zhang, R., Xu, D., Yan, L., Sun, Y., . . . Bao, E. (2019). Renewable and sustainable strategies for improving the thermal environment of Chinese solar greenhouses. Energy Buildings, 202, 109414. https://doi.org/10.1016/j.enbuild.2019.109414

Cao, R., Li, J., Zhao, J., Gao, A., Wei, Y., & Li, Z. (2020). Development of shutter and vent control system for solar greenhouse. Jiangsu Agricultural Sciences, 48(5), 219-226. https://doi.org/10.15889/j.issn.1002-1302.2020.05.045

Cao, Y., Jing, H., Zhao, S., Zou, Z., & Bao, E. (2017). Optimization of back roof projection width and northern wall height in Chinese solar greenhouse. Transactions of the Chinese Society of Agricultural Engineering, 33(7), 183-189. https://doi.org/10.11975/j.issn.1002-6819.2017.07.024

Carini, F., Cargnelutti Filho, A., Bandeira, C. T., Neu, I. M. M., Pezzini, R. V., Pacheco, M., & Tomasi, R. M. (2019). Growth models for lettuce cultivars growing in spring. Journal of Agricultural Science, 11, 147-159. https://doi.org/10.5539/jas.v11n6p147

Carotti, L., Graamans, L., Puksic, F., Butturini, M., Meinen, E., Heuvelink, E., & Stanghellini, C. (2021). Plant factories are heating up: Hunting for the best combination of light intensity, air temperature and root-zone temperature in lettuce production. Frontiers in Plant Science, 11, 592171. https://doi.org/10.3389/fpls.2020.592171

Castañeda-Miranda, R., Ventura-Ramos, E., del Rocío Peniche-Vera, R., & Herrera-Ruiz, G. (2006). Fuzzy greenhouse climate control system based on a field programmable gate array. Biosystems Engineering, 94(2), 165-177. https://doi.org/10.1016/j.biosystemseng.2006.02.012

Chalabi, Z. S., Biro, A., Bailey, B. J., Aikman, D. P., & Cockshull, K. E. (2002a). Optimal control strategies for carbon dioxide enrichment in greenhouse tomato crops - Part 1: Using pure carbon dioxide. Biosystems Engineering, 81(4), 421-431. https://doi.org/10.1006/bioe.2001.0039

Chalabi, Z. S., Biro, A., Bailey, B. J., Aikman, D. P., & Cockshull, K. E. (2002b). Optimal control strategies for carbon dioxide enrichment in greenhouse tomato crops, part II: Using the exhaust gases of natural gas fired boilers. Biosystems Engineering, 81(3), 323-332. https://doi.org/10.1006/bioe.2001.0020

Chang, C.-L., Chung, S.-C., Fu, W.-L., & Huang, C.-C. (2021). Artificial intelligence approaches to predict growth, harvest day, and quality of lettuce (Lactuca sativa L.) in a IoT-enabled greenhouse system. Biosystems Engineering, 212, 77-105. https://doi.org/10.1016/j.biosystemseng.2021.09.015

Chen, D., Zheng, H., Zhang, J., & Qiu, J. (1992). A comprehensive research on the meteorological environment in sun-light greenhouse (III)-A comparative research on the total amount of direct

radiation in the greenhouse with different arc lighting surfaces. Transactions of the Chinese Society of Agricultural Engineering (Transactions of the CSAE), 8(4), 78-82.

Chen, L., Du, S., Li, J., He, Y., & Liang, M. (2017). Online identification method of parameters for greenhouse temperature prediction self-adapting mechanism model. Transactions of the Chinese Society of Agricultural Engineering, 33, 315-321. https://doi.org/10.11975/j.issn.1002-6819.2017.z1.047

Chen, Q. (1993). Numerical Experiments on Direct Light Transmission of Single Roof Greenhouses. Transactions of the Chinese Society of Agricultural Engineering (Transactions of the CSAE), 9(3), 96-101.

Chen, W.-H., Mattson, N. S., & You, F. (2022). Intelligent control and energy optimization in controlled environment agriculture via nonlinear model predictive control of semi-closed greenhouse. Applied Energy, 320. https://doi.org/10.1016/j.apenergy.2022.119334

Chen, W.-H., & You, F. (2022). Semiclosed greenhouse climate control under uncertainty via machine learning and data-driven robust model predictive control. IEEE Transactions on Control Systems Technology, 30(3), 1186-1197. https://doi.org/10.1109/TCST.2021.3094999

Chen, X., Tang, X., Li, X., Liu, T., Jia, L., & Lu, T. (2017). Two-steps prediction method of temperature in solar greenhouse based on twice cluster analysis and neural network. Transactions of the Chinese Society for Agricultural Machinery, 48, 353-358. https://doi.org/10.6041/j.issn.1000-1298.2017.S0.054

Collier, G. F., & Tibbitts, T. W. (1984). Effects of relative humidity and root temperature on calcium concentration and tipburn development in lettuce. Journal of the American Society for Horticultural Science, 109(2), 128-131. https://doi.org/10.21273/JASHS.109.2.128

Critten, D. L. (1991). Optimization of CO2 concentration in greenhouses: A modelling analysis for the lettuce crop. Journal of Agricultural Engineering Research, 48, 261-271. https://doi.org/10.1016/0021-8634(91)80020-F

Dayan, E., Van Keulen, H., Jones, J. W., Zipori, I., Shmuel, D., & Challa, H. (1993a). Development, calibration and validation of a greenhouse tomato growth model: I. Description of the model. Agricultural Systems, 43(2), 145-163. https://doi.org/10.1016/0308-521X(93)90024-V

Dayan, E., Van Keulen, H., Jones, J. W., Zipori, I., Shmuel, D., & Challa, H. (1993b). Development, calibration and validation of a greenhouse tomato growth model: II. Field calibration and validation. Agricultural Systems, 43(2), 165-183. https://doi.org/10.1016/0308-521X(93)90025-W

de Koning, A. N. (1994). Development and dry matter distribution in glasshouse tomato: a quantitative approach: Wageningen University and Research.

De Zwart, H. F. (1996). Analyzing energy-saving options in greenhouse cultivation using a simulation model. Landbouwuniversiteit Wageningen.

Deng, L. (2021). Analysis of soil heat transfer and hourly calculation of soil heat transfer in a single-slope solar greenhouse. Xi'an University of Architecture and Technology.

Dong, R. (2005). Prediction model of CO2 concentration inside the Chinese solar greenhouse. China Agricultural University.

Fan, S., Liu, C., Han, Y., Zhang, L., Chen, X., Chang, X., . . . Du, W. (2021). Current status and prospects of the lettuce industry in Beijing. Vegetables, z1, 12-17.

Fang, H., Yang, Q., Zhang, Y., Cheng, R., Zhang, F., & Lu, W. (2016). Simulation on ventilation flux of solar greenhouse based on the coupling between stack and wind effects. Chinese Journal of Agrometeorology, 37(5), 531-537. https://doi.org/10.3969/j.issn.1000-6362.2016.05.005

Fang, H., Yang, Q., Zhang, Y., Lu, W. Z., Bo, & Zhou, S. (2015). Simulation performance of a ventilated greenhouse based on CFD technology. Chinese Journal of Agrometeorology, 36(2), 155-160. https://doi.org/10.3969/j.issn.1000-6362.2015.02.005

FAO, IFAD, UNICEF, WFP, & WHO. (2024). The State of Food Security and Nutrition in the World 2024 – Financing to end hunger, food insecurity and malnutrition in all its forms. Rome: FAO; IFAD; UNICEF; WFP; WHO.

FAOSTAT. (2024). Crops and livestock products Retrieved October, 2024, from https://www.fao.org/faostat/en/#data/QCL

Farquhar, G. D., von Caemmerer, S., & Berry, J. A. (1980). A biochemical model of photosynthetic CO2 assimilation in leaves of C3 species. Planta, 149(1), 78-90. https://doi.org/10.1007/BF00386231

Fu, J., Zhou, C., & Wang, L. (2020). Methods for calculation of heating load in gutter-connected glasshouse. Transactions of the Chinese Society of Agricultural Engineering, 36(21), 235-242. https://doi.org/10.11975/j.issn.1002-6819.2020.21.028

Gary, C., Barczi, J. F., Bertin, N., & Tchamitchian, M. (1994). Simulation of individual organ growth and development on a tomato plant: a model and a user-friendly interface. Paper presented at the Greenhouse Environment Control and Automation. https://doi.org/10.17660/ActaHortic.1995.399.23

Gijzen, H., Heuvelink, E., Challa, H., Marcelis, L. F. M., Dayan, E., Cohen, S., & Fuchs, M. (1997). HORTISIM: a model for greenhouse crops and greenhouse climate. Paper presented at the II Modelling Plant Growth, Environmental Control and Farm Management in Protected Cultivation. https://doi.org/10.17660/ActaHortic.1998.456.53

Golzar, F., Heeren, N., Hellweg, S., & Roshandel, R. (2021). Optimisation of energy-efficient greenhouses based on an integrated energy demand-yield production model. Biosystems Engineering, 202, 1-15. https://doi.org/10.1016/j.biosystemseng.2020.11.012

Goudriaan, J. (1982). Potential production processes. In F. W. T. Penning de Vries & H. H. van Laar (Eds.), Simulation of plant growth and crop production (pp. 98-113). Wageningen: Pudoc.

Goudriaan, J. (1986). A simple and fast numerical method for the computation of daily totals of crop photosynthesis. Agricultural and Forest Meteorology, 38, 249-254. https://doi.org/10.1016/0168-1923(86)90063-8

Goudriaan, J., & Van Laar, H. H. (1994). Modelling Potential Crop Growth Processes. The Netherlands: Kluwer Academic Publishers.

Goudriaan, J., Van Laar, H. H., Van Keulen, H., & Louwerse, W. (1985). Photosynthesis, CO2 and plant production. In W. Day & R. K. Atkin (Eds.), Wheat growth and modelling (pp. 107-122): Springer.

Guo, Y., Zhao, H., Zhang, S., Wang, Y., & Chow, D. (2021). Modeling and optimization of environment in agricultural greenhouses for improving cleaner and sustainable crop production. Journal of Cleaner Production, 285, 124843. https://doi.org/10.1016/j.jclepro.2020.124843

Guo, Z., & Yu, H. (2012). Forecast Model Construction and Confirmation of Air Humidity in Sunlight Greenhouse. Journal of Agricultural Mechanization Research, 34(3), 94-97. https://doi.org/10.3969/j.issn.1003-188X.2012.03.024

Han, Y., Xue, X., Luo, X., Guo, L., & Li, T. (2014). Establishment of estimation model of solar radiation within solar greenhouse. Transactions of the Chinese Society of Agricultural Engineering, 30(10), 174-181. https://doi.org/10.3969/j.issn.1002-6819.2014.10.022

Hao, J., Zhang, L., Li, P., Sun, Y., Li, J., Qin, X., . . . Han, Y. (2018). Quantitative proteomics analysis of lettuce (Lactuca sativa L.) reveals molecular basis-associated auxin and photosynthesis with bolting

induced by high temperature. International Journal of Molecular Sciences, 19(10), 2967. https://doi.org/10.3390/ijms19102967

He, F., Ma, C., & Zhang, J. (2009). Dynamic Forecasting Model of Humidity in Greenhouse. Transactions of the Chinese Society for Agricultural Machinery, 40(10), 173-177.

He, X., Wang, P., Song, W., Wu, G., Ma, C., & Li, M. (2022). Experimental study on the feasibility and thermal performance of a multifunctional air conditioning system using surplus air thermal energy to heat a Chinese solar greenhouse. Renewable Energy, 198, 1148-1161. https://doi.org/10.1016/j.renene.2022.08.100

Heuvelink, E. (1996). Tomato growth and yield: quantitative analysis and synthesis: Heuvelink.

Heuvelink, E. (1999). Evaluation of a dynamic simulation model for tomato crop growth and development. Annals of Botany, 83(4), 413-422. https://doi.org/10.1006/anbo.1998.0832

Heuvelink, E., & Bertin, N. (1994). Dry-matter partitioning in a tomato crop: comparison of two simulation models. Journal of Horticultural Science, 69(5), 885-903.

Hu, J., Lei, W., Lu, Y., Wei, Z., Liu, H., & Gao, M. (2023). Solar greenhouse temperature prediction model based on 1D CNN-GRU. Transactions of the Chinese Society for Agricultural Machinery, 54(8), 339-346. https://doi.org/10.6041/j.issn.1000-1298.2023.08.033

Huang, L. (2021). Dynamic thermal environment and heating load forecast for solar greenhouse. PhD, Xi'an University of Architecture and Technology.

Huang, L., Deng, L., Li, A., Gao, R., Zhang, L., & Lei, W. (2020). Analytical model for solar radiation transmitting the curved transparent surface of solar greenhouse. Journal of Building Engineering, 32, 101785. https://doi.org/10.1016/j.jobe.2020.101785

Ioslovich, I. (2009). Optimal control strategy for greenhouse lettuce: Incorporating supplemental lighting. Biosystems Engineering, 103(1), 57-67. https://doi.org/10.1016/j.biosystemseng.2009.01.015

Ioslovich, I., Gutman, P. O., & Linker, R. (2009). Hamilton-Jacobi-Bellman formalism for optimal climate control of greenhouse crop. Automatica, 45(5), 1227-1231. https://doi.org/10.1016/j.automatica.2008.12.024

Ioslovich, I., Moran, M. I. R. S., & Gutman, P. (2005). Nonlinear Dynamic Lettuce Growth Model: Parameter Selection and Estimation for N-Limited Experiments. Paper presented at the Proceedings of the 44th IEEE Conference on Decision and Control.

IPCC. (2019). Climate Change and Land Retrieved October, 2024, from https://www.ipcc.ch/srccl/

Jackson, R. D., Idso, S. B., Reginato, R. J., & Pinter Jr, P. J. (1981). Canopy temperature as a crop water stress indicator. Water resources research, 17(4), 1133-1138.

Jamieson, P. D., Porter, J. R., & Wilson, D. R. (1991). A test of the computer simulation model ARCWHEAT1 on wheat crops grown in New Zealand. Field Crops Research, 27(4), 337-350. https://doi.org/10.1016/0378-4290(91)90040-3

Jarvis, P. G. (1976). The interpretation of the variations in leaf water potential and stomatal conductance found in canopies in the field. Philosophical Transactions of the Royal Society of London. B, Biological Sciences, 273(927), 593-610.

Jin, C., Mao, H., Chen, Y., Shi, Q., Wang, Q., Ma, G., & Liu, Y. (2020). Engineering-oriented dynamic optimal control of a greenhouse environment using an improved genetic algorithm with engineering constraint rules. Computers and Electronics in Agriculture, 177, 105698. https://doi.org/10.1016/j.compag.2020.105698

Jolliet, O., Danloy, L., Gay, J.-B., Munday, G. L., & Reist, A. (1991). HORTICERN: an improved static model for predicting the energy consumption of a greenhouse. Agricultural Forest Meteorology, 55(3-4), 265-294.

Jones, J. W., Dayan, E., Allen, L. H., Van Keulen, H., & Challa, H. (1991). A dynamic tomato growth and yield model (TOMGRO). Transactions of the ASAE, 34(2), 663-672. https://doi.org/10.13031/2013.31715

Kalogirou, S. A. (2022). Solar thermal systems: components and applications-introduction.

Kalogirou, S. A., & Florides, G. A. (2004). Measurements of ground temperature at various depths.

Katsoulas, N., Bartzanas, T., Boulard, T., Mermier, M., & Kittas, C. (2006). Effect of vent openings and insect screens on greenhouse ventilation. Biosystems Engineering, 93(4), 427-436. https://doi.org/10.1016/j.biosystemseng.2005.01.001

Katsoulas, N., & Stanghellini, C. (2019). Modelling crop transpiration in greenhouses: Different models for different applications. Agronomy Journal, 9(7), 392. https://doi.org/10.3390/agronomy9070392

Katzin, D., van Henten, E. J., & van Mourik, S. (2022). Process-based greenhouse climate models: Genealogy, current status, and future directions. Agricultural Systems, 198, 103388. https://doi.org/10.1016/j.agsy.2022.103388

Katzin, D., van Mourik, S., Kempkes, F., & van Henten, E. J. (2020). GreenLight – An open source model for greenhouses with supplemental lighting: Evaluation of heat requirements under LED and HPS lamps. Biosystems Engineering, 194, 61-81. https://doi.org/10.1016/j.biosystemseng.2020.03.010

Kittas, C., Boulard, T., Mermier, M., & Papadakis, G. (1996). Wind induced air exchange rates in a greenhouse tunnel with continuous side openings. Journal of Agricultural Engineering Research, 65(1), 37-49.

Kittas, C., Boulard, T., & Papadakis, G. (1997). Natural ventilation of a greenhouse with ridge and side openings: sensitivity to temperature and wind effects. Transactions of the ASAE, 40(2), 415-425. https://doi.org/10.13031/2013.21268

Körner, O., & Van Straten, G. (2008). Decision support for dynamic greenhouse climate control strategies. Computers and Electronics in Agriculture, 60(1), 18-30. https://doi.org/10.1016/j.compag.2007.05.005

Kuijpers, W. J., Antunes, D. J., van Mourik, S., van Henten, E. J., & van de Molengraft, M. J. G. (2022). Weather forecast error modelling and performance analysis of automatic greenhouse climate control. Biosystems Engineering, 214, 207-229. https://doi.org/10.1016/j.biosystemseng.2021.12.014

Lambora, A., Gupta, K., & Chopra, K. (2019, 14-16 Feb. 2019). Genetic algorithm- A literature review. Paper presented at the 2019 International Conference on Machine Learning, Big Data, Cloud and Parallel Computing (COMITCon).

Lawrence, M. G. (2005). The relationship between relative humidity and the dewpoint temperature in moist air: A simple conversion and applications. Bulletin of the American Meteorological Society, 86(2), 225-234. https://doi.org/10.1175/BAMS-86-2-225

Lazof, D. B., Bernstein, N., & Läuchli, A. (1991). Growth and development of the Lactuca sativa shoot as affected by NaCl stress: consideration of leaf developmental stages. Botanical Gazette, 152(1), 72-76. https://www.jstor.org/stable/2995493

Li, J., Wang, W., Su, Y., & Ji, Q. (2016). Spatial pattern and interrelation of soil water content and thermal conductivity in greenhouse. Transactions of the Chinese Society of Agricultural Engineering, 32(19), 127-132. https://doi.org/10.11975/j.issn.1002-6819.2016.19.018

Li, M., Zhou, C., Ding, X., Wei, X., Huang, S., & He, Y. (2016). Heat insulation and storage performances of polystyrene-brick composite wall in Chinese solar greenhouse. Transactions of the Chinese Society of Agricultural Engineering, 32(1), 200-205. https://doi.org/10.11975/j.issn.1002-6819.2016.01.028

Li, M., Zhou, C., & Wei, X. (2015). Thickness determination of heat storage layer of wall in solar greenhouse. Transactions of the Chinese Society of Agricultural Engineering, 31(2), 177-183. (in Chinese with English abstract). https://doi.org/10.3969/j.issn.1002-6819.2015.02.025

Li, Q., Gao, H., Zhang, X., Ni, J., & Mao, H. (2022). Describing Lettuce Growth Using Morphological Features Combined with Nonlinear Models. Agronomy, 12(4), 860. https://doi.org/10.3390/agronomy12040860

Li, T. (2013). Theory and practice on vegetable cultivation in solar greenhouse. Beijing: China Agriculture Press.

Li, T. (2023). Review and prospects of the development of the protected horticulture industry in China. Paper presented at the China Greenhouse Horticulture Industry Conference 2023, Hangzhou.

Li, X., & Chen, Q. (2004). Calculation of the solar radiation inside the sunlight greenhouse using the Cloud Cover Coefficient Method. Transactions of the Chinese Society of Agricultural Engineering (Transactions of the CSAE), 20(3), 212-216.

Liang, H., Hu, K., Batchelor, W. D., Qin, W., & Li, B. (2018). Developing a water and nitrogen management model for greenhouse vegetable production in China: Sensitivity analysis and evaluation. Ecological Modelling, 367, 24-33. https://doi.org/10.1016/j.ecolmodel.2017.10.016

Lin, D., Zhang, L., & Xia, X. (2021). Model predictive control of a Venlo-type greenhouse system considering electrical energy, water and carbon dioxide consumption. Applied Energy, 298. https://doi.org/10.1016/j.apenergy.2021.117163

Liu, C., Ma, C., Wang, P., Zhao, S., Cheng, J., & Wang, M. (2015). Theoretical analysis and experimental verification of heat transfer through thick covering materials of solar greenhouse. Transactions of the Chinese Society of Agricultural Engineering, 31(2), 170-176. https://doi.org/10.3969/j.issn.1002-6819.2015.02.024

Liu, R., Li, M., Guzmán, J. L., & Rodríguez, F. (2021). A fast and practical one-dimensional transient model for greenhouse temperature and humidity. Computers and Electronics in Agriculture, 186, 106186. https://doi.org/10.1016/j.compag.2021.106186

Liu, X., Zhao, J., Shi, C., & Zhao, B. (2007). Study on soil layer of constant temperature. Acta Energiae Solaris Sinica, 28(5), 494-498. https://doi.org/10.3321/j.issn:0254-0096.2007.05.007

Liu, Y., Ding, W., & Zhang, J. (2004). Time for uncovering and covering heat preservation curtain for sunlight greenhouses. Transactions of The Chinese Society of Agricultural Engineering, 4.

Lu, W., Zhang, Y., Fang, H., Ke, X., & Yang, Q. (2017). Modelling and experimental verification of the thermal performance of an active solar heat storage-release system in a Chinese solar greenhouse. Biosystems Engineering, 160, 12-24. https://doi.org/10.1016/j.biosystemseng.2017.05.006

Ma, C., Lu, H., Li, R., & Qu, M. (2010). One-dimensional Finite difference model and numerical simulation for heat transfer of wall in Chinese solar greenhouse. Transactions of the Chinese Society of Agricultural Engineering, 26(6), 231-237. https://doi.org/10.3969/j.issn.1002-6819.2010.06.040

Ma, C., Wang, L., Ding, X., Hou, C., & Han, J. (2008). Theories and methods for calculation of ventilation rate in design rule for greenhouse ventilation. Journal of Shanghai Jiao Tong University (Agricultural Science), 26(5), 416-419,423. https://doi.org/10.3969/j.issn.1671-9964.2008.05.016

Ma, C., Zhao, S., Cheng, J., Wang, N., Jiang, Y., Wang, S., & Li, B. (2013). On Establishing Light Environment Model in Chinese Solar Greenhouse. Journal of Shenyang Agricultural University, 44(5), 513-517. https://doi.org/10.3969/j.issn.1000-1700.2013.05.001

Mahmood, F., Govindan, R., Bermak, A., Yang, D., & Al-Ansari, T. (2023). Data-driven robust model predictive control for greenhouse temperature control and energy utilisation assessment. Applied Energy, 343, 121190. https://doi.org/10.1016/j.apenergy.2023.121190

management, H. g. (2024). ISII supports and automatically controls all your greenhouse needs, 2024, from https://hoogendoorn.com/en/our-solutions/isii/

Mao, H., Jin, C., & Chen, Y. (2018). Research progress and prospect on control methods of greenhouse environment. Transactions of the Chinese Society for Agricultural Machinery, 49(2), 1-13. https://doi.org/10.6041/j.issn.1000-1298.2018.02.001

Marcelis, L. F. M. (1996). Sink strength as a determinant of dry matter partitioning in the whole plant. Journal of experimental botany, 47(Special Issue), 1281-1291. https://doi.org/10.1093/jxb/47.Special_Issue.1281

Marcelis, L. F. M., Heuvelink, E., & Goudriaan, J. (1998). Modelling biomass production and yield of horticultural crops: a review. Scientia Horticulturae, 74, 83-111. https://doi.org/10.1016/S0304-4238(98)00083-1

Martinez-Gracia, A., Arauzo, I., & Uche, J. (2019). Solar energy availability Solar Hydrogen Production (pp. 113-149): Elsevier.

Mathieu, J., Linker, R., Levine, L., Albright, L., Both, A. J., Spanswick, R., . . . Langhans, R. (2006). Evaluation of the Nicolet model for simulation of short-term hydroponic lettuce growth and nitrate uptake. Biosystems engineering, 95(3), 323-337. https://doi.org/10.1016/j.biosystemseng.2006.07.006

Mayne, D. Q. (2014). Model predictive control: Recent developments and future promise. Automatica, 50(12), 2967-2986. https://doi.org/10.1016/j.automatica.2014.10.128

Meng, L., Yang, Q., Bot, G. P. A., & Wang, N. (2009). Visual simulation model for thermal environment in Chinese solar greenhouse. Transactions of the Chinese Society of Agricultural Engineering, 25(1), 164-170.

Mohmed, G., Heynes, X., Naser, A., Sun, W., Hardy, K., Grundy, S., & Lu, C. (2023). Modelling daily plant growth response to environmental conditions in Chinese solar greenhouse using Bayesian neural network. Scientific Reports, 13(1), 4379. https://doi.org/10.1038/s41598-023-30846-y

Mokhtar, A., El-Ssawy, W., He, H., Al-Anasari, N., Sammen, S. S., Gyasi-Agyei, Y., & Abuarab, M. (2022). Using machine learning models to predict hydroponically grown lettuce yield. Frontiers in Plant Science, 13, 706042. https://doi.org/10.3389/fpls.2022.706042

Monteith, J. L. (1965). Evaporation and environment. Symposia of the Society for Experimental Biology, 19, 205-234.

Monteith, J. L. (1995). A reinterpretation of stomatal responses to humidity. Plant, Cell & Environment, 18(4), 357-364. https://doi.org/10.1111/j.1365-3040.1995.tb00371.x

Monteith, J. L., & Unsworth, M. H. (2013). Principles of environmental physics: plants, animals, and the atmosphere (4th ed.). Oxford: Academic Press.

Morcego, B., Yin, W., Boersma, S., van Henten, E., Puig, V., & Sun, C. (2023). Reinforcement Learning versus Model Predictive Control on greenhouse climate control. Computers and Electronics in Agriculture, 215, 108372. https://doi.org/10.1016/j.compag.2023.108372

Mortensen, L. M. (1986). Effect of relative humidity on growth and flowering of some greenhouse plants. Scientia Horticulturae, 29(4), 301-307. https://doi.org/10.1016/0304-4238(86)90013-0

Nijskens, J., Deltour, J., Coutisse, S., & Nisen, A. (1984). Heat transfer through covering materials of greenhouses. Agricultural and Forest Meteorology, 33(2), 193-214. https://doi.org/10.1016/0168-1923(84)90070-4

Norton, T., Sun, D.-W., Grant, J., Fallon, R., & Dodd, V. (2007). Applications of computational fluid dynamics (CFD) in the modelling and design of ventilation systems in the agricultural industry: A review. Bioresource Technology, 98(12), 2386-2414. https://doi.org/10.1016/j.biortech.2006.11.025

Ouammi, A. (2021). Model predictive control for optimal energy management of connected cluster of microgrids with net zero energy multi-greenhouses. Energy, 234, 121274. https://doi.org/10.1016/j.energy.2021.121274

Papadakis, G., Frangoudakis, A., & Kyritsis, S. (1992). Mixed, forced and free convection heat transfer at the greenhouse cover. Journal of Agricultural Engineering Research, 51, 191-205.

Pardossi, A., Tognoni, F., & Incrocci, L. (2004). Mediterranean greenhouse technology. Chronica horticulturae, 44(2), 28-34.

Payne, H. J., van Henten, E., & van Mourik, S. (2024). Prediction uncertainty of greenhouse electrical power and gas demand: Part 1, the role of parameter uncertainty. Biosystems Engineering, 239, 35-48. https://doi.org/10.1016/j.biosystemseng.2024.01.006

Pearson, S., Wheeler, T. R., Hadley, P., & Wheldon, A. E. (1997). A validated model to predict the effects of environment on the growth of lettuce (Lactuca sativa L.): implications for climate change. Journal of Horticultural Science, 72(4), 503-517. https://doi.org/10.1080/14620316.1997.11515538

Penning De Vries, F. W. T., & Van Laar, H. H. (1982). Simulation of growth processes and the model BACROS. In F. W. T. Penning de Vries & H. H. van Laar (Eds.), Simulation of plant growth and crop production (pp. 114-135). Wageningen: Pudoc.

Pérez Parra, J., Baeza, E., Montero, J. I., & Bailey, B. J. (2004). Natural Ventilation of Parral Greenhouses. Biosystems Engineering, 87(3), 355-366. https://doi.org/10.1016/j.biosystemseng.2003.12.004

PRC, M. o. A. o. t. (2018). Code for ventilation design of greenhouse (Vol. NY/T 1451-2018).

Priva. (2024). Greenhouse climate control: Improve growth and yield, 2024, from https://www.priva.com/horticulture/greenhouse-climate-control

Qi, F., Wei, X., & Zhang, Y. (2017). Development status and future research emphase on greenhouse horticultural equipment and its relative technology in China. Transactions of the Chinese Society of Agricultural Engineering, 33(24), 1-9. https://doi.org/10.11975/j.issn.1002-6819.2017.24.001

Qiao, X., Zheng, W., Zhang, X., Shan, F., Wang, M., & Liang, D. (2022). Study on solar greenhouse environment prediction method based on LSTM-GRU. Jiangsu Agricultural Sciences, 50(16), 211-218.

Qin, L., Ma, G., Chu, Z., & Wu, G. (2016). Molding and control of greenhouse temperature-humidity system based on grey prediction model. Transactions of the Chinese Society of Agricultural Engineering, 32, 233-241. https://doi.org/10.11975/j.issn.1002-6819.2016.z1.032

Qu, Y., Ning, D., Lai, Z., Cheng, Q., & Mu, L. (2011). Neural networks based on PID control for greenhouse temperature. Transactions of the Chinese Society of Agricultural Engineering, 27(2), 307-311.

Rahimikhoob, H., Delshad, M., & Habibi, R. (2023). Leaf area estimation in lettuce: Comparison of artificial intelligence-based methods with image analysis technique. Measurement, 222, 113636. https://doi.org/10.1016/j.measurement.2023.113636

Rastogi, M., Singh, S., & Pathak, H. (2002). Emission of carbon dioxide from soil. Current science, 82(5), 510-517.

Rawson, H. M., Begg, J. E., & Woodward, R. G. (1977). The effect of atmospheric humidity on photosynthesis, transpiration and water use efficiency of leaves of several plant species. Planta, 134(1), 5-10. https://doi.org/10.1007/BF00390086

Reidsma, P., & Descheemaeker, K. (2019). The Art of Modelling. Wageningen: Wageningen University & Research.

Righini, I., Vanthoor, B., Verheul, M. J., Naseer, M., Maessen, H., Persson, T., & Stanghellini, C. (2020). A greenhouse climate-yield model focussing on additional light, heat harvesting and its validation. Biosystems Engineering, 194, 1-15. https://doi.org/10.1016/j.biosystemseng.2020.03.009

Rohde, W., & Forni, F. (2023). Lettuce modelling for growth control in precision agriculture. European Journal of Control, 74, 100843. https://doi.org/10.1016/j.ejcon.2023.100843

Rosental, L., Still, D. W., You, Y., Hayes, R. J., & Simko, I. (2021). Mapping and identification of genetic loci affecting earliness of bolting and flowering in lettuce. Theoretical and Applied Genetics, 134(10), 3319-3337. https://doi.org/10.1007/s00122-021-03898-9

Roy, J. C., Boulard, T., Kittas, C., & Wang, S. (2002). Convective and ventilation transfers in greenhouses, part 1: the greenhouse considered as a perfectly stirred tank. Biosystems Engineering, 83(1), 1-20. https://doi.org/10.1006/bioe.2002.0107

Rutquist, P. E., & Edvall, M. M. (2010). Propt-matlab optimal control software. Tomlab Optimization Inc, 260(1), 12.

Sanchez-Molina, J. A., Li, M., Rodriguez, F., Guzman, J. L., Wang, H., & Yang, X. (2017). Development and test verification of air temperature model for Chinese solar and Spainish Almeria-type greenhouses. International Journal of Agricultural and Biological Engineering, 10(4), 66-76. https://doi.org/10.25165/j.ijabe.20171004.2398

Schuepp, P. H. (1993). Tansley review No. 59. Leaf boundary layers. New Phytologist, 125, 477-507. https://www.jstor.org/stable/2558258

Seginer, I. (1997). Some artificial neural network applications to greenhouse environmental control. Computers and Electronics in Agriculture, 18(2-3), 167-186. https://doi.org/10.1016/S0168-1699(97)00028-8

Seginer, I. (2003). A dynamic model for nitrogen-stressed lettuce. Annals of Botany, 91(6), 623-635. https://doi.org/10.1093/aob/mcg069

Seginer, I., Buwalda, F., & van Straten, G. (1999). Lettuce growth limited by nitrate supply. Paper presented at the III International Workshop on Models for Plant Growth and Control of the Shoot and Root Environments in Greenhouses. https://doi.org/10.17660/ActaHortic.1999.507.16

Seginer, I., Linker, R., Buwalda, F., Van Straten, G., & Bleyaert, P. (2003). The NICOLET lettuce model: a theme with variations. Paper presented at the International Workshop on Models for Plant Growth and Control of Product Quality in Horticultural Production 654.

Seginer, I., Shina, G., Albright, L. D., & Marsh, L. S. (1991). Optimal temperature setpoints for greenhouse lettuce. Journal of Agricultural Engineering Research, 49, 209-226. https://doi.org/10.1016/0021-8634(91)80040-L

Seginer, I., van Straten, G., & Buwalda, F. (1998). Nitrate concentration in greenhouse lettuce: a modeling study. Paper presented at the II Modelling Plant Growth, Environmental Control and Farm Management in Protected Cultivation. https://doi.org/10.17660/ActaHortic.1998.456.21

Sethi, V. P. (2009). On the selection of shape and orientation of a greenhouse: Thermal modeling and experimental validation. Solar Energy, 83(1), 21-38. https://doi.org/10.1016/j.solener.2008.05.018

Shimizu, H., Kushida, M., & Fujinuma, W. (2008). A growth model for leaf lettuce under greenhouse environments. Environmental Control in Biology, 46(4), 211-219. https://doi.org/10.2525/ecb.46.211

Sinclair, T. R., & Seligman, N. a. (2000). Criteria for publishing papers on crop modeling. Field Crops Research, 68(3), 165-172. https://doi.org/10.1016/S0378-4290(00)00105-2

Spitters, C. J. T., Van Keulen, H., & Van Kraalingen, D. W. G. (1989). A simple and universal crop growth simulator: SUCROS87. In R. Rabbinge, S. A. Ward & H. H. van Laar (Eds.), Simulation and systems management in crop protection (pp. 147-181). Wageningen: Pudoc.

Srinivasan, B., Palanki, S., & Bonvin, D. (2003). Dynamic optimization of batch processes: I. Characterization of the nominal solution. Computers & Chemical Engineering, 27(1), 1-26. https://doi.org/10.1016/S0098-1354(02)00116-3

Stangheilini, C. (1987). TRANSPIRATION OF GREENHOUSE CROPS: an aid to climate management. Wageningen University and Research, The Netherlands.

Stanghellini, C., van't Oosfer, B., & Heuvelink, E. (2019). Greenhouse horticulture: technology for optimal crop production. Wageningen: Wageningen Academic Publishers.

Stützel, H., & Chen, T. (2020). 5 Models of Vegetable Growth and Development (Vol. 10).

Su, Y., Yu, Q., & Zeng, L. (2020). Parameter self-tuning pid control for greenhouse climate control problem. IEEE Access, 8, 186157-186171. https://doi.org/10.1109/ACCESS.2020.3030416

Sun, W., Guo, W., Xu, F., Wang, L., Xue, X., Li, Y., & Chen, Y. (2015). Application effect of surplus air heat pump heating system in Chinese solar greenhouse. Transactions of the Chinese Society of Agricultural Engineering, 31(17), 235-243. https://doi.org/10.11975/j.issn.1002-6819.2015.17.031

Sun, W., Wei, X., Zhou, B., Lu, C., & Guo, W. (2022). Greenhouse heating by energy transfer between greenhouses: System design and implementation. Applied Energy, 325. https://doi.org/10.1016/j.apenergy.2022.119815

Sun, W., Zhang, Y., Yang, Q., Xue, X., & Guo, W. (2017). Nighttime cooling of solar greenhouse in summer based on water source heat pump system. Research of Agricultural Modernization, 38(5), 885-892. https://doi.org/10.13872/j.1000-0275.2017.0028

Sun, W., Zhou, B., Xu, F., Shang, C., Lu, C., & Guo, W. (2019). Performance of positive pressure fan-pad cooling system and cooling load model for Chinese solar greenhouse. Transactions of the Chinese Society of Agricultural Engineering, 35(16), 214-224. https://doi.org/10.11975/j.issn.1002-6819.2019.16.024

Sweeney, D. G., Hand, D. W., Slack, G., & Thornley, J. H. M. (1981). Modelling the growth of winter lettuce. Mathematics and plant physiology, 217-229.

Talbot, M.-H., & Monfet, D. (2024). Development of a crop growth model for the energy analysis of controlled agriculture environment spaces. Biosystems Engineering, 238, 38-50. https://doi.org/10.1016/j.biosystemseng.2023.12.012

Tang, C., Shi, B., & Gu, K. (2011). Experimental investigation on evaporation process of water in soil during drying. Journal of Engineering Geology, 19(6), 875-881. https://doi.org/10.3969/j.issn.1004-9665.2011.06.012

Tap, F. (2000). Economics-based optimal control of greenhouse tomato crop production. Wageningen University and Research, The Netherlands.

Tei, F., Aikman, D. P., & Scaife, A. (1996). Growth of lettuce, onion and red beet. 2. Growth modelling. Annals of Botany, 78(5), 645-652.

Thompson, H. C., Langhans, R. W., Both, A.-J., & Albright, L. D. (1998). Shoot and root temperature effects on lettuce growth in a floating hydroponic system. Journal of the American Society for Horticultural Science, 123(3), 361-364. https://doi.org/10.21273/JASHS.123.3.361

Thornley, J. H. M., & Hurd, R. G. (1974). An analysis of the growth of young tomato plants in water culture at different light integrals and CO2 concentrations: II. A mathematical model. Annals of Botany, 38(2), 389-400. https://doi.org/10.1093/oxfordjournals.aob.a084822

Tian, Y. (2021). Study on natural ventilation and enhancement in single-slope solar Greenhouse. Xi'an University of Architecture and Technology.

Tibbitts, T. W., & Bottenberg, G. (1976). Growth of lettuce under controlled humidity levels. Journal of the American Society for Horticultural Science, 101(1), 70-73. https://doi.org/10.21273/JASHS.101.1.70

Tiwari, G. N. (2003). Greenhouse technology for controlled environment: Alpha Science Int'l Ltd.

Tong, G., Che, Z., Bai, Y., & Yamaguchi, T. (2008). Air Exchange Rate Calculation for Solar Greenhouse Using Thermal Balance Method. Journal of Shenyang Agricultural University, 39(4), 459-462. https://doi.org/10.3969/j.issn.1000-1700.2008.04.017

Tong, G., & Christopher, D. M. (2009). Simulation of temperature variations for various wall materials in Chinese solar greenhouses using computational fluid dynamics. Transactions of the Chinese Society of Agricultural Engineering, 25(3), 153-157.

Tong, G., & Christopher, D. M. (2019). Temperature variations in energy storage layers in Chinese solar greenhouse walls. Transactions of the Chinese Society of Agricultural Engineering, 35(7), 170-177. https://doi.org/10.11975/j.issn.1002-6819.2019.07.021

Tong, G., Christopher, D. M., & Li, B. (2009). Numerical modelling of temperature variations in a Chinese solar greenhouse. Computers and Electronics in Agriculture, 68(1), 129-139. https://doi.org/10.1016/j.compag.2009.05.004

Tong, G., Christopher, D. M., Li, T., & Bai, Y. (2010). Influence of thermal blanket position on solar greenhouse temperature distributions. Transactions of the Chinese Society of Agricultural Engineering, 26(10), 253-258. https://doi.org/10.3969/j.issn.1002-6819.2010.10.043

Tong, G., Christopher, D. M., & Zhang, G. (2018). New insights on span selection for Chinese solar greenhouses using CFD analyses. Computers and Electronics in Agriculture, 149, 3-15. https://doi.org/10.1016/j.compag.2017.09.031

United Nations. (2024). World Population Prospects 2024 Retrieved October, 2024, from https://population.un.org/wpp/Download/Standard/MostUsed/

Van Beveren, P. J. M., Bontsema, J., Van Straten, G., & Van Henten, E. J. (2015). Optimal control of greenhouse climate using minimal energy and grower defined bounds. Applied Energy, 159, 509-519. https://doi.org/10.1016/j.apenergy.2015.09.012

Van Henten, E. J. (1994a). Greenhouse climate management: an optimal control approach. Wageningen University and Research, The Netherlands.

Van Henten, E. J. (1994b). Validation of a dynamic lettuce growth model for greenhouse climate control. Agricultural Systems, 45(1), 55-72. https://doi.org/10.1016/S0308-521X(94)90280-1

Van Henten, E. J. (2003). Sensitivity Analysis of an Optimal Control Problem in Greenhouse Climate Management. Biosystems Engineering, 85(3), 355-364. https://doi.org/10.1016/S1537-5110(03)00068-0

Van Henten, E. J., & Bontsema, J. (2009). Time-scale decomposition of an optimal control problem in greenhouse climate management. Control Engineering Practice, 17(1), 88-96. https://doi.org/10.1016/j.conengprac.2008.05.008

van Holsteijn, H. M. C. (1980). Growth of lettuce: Quantitative analysis of growth: Veenman.

van Keulen, H., Penning de Vries, F. W. T., & Drees, E. M. (1982). A summary model for crop growth. In F. W. T. Penning de Vries & H. H. van Laar (Eds.), Simulation of plant growth and crop production (pp. 87-97). Wageningen: Pudoc.

van Laar, H. H., Goudriaan, J., & van Keulen, H. (1997). SUCROS97: Simulation of crop growth for potential and water-limited production situations. As applied to spring wheat. Wageningen: AB-DLO, TPE.

Van Ooteghem, R. J. C. (2010). Optimal control design for a solar greenhouse. Wageningen University and Research, The Netherlands.

Van Ploeg, D., & Heuvelink, E. (2005). Influence of sub-optimal temperature on tomato growth and yield: a review. The Journal of Horticultural Science and Biotechnology, 80(6), 652-659. https://doi.org/10.1080/14620316.2005.11511994

Van Straten, G., Van Willigenburg, G., Van Henten, E., & Van Ooteghem, R. (2010). Optimal control of greenhouse cultivation. Boca Raton: CRC Press.

Vanthoor, B. H. E. (2011). A model-based greenhouse design method. Wageningen University and Research, The Netherlands.

Vanthoor, B. H. E., De Visser, P. H. B., Stanghellini, C., & Van Henten, E. J. (2011). A methodology for model-based greenhouse design: Part 2, description and validation of a tomato yield model. Biosystems engineering, 110(4), 378-395. https://doi.org/10.1016/j.biosystemseng.2011.08.005

Vanthoor, B. H. E., Stanghellini, C., Van Henten, E. J., & De Visser, P. H. B. (2011). A methodology for model-based greenhouse design: Part 1, a greenhouse climate model for a broad range of designs and climates. Biosystems Engineering, 110(4), 363-377. https://doi.org/10.1016/j.biosystemseng.2011.06.001

Vanthoor, B. H. E., Van Henten, E. J., Stanghellini, C., & De Visser, P. H. B. (2011). A methodology for model-based greenhouse design: Part 3, sensitivity analysis of a combined greenhouse climate-crop yield model. Biosystems Engineering, 110(4), 396-412. https://doi.org/10.1016/j.biosystemseng.2011.08.006

Villarreal-Guerrero, F., Kacira, M., Fitz-Rodríguez, E., Kubota, C., Giacomelli, G. A., Linker, R., & Arbel, A. (2012). Comparison of three evapotranspiration models for a greenhouse cooling strategy with natural ventilation and variable high pressure fogging. Scientia Horticulturae, 134, 210-221. https://doi.org/10.1016/j.scienta.2011.10.016

Volente, G. (2022). Lettuce temperature tolerance, 2024, from https://www.greenhousetoday.com/lettuce-temperature-tolerance/

Wallach, D., Makowski, D., Jones, J. W., & Brun, F. (2019). Chapter 6 - Uncertainty and Sensitivity Analysis. In D. Wallach, D. Makowski, J. W. Jones & F. Brun (Eds.), Working with Dynamic Crop Models (Third Edition) (pp. 209-250): Academic Press.

Wang, N., Ma, C., Zhao, S., Jiang, Y., & Song, J. (2013). Measurement of Transmissivity of Solar Greenhouse Covering Materials. Journal of Shenyang Agricultural University, 44(5), 531-535. https://doi.org/10.3969/j.issn.1000-1700.2013.05.004

Wang, X. (2017). Research of estimation model for temporal and spatial distribution of environmental elements in solar greenhouse. Msc, Shihezi University, Shihezi, China.

Wu, C., Zhao, X., & Guo, W. (2007). Simulation and analysis of the temperature inside the sunlight greenhouse. Transactions of the Chinese Society of Agricultural Engineering, 23(4), 190-195. https://doi.org/10.3321/j.issn:1002-6819.2007.04.038

Wu, X., Liu, X., Yue, X., Xu, H., Li, T., & Li, Y. (2021). Effect of the ridge position ratio on the thermal environment of the Chinese solar greenhouse. Royal Society Open Science, 8(5), 201707. https://doi.org/10.1098/rsos.201707

Xiao, J., Wang, Q., Wang, X., Hu, Y., Cao, Y., & Li, J. (2023). An earth-air heat exchanger integrated with a greenhouse in cold-winter and hot-summer regions of northern China: Modeling and experimental analysis. Applied Thermal Engineering, 232, 120939. https://doi.org/10.1016/j.applthermaleng.2023.120939

Xiao, X., Kuang, X., Sauer, T. J., Heitman, J. L., & Horton, R. (2015). Bare soil carbon dioxide fluxes with time and depth determined by high-resolution gradient-based measurements and surface chambers. Soil Science Society of America Journal, 79(4), 1073-1083.

Xu, D., Du, S., & Van Willigenburg, G. (2018). Adaptive two time-scale receding horizon optimal control for greenhouse lettuce cultivation. Computers and Electronics in Agriculture, 146, 93-103. https://doi.org/10.1016/j.compag.2018.02.001

Xu, D., Du, S., & Van Willigenburg, G. (2019). Double closed-loop optimal control of greenhouse cultivation. Control Engineering Practice, 85, 90-99. https://doi.org/10.1016/j.conengprac.2019.01.010

Xu, D., Du, S., & Van Willigenburg, L. G. (2018). Optimal control of Chinese solar greenhouse cultivation. Biosystems Engineering, 171, 205-219. https://doi.org/10.1016/j.biosystemseng.2018.05.002

Xu, H., Cao, Y., Li, Y., J, G., W, J., & Z, Z. (2019). Establishment and application of solar radiation model in solar greenhouse. Transactions of the Chinese Society of Agricultural Engineering, 35(7), 160-169. https://doi.org/10.11975/j.issn.1002-6819.2019.07.020

Xu, W., Guo, H., & Ma, C. (2022). An active solar water wall for passive solar greenhouse heating. Applied Energy, 308, 118270. https://doi.org/10.1016/j.apenergy.2021.118270

Yang, Q., Wei, L., & Yu, H. (2004). Study on CO2 transfer and ecosystem optimization of poultry-vegetable coexisting solar greenhouse. Chinese Journal of Agrometeorology, 25(02), -.

Yang, X., Zhu, G., Jiang, X., Huang, K., & Li, X. (2014). Development and demonstration of intelligent controller in solar greenhouse. Journal of Chinese Agricultural Mechanization, 35(3), 95-98. https://doi.org/10.13733/j.jcam.issn.2095-5553.2014.03.025

Yau, M. K., & Rogers, R. R. (1996). A short course in cloud physics: Elsevier.

Yin, X., & Van Laar, H. H. (2005). Crop systems dynamics: an ecophysiological simulation model for genotype-by-environment interactions. Wageningen: Wageningen Academic Publishers.

Yu, H., Chen, Y., Hassan, S. G., & Li, D. (2016). Prediction of the temperature in a Chinese solar greenhouse based on LSSVM optimized by improved PSO. Computers and Electronics in Agriculture, 122, 94-102. https://doi.org/10.1016/j.compag.2016.01.019

Zhang, G., Fu, Z., Yang, M., Liu, X., Dong, Y., & Li, X. (2019). Nonlinear simulation for coupling modeling of air humidity and vent opening in Chinese solar greenhouse based on CFD. Computers and Electronics in Agriculture, 162, 337-347. https://doi.org/10.1016/j.compag.2019.04.024

Zhang, J. (2003). Evaluation for physical model of environmental factors in energy-saving solar greenhouse. Msc, Nanjing Agricultural University, Nanjing, China.

Zhang, J., Zhao, S., Dai, A., Wang, P., Liu, Z., Liang, B., & Ding, T. (2022). Greenhouse Natural Ventilation Models: How Do We Develop with Chinese Greenhouses? Agronomy, 12(9), 1995. https://doi.org/10.3390/agronomy12091995

Zhang, K., Burns, I. G., Broadley, M. R., & Turner, M. (2003). Developing a dynamic model for glasshouse lettuce growth and nitrate accumulation. Paper presented at the International Workshop on Models for Plant Growth and Control of Product Quality in Horticultural Production. https://doi.org/10.17660/ActaHortic.2004.654.6

Zhang, Q., Yu, H., Zhang, Z., Dong, L., Zhang, Q., Shao, C., . . . Wang, X. (2012). Airflow simulation in solar greenhouse using CFD model. Transactions of the Chinese Society of Agricultural Engineering, 28(16), 166-171. https://doi.org/10.3969/j.issn.1002-6819.2012.16.026

Zhang, X., Lv, J., Xie, J., Yu, J., Zhang, J., Tang, C., . . . Wang, C. (2020). Solar radiation allocation and spatial distribution in Chinese solar greenhouses: Model development and application. Energies, 13(5), 1108. https://doi.org/10.3390/en13051108

Zhang, X., Wang, H., Zou, Z., & Wang, S. (2016). CFD and weighted entropy based simulation and optimisation of Chinese Solar Greenhouse temperature distribution. Biosystems Engineering, 142, 12-26. https://doi.org/10.1016/j.biosystemseng.2015.11.006

Zhang, X., Wang, Y., Huang, G., Feng, F., Liu, X., Guo, R., . . . Mei, X. (2020). Atmospheric humidity and genotype are key determinants of the diurnal stomatal conductance pattern. Journal of Agronomy and Crop Science, 206(2), 161-168. https://doi.org/10.1111/jac.12375

Zhang, Y., Henke, M., Li, Y., Yue, X., Xu, D., Liu, X., & Li, T. (2020). High resolution 3D simulation of light climate and thermal performance of a solar greenhouse model under tomato canopy structure. Renewable Energy, 160, 730-745. https://doi.org/10.1016/j.renene.2020.06.144

Zhang, Y., Ma, C., Liu, Y., & Han, J. (2010). Numerical simulation and experimental verification of heat transfer through multi-layer covering of greenhouse. Transactions of the Chinese Society of Agricultural Engineering, 26(4), 237-242. https://doi.org/10.3969/j.issn.1002-6819.2010.04.040

Zhang, Y., & Zou, Z. (2017). Optimization experiment of light transmittance and active lighting mechanism of solar greenhouse. Transactions of the Chinese Society of Agricultural Engineering, 33(11), 178-186.

Zheng, R., Yang, W., & Liu, Z. (2023). Numerical simulation of humid heat characteristics in solar greenhouse under different ventilation modes. Journal of China Agricultural University, 28(3), 140-150. https://doi.org/10.11841/j.issn.1007-4333.2023.03.13

Zhou, X., Liu, Q., Katzin, D., Qian, T., Heuvelink, E., & Marcelis, L. F. M. (2023). Boosting the prediction accuracy of a process-based greenhouse climate-tomato production model by particle filtering and deep learning. Computers and Electronics in Agriculture, 211, 107980. https://doi.org/10.1016/j.compag.2023.107980

Zhu, Y., Cai, H., Song, L., & Chen, H. (2017). Oxygation improving soil aeration around tomato root zone in greenhouse. Transactions of the Chinese Society of Agricultural Engineering (Transactions of the CSAE), 33(21), 163-172. https://doi.org/10.11975/j.issn.1002-6819.2017.21.019

Zou, W., Zhang, B., Yao, F., & He, C. (2015). Verification and forecasting of temperature and humidity in solar greenhouse based on improved extreme learning machine algorithm. Transactions of the Chinese Society of Agricultural Engineering, 31(24), 194-200. https://doi.org/10.11975/j.issn.1002-6819.2015.24.029

Zu, L., Liu, P., Zhao, Y., Li, T., & Li, H. (2023). Solar Greenhouse Environment Prediction Model Based on SSA-LSTM. Transactions of the Chinese Society for Agricultural Machinery, 54(2), 351-358. https://doi.org/10.6041/j.issn.1000-1298.2023.02.036